The University Of Sheffield.

Statistical Approaches to Investigating Star Formation

Suraiya Akter

Department of Physics & Astronomy

The University of Sheffield

A dissertation submitted in candidature for the degree of Doctor of Philosophy at the University of Sheffield

November, 2020

Contents

List of Figures

List of Tables

Declaration

I declare that no part of this thesis has been accepted, or is currently being submitted, for any degree or diploma or certificate or any other qualification in this University or elsewhere. This thesis is the result of my own work unless otherwise stated.

Chapter 2 has been based on Akter & Goodwin (2019).

Acknowledgement

I would like to express my sincere gratitude to my supervisor Simon Goodwin for his guidance, true dedication, patience and continuous support. His cheerfulness and great experience in astronomy and astrophysics really made this research a pleasure.

I would like to thank Paul Kerry for his computing support whenever I needed it. Thanks to Dan, Becky, Manu, Joachim, Liam and everyone in the Department of Physics and Astronomy who have provided me help.

A special thanks go to my mother Nurun Nahar, father Jakir Hossain, my brothers Jalal, Belal, Ashik and sister, Nasima.

Changing a career path from being an engineer to an astrophysicist was not easy. I started and continued it with the support and encouragement of my son Orowa. Thanks Baba for everything. My greatest achievement in this world is being the mum of yourself and Aunogh.

Abstract

We know that many stars form in binary systems and their properties provide us with some understanding of how stars form. Binary stars are the only means of directly determining stellar mass. The mass of a star is an important factor for understanding the formation, evolution and observable characteristics of stars. The first study seeks to estimate the fraction of binary systems in stellar clusters with different underlying densities and morphologies. A nearest neighbour method is developed that retrieves close to the true binary fraction when tested against Monte Carlo simulations of star clusters.

In Study 2, attention is shifted to the statistics of the Initial Mass Functions (IMF), a fitted distribution to observed stellar mass data. Many modern studies of the IMF focus on a particular functional form and the parametric fits of those forms. In this chapter, the implications of the parametric fits are examined in more detail. It is shown that the combination of small sample sizes, heavy-tailed distributions, and the use of parametric methods together lead to an inability to detect quite significant differences in the underlying IMF, even when those differences are explicitly modelled and simulated. It is shown that alternative non-parametric methods can do a better job of allowing us to detect key properties of the IMF.

Study 3 reconsiders visual binaries, but now considers the impact of observational selection effects. For visual binaries, an instantaneous observation provides us with their projected separation and the brightness of the member stars. However, they can only be detected if they pass observational selection effects i.e. the projected separation between member stars is wide enough with respect to the luminosity difference. This observational selection effect makes it difficult for us to uncover the true properties of the binary systems in a cluster. In Study 3, a method is developed to compare sample distributions to simulated data to recover true properties in the absence of selection effects. However, while this method is quite successful without selection effects, it is shown that as selection effects grow stronger the "shape" of the sample distribution changes and affects our results. This helps to illustrate some fundamental limitations in distribution comparison methods. In the end, the analysis

is extended to show how improvements in measurement techniques such as Adaptive Optics and interferometry mitigate selection effects just enough to drastically improve the accuracy of this method.

Chapter 1

Introduction

1.1 Introduction

Stars are the building blocks of galaxies and a fundamental constituent of the Universe. Understanding their age, distribution, and composition are important in helping us retrace the history, dynamics, and evolution of galaxies. Stars also host planets, a few of which may be capable of supporting life. Stars produce all the crucial heavy elements for life on Earth such as carbon, nitrogen, oxygen, and phosphorus. Consequently, the study of the formation, evolution and death of stars is a central focus in the field of astronomy. With the advent of improved observational techniques and powerful computers, observers and theorists now have a better understanding of these processes.

Stars are generally born in dense molecular clouds (Allison et al. 2009). Very often a star cluster[1] contains 10^2 – 10^5 stars and most of them form in binary and multiple systems (Reipurth, Jewitt & Keil 2007, Kouwenhoven et al. 2010, Duchêne & Kraus 2013). Many stars form in embedded clusters, some of which remain bound and evolve to open clusters; the rest dynamically dispersing and become a part of the Galactic field.

Stars form with a range of masses - the most important determinant of its lifespan and evolution. This mass range spans from $0.08M_{\odot}$ to over $100M_{\odot}$ and despite the specifics of any cluster's origin, their mass distribution seems to be universal.

This chapter provides the background of Chapters 2, 3 and 4. Section 1.2 introduces the young stellar objects and their evolution towards becoming a main sequence star. Section 1.3 outlines binary and multiple stellar properties from both an observational and theoretical perspective. Finally, section 1.4 discusses the Initial Mass

[1]In this thesis star cluster is defined as a group of stars of same age in a region.

Function (IMF) and a few popular observational fitted models in their functional form.

1.2 Young Stellar Objects and their Evolution

The space between stars is not a vacuum – it consists of an interstellar medium (ISM). The ISM consists of different phases including Molecular clouds, providing the raw material for star formation. Molecular clouds are large clouds of gas and dust, with typical temperatures of around 10-100K and number densities of $10^3 \mathrm{cm}^{-3}$.

From the Interstellar Medium (ISM) to Pre-Main Sequence (PMS) stars, young stellar objects (YSO) pass through a series of evolutionary stages. A good number of papers study these stages (Tobin et al. 2012, Meixner et al. 2013, Codella et al. 2014, Frank et al. 2014, Murillo et al. 2015, Nayak et al. 2016).

1.2.1 Molecular Clouds

Molecular clouds form the part of the ISM where star formation happens. They come in different sizes, ranging from Bok globules with masses of $\sim 10 \mathrm{M}_\odot$ and size (0.04-1.8 pc) (Clemens et al. 1991, Garnett et al. 1999), to giant molecular clouds (GMCs) with masses of $\sim 10^6 \mathrm{M}_\odot$ and size ~ 50 pc (Roman-Duval et al. 2010).

In Molecular Clouds, Hydrogen mainly exists in molecular form and cannot be detected directly due to its lack of excitable states in environments with temperatures < 200K. To observe molecular clouds, astronomers use "tracers" where dust or excitable molecules are used to estimate the underlying H_2 distribution. After Hydrogen, Carbon monoxide (CO) is the most abundant molecule in Molecular Clouds at high column densities (Bolatto et al. 2013). The observed CO intensity is a good tracer of H_2 column density mapping via the empirical constant X factor. At very low temperatures (< 10K) CO freezes out on dust grains (Tafalla et al. 2004). Other tracers such as CS, HCN, NH_3 are used to map H_2, where each of the molecules can trace different regions of the Molecular Cloud of varying density (Evans 1999).

Dust particles are embedded in molecular gas, estimated to be roughly 1% of the total mass of the molecular cloud and can act as a tracer (Whittet 2015). Warmed by radiation from nearby young stars, or coupled to gas, the peak thermal emission of dust can be traced in the sub millimetre region (Motte et al. 1998, Enoch et al. 2007). The dust can also scatter optical and near-IR light from background stars and by extinction mapping can become a tracer of the cloud (Lombardi & Alves 2001).

Linewidths from the tracers provide evidence of supersonic and subsonic gas tur-

bulence. Larson (1981) related the velocity dispersion $\sigma(v)$ of a region to its size L

$$\sigma(v) \propto L^{\beta} \tag{1.1}$$

Where, $\beta \sim 0.5$. Turbulence is a dissipative process and Kolmogorov (1941) describes how energy can cascade down from large-scale to small-scale 'eddies' and ultimately being dissipated into heat by viscosity. The energy spectrum follows a power-law relationship with wave number κ.

$$E(\kappa) = \kappa^{n} \tag{1.2}$$

Here, the spectrum of the turbulence is measured by n, with $n \sim 4$ for Kolmogorov's incompressible energy spectrum.

Brunt & Mac Low (2004) later showed that the Molecular Cloud resemble more like Burgers (1974) supersonic compressible turbulence. For Burgers turbulence most of its energy is dissipated by shocks. The Molecular Cloud is supported against self-gravity by its supersonic turbulent velocity. Turbulence in the ISM plays an important role in star formation (Elmegreen & Scalo 2004, Scalo & Elmegreen 2004, McKee & Ostriker 2007) by controlling the fragmentation of molecular clouds. Galactic molecular clouds are observed to have supersonic turbulence (McKee & Ostriker 2007) with Reynolds numbers up to 10^7 and magnetic Reynolds numbers up to 10^4 (Draine 2011). On a global scale this turbulence supports the cloud against gravitational collapse (Federrath & Klessen 2012, Padoan et al. 2014). At the same time, on a local scale, the turbulent motions generate compression and shocks and these compressive supersonic turbulent shocked layers of gas create a large density gradient within the molecular cloud.

Under the right conditions, these high-density fluctuations can become gravitationally unstable and dissociate themselves from the overall turbulent flow. The largest and most massive of these clumps are potential sites of star formation. The degree of compressive force of the turbulent media is thought to be the reason behind the rate and efficiency at which stars form from the molecular cloud (Padoan & Nordlund 2011, Hennebelle & Chabrier 2011, Federrath & Klessen 2012, Basu & Auddy 2017). The presence of compressive turbulence breaks the massive clump into a number of cores (which contributes to the multiplicity and the mass ratio distributions) to build up a cluster of stars with a wide range of masses.

As a result of turbulent processes, gas and dust are organized in Molecular Clouds in a self-similar manner (Scalo & Elmegreen 2004). The structure is found to be hierarchical (Rosolowsky et al. 2008) in terms of sizes and densities as 'clumps' and

Table 1.1: Physical properties of molecular clouds, clumps and cores. Adapted from Rigby (2016)

Property	Clouds[a]	Clumps[b]	Cores[b]
Mass ($M_\odot$)	$10^2 - 10^6$	$30 - 10^{2c}$	0.2-30[d]
Size (pc)	1-50	0.3-3	0.03-0.2
Density (cm^{-3})	50-800	$10^2 - 10^4$	$10^4 - 10^6$
Temperature (K)	4-8	10-20	8-13[d]
Velocity width (km/s)	0.3 -3.0	0.3-3.0	0.1-0.3

[a] Refers to Molecular cloud properties from the Galactic Ring Survey (Roman-Duval et al. 2010).
[b] Taken from Physical properties of clumps and Cores (Bergin & Tafalla 2007).
[c] From Clump masses from the Bolocom Galactic Plane Survey (Dunham et al. 2011).
[d] Core masses and temperature from Polychroni et al. (2013).

'cores' where cores are the site of star formation. These self-similar patterns are observed from dense cores to giant molecular clouds (Bergin & Tafalla 2007).

High resolution observations also show filaments in Molecular Clouds (André et al. 2014, Marsh et al. 2016, Benedettini et al. 2018). Perturbations make these self-gravitating filaments unstable (Inutsuka & Miyama 1997) and they fragment into dense cores. As a result, these gravitationally bound cores are primarily embedded within filaments (Molinari et al. 2010, Schisano et al. 2014, André et al. 2014).

Significant levels of turbulence provide angular momentum to the core and facilitate fragmentation (Goodwin et al. 2007). Depending on the number of thermal Jean masses, the gravitationally bound prestellar core fragments into a number of stars with different masses. The stellar mass also depends on the reservoirs of gas available to the stars (for the initial core, or accreted later, or limited by ejection or feedback).

The physical properties of molecular clouds, clumps and cores are summarised in Table 1.1. From this table it can be seen that the density of a core is on average 100 times higher than the clumps as well as 10^4 higher than the Molecular Cloud as a whole. In terms of sizes, cores are smaller (0.03-0.2pc), than clumps (0.3-3pc) and the Molecular Clouds (1-50 pc). Cores are at the bottom of the hierarchy of interstellar cloud structures (Larson 1981) and are discussed next.

Figure 1.1: Star formation image of M42 of the Orion Nebula. This turbulent star formation in the region is one of the most photogenic celestial objects. More than 3,000 stars of various sizes from the massive, young stars with pillars of dense gas and dust can be found in this image. Image: NASA, ESA, M. Robberto (Space Telescope Science Institute/ESA) and the Hubble Space Telescope Orion Treasury Project Team.

1.2.2 The formation of cores and clumps in molecular clouds

Fig 1.1 shows young star cluster the Orion Nebula Cluster (M42), in the Orion Nebula $\sim$ 440 pc away. Massive young and hot stars in the center of the nebula have blown out most of the dust and gas (their birth material), showing a cavity in the dark cloud.

Prestellar cores are gravitationally bound and centrally concentrated starless cores. They may collapse and fragment to form one or multiple stars, depending on several parameters such as the core mass, density and turbulence (Goodwin et al. 2004*a*, Delgado-Donate et al. 2004, Walch et al. 2010, Lomax et al. 2014). Collapse happens when the self-gravity of the core overcomes the thermal and turbulent pressure and the core exceeds the Jean's mass (Jeans 1902) $M_{\rm Jeans}$,

$$M_{\rm Jeans} = \frac{\pi c_s^3}{6\sqrt{G^3\rho}} \tag{1.3}$$

Where ρ is the average density of the core, c_s is the thermal sound speed and G is the gravitational constant.

For a molecular cloud, at around 10 K the sound speed is $0.2\,{\rm km\,s^{-1}}$. The typical volume density of a core is $\rho \sim 10^{-19}{\rm g\,cm^{-3}}$, so the Jeans mass is around a solar mass.

1.2.3 Low Mass Star Formation

Gravitational collapse is responsible for the formation of a star from a prestellar core. Low-mass stars form from dense and cold prestellar cores, and evolve into protostars and then Pre-Main Sequence (PMS) stars. Young Stellar Objects (YSO) are generally identified in the infrared and their evolutionary stages are characterised by their spectrum, ranging from the submillimetre to the visible. This classification is based on their characteristic Spectral Energy Distributions (SEDs) developed by Lada (1987) and Myers & Ladd (1993). Early stellar evolution is divided into four classes from Class 0 to Class III (André 1993, Evans et al. 2009, Dunham et al. 2014). The term "protostar" refers to Class 0 and I sources, whereas Class II and III objects are Pre-Main Sequence (PMS) stars.

1.2.3.1 Stages of star formation

Here is the brief description of each evolutionary stage from Class 0 to Class III. Fig.1.2 presents the evolution of the SED of a low-mass core during the star formation process (Meixner et al. 2013).

Class 0 sources

The Class 0 is the main mass accretion phase in the formation of a low-mass star. This evolutionary stage is short-lived and lasts roughly for the duration of a free-fall timescale (which is $< 10^5$ yrs, e.g. Evans et al. (2009), Enoch et al. (2008)). During this accretion stage a disk forms around the central protostars along with powerful and collimated CO bipolar outflows (Pudritz et al. 2007). The temperature of the core is a few 10s of K and it emits radiation as a blackbody peaking in the sub-mm at 100 μm (first panel of Fig.1.2). Class 0 sources are deeply embedded and can only be detected by long wavelength observations.

Class I sources

The start of the class I stage takes place when the envelope exceeds 70 K (Chen et al. 1995). Class I protostars are surrounded by an accretion disk and a circumstellar envelope of gas and dust. Class I objects are optically invisible, but can be detected in the near infra red (NIR). The SED is a combination of the blackbody radiation from the protostar and the contribution from the envelope (second panel of Fig.1.2). These sources still have mass accretion from the surrounding envelope though the outflows are less powerful and collimated than those from Class 0 objects (Andre et al. 1999).

Class II sources

The class II evolutionary stage starts when there is no more dense circumstellar envelope as it has been accreted, or dispersed by the outflow. Class II objects are classical T Tauri stars (CTTs). During this stage, the central object generates most of the energy. These are usually optically visible stars surrounded by a weak millimeter continuum emission disk (Piétu et al. 2014). The CTT stars continue to accrete material from the disc and they are characterised by strong Hα and X-ray emission as a result of an accretion shock (third panel of Fig.1.2). The SEDs of Class II objects peak at optical and IR wavelengths, and effective temperature is in the range of 650-2880K (Andre et al. 1999). The disk adds an IR excess to the SED (Beckwith 1999).

Class III sources

Class III stage PMS stars are weak-line T Tauri stars (WLTTs). In these sources, the disk has largely been accreted/dissipated and all that is left is a 'debris disk'. They have a simple blackbody with very weak IR excess (fourth panel of Fig.1.2). The star is similar to a main sequence star, but has a larger radius as it is still contracting. The peak emission is in the optical or NIR, and the effective temperature is $>$ 2880K

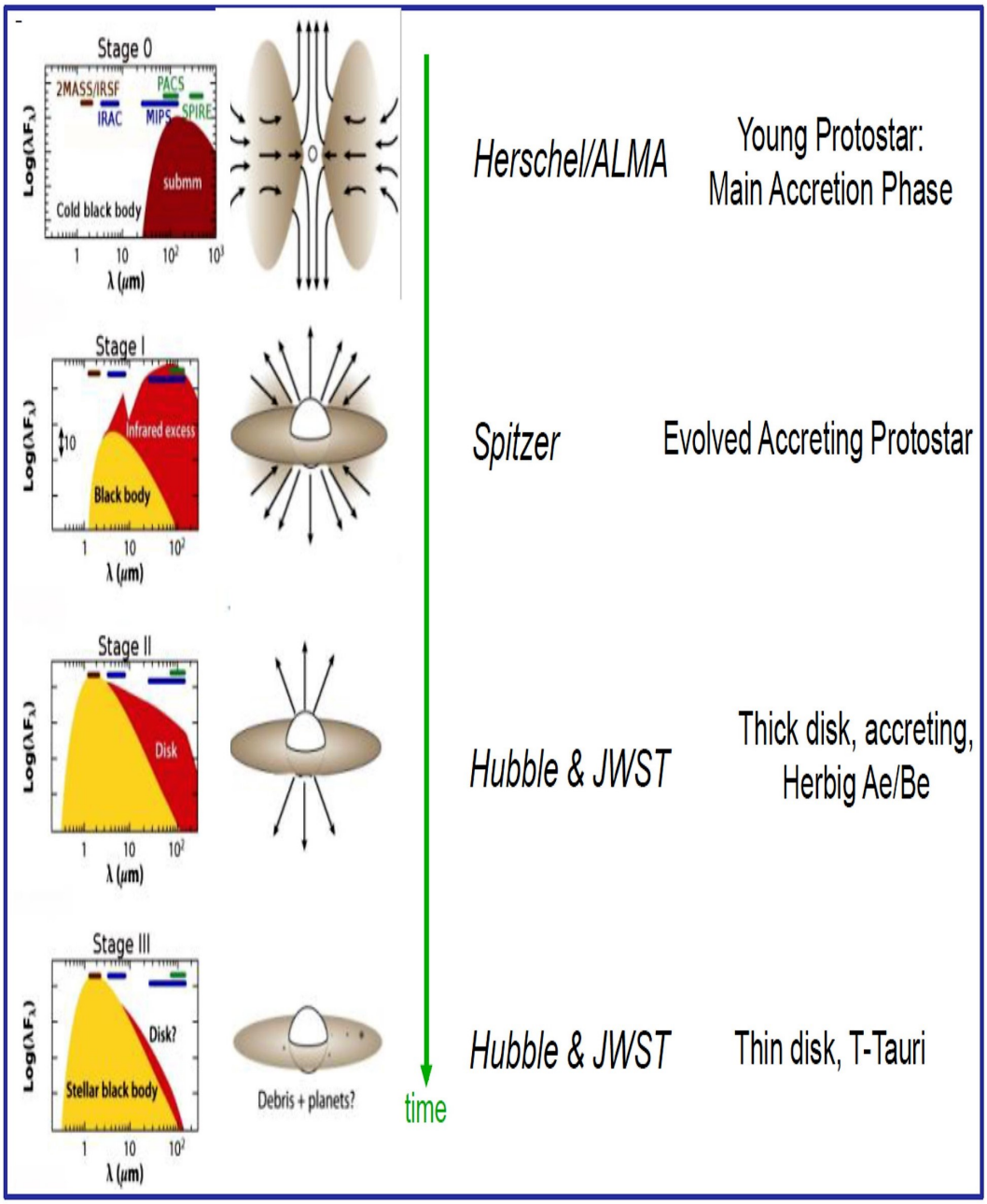

Figure 1.2: Spectral energy distribution shapes of young stellar objects of class 0 to class III. SED of class 0 deeply embedded protostar sources resembles a blackbody with peaks in the sub-mm (top left). Class I objects with accreted $\sim$ 50 % from the surrounding envelope show SED of a warmer black body and an excess IR (top right). For the class II phase, most of the envelope has been accreted except a disc resulting an IR excess (bottom left). SED of class III sources are very similar to main sequence stars but they might also exhibit a very shows small excess IR excess due to a scrapped disc. Adapted from Meixner et al. (2013).

(Andre et al. 1999). Eventually, Class III objects move to the main sequence and start burning hydrogen in their cores. The Physics behind the different stages of star formation are discussed next.

1.2.3.2 The physics of core collapse

Initially as the core collapses it can remove the compressional heat from contraction by the thermal coupling of gas and dust. At the typical densities of $10^{-19}\mathrm{g\,cm^{-3}}$ a prestellar core is optically thin. The temperature remains constant at 10K keeping the collapse isothermal. If the thermal pressure is neglected, the characteristic time scale for the core collapse and the envelope infall can be determined by the free fall time t_{ff} Masunaga et al. (1998):

$$t_{\mathrm{ff}} = \left(\frac{3\pi}{32G\rho}\right)^{1/2} \tag{1.4}$$

During the collapse, the value of M_{Jeans} falls as the density of gas ρ increases and the sound speed c_s is constant. The isothermal collapse phase ends when the density reaches $\sim 10^{-13}\mathrm{g\,cm^{-3}}$, the core becomes opaque and it is no longer able to radiate away effectively the heat of the collapse. The thermal behaviour of the core gas can be described by a barotropic equation of state. The sound speed becomes

$$c_s^2 = \frac{P(\rho)}{\rho} = \rho^{\gamma-1} \tag{1.5}$$

where P is the pressure, ρ the density, c_s, the general isothermal sound speed and γ is the polytropic index.

In early adiabatic phase, the molecular hydrogen behaves like a monatomic gas with $\gamma = 5/3$, as the rotational state of the gas has not yet been excited. Once the rotational state is excited, the gas behaves as a diatomic gas with $\gamma = 7/5$. Fig. 1.3 shows the temperature-density relationship for a barytropic equation of state showing an isothermal collapse followed by adiabatic one.

The core begins to increase in temperature and the collapse changes from isothermal to adiabatic. In the early adiabatic stage, the temperature rises slowly with density. At this critical density, the minimum Jeans mass is around $10^{-2}M_{\odot}$ and is known as the opacity limit for fragmentation. The core collapses and the first protostar(s) form during this time. The protostars initially have a size of ~ 1 au and are only able to radiate on a Kelvin-Helmholtz timescale. The protostars keep accreting more material from surrounding envelope, accretion disk and increase in temperature.

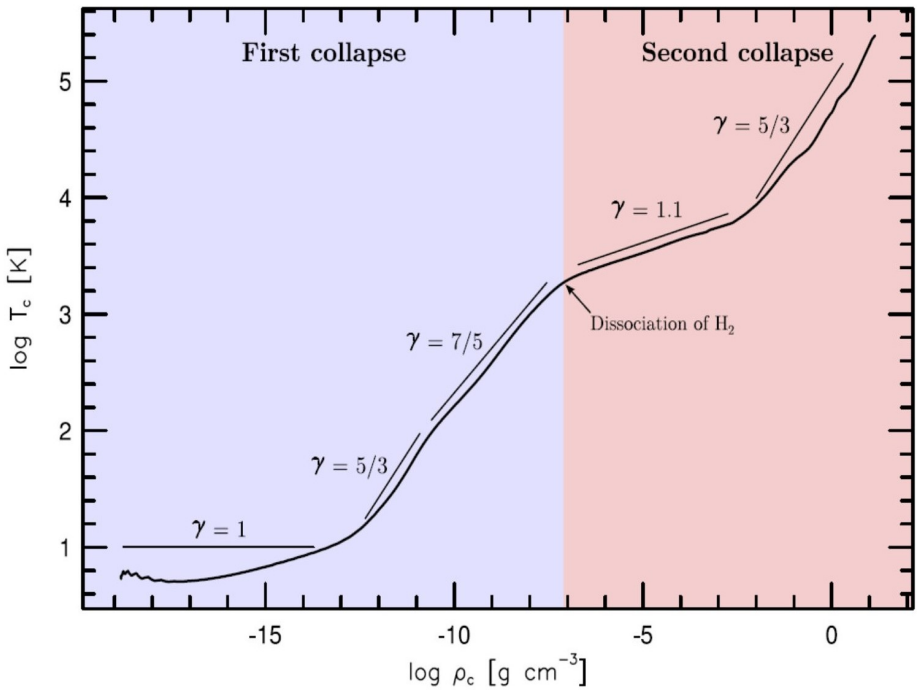

Figure 1.3: Change in core temperature with density during core collapse for a barytropic equation of state with adiabatic index as simulated by Masunaga & Inutsuka (2000). The boundary between two collapses represents the initiation of H_2 dissociation at temperature $2000K$. Adapted from Masunaga & Inutsuka (2000) by Rawiraswattana (2012).

This situation continues until the central core temperature reaches around 2000K and the molecular hydrogen starts to dissociate. The dissociation process provides a heat sink for the protostar to consume most of the gravitational energy (Masunaga & Inutsuka 2000). The protostar then rapidly and almost isothermally collapses to stellar densities ($\sim 1\,\mathrm{g\,cm^{-3}}$, Inutsuka (2012)), then continues to evolve as a pre-main sequence star.

1.2.4 Formation mechanisms of multiple star systems

Stellar multiplicity is a direct outcome of the star formation process. Present star formation theory emphasises that multiple star systems are formed by core and/or disc fragmentation during the early adiabatic collapse phase (Tohline 2002, Goodwin et al. 2007) rather than capture methods.

Core fragmentation

Core fragmentation can happen during the first isothermal, first adiabatic or second

isothermal collapse (Machida et al. 2008). A key factor in core fragmentation is the turbulence in the core. The internal turbulence can generate a complex high-density structure which is gravitationally unstable. Simulations have shown that cores with different levels of turbulence fragment and produce a different number of stars (Bate et al. 2002, 2003, Delgado-Donate et al. 2004, Goodwin et al. 2004*b*, Bate 2009, Lomax et al. 2014).

Disc fragmentation

Prestellar cores have angular momentum, as a result of inherited turbulence (at subsonic levels) from the molecular cloud (Burkert & Bodenheimer 2000). Material with low and high angular momentum respectively forms the central protostar and the circumstellar disc around that. A massive disc under some conditions (such as the ability of the disk to cool down) will be able to fragment, forming a multiple system (Bonnell 1994, Goodwin et al. 2007). Whitworth & Lomax (2016) suggested that the formation of brown dwarfs and low-mass H-burning stars requires disc fragmentation. It is most likely to take place where the radius is ~ 70 to 100 au, and the temperature is below 20K ($c_s \leq 0.3 \mathrm{km\,s^{-1}}$). The fragmentation of a disc is usually determined by the Toomre parameter Q (Toomre 1964) which represents how gravitationally stable the disc is. The Toomre parameter Q at a radius R in a disc is given by

$$Q(R) = \frac{c_s(R)\kappa(R)}{\pi G \Sigma(R)} \tag{1.6}$$

Where $c_s(R)$ is the isothermal sound speed, $\kappa(R)$ is the epicyclic frequency, and $\Sigma(R)$ is the surface density, at radius R.

An accretion disk can become gravitationally unstable if the Toomre parameter becomes smaller than its critical value, $Q < Q_{\mathrm{crit}} \sim 1$ (Toomre 1964).

Capture

For one star to capture another and form a binary, there needs to be a loss of energy from the system. In a three body encounter the energy can be transferred to a third star. To facilitate formation of a new binary system, each of the three stars with certain velocities and impact angles should occupy the same location at the same time. Meeting all these conditions are extremely rare in the Galactic field (Goodman & Hut 1993).

Griffiths et al. (2018) showed soft capture could be one possible mechanism for forming Massive Very Wide Binaries (MVWBs). They performed N-body simulations and showed MVWBs can be formed by this method during the dissolution of clumpy, gravitationally unbound expanding stellar associations. As a result of their

low binding energy, MVWBs are easily destroyed in encounters with other stars. They generally survive at low-density, and are usually destroyed at high-density in the presence of other massive stars.

1.3 Multiplicity

Having reviewed the physics of stellar evolution, we focus our attention specifically on the phenomenon of Multiplicity. Multiplicity can be defined by the multiplicity frequency (Reipurth & Zinnecker 1993) MF:

$$\mathrm{MF} = \frac{\mathrm{B} + \mathrm{T} + \mathrm{Q} + \ldots}{\mathrm{S} + \mathrm{B} + \mathrm{T} + \mathrm{Q} + \ldots} \tag{1.7}$$

Where S, B, T, and Q refer to the number of single, binary, triple, and quadruple systems, respectively. Another characteristic of multiplicity is the companion star fraction CSF, which is defined as the average number of companions in a stellar population and can be larger than unity:

$$\mathrm{CSF} = \frac{\mathrm{B} + 2\mathrm{T} + 3\mathrm{Q} + \ldots}{\mathrm{S} + \mathrm{B} + \mathrm{T} + \mathrm{Q} + \ldots} \tag{1.8}$$

In this section, relevant literature in the study of multiplicity is reviewed. A classification of binary systems is first described that forms a useful reference point for the rest of the thesis. The importance of binary systems is then discussed, especially regarding how they allow us to determine crucial stellar properties. In the next subsection, the methods available to measure binary fractions in stellar clusters are discussed, and in particular how shortcomings in existing approaches motivate us to develop the methods discussed in Chapters 2 and 4 of this thesis. The review is completed by describing available observational data we have on multiplicity in known stellar clusters.

1.3.1 Types of Binary Stars

Binaries are generally classified according to their method of detection. There are mainly three different types:

Visual Binaries

Visual binaries are the most common type of observed binary stars. Visual binaries are relatively close to us, where the component stars can be individually detected by a telescope. Long-term observations can resolve the relative motions of the members

of the system, and these positions are used to calculate the orbits of the stars. So far $\sim 130,000$ visual binary systems have been detected (Kovaleva et al. 2016).

Spectroscopic Binaries

Some binary stars are too close to be resolved separately by current telescopes. Doppler shifts can infer the presence of those binary systems in their spectral lines. Such systems are called spectroscopic binaries where the spectrum comes from the component stars. Analysis of the spectral line shifts against time provides us information about the radial velocities of the component stars. The orbital periods of these spectroscopic binaries range from a few hours to months, with separations of much less than an au in many cases.

Eclipsing Binaries

Eclipsing binary systems are special type of variable stars, where their detection depends on periodic changes in brightness. In this case, the orbital plane of the binary system lies edge-on to us and the component stars periodically eclipse one another. This photometric variation method is mostly sensitive to close binary systems, because the probability of detecting occultations are higher for closer systems. From the light curves of the two components, astrophysical properties such as stellar mass, their relative diameters etc. can be determined.

1.3.2 Importance of binary stars

Stellar mass provides one of the most important properties for understanding the formation, evolution and observable characteristics of stars. In astrophysics, the study of binary star orbits allow us to measure the masses of their component stars and allow us to determine other stellar parameters, such as radius, density etc. The masses of many single stars can then be estimated by extrapolations made from the mass of the observed binaries.

1.3.2.1 Determination of Stellar Mass from Visual Binaries

For visual binary systems, long term monitoring can provide astronomers with the relative positions of the two stars, the semi-major axis a, orbital orientation and their centre of mass (example: Fig 1.4 where the visual binary Sirius A & Sirius B orbit around each other). At the star's distance d, the subtended angles from the centre of mass are $\theta_1 = r_1/d$ and $\theta_2 = r_2/d$ (r_1 and r_2 respectively are distance of the primary and secondary stars from the centre of mass). From parallax measurements, one can

deduce d. Therefore, the mass ratio can be found from observations of the orbits which is given as:

$$\frac{M_1}{M_2} = \frac{r_2}{r_1} = \frac{\theta_2}{\theta_1} \tag{1.9}$$

Kepler's third law (for total mass) and equation (1.9) are used to calculate component mass for visual binary star systems.

1.3.2.2 Determination of Stellar Mass from Spectroscopic Binaries

For spectroscopic binary systems, the periodic shift of their spectral lines is the indicator of two stars orbiting around each other. The velocity of the system stars can be measured from the Doppler shifted lines. For a binary system, the massive star is proportionally closer to the center of mass and moves slower than the low-mass star and therefore for spectroscopic binaries, the massive star has a smaller Doppler shift in its spectral lines. The size of the shift in wavelength is related to the velocity of the star towards us or away from us.

For the total mass, Kepler's third law can be written as

$$M_1 + M_2 = \frac{P}{2\pi G}(v_1 + v_2)^3 \tag{1.10}$$

Here, v_1 and v_2 are respectively the velocity of the primary and secondary stars.

Despite these two equations (mass ratio and total mass), the individual mass determination is not straight forward. The orbital plane is usually inclined and not right along our line of sight ($i = 90^o$). The inclination angle (i) can be approximately determined from the radial velocity vs. time curve. Since v cannot be measured, the observed radial velocity $v_r = v\sin(i)$ is instead considered. Equation (1.10) becomes

$$M_1 + M_2 = \frac{P}{2\pi G}\frac{(v_{1r} + v_{2r})^3}{\sin^3 i} \tag{1.11}$$

If the binary is eclipsing, then $i \sim 90^o$.

1.3.2.3 Determination of Stellar Mass and Radius from Eclipsing Binaries

For eclipsing binaries, their size of orbit in au and velocity help us to determine the individual masses. Besides mass, the light curve is used to derive the star's diameters. Such systems provide the most complete properties of stars.

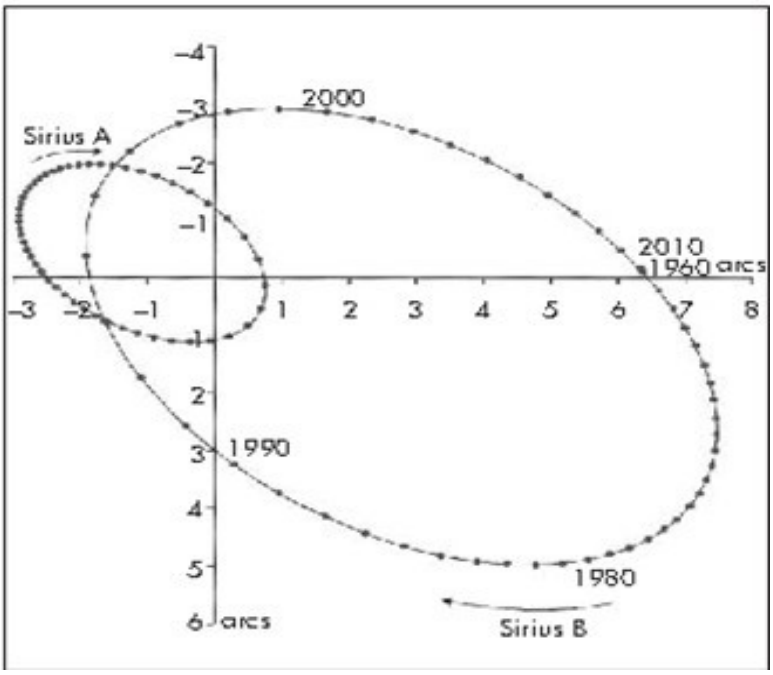

Figure 1.4: The orbits of Sirius A & Sirius B with the center of mass fixed as the focus (Pettini 2009)

1.3.3 Multiplicity of Main Sequence (MS) and Pre-Main Sequence (PMS) Stars

Having established the types and importance of binary stars, this chapter now consider the best available evidence we have on the multiplicity of observed stellar clusters, in both Main Sequence and Pre-Main Sequence stars.

Despite the presence of gas and dust making it extremely hard to observe, combinations of various imaging techniques have been used to resolve the binary populations in protostellar cores (Haisch et al. 2004, Connelley et al. 2009), class 0/I protostellar cores (Evans et al. 2009, Chen et al. 2013, Tobin et al. 2016), T Tauri stages in star-forming regions (Ratzka et al. 2005, Pomohaci et al. 2019) and in open clusters (Kraus & Hillenbrand 2009).

Observations show that multiplicity fraction of higher mass stars (such as O and B) are greater than lower mass stars (Gullikson & Dodson-Robinson 2012, Duchêne & Kraus 2013, Chini et al. 2013, Ward-Duong et al. 2015). Due to dynamical evolution, the fraction decreases with age. Therefore, young PMS stars have higher multiplicity fraction than the field stars (Goodwin & Kroupa 2005, Lada & Lada 2003, Chen et al. 2013).

In this section, a brief review of multiplicity is presented for MS and PMS multiple stellar systems. Main Sequence stars are grouped (Duchêne & Kraus 2013) by mass,

low and very low mass and intermediate and high mass star types.

1.3.3.1 Multiplicity on the Main Sequence (MS)

Solar type stars

In the seminal study on multiplicity, Duquennoy & Mayor (1991) found the MF of solar type F and G dwarfs in the local neighbourhood, was 0.58. The separation distribution was found to be log-normal with a peak at 40 au. With a larger sample, Raghavan et al. (2010) revised this fraction as 0.46. More specifically, they found that super-solar G dwarfs (1-1.3 $M_{\odot}$) have a higher multiplicity (0.54) than sub-solar G dwarfs (0.7-1 $M_{\odot}$) of 0.44.

Low mass and very low mass stars

Following the trend of decreasing multiplicity with mass, it was found that within 52 pc M dwarfs have a multiplicity of 0.32 ± 0.06 (Bergfors et al. 2010). They are tightly bound with a mean separation 16 au (Janson et al. 2012).

Ward-Duong et al. (2015) conducted the M-dwarfs in Multiples (MINMS) survey of a large number (245) of K7-M6 dwarfs within 15 pc. They found a companion fraction (CSF) of about 0.235 ± 0.032 over the 3 au to 10,000 au separation range. With the large sample size, the uncertainties of this study are reduced by a factor of 2 than the previous studies, which shows that the CSF of M dwarf is lower than the solar-type stars (Raghavan et al. 2010) and higher than Brown dwarfs (Burgasser et al. 2007). For brown dwarfs, the multiplicity fraction is 0.15-0.25 (Basri & Reiners 2006, Burgasser et al. 2007) with a mean separation 4.6 au.

For field VLM objects, Allen (2007) gathered data from various surveys and estimated the multiplicity fraction between 0.20 and 0.24.

Intermediate and high mass stars

Based on the various surveys, Duchêne & Kraus (2013) concluded that MF for 1.5-5 $M_{\odot}$ stars is around 0.5, within the separation range 50–2000 au. De Rosa et al. (2011, 2013) found multiplicity frequency of intermediate mass stars to be of 0.4-0.48 with a mean separation 387 au.

For O type high mass stars, the multiplicity frequency is 0.8 (Mason et al. 2009, Sana & Evans 2011, Chini et al. 2012).

1.3.3.2 Multiplicity on the Pre-Main Sequence (PMS)

Chen et al. (2013) published the largest survey of protostellar binary/multiple systems. With 33 Class 0 protostars, with separations ranging from 50 au to 5000 au, they derived the multiplicity frequency (MF) and companion star fraction (CSF) as 0.64 ± 0.08 and 0.91 ± 0.05 respectively. The derived MF and CSF in this survey are much higher than the values found for Class I young stellar objects multiplicity. Observations of Class I objects over the 50–2000 au separation range were found to have CSF values, 0.369 ± 0.05 (Duchene et al. 2004, Connelley et al. 2009).

Tobin et al. (2016) presented a survey of 94 protostars in Perseus molecular cloud with overall MF 0.40 ± 0.06 and CSF 0.71 ± 0.06. For class 0 YSO, the MF and CSF were respectively 0.57 ± 0.09, 1.2 ± 0.02 and for class I objects they were both 0.23 ± 0.08. They found distribution of the companion separations as bimodal, with one peak around at ~ 75 au and another at ~ 3000 au.

Surveys conducted in Taurus and Upper Scorpius (Kraus et al. 2008, 2011) provide stellar multiplicity characteristics over the separation range 3–5000 au. In Taurus, within 5-1000 au and among class II/III stages, stars have a Companion Fraction (CSF) of 0.79 within the stellar mass range of 0.25–0.7 $M_{\odot}$, whereas for a stellar mass range of 0.7-2.5 $M_{\odot}$ this is 0.64.

From several surveys, Biller et al. (2011) demonstrated that at projected separations of 5–10 au, most young BDs and VLM stars have no companions.

Observations made by Baines et al. (2006) and Wheelwright et al. (2010) showed a high multiplicity fraction of pre-main-sequence intermediate mass (between 2 $M_{\odot}$ and 10 $M_{\odot}$ stars). Also known as Herbig Ae/Be stars, their multiplicity fraction is more than 70%. The mass ratio is higher for this group with near equal mass systems. Also with higher mass, Herbig Ae had higher multiplicity fraction than Be.

Pomohaci et al. (2019) surveyed 32 Massive Young Stellar Objects (MYSOs) from the RMS catalogue with a physical separation range of 400–46000 au. They found MF of MYSO's to be 0.31 ± 0.08 and a CSF of 0.53 ± 0.09.

1.3.4 Existing methods to analyse binary populations

A considerable focus of this thesis is the development of methods to analyse binary populations and determine properties such as binary fractions. We therefore now review some important milestones in the literature regarding analysing binary populations, and how that shaped the questions that are further explored in the thsis.

1.3.4.1 Binary pairs

The statistical investigation of binary fractions goes back to the first astronomical statistician, Michell (1767), who used statistical methods to argue for the existence of physical binary systems. In order to do so, Michell measured the angular separation of neighbouring stars in the plane of the sky. He believed that in some cases the nearest neighbour was orbiting its neighbour rather than being nearby by pure chance. In a random distribution of single systems, the chance of two stars at very close separation is extremely low. Michell calculated the probability of two nearby stars being closer than separation S as Halbwachs (1988):

$$P(S) = S^2/4 \tag{1.12}$$

It follows that the probability that a pair is wider than S is $1-P(S)$. Furthermore, if a total of N stars are randomly distributed in the sky then the probability that no pair is closer than S is given by:

$$((1 - P(S))^N)^N \tag{1.13}$$

Michell took the Pleiades as a case study and calculated that the likelihood of finding such a distribution of separations randomly was about one in half a million. He concluded that stars might be bound in these binary or multiple star systems due to gravitational pull, providing the first rigorous argument for the existence of physical binary stars. Michell's finding can be expressed by the Struve (1852) formula: the expected number of optical pairs from a total of N stars in an area, A separated by less than S (assumed to be small) from another star is:

$$n(S) = N(N - 1)(\pi S^2)/(2A) \tag{1.14}$$

Subsequently, a few methods have been developed to detect the existence of binary stars. The main problem is to distinguish between physical pairs in genuine binary systems, and optical pairs, which are unrelated stars that happen by chance to be on the same line of sight. Ultimately, all physical binary systems should be confirmed through the detection of their orbital motion. In practice, however, this is feasible only for what are referred to as close binaries, which have orbital periods of days to years and separations under 10 au (Halbwachs et al. 2003). For wide binaries, which can have orbital periods greater than 10^5 years and separations over 20,000 au (Yoo et al. 2004), orbital periods are not a feasible approach to detecting such binaries.

There are two standard methods to detect such wide binary systems. The first are

what are referred to as Common Proper Motion methods, the second use statistical signals such as those obtained by two-point correlation functions (2PCF).

Common proper motion

Common proper motion (CPM) methods can be used to detect binaries where physical pairs move uniformly in a specific direction of the sky. This can be detected with several epochs of observations. Resolved binary stars detected by the CPM technique are called CPM doubles and have angular separations from several arcsecs to several arcmins. In contrast, optical pairs will have no such uniform motion.

The CPM method is the best method available to identify specific binary pairs. However, this is a difficult method clearly requires a relatively large amount of data over a long time period to identify the motions (as opposed to for example just positional data). Furthermore, in order to verify the CPM of two stars with precision, the proper motions must be relatively large, and therefore relatively nearby.

The Gaia mission has helped address this limitation and is designed to measure the distance, position and motion of stars with previously unachievable precision. It aims to catalog approximately 1 billion astronomical objects (not exclusively stars but also asteroids, Kuiper-belt objects, supernovae, etc.). It does so by cataloging each target object around 70 times over the first five years, providing a huge wealth of detailed data on the motion of these objects. However, this mission still has its limitations.

Detection of binary systems by common proper motion is a difficult job. Good proper motions are only feasible within 300 pc as astrometric detection weakens with distance (Sahlmann et al. 2016).

At present there are two technologies to improve angular resolution and contrast sensitivity. Adaptive optics (AO) can help to detect secondary faint companions below 0.1. The resolution can go down to about 0.1 arcsec (which at 500pc is 50au), but requires good astrometry and multiple epochs to get accurate proper motions. Interferometry technologies refer to where an array of telescopes provides an output with combined strong angular resolution. To achieve both strong angular resolution and high contrast sensitivity images, astronomers use interferometry along with AO. For example 8-10 m VLT or Keck (Hippler 2019) interferometry can detect images with angular resolution of 1 arcsec. With AO, the resolution can improve up to 30-60 milliarcsecond (mas).

Gaia is not equipped with any of the two technologies and suffers from poor resolution and contrast sensitivities as a result. Gaia can find proper motions down to

1 mas/year (Simon 2018) and due to the level of resolution (0.4-0.5 arcsec), it cannot resolve binaries <250au beyond 500pc (which is well above the peak of separation distributions - see section 1.3.3.1). As a result of poor angular resolution, it cannot detect close binary companions (Ziegler et al. 2018, Brandeker & Cataldi 2019). Gaia's ability to resolve tight binaries are comparable to the Hubble Space Telescope (Collaboration et al. 2016). The only exception is Gaia can find astrometric tight binaries (< few au), if the binary orbit is able to alter the brighter component's velocity enough to detect a variable proper motion (or radial velocity).

Gaia does not have near Infrared photometry facility where the K contrast ratio is much less than V band. Therefore, observations of a fainter member of a binary pair in that visible range is not possible. It can't detect anything embedded like young stellar regions and its observation is again constrained to field objects where the region isn't too crowded.

The objects need to be brighter than 20 mag and observations of a fainter member of a binary pair in that visible range is not possible. Overall, Gaia will help detect a good number of systems, but it has a 'blind spot' for binaries at the typical separation of most binaries. We can see, Gaia is not ideal in helping us overcome the impact of the selection effects.

Therefore, even with the new level of precision the Gaia mission offers, CPM methods as a whole can be quite restricted in their ability to generate a large catalogue of binaries. CPM methods are not considered in much more detail for the remainder of this thesis.

Two point correlation functions

As opposed to CPM methods, an alternative are methods that rely on statistical arguments based purely on the positions of the stars, similar to Michell. In contrast to CPM methods, which require much more detailed proper motion data, using only stellar position data means one can make use of larger samples of more distant stars. In general, these methods do not identify specific pairs of candidate binaries (as in the CPM method, which checks specific pairs by design). Instead, it estimates quantities such as the prevalence or density of binaries in a given cluster.

In cosmology, a widely used cluster measuring technique is the angular two-point correlation function (2PCF) to study the large-scale structure of the Universe as well as galaxy cluster distributions. The main idea of the 2PCF is to measure the excess probability of finding two objects (such as galaxies or stars) at a certain separation when compared to a fully random distribution. The 2PCF function is defined as:

$$w(\theta) = \frac{F(\theta)}{P(\theta)} - 1 \tag{1.15}$$

Where $F(\theta)$ is the observed number of pairs with separation around θ and $P(\theta)$ is the expected number of pairs with separation around θ if the distribution of objects is totally random. If $w(\theta) = 0$, it means that at the separation θ, the number of pairs is as one would expect at random. However, the larger it grows, the more pairs exist at that separation. In other words, the quantity $w(\theta)$ measures the "clumpiness" of the stellar positions. This excess clumpiness is usually attributed to the existence of pairs that are bound by gravity (i.e. physical as opposed to optical binaries). As pointed out shortly however, this assumption ignores the effect of underlying cluster morphology.

Bahcall & Soneira (1981) first used the 2PCF method to measure the excess of observed wide binary stars separated by an angle θ against a randomly distributed sample. Alongside the 2PCF method, they also calculated the first and second nearest stellar separation distribution for part of the catalogue sample.

These methods indicated that there were more stars with neighbours close to them than would be expected by chance. Like Michell, they concluded physical binaries are the reason for close stellar separations with the excess clustering effects (in their words: "that the stars which seem close together in the sky are in fact close together in space"). Combining 2PCF, first and second nearest neighbour distributions and the photometric parallax measure they concluded within 0.1 pc there are around 15% of the stars in multiple systems.

The use of the 2PCF method by Bahcall and Soneira pointed towards a clear advantage of the technique: it was much quicker and easier than using extensive proper motion data. However there were also some clear disadvantages.

Firstly, the 2PCF method cannot distinguish between excess pairs within separations because they represent bound pairs, or if they are simply a result of the underlying cluster morphology. For example, if the cluster morphology is fractal, one might expect excess pairs within close separation distances as a consequence of the subcluster structure as opposed to being attributable to physical binaries. It is an effort to develop better models of binary distributions while accounting for cluster morphologies that forms the basis of Chapter 2.

Secondly, the method needs a reasonably large sample. For small samples, the random noise increases with increased angular separation (Longhitano 2011). Subsequent work trying to verify some of the conclusions of the Bahcall and Soneira study showed that the sparsity of the data caused a considerable over-estimation of the

wide binary density (Garnavich 1988, Longhitano 2011). Part of the challenges of sparsity and reliable estimation is related to the impact of observational selection effects. As discussed in (Longhitano & Binggeli 2010), over-simplifying selection effects in models of the binary populations can lead to considerable problems in our ability to infer the true parameters. Chapter 4 considers explicitly the process of inferring the parameters of underlying binary distributions when selection effects are present.

1.3.5 The study of binary systems in this thesis

So far a number of different methods used to analyse the multiplicity of stellar clusters have been presented. As established, common proper motion (CPM) methods allow us to identify specific pairs of binaries, but are constrained to nearby stars. Therefore, the focus of this thesis will be on methods that rely on establishing a statistical signal from some distribution of stellar position data. 2PCF methods were introduced, which compares the separations of a random distribution of stars with the observed separations. 2PCF methods have many benefits in that they rely on much simpler datasets (positional data) than CPM methods. However, at least two shortcomings emerged in our analysis of available methods.

Firstly, the methods described are not well adapted to more dense or complex morphologies in a stellar cluster under consideration. In its simplest form, the 2PCF method treats the "clumpiness" of the stellar distribution as a feature which is attributed to binary pairs. However, this can also be attributed to complex morphological features of the cluster, such as a fractal substructure.

This leads us to consider in Chapter 2 a method to detect binary fractions even in the presence of complex morphologies. The core idea is that instead of considering the distribution of separations between the stars, what is considered instead is the distribution of the *ratios* between the closest and the tenth-closest neighbour of each star. It is shown that this quantity allows one to avoid many of the challenges that would otherwise arise in analysing binary distributions in these complex morphologies.

In order to do so, a Monte Carlo process is introduced to generate stellar clusters of different morphologies and different values of the binary fraction. It can be shown that the nearest neighbour ratio method developed is able to quite robustly estimate the true binary fractions despite the complex morphologies.

A second issue with existing methods is the high sensitivity to selection effects in the data. This raises an important question as to how exactly selection effects distort the conclusions one can draw about binary populations from observational data.

In Chapter 4, selection effects are analysed in detail in an effort to demonstrate how exactly they hinder efforts to extract the true properties of binary systems. When binary populations in a star cluster are observed, selection effects obscure their true properties. If the binary separation is very wide, they appear as two single stars. When the separation is small, they still remain unresolved as one individual star. When the luminosity of both stars are nearly the same, they are observed as a single star with double brightness. When the secondary star is many times fainter than the primary, it becomes unnoticed most of the time. Therefore, selection effects are an observational problem that obstructs the resolution of a good fraction of visual binary systems and their associated orbital parameter distributions. Is there any way to extract the true properties from an observed population?

The chapter assesses whether it is possible to retrieve the true properties of an observed binary stellar population that has gone through selection effects. It begins by simulating binary stellar populations using a Monte Carlo method. It then investigates the inverse problem of retrieving the true parameters from the observed data under (i) an ideal situation when there are no selection effects and (ii) a 'realistic' situation, when there are selection biases. To do so, the chapter establishes a Binary Search Tree method to retrieve the true parameters. It turns out that the method performs very well without selection effects, but is drastically undermined when selection effects are incorporated. Analysing the differences in the samples allows us to analyse the fundamental limitations of such distribution comparison methods in the presence of selection effects, and suggests some paths forward to accommodate this.

1.4 The Initial Mass Function (IMF)

The Initial Mass Function (IMF) is the distribution function of stellar masses at birth and an important tool to understand the star formation process. The IMF informs our understanding of stellar formation theories, the evolution of stellar clusters, the production of metals by supernovae, stellar physics, Galactic and extragalactic physics. In this section, relevant background literature on the IMF is briefly reviewed, including claims about Universality, the physical process that underpins its formation, and the functional forms that are used to describe the IMF. This will help motivate the need to assess the suitability of the functional forms for the study of IMFs, which forms the basis of Chapter 3.

1.4.1 The Functional forms of the IMF

We now consider attempts that have been made to characterise the shape of the IMF using functional forms to approximate the empirical distributions.

As elaborated in previous sections, the processes that underpin star formation are complex, and the aggregation of these complex processes will result in the initial distribution of masses of those stars - the IMF. It is worth pointing out that the functional forms that are about to be described do *not* necessarily make use of knowledge of these underlying process to derive the formulas that describe the shape. Instead, they are the functions that are just "fitted" to the empirical distributions, and thereafter used as a reference point for the supposed underlying distribution. This approach is obviously more convenient, especially in the face of incomplete knowledge as to the underlying processes. However, it is important to emphasize at this stage that the following "canonical" distributions are not derived from fundamental principles of star formation, but rather a statistical fit to available data. The implications of this distinction are referenced more heavily in Chapter 3, but this initial review is concerned with establishing the key existing ideas in the IMF literature.

Salpeter (1955) obtained a first estimate of the initial mass function for the mass range $1.0 < \mathrm{m/M_\odot} < 10$, of the form:

$$\frac{\mathrm{d}n}{\mathrm{d}m} \propto m^{-\alpha} \tag{1.16}$$

Here, $\alpha = 2.35$, indicates that massive stars are less frequent. Kroupa (2001*b*) introduced the IMF in terms of power law functions in three mass ranges.

$$N(M) \propto \begin{cases} M^{-\alpha_0}, & m_0 < m < m_1 \\ M^{-\alpha_1}, & m_1 < m < m_2 \\ M^{-\alpha_2}, & m_2 < m < m_3 \\ M^{-\alpha_3}, & m_3 < m \end{cases}, \tag{1.17}$$

Where,

$$\begin{aligned} \alpha_0 &= 0.3 \pm 0.7, & m_0 &= 0.01 \\ \alpha_1 &= 1.3 \pm 0.5, & m_1 &= 0.08 \\ \alpha_2 &= 2.3 \pm 0.3, & m_2 &= 0.5 \\ \alpha_3 &= 2.7 \pm 0.3, & m_3 &= 1.0 \end{aligned} . \tag{1.18}$$

Chabrier (2003) adopted an IMF with a log-normal distribution merging with a power law at the high mass end. He derived the IMF from the galactic field, globular clusters and young clusters data. Later Krumholz (2015) adopted this IMF for two

different mass ranges-

$$\frac{\mathrm{d}n}{\mathrm{d}\log m} \propto \begin{cases} \exp\left[-\frac{(\log m - \log 0.22)^2}{2\times 0.57^2}\right], & m < 1 \\ \exp\left[-\frac{(-\log 0.22)^2}{2\times 0.57^2}\right] m^{-1.35}, & m \geq 1 \end{cases}, \tag{1.19}$$

Parravano et al. (2010) represented the IMF by a smoothed two-power law (STPL).

Maschberger (2013) derived an IMF with fewer parameters as a stable distribution. It provides a closed functional form and convenience to work with CDF, PDF and even the inverse CDF allowing us to sample easily from a distribution. Its probability distribution function is

$$P_{L3}(m) = A\left(\frac{m}{\mu}\right)^{\alpha}\left(1+(\frac{m}{\mu})^{1-\alpha}\right)^{-\beta} \tag{1.20}$$

$$A = \frac{(1-\alpha)(1-\beta)}{\mu}\frac{1}{G(m_{\mathrm{up}}-m_{\mathrm{low}})} \tag{1.21}$$

Where, $G(m)$ is the auxiliary function

$$G(m) = \left(1+(\frac{m}{\mu})^{1-\alpha}\right)^{1-\beta} \tag{1.22}$$

Here, m_{low} is the lower mass limit, m_{up} is the upper mass limit, μ is the characteristic mass, α is the slope from characteristic mass to higher masses and β determines the inclination of the slope from lower mass stars to characteristic mass.

For a standard IMF, Maschberger (2013) recommended the values of parameters as $m_{\mathrm{low}} = 0.01$ $\mathrm{M}_{\odot}$, $m_{\mathrm{up}}= 150\mathrm{M}_{\odot}$, $\mu= 0.2\mathrm{M}_{\odot}$, α =2.3 and β =1.4.

Fig. 1.5 shows the mass probability distribution function used by Maschberger (2013) (black), Chabrier (2003) (green) and Kroupa (2002) (blue). In all the IMF formulations the unit of m is $\mathrm{M}_{\odot}$. All the probability distributions are equally applicable where IMF decreases rapidly at high mass. Stars more than 10 m are very rare.

1.4.2 IMF Universality

Stars come with a range of masses, starting with hydrogen burning 0.08 $\mathrm{M}_{\odot}$ as the lower stellar mass limit to canonical upper stellar mass as 150 $\mathrm{M}_{\odot}$ (Oey & Clarke 2005, Weidner & Kroupa 2006). Crowther et al. (2010) later found stars as massive as 300 $\mathrm{M}_{\odot}$. The vast majority (90%) of stars in the IMF are M-dwarfs, with a peak found between 0.1 to 0.4 $\mathrm{M}_{\odot}$ (Lada 2006, Goodwin 2010).

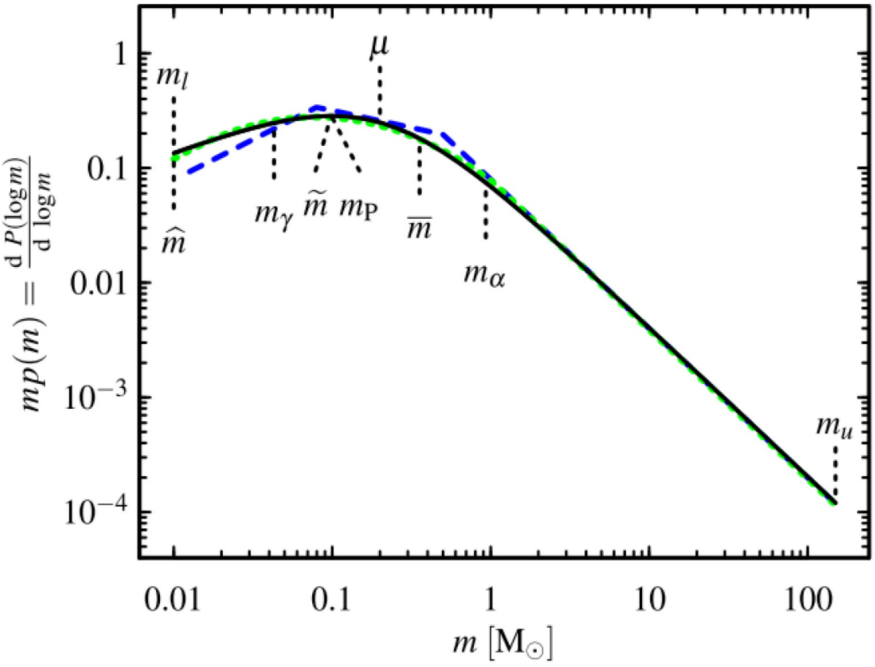

Figure 1.5: Probability distribution function of stellar mass. Colour green presents IMF fitted function by Chabrier (2003), blue - Kroupa (2002) and black by Maschberger (2013). Adapted from Maschberger (2013).

The IMF presents strong evidence of universality in diverse environments such as local young clusters, the local field and associations (Kroupa 2002, Chabrier 2003, Bastian et al. 2010). Though the IMF is near universal in the Milky Way and neighboring galaxies (Covey et al. 2007), some star forming regions have been shown to deviate from this. For example, Taurus shows an excess of $0.6 - 0.8\mathrm{M}_\odot$ stars compared to other nearby star-forming regions like IC 348, Chameleon I and the Orion Nebula Cluster (Luhman 2012). Recent indirect studies have shown that the low-mass IMF slope may vary outside the Milky Way (Treu et al. 2010, Van Dokkum & Conroy 2011, Cappellari et al. 2012).

One way to make sense of the presence (or absence) of Universality is to study the underlying star formation process that determines the stellar masses observed in the IMF. Figure 1.6 depicts an outline of the general shape of the IMF, and indicate the physical processes that are believed to be responsible for producing stars within each of the three distinct mass ranges. These processes are reviewed briefly now.

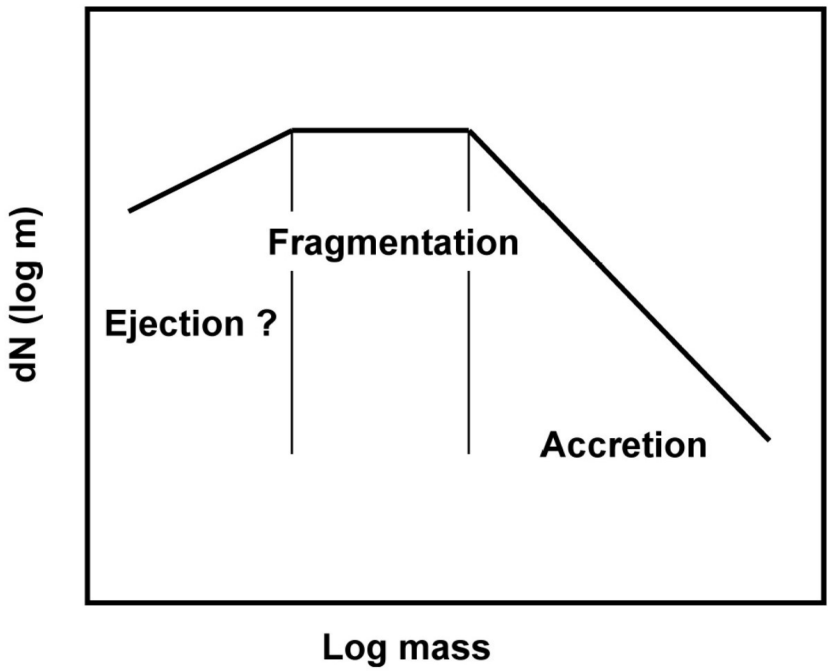

Figure 1.6: Schematic diagram of IMF showing physical process responsible for mass distribution at different regions. The peak of the IMF and the characteristic stellar mass are attributed to gravitational fragmentation, while lower mass stars are believed as being due to fragmentation plus ejection or truncated accretion, while higher-mass stars are thought as being due to accretion. Adapted from Bonnell et al. (2006).

1.4.3 Star formation processes underlying the IMF

This section briefly discusses the physical process that is believed to underlie the general shape of the IMF, which is pictured in Figure 1.6. As can be seen from this image, there are three broad mass ranges of interest, as hypothesized by Bonnell et al. (2006).

Bonnell et al. (2006) suggested that the lower mass stars (first two sections in the Figure) are formed by the gravitational core fragmentation process. The characteristic stellar mass and the peak of the IMF are due to core fragmentation and the thermal physics regulates the mean Jean's mass (section 1.2.2, 1.2.3). In molecular cloud turbulence plays an important contribution in generating (section 1.2.1) filament and fragmenting prestellar cores. The formation of low mass stars and brown dwarfs is attributed to the fact that they can not increase their mass through accretion. Reipurth & Clarke (2001) suggested multiple systems ($N > 2$) in a core can be unstable and the lowest mass star (generally brown dwarf) gets ejected. The ejection is thought to happen just after the brown dwarf forms (Goodwin & Kroupa 2005)

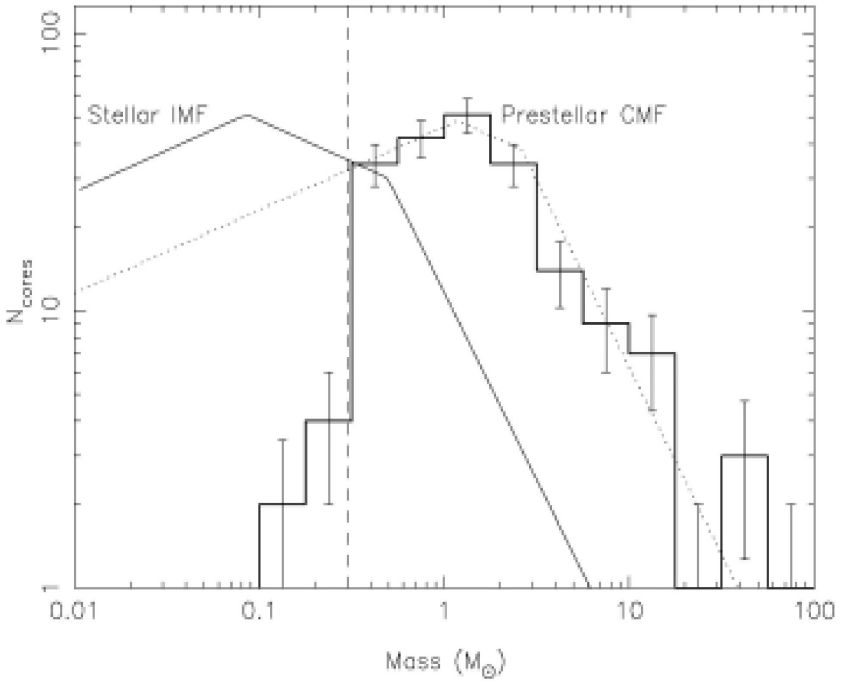

Figure 1.7: The CMF for the Orion AN and Orion BN regions. The average completeness limit for the two regions is shown as a dashed line. A three-part stellar IMF, normalized to the peak in N of the CMF, is overlaid as a thin solid line. The dotted line shows a three-part mass function with the same slopes as the IMF (Nutter & Ward-Thompson 2007).

and the lack of gas accretion limits it to grow further. Disk fragmentation can also be another mechanism to form lower mass stars.

Stars more than 8 $M_\odot$ are referred to as high-mass stars and their formation are explained by two different theories: monolithic core accretion, and competitive accretion (Rivilla et al. 2013). Monolithic core accretion is a scaled-up version of low-mass star formation from a core where the gas accretes onto the protostar through an accretion disk with significantly enhanced accretion rates compared to their low-mass siblings (Hennebelle & Chabrier 2008). In contrast, in the Competitive Accretion model, all stars accrete from the same gas reservoir. At birth each star is smaller than the typical stellar mass, and they compete for gas in the potential. The more time a star remains in the centre, it accretes more gas achieving a higher mass (Bonnell et al. 2006).

1.4.3.1 The Core Mass Function

As can be seen from the description of the physical process so far, much of the IMF formation is a result of fragmentation of cores of various sizes. It follows therefore that the distribution of the masses of the cores (the Core Mass Function, CMF) is also important in developing an understanding of the IMF. Indeed, the CMF is used extensively when simulating the star formation process in Chapter 3. This is reviewed briefly now.

Motte et al. (1998) first noticed the observational similarity between the IMF and Core Mass Function (CMF) (Testi & Sargent 1998, Johnstone et al. 2000, Alves et al. 2007, Nutter & Ward-Thompson 2007, Simpson et al. 2008, Enoch et al. 2008). In Figure 1.7, Nutter & Ward-Thompson (2007) shows a three-part stellar IMF (thin solid line), normalized to the peak in N of the CMF (dotted solid line) for the Orion AN and BN regions. The dashed line shows the average completeness limit for the two regions. The CMF is consistent with the same slopes as the three-part power-law IMF. Both mass functions decline to lower masses below a peak value. At higher masses, they fit by negative power-law slopes. The difference is the shifting of the peak mass, 0.08 $M_\odot$ for the IMF and 1.3 $M_\odot$ for the CMF.

Through simulations, Padoan et al. (1997) and Padoan & Nordlund (2002) proposed the turbulence-based central limit theory that produces the lognormal shape of CMF. Observation of nearby star forming regions demonstrated a CMF of lognormal shape (Enoch et al. 2008, Benedettini et al. 2018). Alves et al. (2007) showed that a power law is more suitable for the higher mass CMF.

Finally, Goodwin & Kroupa (2005), Goodwin et al. (2008) suggested that the observed number of multiple stellar systems could be reproduced if each core spawns 2 or 3 stars.

1.4.4 The study of IMFs in this thesis

The focus of this thesis will not be to interrogate any existing properties of the IMF - Universality, formation processes, etc. - but rather to take a step back and review the methodology that is used to analyse IMFs in the first place.

As has been shown so far - IMFs are rich phenomenon with complex characteristics. However, the study of IMF often rests on a simplifying assumption - that we can reduce this richness to the study of the functional representation of the IMF, and in particular the study of a small number of parameters that define that form. The study of IMFs has become very intertwined with the study of its parameters.

There is nothing wrong with this in principle - a simplifying model of a complex

phenomenon is often the best starting point to build deep understanding. It also offers a pragmatic convenience in the sharing of data and methods. However, as this thesis will aim to show, this simplification to the study of parameters can lead to undesired consequences when trying to ask subtle questions about the underlying nature of the IMF.

The key idea that will be explored is that focusing the analysis of the IMF on its parameters can massively obscure important differences in the underlying properties of the IMF. In particular, in Chapter 3, a toy star formation model will be developed to mimic the process described above, but one that can be tuned to represent different ground truths about the IMF. For example, the model can simulate a scenario with the IMF is Universal, and produces distributions that match the Canonical Form. The model can also be used to simulate a scenario where the IMF is Universal, but produces distributions that do not match the Canonical Form. Finally, the model can be tuned to simulate a scenario where the IMF is not Universal, so that clusters sampled from different parts of space have different underlying distributions.

In each of these scenarios (which we refer to as the Canonical, Non-Canonical and Non-Universal hypotheses), the sample data is fit to parameters and used to make inferences about the ground truth (i.e. detecting which hypothesis might have been true). The parameter fitting and inference is done in the same manner used in modern astrophysical studies. Strikingly, it is shown that despite have extremely different ground truths for each Hypothesis, in each case, the parametric inference methods cannot reliably distinguish between the processes.

As will be shown, the reason this indistinguishability arises is because of a combination of three problems: small sample sizes, heavy tailed data, and heuristic parametric methods used in place of robust goodness of fit tests. It is then shown that non-parametric approaches are much more successful at inferring the underlying true state of the world, in particular in distinguishing the Non-Universal and the Universal hypotheses. Further implications for IMF methods and models are discussed throughout the chapter.

1.5 Structure of the thesis

The overall thesis is organised as follows:

Chapter 2 focuses on the detection of binary fractions in complex morphologies. A visual binary star system will result in a pair of stars that are likely to appear closer to each other than would be expected by random chance throughout that region. Using this perspective, this chapter tackles the problem of detecting binary systems

in densely populated star regions. In these systems the compact distance between stars make binary detection difficult. Using a nearest neighbour ratio technique, it is shown how one can extract information on likely binary fractions in a star region for any underlying density and morphology.

Chapter 3 focuses on critically assessing the methodology used to examine Initial Mass Functions (IMFs). In this chapter, parametric methods to examine IMFs are examined in detail. It is shown how an over-reliance on these parametric methods can lead to incorrect conclusions regarding the true nature of the underlying IMF, such as whether it is Universal or Canonical. After demonstrating this inaccuracy through a series of simulations and inferences, alternative methods are discussed to better detect underlying IMF properties.

Chapter 4 returns to the study of binary fractions, but now focusing on the question of how selection effects impact the inferences one is able to make. The true binary fraction in a stellar population tends to be significantly more than the observed one due to the obstruction by these selection effects. In this chapter, an inverse method to infer binary fraction properties is developed that relies on comparing the distribution of separations (S) and mass ratios (q) with that of a Monte Carlo process. While it is highly effective at detecting these properties without selection effects, it is much less accurate when the selection effects are introduced. By comparing the effectiveness of this method across various selection effect sizes, the chapter is able to show how the truncation of the (q, S) distribution dictates the limits of what can be inferred from observational data.

Chapter 2

Finding binary star fractions in any distribution by a Nearest Neighbour method

2.1 Introduction

Most young stars form in clusters (Lada & Lada 2003, Kruijssen 2012), such as small groups like Taurus and larger clusters like Orion. The study of these systems help us to explore the star formation and evolution process.

An important property of such clusters is the likely binary fraction. Uncovering this property is not an easy task. The thesis introduction described different models available to find the binary fraction of stellar populations (Michell 1767, Struve 1852, Bahcall & Soneira 1981). These methods require a model of the background distribution. They are mostly useful for the field, but in dense clusters it is unclear if the method uncovers binaries or just picks up single systems that are close because of the underlying structures. The smaller the separation between nearby stars, the harder it is to distinguish a pair of binaries.

In this chapter, this issue will be focused to estimate binary population fractions in a cluster with any underlying density structure by making use of a nearest neighbour method. Here is the first outline of the general idea at a high level, and the details are provided in the subsequent sections.

In general, visual binaries are detected as those stars that are closer together than one might expect by random chance. The problem is, for more complex and dense distributions the idea of "closer than random chance" varies. Ideally, we wish to have a systematic statistical methodology to find binary fractions that is both user-friendly

and can be deduced using only stellar positions.

The strategy for this study is to attempt to control the underlying density while measuring the distance between nearby stars. For each star, the distance to the closest neighbour ("d_1") and the tenth-closest neighbour ("d_{10}") is measured. The ratio between these terms ("d_1/d_{10} ratio") becomes the focus of this analysis. Using simulations of four different complex distributions, it is shown this quantity is not sensitive to variations in the underlying mythologies. Furthermore, the cumulative distribution profile of this ratio allows us to explore differences between random and binary star populations. These differences are finally used to estimate the fraction of a cluster that consists of binary systems. The results are verified using Monte Carlo simulations.

The rest of the chapter will elaborate on these ideas. Section 2.2, defines the relevant terms, simulation procedures, and outline the methods. Section 2.3 performs exploratory analysis to demonstrate the usefulness of the d_1/d_{10} ratio, and use this to develop the procedure for estimate the binary fraction of a cluster. Section 2.4 concludes and summarises the procedure.

2.2 Methodology

This section describes multiplicity, morphology, the simulation procedure of clusters, and the nearest neighbour ratio method itself. The assumptions and parameters used for simulations are also detailed.

2.2.1 Multiplicity

To calculate the number of stellar systems from the total number of stars, the following expression is used (Kouwenhoven et al. 2009):

$$N_{\rm sys} = \frac{N_{\rm tot}}{1 + f_{\rm bin}} \tag{2.1}$$

Where $N_{\rm sys}$ is the total number of stellar systems (binary and single systems), $N_{\rm tot}$ is the total number of stars, and $f_{\rm bin}$ is the binary fraction in the stellar cluster.

2.2.2 Stellar Cluster Morphology and Simulation

According to Lada & Lada (2003), 70% - 90% of stars form in embedded clusters, some of which remain bound and evolve to open clusters, the rest dynamically dispersing and become part of the Galactic field. Embedded clusters inherit highly

sub-structured patterns of molecular clouds (Cartwright & Whitworth 2004) which influences the formation and evolution of star clusters.

Based on the surface density profile of the distribution of stars, Lada & Lada (2003) proposed two types of morphologies: sub-structured and centrally concentrated. For this study, both these morphologies are used to simulate dense star populations. Fractal geometry (Cartwright & Whitworth 2004, Goodwin et al. 2004*a*) is used to create clusters with substructure, and Plummer spheres (Plummer 1911) to create centrally concentrated clusters. Examples of these clusters, projected to two dimensions, are visualised in Figure 2.1.

2.2.2.1 Fractal Distributions

Young star-forming clusters are observed to have highly substructured pattern similar to molecular clouds (Cartwright & Whitworth 2004). Goodwin et al. (2004*a*) described substructure as fractal, with only one parameter, the fractal dimension D. With parameter D, it is easy to reproduce substructure which uses a box fractal method to generate a fractal shaped stellar cluster. It uses a cube of side $N_{\rm div}$ (generally, $N_{\rm div} = 2$ is used), to create the fractal geometry. A first-generation parent is placed at the centre of the cube, from which are produced ${N_{\rm div}}^3$ sub-cubes, with each carrying a first-generation child in its centre. The fractal continues to grow by determining which of the children themselves become parents, and create their next generation. This is set by the fractal dimension, D, where the probability of a child becoming a parent is ${N_{\rm div}}^{D-3}$. For lower D, the probability of a child becoming a parent is lower. Children that do not mature are removed, along with their parent. A little noise is then added to the positions of the remaining children, to avoid a gridded structure, and they become the parents of the next generation, each one with ${N_{\rm div}}^3$ children (the second generation).

Each new parent then produces second-generation children in equal volume sub-sub-cubes, with each second-generation child having a ${N_{\rm div}}^{D-3}$ probability of becoming a second-generation parent. This process continues repetitively until there are an excess number of children remaining than are needed. Children are then removed randomly until the required number is achieved, and the surviving children become members of the population (star cluster).

The clumpiness gets higher with a decrease in parameter D. With an increase in D, the cluster becomes more uniformly distributed. Following Goodwin et al. (2004*a*), this analysis simulates highly substructured, moderately clumpy and smooth clusters using $D = 1.6$, 2.0 and 3.0 respectively. In the results section, it is investigated

whether the nearest neighbour ratio can retrieve the stellar population properties despite different cluster morphologies.

2.2.2.2 The Plummer Sphere

The polytropic sphere with $n = 5$ is known as the Plummer sphere (Plummer 1911). It has been used for radial profiles of globular clusters. The density distribution of the Plummer sphere is:

$$\rho_{(r)} = \left(\frac{3M}{4\pi a^3}\right)\left(1 + \frac{r^2}{a^2}\right)^{-5/2} \tag{2.2}$$

Where, M is the total mass of the system and a is the Plummer radius. The relationship between the half-mass radius ($R_{\rm h}$) of the cluster and the Plummer radius is $1.3a = R_{\rm h}$. The density decreases quickly at large radii.

2.2.3 Generating Artificial Binary Stars

The simulations in this study begin with a stellar cluster generated from a specified morphology (Plummer sphere or Fractal with a given dimension) and a given density, as specified above. It then proceeds to assign artificial binary members to a specified fraction of these stars. Here is the detail to show how these artificial binary systems are generated.

Consider first a random star from the existing distribution. The semi-major axis between binary stars, a, is obtained according to Öpik (1924):

$$a = 10^{3.3R_1} \tag{2.3}$$

Where R_1 is a uniform random number between 0 and 1. In our study, a varies between 1 and 2000 au.

Then, the binary star is placed at (x, y, z) from the position of the random star. Assuming zero eccentricity:

$$z = (1 - 2R_2)a \tag{2.4}$$

$$x = \sqrt{a^2 - z^2\cos(2\pi R_3)} \tag{2.5}$$

$$y = \sqrt{a - z^2\sin(2\pi R_3)} \tag{2.6}$$

Where R_2 and R_3 are also uniform random numbers between 0 and 1.

This process is repeated for some given fraction of the original distribution of stars to ensure the desired fraction of binary systems in the final population is reached. It is worth noting that in this study, the total number of stars stays constant, whereas the binary fraction impacts the number of stellar systems in the realisation.

As an example, consider a realisation where the desired number of stars is 5000. If this is realized for a binary fraction of 0% (100% single stars), there are 5000 corresponding (single) star systems. For 20%, 40%, 60%, 80% and 100% binary fractions, the process initially generates single stellar systems of 4167, 3571, 3125, 2778 and 2500. Binary stars are added artificially to enough of these systems that the desired final total number of 5000 ± 1 stars is reached, alongside the desired binary fraction.

2.2.4 Nearest Neighbour Formulation

The aim of the study is to develop a metric to quantify how close each star's closest neighbour is, while accounting for the underlying density of the cluster. For this, the ratio of the distance to the nearest neighbour (d_1) to the distance to the tenth-nearest neighbour (d_{10}) is used. For a given cluster, the distances of neighbours from a particular star will depend on the stellar density, morphology, binary fraction and position of the star. For example in a lower density cluster, the neighbour's distances from a query star (including d_1 and d_{10}) will be greater than those of a denser cluster. One of the advantages therefore of using the d_1/d_{10} ratio as our metric of interest (instead of d_1 or d_{10} in isolation), is that it allows us to eradicate (or at least minimise) the scaling effects due to differences in the population's density. This robustness of the method to stellar density allows us to focus on more interesting sources of variation in the d_1/d_{10} ratio, such as the effect of the of binary systems. In principle, for a given binary, the d_1/d_{10} ratio will become much smaller than two closely situated random stars.

The nearest neighbour search is a computational problem for finding points in a data set that are nearest to a given query point. For a certain dataset and a query point, it analyses how much the distance to the nearest neighbour differs from the distance to other data points. To evaluate the proposed method, the Euclidean distance will be used to calculate the distance:

$$d = \sqrt{(x_1 - x_2)^2 + (y_1 - y_2)^2 + (z_1 - z_2)^2} \tag{2.7}$$

For simplicity, the approximation of nearest neighbour distance method will be

used by projecting three dimensional data into two dimensional space. Therefore the ratio between the 1st and 10th nearest neighbour distances is a dimensionless number.

This ratio is obtained for all stars, and examine the distribution of this ratio across all stars in a given cluster. Since the ratio is smaller for pairs of binaries, it follows that clusters with a binary fraction will have distributions with a significant peak around low ratios. Clusters without a binary fraction are unlikely to display this peak.

2.2.5 Goodness of fit to obtain parameter estimates

Once the distribution of the nearest neighbour ratios for a given cluster is obtained, one needs to have a consistent method to detect the proportion of the d_1/d_{10} ratios that could belong to binary systems in the cluster.

This was achieved through fitting the cumulative distribution function (CDF) of these ratios to a given parametric distribution, using Python's lmfit package's iterative least-square minimization technique. This minimisation technique searches the parameter space of a family of distributions to minimize the least-square statistic.

During the exploratory study, it was established which parametric family best fit the data. For single population data (either 100% binary or single stellar systems), Gaussian distributions proved to be the best fit, while a mixture of two Gaussians was found to best fit mixed single and binary population data.

The single Gaussian probability distributions used for pure random single or binary stellar systems had two free parameters (degrees of freedom): mean (μ) and standard deviation (σ). For consistency with other findings, however, they will be referred to as μ_1 and σ_1 when estimating populations with purely single stellar systems, and μ_2 and σ_2 when estimating populations with purely binary systems.

Double Gaussian probability distributions were used to model populations consisting of both single and binary systems, with a total of six parameters. The parameters are w_1, μ_1 and σ_1 correspond to one subpopulation (single systems), and w_2, μ_2 and σ_2 for the second subpopulation (binary systems). The estimated weight of the distribution between the two subpopulations is determined by w_1 and w_2. As the sum of the two subpopulation's weight functions equal 1 ($w_1 + w_2 = 1$), there are five degrees of freedom in total. For our study, w_2 is the estimated fraction of binary systems for a given population.

2.3 Results

2.3.1 Population with Single Stellar Systems

As mentioned in section 2.2, there are stellar clusters with fractal distributions which come with different fractal dimension (D) as well as the Plummer distribution types. In Figure 2.1 four different types of morphologies are visualised with a total of 5000 stars each and 0% binary fractions (ie; 100% single stellar systems). In this figure the top left (panel a) and right (panel b) and bottom left (panel c) present stars with a fractal distribution with dimensions, $D = 1.6$, 2.0 and 3.0 respectively. For highly substructured stellar cluster (fractal dimension $D = 1.6$) the morphology is very clumpy. The clumpiness eases with increase in D and becomes nearly uniform when $D = 3.0$. The bottom right (panel d) shows stars distributed in a Plummer sphere (created using the method of Aarseth et al. (1974) with 0% binary fractions). They are distributed in almost a radially even way where stellar density decreases with increase in radius. The distributions are created in three dimensions and projected into two dimensions as seen along an arbitrary z-axis. The projection is 5×10^5 au on a side (roughly 2 pc).

The procedure of Section 2.2.4 was followed to get the ratio of the distance of the nearest neighbour, d_1, to the distance of the tenth nearest neighbour, d_{10} (d_1/d_{10}). The advantage of tenth over other nearest neighbours as this is far enough away to go beyond local multiple systems and at the same time close enough to avoid large-scale (surface) density variations. It is also a large enough number to avoid too much noise in the distance of the tenth nearest neighbour.

Figure 2.2 shows the cumulative distribution of nearest neighbour ratios (d_1/d_{10}) for all the stars distributed in panels (a), (b), (c) and (d) of Fig.2.1. Despite visual differences of all the four projected distributions, their d_1/d_{10} distributions look very similar. Ideally, if there are no binaries and the ten nearest neighbours are distributed uniform randomly, then the distance ratio (d_1/d_{10}) is around 0.3 ($\sim 1/\sqrt{10}$). Following the χ^2 minimisation technique detailed in Section 2.2.5, this CDF was fit with a single Gaussian CDF. A Gaussian fit to their CDFs provides us with the μ_1 and σ_1 of d_1/d_{10} are 0.22 ± 0.18 (red line, top left $D = 1.6$ fractal), 0.24 ± 0.17 (black line, top right $D = 2$ fractal), 0.25 ± 0.17 (brown line, bottom left $D = 3$ fractal), and 0.26 ± 0.16 (green line, bottom right Plummer sphere). The CDF's are very close to Gaussian with the mean values of $d_1/d_{10} \sim 0.3$.

As can be seen, for fractal populations, the d_1/d_{10} distribution moves slightly further to the left with a decrease in fractal dimension, D. Also, d_1/d_{10} ratios tend

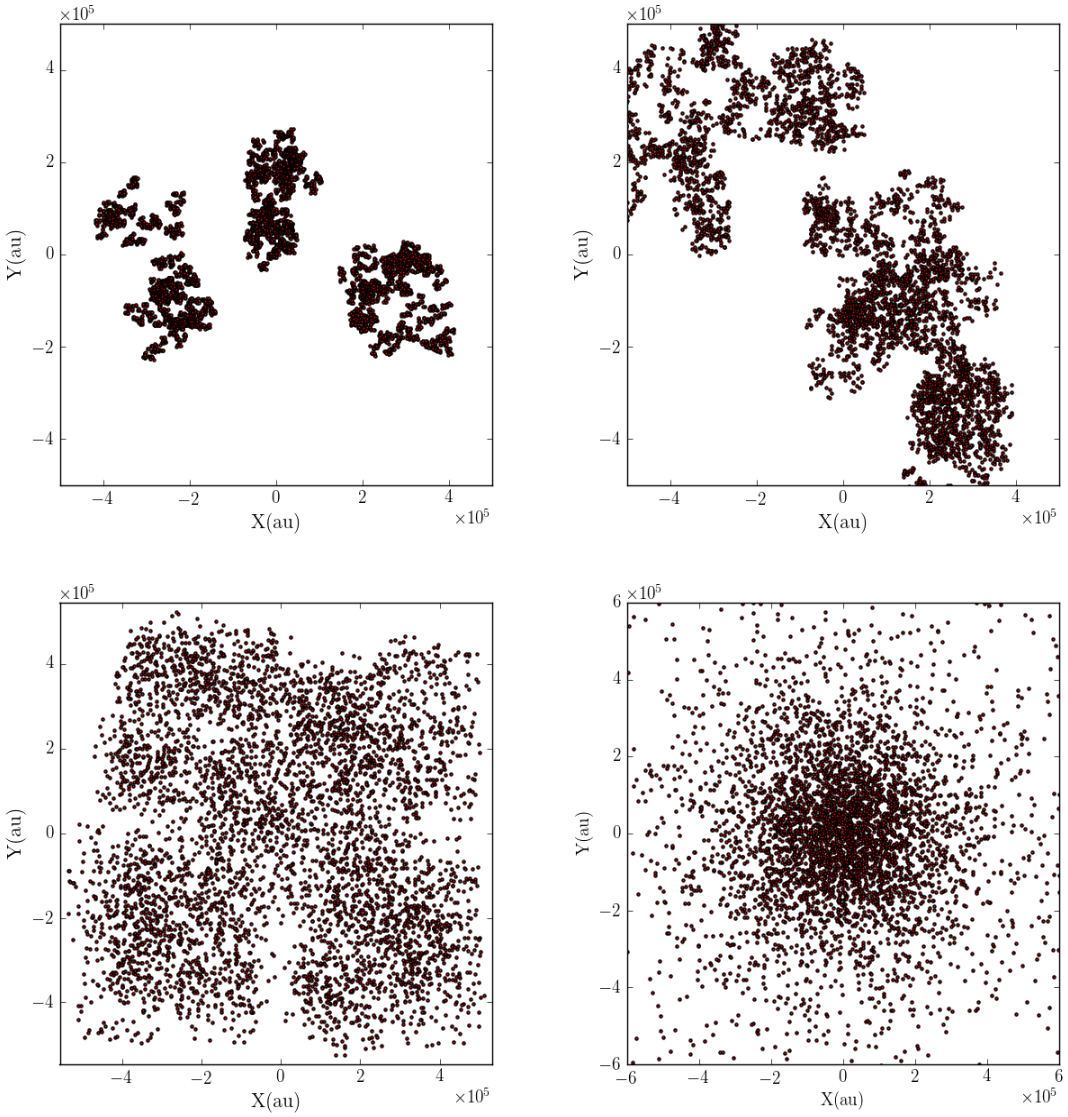

Figure 2.1: Projected distributions of $N = 5000$ stars density distributions with no binaries. Top left (panel a) is a $D = 1.6$ fractal, top right (panel b) a $D = 2.0$ fractal, bottom left (panel c) a $D = 3.0$ fractal, and bottom right (panel d) a Plummer sphere. The X-Y size scales are ~ 2 pc to mimic realistic clusters.

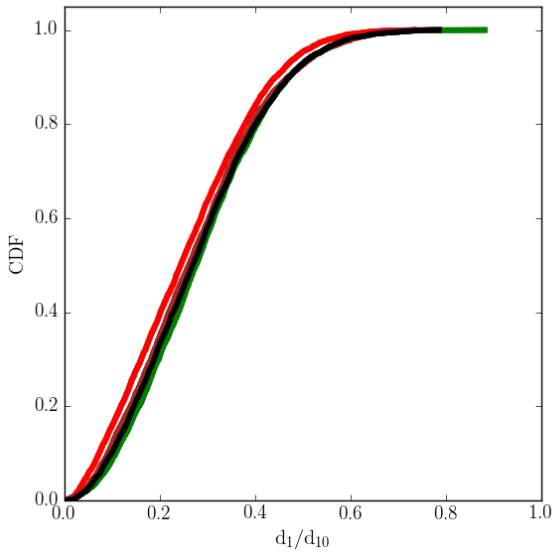

Figure 2.2: Cumulative Distributions of the d_1/d_{10} ratios for the four $N = 5000$ density distributions in Fig.2.1. Fractal Dimension D = 1.6 is the red line (top left in Fig.2.1), D =2.0 is the black line (top left in Fig.2.1), D=3.0 is the brown line (bottom left in Fig.2.1), and the Plummer sphere is the green line (bottom right in Fig.2.1).

.

to have slightly smaller values in the three fractal distributions than in Plummer spheres. It will be shown later that the differences are negligible compared to the changes in the d_1/d_{10} distributions due to inclusion of binaries.

To test the robustness of this, Fig.2.3 presents the cumulative distribution of d_1/d_{10} ratios for 1000 realisations of stellar populations. 750 realisations were carried out for populations with fractal distribution ($D = 1.6$, 2.0 and 3.0) and 250 realisations with Plummer spheres. The total number of stars was kept at 5000. The variation of the CDFs for each of these realisations are now examined.

The blue error bars display the minimum and maximum values, whereas the green error bars indicate 25 and 75 percentile values for all these realisations. Despite different types of morphologies, it can be seen the variation of the CDFs of d_1/d_{10} is generally low. Therefore, one can say for 100% single systems, despite different underlying morphologies, the CDF will not deviate drastically and tends to follow a similar shape. The simulations obtain a small range of means, μ_1 (0.2 to 0.29) and standard deviations, σ_1 (0.16 to 0.19) for the best fit Gaussian parameters to these cumulative profiles with no objects closer than expected by random chance. In conclusion, for single system population stars the ratio d_1/d_{10} is relatively insensitive to morphology.

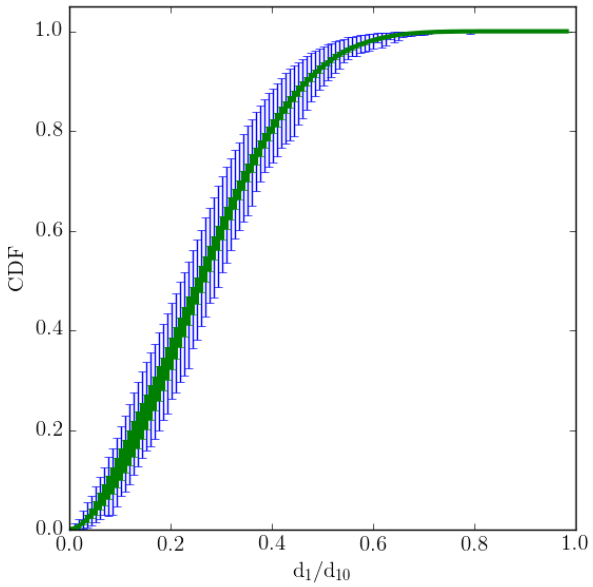

Figure 2.3: The spread of the cumulative distributions of d_1/d_{10} ratios for 1000 realisations (250 of each type). The green error bars show the spread of the 25 to 75 per cent of distributions, the blue error bars show the extremes of all 1000 realisations. All realisations can be well-fitted with Gaussians with means, μ_1 0.20–0.29 and standard deviations, σ_1 0.16–0.19.

The d_1/d_{10} ratios will change abruptly when the binary fraction is increased. Therefore, if the cumulative distribution does not fit the single Gaussian distribution with the above-mentioned range of means and standard deviations, it is an indicator of the presence of binary systems. The next section examines how this property holds when this methodology is applied to differing fraction of binary and single stellar systems.

2.3.2 Binary Addition

Fig.2.1 - Fig.2.3, show the d_1/d_{10} distributions of single stellar populations and how to estimate their parameters by the Gaussian CDF fit method. The effect of adding binaries to the distributions can now be investigated.

It can be seen that d_1/d_{10} is a scale-free number which is small for stars in a binary system and comparatively large for two random single system stars. Therefore, adding a certain binary system fraction with single stellar systems will show a change in the (d_1/d_{10}) ratio. In what follows, populations with different binary fractions are visualised. The cumulative distributions of the nearest neighbour ratios, d_1/d_{10}, are also shown. The best fit to these cumulative distributions are then used to estimate

the binary fractions in that stellar cluster. It is then examined how robust such nearest neighbour ratio distributions are to differences in morphology and density, both in terms of purely single and purely binary system populations, as well as mixed single and binary system populations of varying multiplicities.

As discussed in Section 2.2.3, binary systems are generated with an Öpik's Law separation distribution between 1 and 2000 au in 3D and projected into 2D.

2.3.2.1 Recovering binary fractions

Let us start with a Plummer sphere morphology with different binary fractions and a total of 5000 stars. The left column of Fig.2.4 presents 5000 single stellar systems (top), middle has 2500 binary systems (100% binary) and bottom has a mix of 3333 single (1667) and binary (1666) systems (50% binary fraction), onto the two-dimensional plane. Despite the variation of binary fractions, distributions of the stars in these three left hand panels do not look that different apart from being visually sparser with an increase in binary fractions. This visual distribution therefore is not enough to estimate the binary stellar fractions contained in these clusters.

The right column shows the CDFs of the d_1/d_{10} ratio corresponding to each of the distributions from the left. In the case of a binary system d_1 is much smaller than two random single stars next to each other. On the other hand, d_{10} only depends on the stellar density of the cluster and should not in general be affected by whether the query star is a member of a binary system. d_1/d_{10} is therefore a scale free number that is small for stars in a binary system and comparatively large for two random single system stars. It can be seen therefore that the CDF of the ratio looks considerably different as the binary fraction varies.

The top right panel of Fig.2.4 (0% binary) shows the d_1/d_{10} (red) has a range of values from near 0.005 to almost 0.76 where the CDF reaches its maximum value 1.0. The resulting fit (dashed green) parameters μ_1 and σ_1 are respectively 0.26 and 0.16.

The middle right panel presents the cumulative distribution of d_1/d_{10} of 2500 binary systems (100% binary) taken from the stellar positions of the left middle panel. The CDF starts at 8×10^{-6} and reaches its maximum value 1.0 at a d_1/d_{10} of 0.03 which is less than $\frac{1}{20}$th times what is found for 0% binary systems in the top right panel. This small d_1/d_{10} value means almost all stars have a companion much closer than expected by random chance. A single Gaussian CDF is fit to the cumulative distribution of the d_1/d_{10} ratios. The resulting fit parameters μ_2 (binary stellar system mean), and σ_2 (binary stellar system standard deviation) are respectively 0.005 and 0.008. The μ_2 and σ_2 have much smaller values compared to

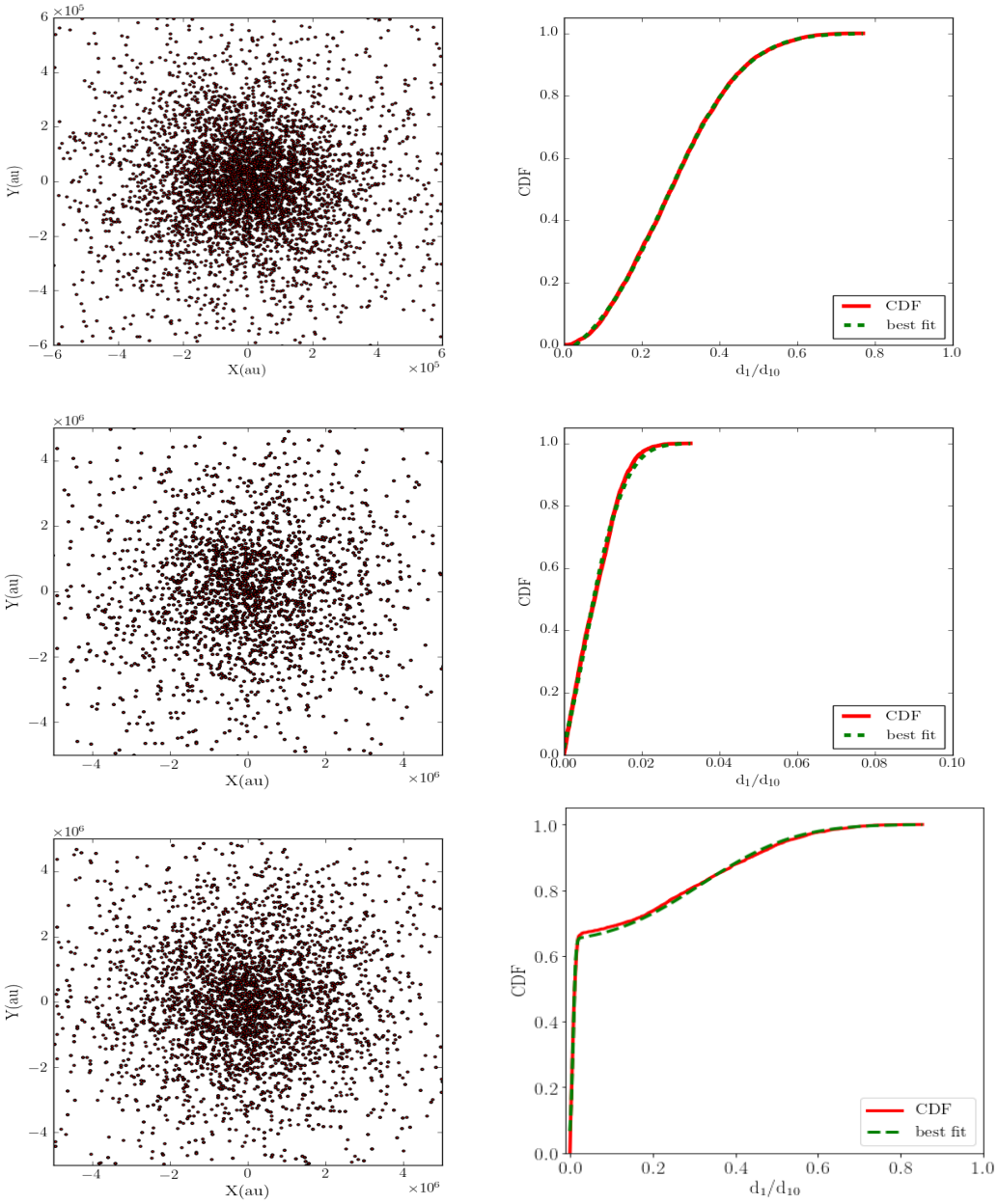

Figure 2.4: Projected views of stars in Plummer spheres with $N = 5000$ stars alongside the d_1/d_{10} cumulative distributions and their best fit Gaussians. Top row: 0 per cent binary fraction. Middle row: 100 per cent binary fraction. Bottom row: 50 per cent binary fraction.

μ_1 and σ_1 from single stellar system population.

So far there has been a consideration of either single or binary stellar system populations. In reality, a stellar population has both single and binary stellar systems. The bottom right panel shows cumulative distributions of d_1/d_{10}, and its Double Gaussian CDF fit, from the population in left bottom panel. The cumulative distribution of d_1/d_{10} shows two peaks (one peak close to 0 and another one further away from it) indicating two subpopulations. Adding binaries with single stellar systems has thus led to two peaks. The double Gaussian CDF was a reasonable fit for these peaks representing the single and binary stellar populations contained in the cluster. The initial peak resembles binary stellar system subpopulation whereas the second peak resembles the single stellar subpopulation.

The CDF parameters for double Gaussian fits are two weight fractions (w_1, w_2), two means (μ_1, μ_2) and two standard deviations (σ_1, σ_2). The parameters w_1, μ_1 and σ_1 correspond to the single stellar systems, and $w_2(= 1 - w_1)$, μ_2 and σ_2 correspond to the binary system. For the bottom right panel the best fits for μ_1, σ_1, and w_1 are 0.31, 0.18 and 0.36 and for μ_2, σ_2, and w_2 are 0.007, 0.005, and 0.64. These parameter values resemble the corresponding parameters in the single and binary system populations found for top and middle panels. In this example, the estimated Gaussian binary fraction was found to be 14% higher than the actual binary fraction.

Fig.2.5 presents another example to showcase how adding a small binary fraction changes the CDF from single to binary Gaussian distributions. Here, the top left panel presents a total $N = 5000$ stars projected onto two dimensions in a very clumpy fractal distributed ($D = 1.6$) cluster. For this population, we have added 20% binary systems with 80% single stellar systems. In the top right panel of Fig.2.5, the CDF of d_1/d_{10} is presented. It can be seen that it gives rise to two peaks, one representing binary systems (with mean $\mu_2 = 0.00013$ and standard deviation $\sigma_2 = 0.0001$) and then a broader single system (single random pairing system, mean $\mu_1 = 0.28$ and standard deviation $\sigma_1 = 0.17$). A double Gaussian CDF fit was an extremely good fit for the CDF of the d_1/d_{10} ratio, with the weight w_2 indicating an estimated 30% binary fraction.

The parameters of the two Gaussian CDFs required to fit the 50 per cent binary fraction Plummer distribution in the bottom panel of Figure 2.4 and the 20 per cent binary fraction $D = 1.6$ fractal in Figure 2.5 are very similar. The only significant difference is the relative weightings (w_2) which are directly related to the added binary fractions. In each case, the binary weight component (w_2) is slightly higher than the added binary fraction: estimating 64% for a binary fraction of 50%, and 30% for a binary fraction of 20%.

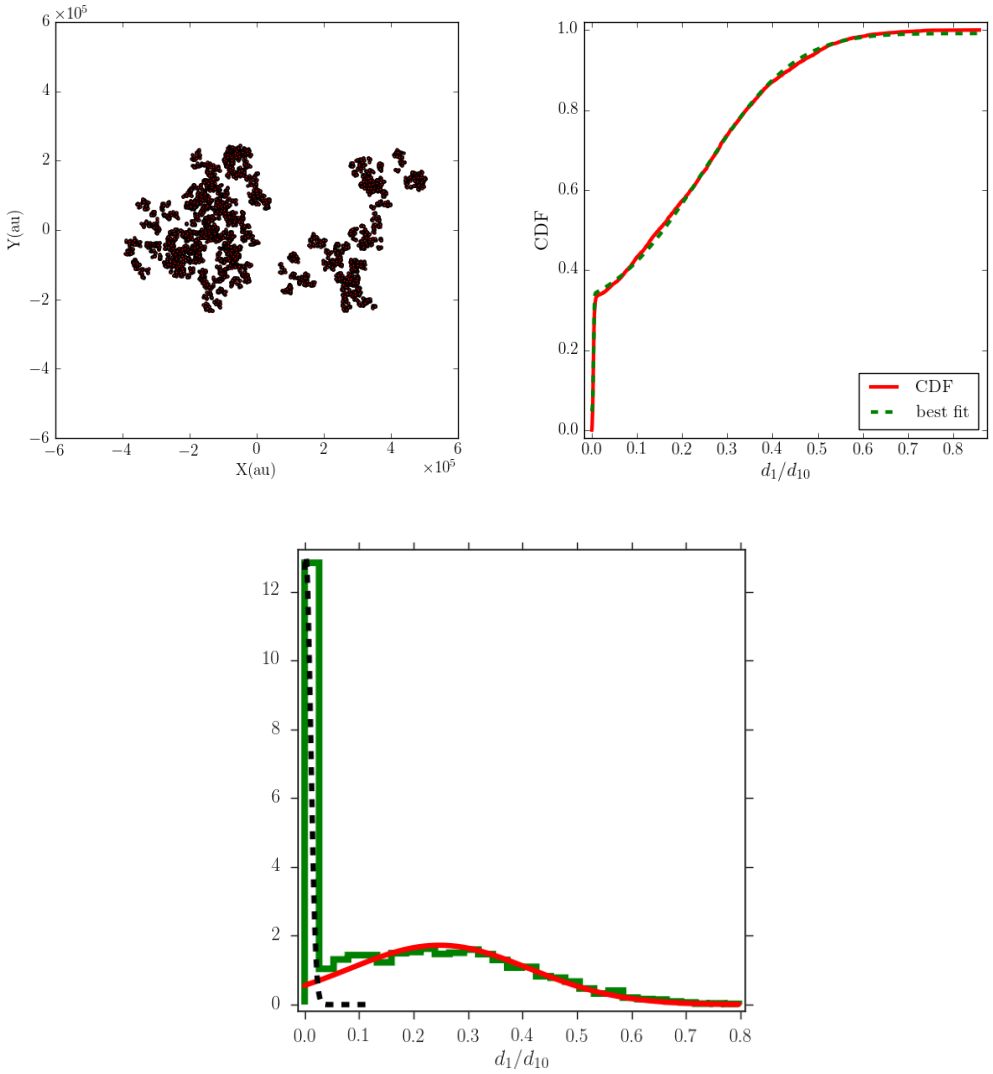

Figure 2.5: Top (Left panel): a projected view of an $N = 5000$, $D = 1.6$ fractal with a 20 per cent binary fraction. Top (Right panel): the cumulative distribution of d_1/d_{10} (red line) with a two Gaussian best-fit (green dashed-line). Bottom: shows the same d_1/d_{10} distribution in histogram form. The green line presents d_1/d_{10} distribution in combined histogram form for 5000 stars, red in single system (0%) and black line for 5000 stars in (100%) binary systems.

The difference between the Gaussian weightings and the underlying binary fractions is due to a small number of nearest neighbour pairs of single systems, where the separation was small enough to be considered as possible binaries. To understand this overestimation of binary fraction, let us examine how the Gaussian curve fitting attempts to allocate weight between two sub-populations (single and binary systems) in the data.

The bottom panel of Fig.2.5 "decomposes" the 20% binary cluster pictured in the top panels by showing the d_1/d_{10} ratio distribution of a 0% binary system (red) and a 100% binary system (black), each with $N = 5000$. These correspond to the single and binary systems of the original cluster respectively, with the ratios of the former ranging from 0.0055 to 0.8 and the latter ranging from 2×10^{-5} to 0.06. It can be seen there is a region of overlap of d_1/d_{10} ratios where simple spatial data cannot draw a distinction between binary pairs and extremely close single stellar systems. The histogram from the original 20% binary fraction cluster in the top panels is presented in green, and it can be seen how it combines the two histograms.

This figure also gives us a clue as to why we are seeing the value of w_1 being slightly under-estimated and by extension the binary fraction w_2 slightly overestimated (i.e. why does the fitting procedure place more weight on the binary "sub-distribution"?). Since the d_1/d_{10} ratio cannot fall below 0, it can be seen that the wider single system ratio distribution is often truncated in its bottom tail. As a result it has a lower weight assigned to it, and this additional weight is allocated to the binary system sub-distribution.

Consider now to see how the estimated binary fraction behaves when the methodology is applied to different fractions of binary systems. To explore the robustness of this method across a variety of initial conditions, realisations are run across different total numbers of stars (500 and 5000) and four different morphologies (fractal distribution with $D = 1.6$, 2.0, 3.0 and Plummer spheres). For each initial condition we added 20%, 40%, 60% and 80% binary fractions with single system stars and carried out 1000 realisations for each fraction of added binaries. In each case the binary fraction was estimated using the w_2 weight as per the methods described so far.

In Figure 2.6, the estimated weight parameter w_2 for each added binary fraction is plotted. The black solid line and dashed red line showcase 5000 and 500 stars respectively, distributed in a fractal type morphology. The orange solid lines and dashed green lines present 5000 and 500 stars respectively, distributed in Plummer sphere morphologies.

The first thing to note is that the relationship does not vary for 500 or 5000 stars, and whether we are looking at fractal or Plummer sphere morphologies. In other

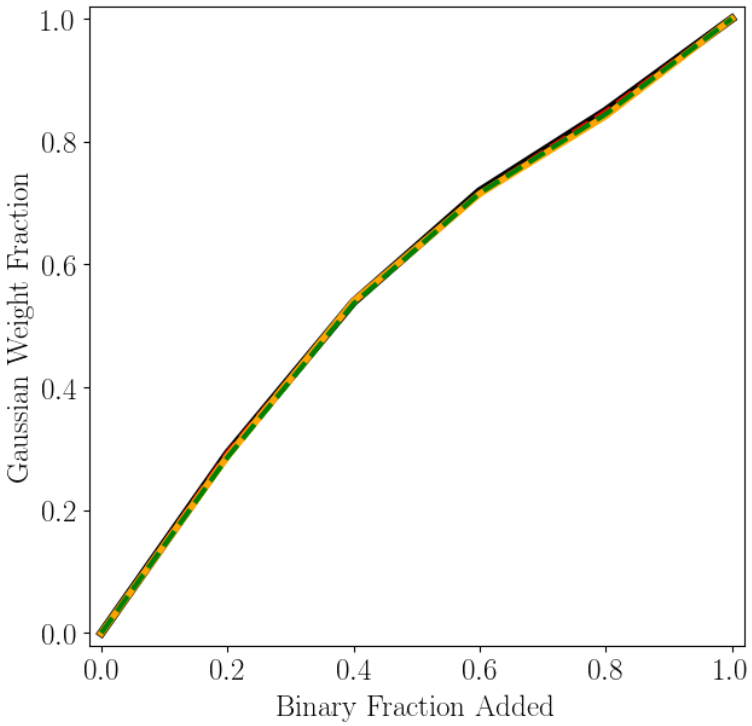

Figure 2.6: The binary fraction against the relative weight of the Gaussian binary fit. The solid lines are $N = 500$ star clusters, and the dashed-lines are $N = 5000$ star clusters. Black lines are fractal distributions, and red lines are Plummer spheres. All four lines lie almost on top of each other.

words, the method is consistent in its prediction of the binary fraction. Using d_1/d_{10} as a measure therefore diminishes the effects of stellar density and cluster morphology on the estimate. The second thing to note is that the relationship between the true binary fraction and the Gaussian weightings is nearly (but not quite) one-to-one. As expected, the Gaussian increases from zero when the binary fraction is zero, to a weighting of unity when the binary fraction is 100%. For 20%, 40%, 60% and 80% added binary fraction the median Gaussian weight fraction for fractal (N=500), fractal (N=5000), Plummer (N=500) and Plummer (N=5000) are respectively (0.292, 0.539, 0.719, 0.85), (0.293, 0.538, 0.716, 0.849), (0.287, 0.54, 0.715, 0.842) and (0.286, 0.536, 0.716, 0.845). Therefore, the increase is not quite linear and the difference between the Gaussian weighting and binary fraction is greatest when it is roughly a half (due to have more extremely close random pairs than other binary fraction).

In all these cases, it can be seen that the estimated fraction of binaries consistently overestimates the true fraction of binaries. In all the cases (apart from 0% and 100%),

the weighted binary Gaussian was 4.2 to 14% (approximately 5 to 15%) higher than the added binary fraction in the simulated population.

2.4 Conclusion

This chapter develops a method to estimate the binary fractions of stars that are closer than expected by chance in a stellar cluster. For this purpose, we carried out Monte Carlo simulations of clusters for different morphologies and densities and used nearest neighbour ratios and Gaussian CDF curve fitting techniques. Besides searching for binary stars (ie. gravitationally bound pairs) in astrophysical data, this method potentially applicable to other datasets where detection of close-than-usual pairs are an important procedure.

The method is summarised here:

1. Calculate the first and tenth nearest neighbour ratio, d_1/d_{10} for every object.
2. Construct the CDF of d_1/d_{10}.
3. If the cumulative distribution fits a single Gaussian CDF, then there is only one particular population, either 100% single or 100% binary.
4. If a single Gaussian is the best fit with a mean and standard deviation of 0.20–0.30 and 0.16–0.19 respectively then the data shows no evidence for binaries.
5. A single Gaussian with a mean much lower than 0.2 suggests a 100 per cent binary fraction.
6. If the cumulative distribution fits a double Gaussian CDF, one can interpret that the population is composed of both single and binary stellar systems.
7. From the Double Gaussian fit, one can get weightings of the Gaussian binary directly related to the underlying binary fraction. This Gaussian binary weight (w_2) is 5% - 15% more than the underlying binary fraction.

In reality, the possibility of observing a stellar binary depends on a number of additional criteria. For visual binaries, this depends on a few observational selection effects, such as the magnitude difference and the minimum and maximum angular separation related to the magnitude difference of the binary member stars. Close binary companions can only be observed if the angular separation between the primary and secondary stars is not larger than the angular resolution.

At the same time, too bright a primary star will outshine the secondary star. For a very wide binary system, both members might well appear to be as two unassociated single stars. Therefore, selection effects are an observational problem that obstructs the study of a good fraction of visual binary systems.

In chapter 4, these biases are examined to determine whether generated binary stars are visible or not. A Binary Search Tree method is used to match the similarity of the 2D distribution of binary mass ratios (q) and separation of observed stellar samples with an exhaustive set of reference stellar populations generated through Monte Carlo simulation. In doing so, the analysis seeks to explore how exactly selection effects obscure the true binary properties in observational data.

Chapter 3

IMF Universality

3.1 Introduction

The initial mass function of stars (IMF), which describes the distribution of stellar masses at birth, is of fundamental importance to astronomy. Stellar mass provides astronomers with an understanding of the formation, evolution and properties of stars (such as density, size, temperature etc). For example, the number of massive stars are responsible for supernovae and the rate at which metals are produced.

An extremely important question about such IMFs is whether or not they are universal - is the distribution of mass across the IMF the same regardless of where they are sampled from? The answer to this question is of such fundamental importance that a significant literature has emerged investigating it. Detailed reviews of IMF studies have been given by Bastian et al. (2010), Kroupa et al. (2013), Offner et al. (2014). In these studies, the initial mass function of resolved stellar populations in our Galaxy and nearby galaxies were found to be consistent with universality. However, the matter is far from concluded, with alternative methodologies such as Bayesian analysis (Dib 2014) providing compelling alternative evidence. The methodology of all such studies usually involves proposing some parametric distribution that describes this "canonical" IMF, and checking to see (through a variety of methods) if observed samples match this proposed distribution.

The subject of this chapter is not to answer questions about universality directly. Instead, the study will take a step back and ask some fundamental questions about the methodology used to analyse IMFs in the first place. In particular, the chapter will show that given the heavy-tailed nature of the data, the limited sample sizes, and the parametric inference methods that have become typical in IMF studies, drawing conclusions about the "true nature" of the IMF is extremely difficult. Indeed, it is

shown in this Chapter that even very distinct underlying "true natures" cannot be distinguished from the available samples drawn.

In order to do this, one needs to be precise about what is meant by the "true nature" of the IMF, so one can model it. Ambiguity in the terminology used to study IMFs have been a persistent issue in the literature (see, for example, Hopkins (2018) for a recent review). One of the sources of ambiguity arises from the use of terms such as "universal" or "canonical" in a sometimes interchangeable manner when conducting IMF studies. This study will draw the following distinction:

- *Universality* refers to the hypothesis that the underlying distribution of stellar masses is identical regardless of where they are sampled from
- *Canonicity* (or the canonical assumption) refers to the hypothesis that *given* there is a universal distribution, the distribution fits a specific described set of canonical parameters (described in detail below)

Clearly, the property of canonicity implies the property of universality (but not vice versa). The fact that canonicity implies universality is one reason why these properties are used interchangeably in studies that are attempting to establish universality. If one can show that the available data all fit to a stated canonical form, then it can be argued that the distribution is universal. This approach has its conveniences, but it is also worth mentioning that it has downsides, which this chapter will explore in more detail shortly.

For now, however, disambiguating these two properties allows us to propose three distinct "true natures" in the form of mutually exclusive Hypotheses:

- Hypothesis 1: The IMF is universal and follows the canonical parameters
- Hypothesis 2: The IMF is universal and does not follow the canonical parameters
- Hypothesis 3: The IMF is non-universal

The approach of the Chapter is as follows: for each of the three Hypotheses, Monte Carlo methods are used to simulate a physical star formation process that matches the Hypothesis. This will be used to generate stellar clusters of the typical sample size encountered in astrophysical studies. These samples are passed through the typical inference process used in such studies to try to make claims about the true nature of the IMF. The analysis will seek to show in each case, the inference

process does not reliably support the Hypothesis that was assumed to generate the data, and in some cases in fact better supports incorrect alternative Hypotheses.

Before the chapter gets into the details of this analysis, however, some existing research on IMFs are reviewed. In particular, the chapter begins with a more detailed analysis of the status quo methodology used in IMF studies - parametric fits for functional forms. This allows us to introduce some shortcomings of this approach. We then consider more existing empirical studies on Universality, and theoretical studies that use the IMF as a generating function.

3.1.1 IMFs and Parametric Forms

Consider first some historical perspective. In astronomy, the IMF is considered to be the underlying parent distribution of stellar mass (Kroupa 2001*a*, Bate 2005, Andersen et al. 2008, Haas & Anders 2010, Parravano et al. 2018). Kroupa et al. (2013) defined the IMF as a universal parent distribution function that describes the distribution of stellar masses in individual star-forming events. Early pioneers in astronomy noticed a pattern in the observed stellar mass data, and an early hypothesis of Universality was born (see, for example, Salpeter (1955)).

Before considering the details of specific studies to explore this hypothesis, let us start with a fundamental question - how could one ideally show that the claim of Universality in IMFs was true? That is, given the samples of stellar mass data we possess, how can one show that the underlying distribution of stellar masses is identical in all regions of space? From a statistical perspective, there are two broad approaches one could take here - a non-parametric and a parametric approach.

The non-parametric approach is arguably the most intuitive: compare the distributions of each sample directly and see if they are similar enough to have conceivably had a common underlying distribution. This approach is called 'non-parametric' because one does not presume that these distributions follow any specific parameterised functional form (log-normal, power law, etc), but are instead completely free to vary. The implication of this is that one does not need to make any assumptions about the form the underlying distribution might take, and only looking at direct comparisons between samples. Examples of these kinds of methods include two-sample Kolmogorov-Smirnov or Anderson-Darling tests, which compare pairs of samples at once, or their multi-sample analogues, which allow the comparison of multiple samples at once (Kruskal et al. 1952, Scholz & Stephens 1987). In a review of universality studies by (Bastian et al. 2010), however, it is discussed that this non-parametric approach is generally not the methodology used in such studies.

Instead, existing studies tend to adopt a parametric approach to investigating Universality. In this approach, one must firstly presume some parametric form - for example a log-normal, power-law, or combinations of these. The samples are then fitted to these parametric forms through methods discussed shortly, and questions about Universality instead are simplified to the *comparisons of the parameters rather the comparisons of the samples themselves*. This approach has very much become the de facto methodology to study universality. As summarised in the same review Bastian et al. (2010): "Most researchers conduct this [universality] analysis by fitting a power-law or log-normal IMF to their measurements, and then compare the parameters of their fit to those derived in other IMF studies. A disagreement between the derived parameters is typically interpreted as indicative of astrophysically meaningful IMF variations.". Over time, there has been a growing consensus on the typical parameter fits observed in stellar data, which will be referred to as the canonical parameters. The parametric form, together with the "canonical parameters", are then referred to as the "canonical form" of the IMF. The first such notable example of these parametric/canonical fits was by Salpeter (1955), later refined by Kroupa et al. (1993), Chabrier et al. (2005), Maschberger (2013) and others (a more detailed review of these is present in Section 1.4 of the introduction chapter). Once an understanding of these canonical fits become commonplace as they are today, claims about universality can then (in theory) be checked even more straightforwardly - for subsequent studies, researchers need merely to check whether their fit parameters are reasonably close to the canonical parameters. It is here one can see more clearly how over time the debate about universality and canonicity have become quite entangled (and also why they are still distinct hypotheses, and why this chapter is careful to treat them as such).

The obvious upside of parametric approaches to studying IMFs and Universality is convenience. By specifying and fitting a particular canonical shape, one has a usable, succinct analytic formula for the hypothetical "universal" IMF that can inform further study. This is valuable for both empirical and theoretical studies. On the empirical side, as has already been mentioned, the parametric approach allows studies of universality to be done by comparing a few numbers (the parameters) as opposed to having to utilize the entire sample dataset(s) each time. This also allows us to produce useful rules to thumb to check whether a dataset adheres to the canonical form by simply checking if the fitted parameters are "close enough" to the canonical parameters. On the more theoretical side, the analytical forms can be used as a "target distribution" for developing explanatory physical processes that could generate the IMF. Alternatively, the analytic forms can be taken as a universal form, and then

used as a generative model (especially in simulations) to inform other astrophysical studies. The methods used in this chapter will in fact address these conveniences.

The downside of the parametric approach, however, is that a lot of complexity is lost by mapping the problem down to an analysis of a few parameters. If the universal IMF is the result of a complex set of astrophysical dynamics, the likelihood it adheres to a smooth functional form is quite small. When it comes to making inferences about the underlying distribution therefore, these approaches are constraining the set of possible shapes that the distribution can take, meaning any estimate of the underlying distribution is an *approximation* of the true underlying distribution (if it exists). There's nothing inherently wrong with this approach and is common throughout science, but as this analysis seeks to demonstrate, these parametric constraints can really be misleading when it comes to subtle questions such as universality. Furthermore, there is a tendency over time to utilize these functional approximations in, for example, theoretical studies that treat them as the generating function for simulations. Several examples are reviewed below.

It is useful now to consider some concrete examples of these studies that make use of the parametric approach to IMF analysis. Consider first an example of modelling canonical IMF from observational mass distribution. Chabrier (2003) adopted an IMF with a log-normal distribution merging with a power law at the high mass end. In this work, he took galactic field stars under $1M_{\odot}$ and fitted them with log-normal function (Fig. 3.1). To convert K band luminosity function from galactic field stars Delfosse et al. (2000), Segransan et al. (2003) (Fig. 3.1, filled squares and solid line), into system IMF, he merged members of multiple stars into unresolved systems). He then modified the systems, adding faint stars from Hubble Space Telescope (triangles and short-dashed line) (Zheng et al. 2001).

These observed field stellar mass system distribution with log-normal form of single star mass function or SSMF (presents equation 17 of that paper) and system mass function or SMF (equation 18). In Fig. 3.1 the solid line presents the SSMF and the upper and lower dotted lines their uncertainty. The dashed line shows the SMF and are parameterized by the similar log-normal form of SSMF.

The main feature to point out in Figure 3.1 is the functional form that is being attempted to fit to the sample data is not exactly what one might call particularly close, and it is clear that quite a different set of sample data could conceivable be fit to the same parameters of this functional form.

In general, the parametric approach to studying IMFs effectively reduces a great deal of complexity in possible distributions to a very low-dimensional parameter space, and this can have an effect in the conclusions one draws. Consider the illus-

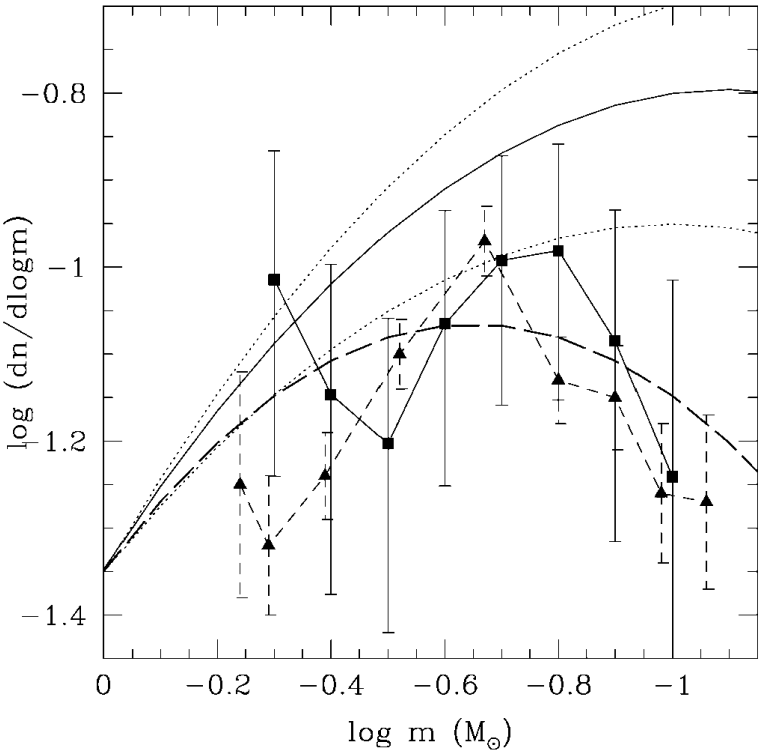

Figure 3.1: Disk field system Mass function derived from the K-band LF (squares with solid line) whereas the triangles with short-dashed line present the HST corrected MF (Taken from Chabrier (2003). These observed mass distribution are fitted with log-normal form of SSMF from equation (17) of his paper (the solid line and the uncertainties are surrounding dotted lines). The dashed line illustrates the log-normal form of SMF given by Eq. (18).

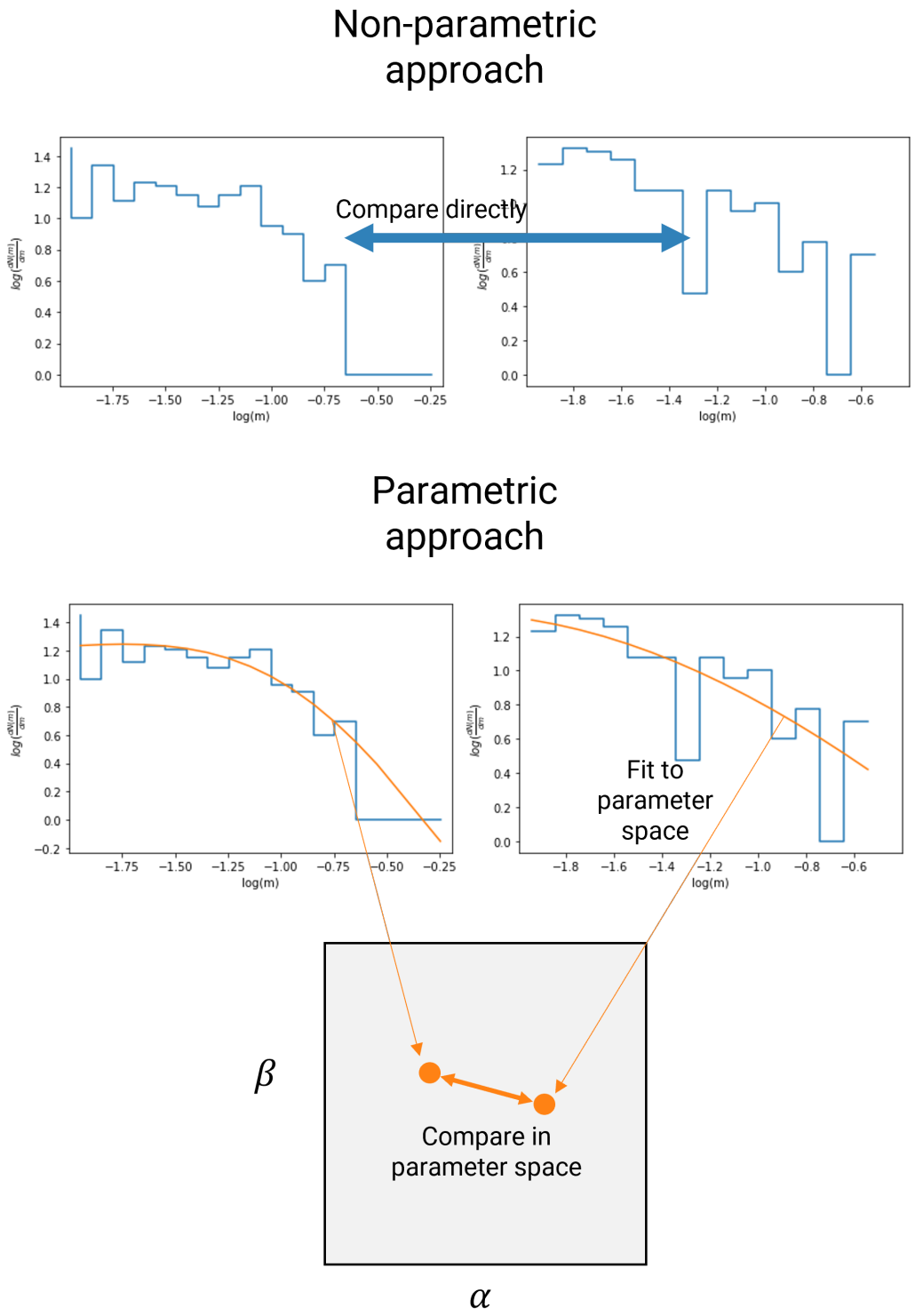

Figure 3.2: Summarising the difference between the parametric and non-parametric approach to comparing IMFs. The non-parametric approach considers the similarities between the full distribution. The parametric approach summarizes the distributions to a small set of parameters, then compares those parameters.

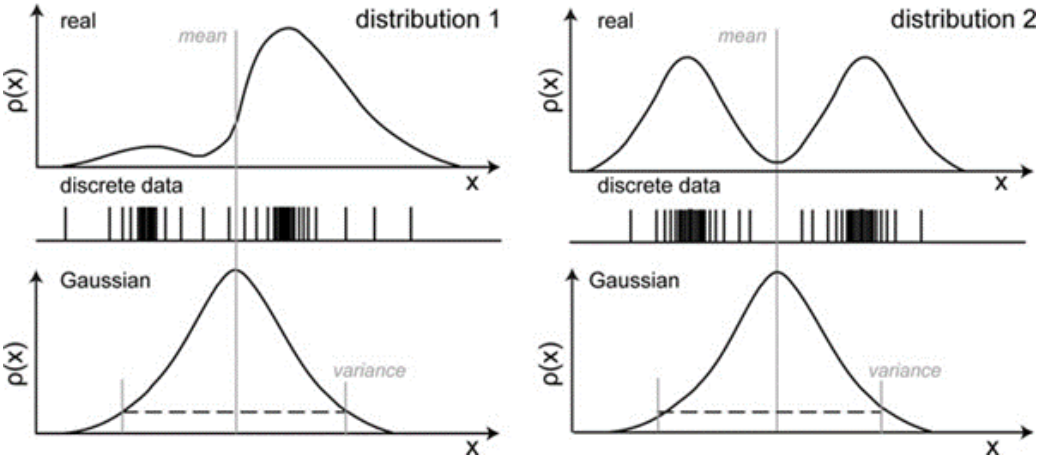

Figure 3.3: An illustration of the potential issues with reducing a distribution to a parametric form. On the top panel, there are two quite distinct distributions. However, when one finds the best fits in the Gaussian functional form, they have the same mean and variance so are considered identical in that parameter space.

trations in Fig. 3.2 and Fig. 3.3. The former demonstrates the differences between the parametric and non-parametric approach to comparing IMFs. In non-parametric approaches, one is comparing the sample distributions directly, with no intermediate steps. With the parametric approach, one must first reduce the complexity of the distribution to a small parameter space, and then compare in the parameter space. In general, however, differences in parameter space cannot fully capture differences in distributional space. For example, in Fig. 3.3, consider a toy example of two quite distinct distributions (top panel). When the best fit of each distribution in the Gaussian parameter space is found, one can see they have the same best fit parameters (mean and variance). Comparisons in parameter space only would lead someone to conclude that they are identical, when in fact they are quite distinct,

Of course, this is just an example of a general phenomenon: parametric approaches lose detail about the data, and this can have knock-on effects. None of this is meant to imply that this is precisely what is happening with IMF studies - it is just meant to demonstrate why one should be careful when relying on parametric/functional forms to draw conclusions. This is all a precursor to the analysis later in the chapter, where it will be shown how the parametric approaches *together with* the nature of the IMF data such as heavy-tailedness and small sample sizes, can mean the conclusions one can draw from analysis are heavily distorted.

The next section touches on two specific areas where the form of the IMF is of central importance - empirical studies on universality, and simulations of physical processes.

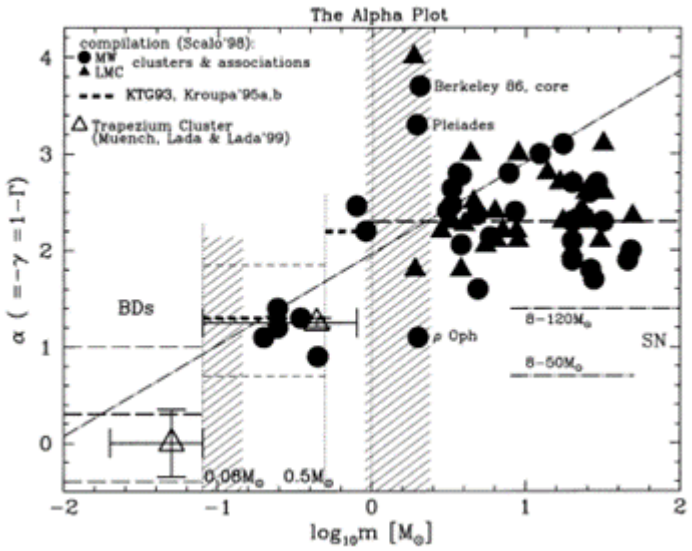

Figure 3.4: The alpha plot, taken from (Kroupa 2001*b*). The data show the compilation by Scalo (1998) of determinations of α over different mass ranges for Milky Way and Large Magellanic Cloud (LMC) clusters and OB associations.

3.1.2 Empirical studies on Universality

This section considers a few important studies that have tried to advance the debate on Universality in IMFs. The literature on Universality is far too large for us to attempt to review it in its entirely; the focus here will instead be on a few key studies that not only advanced the debate, but in the course of doing so explicitly addressed some methodological challenges with trying to draw conclusions using the parametric methods.

As outlined above, the parametric approach to comparing IMFs typically begins by fitting the available data to a parametric form (often called a functional form). As discussed in Section 1.4 in the introduction, there are a number of functional forms that have been proposed for the IMF over the years (Salpeter (1955), Kroupa et al. (1993), Chabrier et al. (2005), Maschberger (2013)). A common feature of these forms is the focus on the exponents of power-law forms across different mass ranges.

A useful technique that has therefore been used to discuss the universality hypothesis is the "alpha plot", shown in Fig. 3.4, taken directly from its introduction in (Kroupa 2001*b*). This visualizes the variation on parameter fits by plotting the power law slope fitted to available stellar data against the mean mass range of said data. Taking the parametric fits at face value, one observation would be that the parameter fits in the low and high-mass ranges seem to cluster around certain mean values, which are referred to as the canonical parameters.

The reliance on parameter fitting introduces variation in the parameter estimates that are the result of the sampling variability in the data. In order to draw conclusions about Universality, therefore, one needs to model this uncertainty and see if the observed variation can be attributed to this sampling variability, as opposed to systematic variability in the underlying IMF. This is a critical step that as will be seen is not tackled by all studies. However, the study by (Kroupa 2001*b*) does indeed attempt to do so by studying the scattering introduced by Poisson noise and also the dynamical evolution of the clusters (i.e. the variation introduce by sampling clusters at different stages of the cluster lifecycle). They do so by taking a simulation approach. They take the canonical parametric form as given, drawing samples of the typical scale observed in samples ($N \sim 10^2, 10^3$), fitting the parameters, and checking the variation in the resulting estimates. They were able to show the resulting samples produced variation in the parameter fits that looked similar to the variation in the real parameter fits. A similar procedure and result was obtained for the variation due to dynamical evolution.

It's important to note that the conclusion that the study draws from this analysis is not that there is *no* systematic variation in the underlying IMF. Rather, they note that if there is systematic variation, it must be smaller than the sampling variation. Another way of making the point is, because our sample sizes are small, there is a lot of sampling variability. There is so much sampling variability, that any true variation in the underlying IMF can't be detected. This is a key point to be revisited and expanded in the analysis that follows. Namely, that the limitations of our small samples *together* with the parametric methods make detection of competing Hypotheses extremely difficult.

A more recent review by Bastian et al. (2010) continues to explore the variation in the parametric fits. They build on the "alpha plot" method introduced by Kroupa (2001*b*), adding a handful of extra samples available at the time as well as uncertainty estimates to parameter fits themselves where available. They do not consider a simulation of sampling variability as in Kroupa (2001*b*), but rather consider on a case by case basis each example of a sample whose parameter fits are outside the window, and argue why they do not provide sufficient evidence for non-universality. Their conclusion is that these samples do not provide enough evidence to support the notion that universality is violated. However, it is worth pointing out in this study, the authors do not have a systematic method for assessing the variation one should expect from the parameter fits (as did (Kroupa et al. 1993) with their simulations). Instead, they seem to operate on rules of thumb of parameter estimates being "close enough" to be from the same underlying distribution.

On the other hand, what the authors of this study do a particularly good job in is highlighting challenges associated with the parametric method for IMFs. For example, they highlight the sensitivity of the fitting procedure to the functional form chosen: "Some studies do not provide uncertainties associated with their analytic fits, and fewer provide a quantitative justification of the functional form they adapt to describe the IMF. Functional forms with more free parameters can better capture the structure in a given IMF measurement, but that structure may not be statistically significant. Moreover, *applying different functional forms to a single derived IMF reveals that the functional form adopted can influence the perceived character of the resultant 'measurement'*" (emphasis added). They discuss the importance of taking a more principled approach to functional forms, such as the use of F-tests to find appropriate parameterizations.

Most significantly, the study concludes with the clearest indication that parametric methods face their limits with these kinds of studies: "Specifically, we recommend that future IMF studies publish their derived space densities, such that IMF variations can be tested by using a direct statistical comparison of two measured IMFs, such as with a KS [Koglomorov-Smirnov] test, rather than by comparing the parameters of the analytic fit adopted to characterize these increasingly rich datasets. By providing a more statistically sound basis for IMF comparisons, we will be better poised to uncover IMF variations where they do exist, and quantify the limits on IMF variations imposed by measurements consistent with a 'universal IMF'."

Dib (2014) was an important subsequent Universality review that took quite a different approach to analysing the parametric fits and reached a very different conclusion. This study argued in favour of the non-universality of the IMF using a Bayesian analysis with a sample of eight young Galactic stellar regions (IC 348, ONC, NGC2024, NGC 6611, NGC 2264, ρ Ophiuchi, Chameleon I, and Taurus). To test the universality of stellar IMFs, he used Bayesian methods to find the probability distributions of the IMF parameters of these eight young Galactic stellar regions. For each region, Dib used three possible IMF functions such as the tapered power law function (Parravano et al. 2010), log-normal distribution at low masses with a power law at higher masses (Chabrier et al. 2005), and a three level power law functions (Kroupa 2002). The IMF distributions with tapered power law, log-normal (with power law) and three level power law functions have respectively three, four and five parameters. From the resulting posterior probability distribution functions (pPDF) of the IMF parameters, he compared the inter-cluster 1D pPDFs and also the 2D surface density probabilities with different likelihood functions and showed that these distributions did not overlap within the 1-σ confidence limit. Most of the

regions showed a deviation of the most probable values of the IMF parameters from the Galactic field IMF parameter values.

Fig. 3.5 (taken from Dib (2014)) shows a binned form of the IMF for young stellar region, Ophiucus, Orion Nebula region, NGC 2264, and NGC 6611. The bins are equal sized $\Delta(\log(\mathrm{M}/M_{\odot})) = 0.1M_{\odot}$ (red lines) and $\Delta(\log(\mathrm{M}\ /M_{\odot})) = 0.2M_{\odot}$ (yellow line) logarithm bins. For each region, the mass distribution was compared with Galactic field IMF functions of the Kroupa (2002)(top rows), the Chabrier et al. (2005) (middle), and the Parravano et al. (2010) (bottom). Visually, it is not easy to assess the quality of the fits for those stellar regions. However, one can see the functional fit is better for those with larger samples such as Orion Nebula ($N = 1519$), NGC 2264 ($N = 990$) than Ophiucus ($N = 114$ stars) and NGC 6611 ($N = 355$). This is true for all the IMF functions, regardless of the bin sizes mentioned above. This analysis will consider carefully the effect sample size has on the ability to fit such data, both in terms of the variation and the bias produced by the estimates.

What is interesting about (Dib 2014) is that despite taking a very different approach (a Bayesian one), the analysis still falls under the umbrella of parametric methods, so is subject to many of the issues that were raised before. The main one is that it doesn't specifically provide a model of how much variation one *should* expect in the pPDFs of the parameter estimates given the sampling variation in the data. So it is hard to say whether the fact that there was a lack of overlap is indicative of different underlying distributions or just a natural consequence of drawing small samples[1]. As such, while the analysis overall provides an interesting new methodological direction and supportive evidence for non-universality, it is very hard to conclude whether this is sufficient to overrule the conclusions by the previous studies that were mentioned.

Overall, one can see there is still robust disagreement as to the true nature of the IMF. In particular, some of these major studies have flagged that parametric methods together with the sample limitations have their shortcomings when trying to draw specific inferences on properties of the underlying distributions.

[1]To be clear, the paper does provide a verification that for a given synthetic dataset the true parameters were retrieved. However, as was shown through simulations in (Kroupa 2001*b*) and as will be shown in the simulations in this chapter, high variations in samples is to be expected, and by design different possible samples draw should indeed display variation in the estimated parameter pPDFs that are generated.

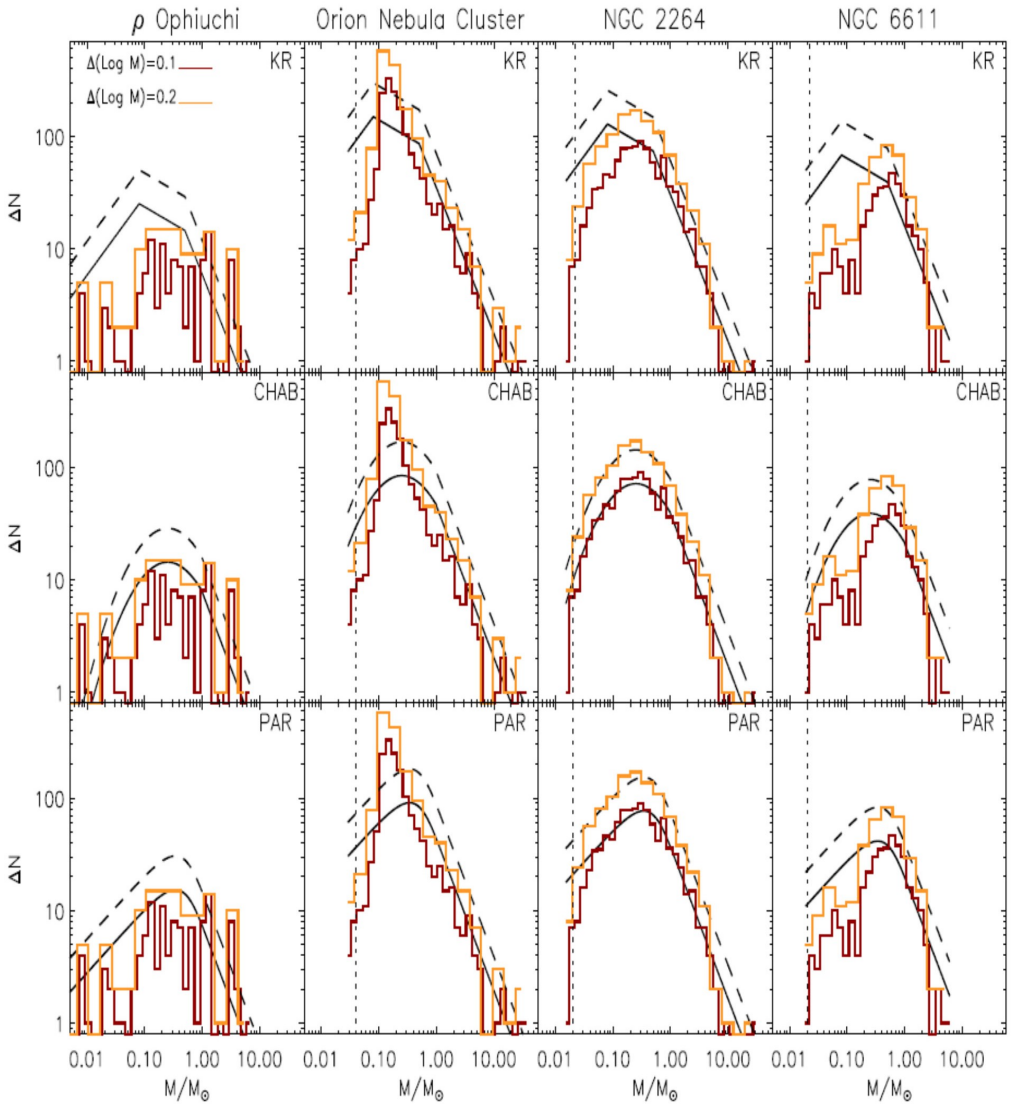

Figure 3.5: The number of stars ΔN per logarithmic bin size $\Delta(\log(\mathrm{M}/\mathrm{M}_{\odot}))$ for the young stellar region, Ophiucus, Orion Nebula Cluster, NGC 2264, and NGC 6611. Stellar masses are binned with logarithmic bin sizes of $\Delta(\log(\mathrm{M}/M_{\odot})) = 0.1M_{\odot}$ (red lines) and $\Delta(\log(\mathrm{M}/M_{\odot})) = 0.2M_{\odot}$ (yellow line). The full and dashed blacks lines represent the Kroupa (2002) mass function (first row), the Chabrier et al. (2005) mass function (middle row), and the Parravano et al. (2010) mass function (bottom row) with their Galactic IMF parameters. All functions are normalized (from Dib (2014)).

3.1.3 Uses of the canonical IMF

As the review papers above introduced, there are fundamental challenges in trying to understand the true nature of the underlying distribution of the IMF, given the limitations in samples and methods. Clearly the debate on whether the IMF is Universal is far from settled, and it seems premature to state with confidence that the underlying IMF can be modelled as a single fixed distribution of any kind (Universality). But one can also extend this uncertainty to the more specific hypothesis of canonicity - that the underlying IMF is Universal *and* it follows some specific parameters that were fitted from the available empirical data. In other words, it seems like a step too far to go from the limited samples we have available to some canonical form we believe is the generating function from star formation dynamics.

First and foremost, as established by (Kroupa 2001*b*), sampling variation is unavoidably large because of our limited sample sizes and nature of the data. This means any study is quite susceptible to sampling bias, and an approach that tries to fit the data based purely on the few available samples is quite exposed to error in estimates for the true parameters. Secondly, also noted by (Kroupa 2001*b*) and also shown in our analysis below, small samples can be quite biased in their parameter estimates. In the analysis that follows, it is shown parameters like the high mass exponent can be systematically biased away from the true value, because small samples simply cannot recreate the heavy tails faithfully. By "systematically biased", it means the expected value of the high mass exponent for samples is different from the high mass exponent of the underlying distribution - *it is a biased estimator*. Therefore, just taking the sample's fitted exponent and assuming the underlying distribution has the same value is likely to lead to an incorrect estimate of the canonical form.

A reasonable question to ask here is - does it matter? What are the implications of using an incorrect or biased IMF? The answer is a great number of modern astrophysical theories rest heavily on the canonical form of the IMF. As quoted by (Krumholz 2015), "The IMF is perhaps the single most important distribution in stellar and galactic astrophysics. Almost all inferences that go from light to physical properties for unresolved stellar populations rely on an assumed form of the IMF, as do almost all models of galaxy formation and the ISM".

Furthermore, a common tactic for astrophysical studies are simulations, and many such studies explicitly *take the canonical form as the generating function* for their stellar masses. For a few examples of simulations where the canonical IMFs have been using as a stellar mass generating function in just the last few years, see i.e. (Lamb et al. 2010, Howard et al. 2014, Hopkins 2018, Bottrill et al. 2020, Hirai et al.

2020). The conclusions these studies derived about observation and star formation, chemical abundance history etc. all start from the assumption that the generating function for stellar masses follows the canonical form.

For example, Lamb et al. (2010) generate clusters using a 2 power-law stellar clustering distribution. These clusters are then populated with stars randomly chosen from a Kroupa initial mass function (IMF). They tried to find a relation between cluster mass and Maximum stellar mass ($m_{max} - M_{cl}$ relation). They found that simulations with cluster lower-mass limits of $\leq 20\ M_{\odot}$ match best with observations of SMC and Galactic OB star populations. These results suggest that clusters are built stochastically by randomly sampling stars from a universal IMF with a fixed stellar upper-mass limit. In particular, they see no evidence to suggest a $m_{max} - M_{cl}$ relation.

Howard et al. (2014) present a model for the radiative output of star clusters in the process of star formation where gas in a clump (after efficiency SFE) is converted to stars. The model starts with a clump of a specified mass and forms main-sequence stars by sampling the Chabrier IMF. The stellar content is tracked over time which allows the aggregate luminosity, ionizing photon rate, number of stars and star formation rate (SFR) to be determined. They showed that the model can reproduce the expected number of O stars (most massive), which dominate the radiative output of the cluster. They found a nearly linear relationship between SFR (star formation rate) and mass as seen in observations. They conclude that their model is an accurate and straightforward way to represent the output of clusters in hydrodynamical simulations with radiative feedback.

Hirai et al. (2020) used a Simple stellar population (SSP) approximation model to simulate star clusters and galaxies from star particle. They used IMF for stochastic samples of the star particles to compute properties of star clusters and galaxies. The calculation produces an IMF that is statistically indistinguishable from the parametrization of the observed IMF by Chabrier (2005), and a ratio of brown dwarfs to stars which is also in good agreement with observations. Their method shows the observed relationship between the most massive stars and total stellar mass in star clusters can naturally be reproduced. They confirm that this method can form stars with masses following the IMFs.

All these studies rely on the canonical IMF as the true generating function. If the true form is in fact different (indeed, assuming there is a universal form), this would lead to perhaps quite different conclusions in a number of these studies. As this study shows, quite significant differences in the canonical form cannot be detected from the samples that are generated. Therefore, it is very much a possibility that our estimate

of the "canonical form" could be incorrect.

Having reviewed existing approaches to IMF analysis, and the implications of getting incorrect conclusions, the next section will describe the various methods used to conduct the analysis.

3.2 Methods

The overall aim of this chapter is to demonstrate that between the limitations in our sample sizes, the heavy-tailedness of our data, and the parametric inference methods used, it is very difficult to distinguish different ground truths from the available data we have. In order to do this, the Chapter will consider the three different Hypotheses listed previously, and in each case will take the following steps:

1. Firstly, model a star formation process that adheres to the Hypothesis in question to produce stellar cluster IMF samples

2. Secondly, take the generated samples and try to infer the parameters of the underlying generating function, and draw a conclusion as to the best Hypothesis that would fit the data

In each case, it will be shown that Step 2 results in a conclusion that is not fully compatible with the ground truth (i.e. underlying Hypothesis) assumed for Step 1.

Our Methods section covers these two steps: firstly, how does one simulate a star formation process, and secondly, how does one infer parameters and compare hypotheses from "observed" data?

3.2.1 Step 1 - Modelling the ground truth

Consider first the more general question of how to model a star formation process. In order to do this, some existing literature on theories of stellar cluster formation are reviewed and this is used to create a simulation protocol. Finally, the three hypotheses are considered in turn. For each, it is discussed how to accurately realize them through the star formation process.

3.2.1.1 Existing theories of star formation

A number of physical processes play an important role in the complex star formation process and thus affect the outcomes of stellar masses distribution. These include gravity, chemistry, non-ideal MHD, radiation transfer, turbulence, feedback from

young stars etc. (Bonnell et al. 2006). These processes have been discussed in more detail in section 1.4 of the introduction.

There are several studies that discuss the influence of certain stages of the star formation process on the IMF. Offner et al. (2014) reviewed theories for the origin of the stellar Initial Mass Function (IMF) and its universality across various environments. Padoan & Nordlund (2002), Goodwin et al. (2008), Hennebelle & Chabrier (2008), Hennebelle & Chabrier (2009), Oey (2011) and Hopkins (2012) assumed that Initial Stellar Mass (IMF) distributions originate from the Core Mass Function (CMF) and they could be mapped together.

Nutter & Ward-Thompson (2007) observed log-normal type CMFs in the Orion B region and the Pipe nebula and compared them to a standard Kroupa IMF with shifted mass by a factor of 8. Goodwin et al. (2008) later used these observations and found that the CMF could indeed be mapped onto IMF. Benedettini et al. (2018) studied 103 prestellar cores of most of the nearby star-forming molecular clouds from the Herschel Gould Belt Survey and tried to find a relationship between the core mass function and the stellar initial mass function. They found the CMF has a log normal fit like Chabrier et al. (2005) IMF with a central mass of $(0.25 \pm 0.04)M_{\odot}$ and a standard deviation of (0.55 ± 0.04).

Holman et al. (2013) developed a model to map the CMF onto the IMF including the stellar multiplicity. They used observed multiplicities as a function of primary mass, and the binary mass ratio for G and M dwarf primaries. The best fit of their model required core mean mass (in $\log_{10}$) μ_c = -0.03±0.10, the standard deviation of core mass (in $\log_{10}$), σ_c =0.47±0.04, star formation efficiency of 1.01 ± 0.27, average number of stars produced from a core, $N_0 = 4.34 \pm 0.43$, standard deviation of star mass (in $\log_{10}$), $\sigma_s = 0.30 \pm 0.03$ and exponent, $\alpha = 0.87 \pm 0.64$.

Therefore, our star formation process will require us to model the CMF, and how the cores evolve into stars. It is also important to make sure that the resulting IMF looks at least qualitatively like the canonical IMF, which will provide confidence that the samples produced are comparable to real empirical data. In order to do both these things, the analysis will make use of one of the functional IMF forms both as a generating function for the CMF as well as a target outcome for the IMF.

3.2.1.2 Specifying a target functional form

There are a number of options for this functional form Salpeter (1955), Kroupa et al. (1993), Chabrier et al. (2005), Maschberger (2013). This study will use the Maschberger IMF as our target functional form (Maschberger 2013). The reason this

is chosen as the target functional form is because it is extremely convenient to work with, in the sense that it provides closed-form expressions for almost every important function of interest: the CDF, PDF, and even the inverse CDF, allowing one to sample efficiently from a distribution. Furthermore, it is effectively indistinguishable from other IMFs such as those by Kroupa or Chabrier, meaning the results that derived from this analysis generalize easily to these other standard IMFs.

As a reminder, the Maschberger IMF is defined using an auxiliary function (Maschberger 2013):

$$G(m) = \left(1 + \left(\frac{m}{\mu}\right)^{(1-\alpha)}\right)^{(1-\beta)} \tag{3.1}$$

Using this, the CDF of the IMF can be defined as:

$$P[M \leq m] = \frac{G(m) - G(m_{\text{low}})}{G(m_{\text{up}}) - G(m_{\text{low}})} \tag{3.2}$$

And the corresponding PDF is:

$$p(m) = A\left(\frac{m}{\mu}\right)^{-\alpha}\left(1 + \left(\frac{m}{\mu}\right)^{(1-\alpha)}\right)^{-\beta} \tag{3.3}$$

$$A = \frac{(1-\alpha)(1-\beta)}{\mu(G(m_{\text{up}}) - G(m_{\text{low}}))} \tag{3.4}$$

The Maschberger IMF is parameterised with three effective parameters. μ is a scale parameter designating the characteristic mass. α represents the exponent for high mass stars. Finally, β determines the exponent for the low mass stars. It is not actually the exponent itself in the resulting distribution - that is represented exactly by $\gamma = \alpha + \beta(1-\alpha)$. In what follows, we refer to β as the parameter of interest when we are treating it as an input for a procedure involving the Maschberger function. We refer to γ instead when we are measuring the resulting distribution that is generated. Do note however that the two parameterizations are interchangeable transformations of one another - the former is more convenient for analytic calculations and simulation, and the latter is more convenient for visual intuition of the power law slopes. Finally, there also exist "limit" parameters of m_{up} and m_{low} which bound the IMF.

Each of these parameters possesses a "canonical" value which correspond to the proposed "universal" slopes often discussed with regards to IMFs (Bastian et al. 2010). These are: $\alpha = 2.3$, $\beta = 1.4$ ($\gamma = 0.48$), $\mu = 0.2$, and the limits fixed to values of $m_{\text{up}} = 150M_{\odot}$ and $m_{\text{low}} = 0.01M_{\odot}$. Taken together with these "canonical" values,

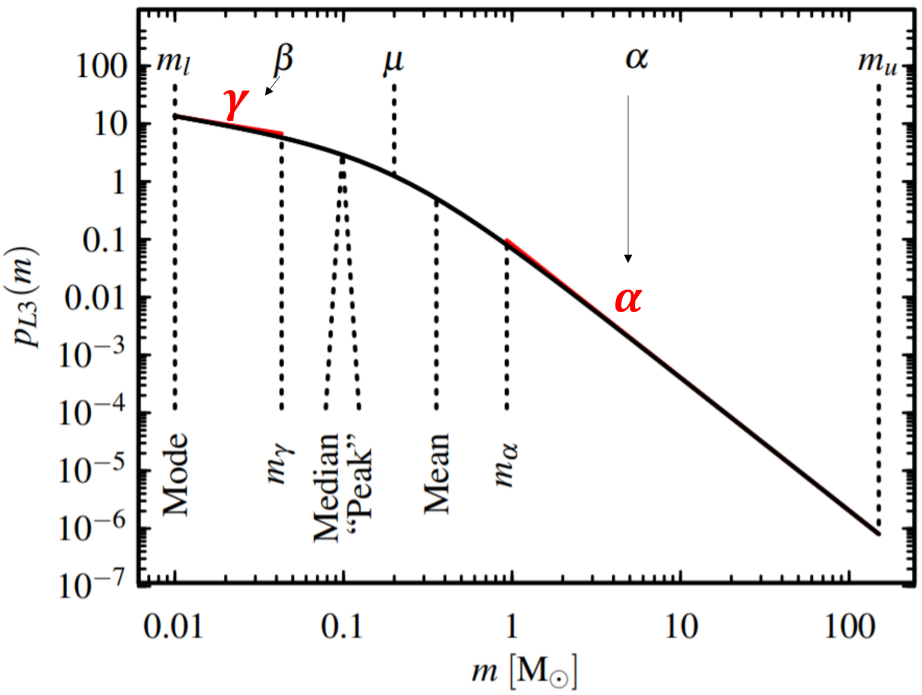

Figure 3.6: Maschberger IMF with canonical parameters: $\alpha = 2.3$, $\beta = 1.4$ ($\gamma = 0.48$), $\mu = 0.2$, with upper and lower bounds of $m_{\text{up}} = 150M_\odot$ and $m_{\text{low}} = 0.01M_\odot$. Taken from Maschberger (2013).

the functional form becomes as the canonical Maschberger IMF. It is illustrated in Figure 3.6.

It is worth at this stage considering how the parameters of the distribution affect its shape. Here it can be seen that the characteristic mass μ acts as a kind of "pivot" in the distribution, determining a central point. For a given characteristic mass, increasing the low-mass exponent β raises the slope to the left of the characteristic mass (measured precisely as γ), which ensures that a larger proportion of the stars are low mass. This conversely shifts distributional weight away from the high mass. On the other hand, increasing the high-mass exponent α means that the distribution decays more quickly from the characteristic mass as the mass increases. This means that there will be *fewer* high mass stars (and proportionately more lower mass stars). The limit parameters m_{up} and m_{low} merely bound the distribution to a meaningful range. Varying these will squeeze the distribution to a narrower range.

Now that a functional form has been selected, all the building blocks are available to finalize the star formation procedure used for the rest of the analysis.

3.2.1.3 Star formation Monte Carlo procedure

The study will make use of the Core Mass Function (CMF) approach to the star formation process. This will require first generating cores with a distribution described by the Maschberger IMF. Then, there will be a fragmentation process that spawns these cores into stars with some efficiency parameter.

The CMF itself therefore has the 5 Maschberger parameters that are free to vary: $\alpha_{\rm CMF}$, $\beta_{\rm CMF}$, $\mu_{\rm CMF}$, $m_{\rm low_{CMF}}$, $m_{\rm up_{CMF}}$. The simulations make use of a range of possible values of these parameters to represent a wide range of initial physical conditions for the process:

1. $\alpha_{\rm CMF}$: Varies from $0.01 - 4.0$, overlapping with the canonical IMF value of 2.3.

2. $\beta_{\rm CMF}$: Varies from $0.01 - 4.0$, overlapping with the canonical IMF value of 1.4.

3. $\mu_{\rm CMF}$: Varies from $0.01 - 2M_{\odot}$, overlapping with the canonical IMF value of $0.2M_{\odot}$.

4. $m_{\rm up_{CMF}}$: The upper bound for the core masses constant at $550M_{\odot}$. This diverges from the canonical IMF value ($150M_{\odot}$) but of course this needs to be much higher, as each core will fragment into $1 - 3$ stars, and star formation efficiency will be smaller than 100%.

5. $m_{\rm low_{CMF}}$: The lower bound for the core masses remains fixed at $0.02M_{\odot}$. This value has a relatively minor effect on the formation process, so it is kept fixed.

In addition to the CMF, one must also specify and parameterise a core fragmentation process. The core fragmentation unfolds as follows: for every core drawn from the CMF, a certain fraction of the mass m can be turned into stars. This fraction is the star formation efficiency, denoted ϵ. Therefore, the total mass of stars that are formed from the core is ϵm. The number of stars N_0 formed in a core vary, and this is taken to be a random integer from 1 to an upper bound N_*. The available mass ϵm is then distributed between these stars in some random proportion.

Alves et al. (2007), Nutter & Ward-Thompson (2007), Enoch et al. (2008) suggest a star formation efficiency (ϵ) of about 30%. Matzner & McKee (2000) studied an X-wind model on a protostellar core and theoretically predicted ϵ in the range of 20% to 70% depending on the geometry of the core. Machida et al. (2009), Machida & Matsumoto (2012) and Price et al. (2012) later numerically presented efficiencies of around 50% for the collapse of magnetized, rotating pre-stellar cores. For our study, ϵ from between 30% and 70% is taken.

The analysis also chooses $N_* = 3$, meaning that the cores split into between 1 and 3 stars with equal probability. This includes the splitting into 2 and 3 stars as proposed in Goodwin et al. (2007). Once split, the mass is distributed between the stars according to a uniform distribution. Therefore, the core fragmentation process has two extra parameters (ϵ, N_*), where the latter is fixed. There also exist latent variables N_0 denoting the number of splits in a given core, and $q(U)$ the distribution of mass amongst these stars[2].

In summary, the entire star formation process can be determined by 5 parameters, which are denoted with θ_{SFIMF}. That is:

$$\theta_{\text{SFIMF}} = (\alpha_{\text{CMF}}, \beta_{\text{CMF}}, \mu_{\text{CMF}}, m_{\text{up}_{\text{CMF}}}, \epsilon) \tag{3.5}$$

For each possible value of θ_{SFIMF}, the star formation process will produce a distinct SFIMF. The star formation process is illustrated in Fig. 3.7.

It is worth highlighting that some of the parameters for the star formation process are very similar to the parameters of the functional Maschberger form. The former of course refers to the parameters of a physical star formation process. The functional Maschberger parameters refer to the parameters of an idealised distribution that astronomers assume the initial mass function holds. In order to better differentiate the parameters of the functional Maschberger form, the following notation can be used:

$$\theta_M = (\alpha_{\text{IMF}}, \gamma_{\text{IMF}}, \mu_{\text{IMF}}, m_{\text{up}_{\text{IMF}}}, m_{\text{low}_{\text{IMF}}}) \tag{3.6}$$

Notice we are using γ_{IMF} as we are considering the low exponent slope of the Maschberger fitted output of the star formation process. Thus, θ_M will be used to refer to fitted parameters of the output distribution and θ_{SFIMF} are "generative" parameters that serve as an input into the process.

3.2.1.4 Modelling specific hypotheses

The previous section outlined the Monte Carlo procedure that takes as an input a given set of SFIMF parameters θ_{SFIMF} and produces samples from a given SFIMF distribution. This section now consider exactly how to use this procedure to model the three competing hypotheses that were laid out in the introduction.

For Hypotheses 1 and 2, one needs to model the Universality hypothesis, where the Universal distribution follows the Canonical parameters (1) and one where it

[2]Note that these are latent variables in the formation process and *not* parameters - they cannot be varied independently of the star formation process.

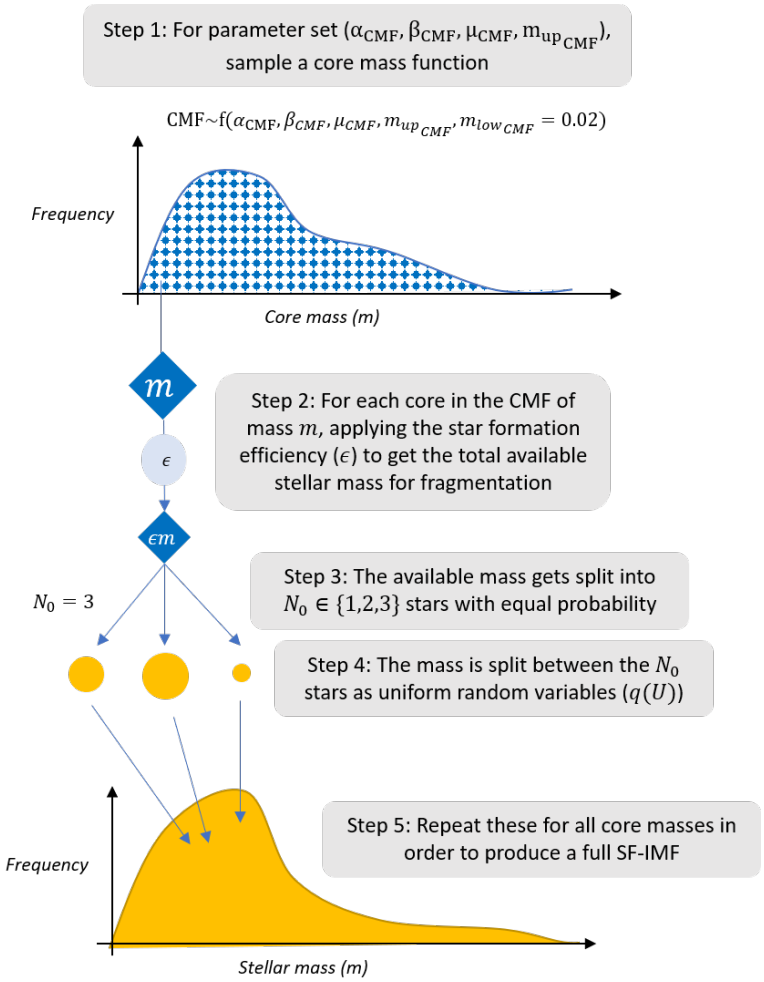

Figure 3.7: Star formation process for a given parameter set (α_{CMF}, β_{CMF}, μ_{CMF}, $m_{\mathrm{up_{CMF}}}$, ϵ).

does not (2). Therefore, different values of the SFIMF parameters will be needed to generate two different distributions, one of which closely matches the canonical IMF, and one that does not. For Hypothesis 3, multiple sets of SFIMF parameters will be used to realize the hypothesis of non-universality - that is, samples drawn from different regions of space have different underlying distributions.

An important point to make here is that the *samples* produced by a Star Formation Monte Carlo process for some fixed SFIMF parameters $\theta_{\rm SFIMF}$ is different from the *distribution* produced by those parameters. When this Chapter refers to samples, it is referring to relatively small sample sizes generated from the process ($N \sim 10^2 - 10^5$). The distribution refers to the asymptotic shape of the IMF that is approached as the Monte Carlo population grows to ∞. Of course, there is no simple analytic expression for this shape - by design it is not some parametric form that can be easily written down and compared to other distributions. Therefore, whenever there is a need to compare the distribution of a given $\theta_{\rm SFIMF}$ to other distributions (i.e. when one needs to see how closely it matches the canonical IMF distribution), one must take a shortcut and generate a sufficiently large Monte Carlo population that the distribution is approximately close to its asymptotic shape. For the purposes of this study, populations of size $N = 10^7$ are treated as our "distribution" of interest to compare to others.

In order to find two SFIMF distributions that can be used to represent Hypotheses 1 and 2, a grid of values for $\theta_{\rm SFIMF}$ was iterated over and used to generate "distributions" of size 10^7. The steps taken ranged over the plausible values presented in the previous section:

- α_{CMF} ranging from 0.01 - 4 in steps of 0.25
- β_{CMF} ranging from 0.01 - 4 in steps of 0.25
- μ_{CMF} ranging from 0.01 - 2 in steps of 0.125
- $m_{up_{CMF}}$ as either 250 or 550
- ϵ taking values randomly from $30\%, 50\%, 70\%$

For each values of $\theta_{\rm SFIMF}$, the generated distribution was compared with the canonical IMF distribution, with the intention of finding generated distributions that are at least *qualitatively* similar to the canonical IMF. In order to do this, this study mimics the following fitting process as per other IMF studies such as i.e. Dib (2014). The generated stellar masses are partitioned into bins evenly distributed in logarithmic space. The log-log plots of the histogram are compared with the log-log plot of

a Maschberger IMF (MIMF) with arbitrary initial parameters. Using a curve fitting procedure, i.e. Python's LMFit package, the parameters of the MIMF are adjusted until there is a "best fit" MIMF that corresponds to our distribution.

Once the best fit parameters are found for each population, one can then follow the standard procedure of comparing the parameters of this best fit with the canonical parameters. For Hypothesis 1, a θ_{SFIMF} was chosen whose distribution's best fit had parameters were as close as possible to the canonical parameters. The input parameters were:

$$\theta_{\text{SFIMF}-1} = (\alpha_{CMF} = 3.25, \beta_{CMF} = 0.75, \mu_{CMF} = 1.25, m_{up_{CMF}} = 550, \epsilon = 0.3) \tag{3.7}$$

The resulting best fit shape parameters were:

$$\theta_{M-1} = (\alpha_{\text{IMF}} = 2.3, \gamma_{\text{IMF}} = 0.45, \mu_{CMF} = 0.24) \tag{3.8}$$

The generated distribution, its best fit Maschberger IMF, and the canonical IMF are pictured in log-log space in Figure 3.8. As can be seen, the distribution generated via the star formation process (SFIMF-1) matches the canonical distribution extremely closely. That is, one can take these set of SFIMF parameters together with the star formation process as our "ground truth" representing Hypothesis 1 - universality and canonicity.

Next, there needs to be picked a set of star formation parameters that results in a generated distribution that is different from the canonical IMF. Of course there are many such possible parameter sets to choose, but this study opts for one that produces a fit that is just outside a window around the canonical parameters - close enough to have qualitative similarity to the canonical IMF, but far enough to be noticeably different. The parameters are:

$$\theta_{\text{SFIMF}-2} = (\alpha_{CMF} = 4, \beta_{CMF} = 0.75, \mu_{CMF} = 0.625, m_{up_{CMF}} = 550, \epsilon = 0.5) \tag{3.9}$$

The resulting best fit shape parameters were:

$$\theta_{M-2} = (\alpha_{\text{IMF}} = 3.21, \gamma_{\text{IMF}} = 0.85, \mu_{CMF} = 0.33) \tag{3.10}$$

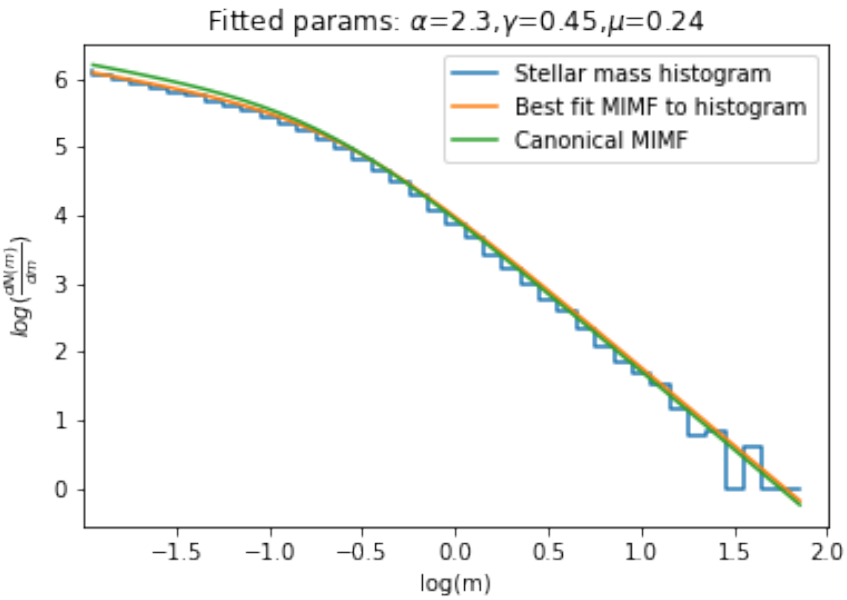

Figure 3.8: log-log histogram with empirical SFIMF-1 population (blue) and their best fits (orange) with canonical Maschberger IMF (MIMF) (green). SFIMF-1 was simulated for a population of size 10^7 with parameter set $\theta_{\text{SFIMF}-1}$: $\alpha_{\text{CMF}} = 3.25$, $\beta_{\text{CMF}} = 0.75$, $\mu_{\text{CMF}} = 1.25M_\odot$, $m_{\text{up}_{\text{CMF}}} = 550.0M_\odot$, $m_{\text{low}_{\text{CMF}}} = 0.01M_\odot$ $\epsilon = 0.3$. The best fit parameters are: ($\alpha_{\text{IMF}} = 2.3$, $\gamma_{\text{IMF}} = 0.45$, $\mu_{\text{IMF}} = 0.24$). The distribution generated by the star formation process matches the canonical distribution very closely.

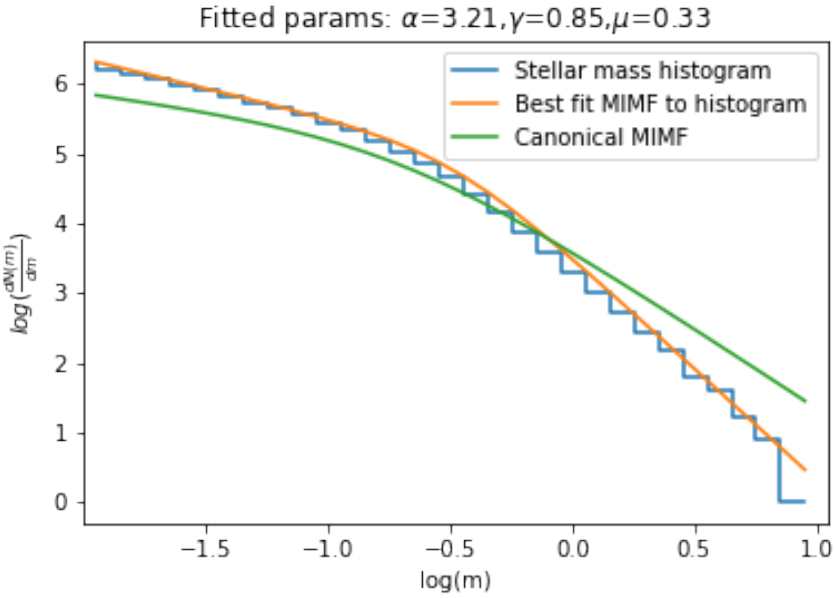

Figure 3.9: log-log histogram with empirical SFIMF-2 population (blue) and their best fits (orange) with canonical Maschberger IMF (MIMF) (green). SFIMF-2 was simulated for a population of size 10^7 with parameter set $\theta_{\text{SFIMF}-1}$: $\alpha_{\text{CMF}} = 4$, $\beta_{\text{CMF}} = 0.75$, $\mu_{\text{CMF}} = 0.625 M_\odot$, $m_{\text{up}_{\text{CMF}}} = 550.0 M_\odot$, $m_{\text{low}_{\text{CMF}}} = 0.02 M_\odot$ $\epsilon = 0.5$. The best fit parameters are: ($\alpha_{\text{IMF}} = 3.21$, $\gamma_{\text{IMF}} = 0.85$, $\mu_{\text{IMF}} = 0.33$). The distribution generated by the star formation process is noticeably different from the canonical IMF.

As before, the generated distribution, its best fit Maschberger IMF, and the canonical IMF are pictured in log-log space in Figure 3.9. As can be seen, the distribution generated via the star formation process (SFIMF-2) is noticeably different from the canonical IMF, with less heavy tails and more low-mass stars. This set of SFIMF parameters together with the star formation process is taken as our "ground truth" representing Hypothesis 2 - universality and non-canonicity.

Finally, for Hypothesis 3, one does not wish to pick a single set of SFIMF parameters at all. Rather, in order to realize this hypothesis, consider a star formation process where each sample population is generated from a SFIMF parameter set picked at random (that is to say, there is no fixed universal distribution). In order to simulate this, the process randomly picks either of the previous two SFIMF parameters ($\theta_{\text{SFIMF}-1}$ and $\theta_{\text{SFIMF}-2}$), or a third chosen as follows:

$$\theta_{\text{SFIMF}-3} = (\alpha_{CMF} = 3, \beta_{CMF} = 0.75, \mu_{CMF} = 0.625, m_{up_{CMF}} = 550, \epsilon = 0.3) \quad (3.11)$$

This was chosen as the third set of parameters because the resulting best fit shape

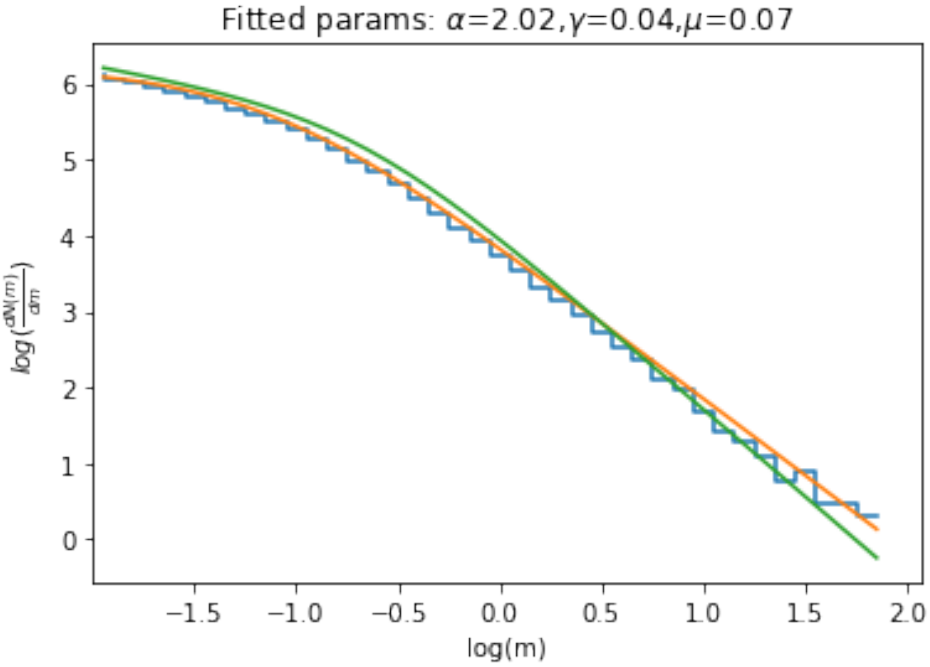

Figure 3.10: log-log histogram with empirical SFIMF-3 population (blue) and their best fits (orange) with canonical Maschberger IMF (MIMF) (green). SFIMF-2 was simulated for a population of size 10^7 with parameter set $\theta_{\text{SFIMF}-3}$: $\alpha_{\text{CMF}} = 3$, $\beta_{\text{CMF}} = 0.75$, $\mu_{\text{CMF}} = 0.625 M_{\odot}$, $m_{\text{upCMF}} = 550.0 M_{\odot}$, $m_{\text{lowCMF}} = 0.01 M_{\odot}$, $\epsilon = 0.3$. The best fit parameters are: ($\alpha_{\text{IMF}} = 2.02$, $\gamma_{\text{IMF}} = 0.04$, $\mu_{\text{IMF}} = 0.07$). The distribution generated by the star formation process produces slopes that are generally flatter than the canonical IMF.

parameters were:

$$\theta_{M-3} = (\alpha_{\text{IMF}} = 2.02, \gamma_{\text{IMF}} = 0.0, \mu_{CMF} = 0.07) \tag{3.12}$$

The distribution generated by this parameter set is pictured in Figure 3.10. As can be seen, the distribution generated by this parameter set produces much flatter slopes than for the canonical IMF.

Therefore, the three different sets of SFIMF parameters ($\theta_{\text{SFIMF}-1}$, $\theta_{\text{SFIMF}-2}$, $\theta_{\text{SFIMF}-3}$) produce distributions that, respectively, match the canonical parameters, are significantly larger than the canonical parameters, and are significantly smaller than the canonical parameters. Therefore, Hypothesis 3 can be modelled by randomly choosing one of these parameter sets whenever a new sample population is generated, mimicking the non-Universality hypothesis.

Table 3.1 summarizes all the parameter sets chosen and the resulting best fit

Table 3.1: Three sets of parameters, listing both their star formation parameters and their asymptotic fitted parameters:

Parameter set	SFIMF Parameters				MIMF Fitted Parameters for N $=10^7$		
	$\alpha_{\rm CMF}$	$\beta_{\rm CMF}$	$\mu_{\rm CMF}$	ϵ	$\alpha_{\rm IMF}$	$\gamma_{\rm IMF}$	$\mu_{\rm IMF}$
$\theta_{\rm SFIMF-1}$	3.25	0.75	1.25	0.3	2.3	0.45	0.24
$\theta_{\rm SFIMF-2}$	4.0	0.75	0.625	0.5	3.21	0.85	0.33
$\theta_{\rm SFIMF-3}$	3.0	0.75	0.625	0.3	2.02	0.04	0.07

parameters for the distributions generated from these parameters.

3.2.2 Step 2 - Statistical inference on generated samples

The previous section laid out the procedure to generate samples of stellar masses under the assumptions for the three competing Hypotheses. We now effectively have a methodology to produce samples according to some pre-determined ground truth. The next step will consider the perspective from the astronomer's point of view - *given* these observed samples, what inference can be made about the underlying ground truth?

In order to do this, for each hypothesis numerous samples of some predetermined size N will be generated, where N takes values of 200, 2000, 10^4 and 10^5. For Hypotheses 1 and 2 the single fixed star formation process determined by $\theta_{\rm SFIMF-1}$ and $\theta_{\rm SFIMF-2}$ was used. For Hypothesis 3 for each sample stellar population, the process first randomly picks from $\theta_{\rm SFIMF-1}$, $\theta_{\rm SFIMF-2}$ or $\theta_{\rm SFIMF-3}$, then conducts the star formation process.

For each sample population drawn, the analysis mimics the process that astronomers do with observed data. The sample is fit to a parametric form (in this case the Maschberger IMF), then the best fit parameters are compared to the canonical parameters. If the best fit parameters fall into an acceptable range around the canonical parameters, the sample is considered as having provided some reasonable support for the Canonical and Universal hypothesis (each is considered case by case). If the canonical parameters fall outside the acceptable window, it is considered as supportive evidence for non-Canonicity or non-Universalism.

For the acceptable ranges, the ranges proposed by Kroupa (2001*b*) were taken as a starting point. For $\alpha_{\rm IMF}$ the acceptable window is considered to be 2.3 ± 0.5. In Kroupa's study, he actually partitions the higher mass range into two sub-ranges with windows of 2.3 ± 0.3 for the "medium" mass range and 2.3 ± 0.7 for the high mass range. This study will take the average range of 2.3 ± 0.5 as acceptable. For

γ, 0.48 ± 0.5 is used (so roughly from 0 to 1) which is close enough to Kroupa's low mass range. A window is not provided for the mean mass μ, but a reasonable range of $\mu \in 0.2 \pm 0.1$ is taken.

For each of the Hypothesis, this fitting and comparison procedure is repeated for numerous samples and across different population sizes, and the Chapter discuss how this provides evidence for or against the competing ground truths.

3.3 Results

This section will consider each Hypothesis in turn, generating samples and seeing what the generated samples might tell us for the underlying ground truth. The main theme to point out is that regardless of the underlying ground truth, the generated samples appear to be very similar, and it is hard to infer the actual ground truth accurately from the available data.

3.3.1 Hypothesis 1

Hypothesis 1 is first considered, where the ground truth is that the true underlying IMF is Universal and Canonical. As was shown in the previous section, this can be simulated by utilizing the star formation process induced by $\theta_{\text{SFIMF}-1}$ (Figure 3.8).

In order to begin, consider first drawing a selection of samples of size 200 from this process in order to demonstrate how much sampling variability plays a role in the fitting process. From Fig. 3.11, out of 300 samples, 4 were picked at random to be shown in the log-log histogram with empirical histograms (blue) and their best fits (orange). The first thing to note is that even though there is a single "universal" IMF as per the hypothesis, the samples generated are extremely variable. The top left, right and bottom left and right panels have fitted parameters values (α_{IMF}, γ_{IMF}, μ_{IMF}) of respectively $(3.65, 0.55, 0.22)$, $(3.56, 0.67, 0.4)$, $(1.79, 0.17, 0.16)$ and $(2.12, 0.24, 0.14)$. Only the final panel (bottom right) had fitted parameters that fell inside the canonical window, even though all the samples were drawn from a distribution that has been shown to sit inside the canonical window.

Fig. 3.12 aggregates this across 300 samples and shows a very clear picture of how much variation would be observed in realised samples from a "Universal", "Canonical" IMF. The top panel of Fig. 3.12 shows the distributions of best fits for α_{IMF} vs γ_{IMF}, middle for α_{IMF} vs μ_{IMF} and bottom for γ_{IMF} vs μ_{IMF} for samples of size 200. In these plots, the blue dots represent each sample's fitted parameters, the green window represents the canonical range for the parameters, the orange dots are best

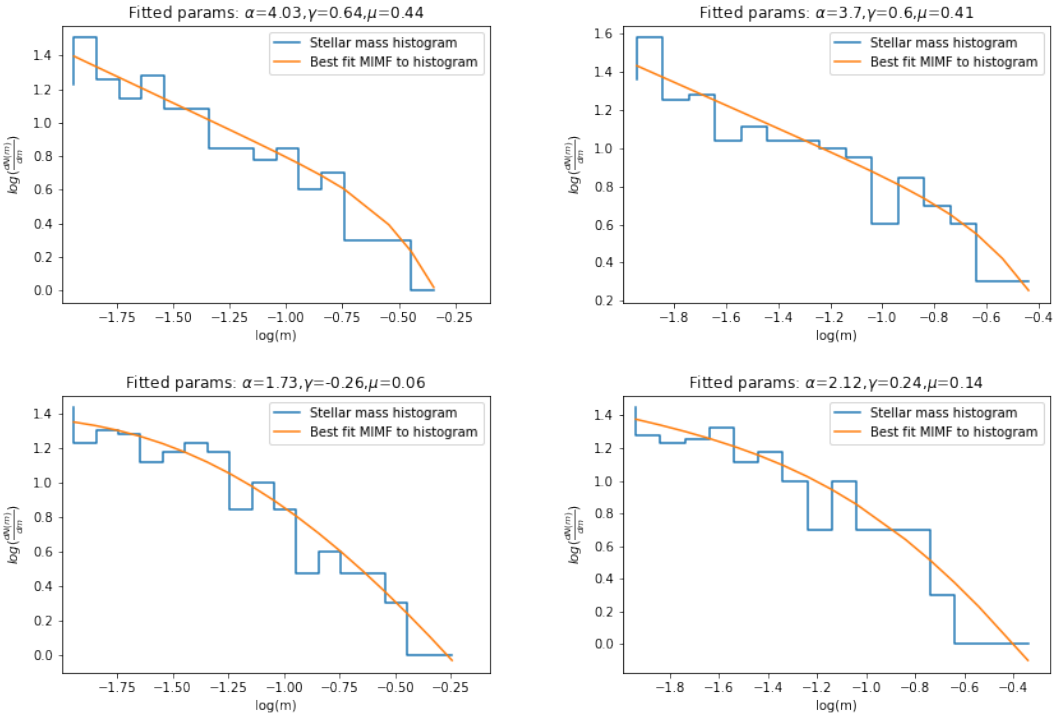

Figure 3.11: Log-log histogram with 4 samples of size 200 from SFIMF-1 population (blue) and their best fits (orange). The best fit parameters of samples from top left, top right, bottom left and bottom right :(α_{IMF}, γIMF, μ_{IMF}) are respectively $(4.03, 0.64, 0.44)$, $(3.7, 0.6, 0.41)$, $(1.73, 0.26, 0.06)$ and $(2.12, 0.24, 0.14)$.

fit parameters that are in the green "canonical" window for all three parameters, and the highlighted red star represents the average value across all samples.

As can be seen from the figure, even though we are assuming a ground truth of Universality and Canonicity, the resulting samples do not seem to support this Hypothesis, and in fact seem to point towards other Hypotheses. This can be summarized by the main summary statistics in Table 3.2.

As can be seen, the mean values of the parameter fits are just outside the canonical window but instead biased upwards, providing better support for Hypothesis 2 (non-canonicity) than Hypothesis 1.

More interestingly, the standard deviation for the parameter fits is very wide, meaning each individual parameter is very often outside the canonical window. In fact, it is only 22% of samples where all three parameters fall inside the sample window. This means that on 78% of samples, the canonical window rule of thumb would be violated, providing much better support for either Hypothesis 2 (non-canonicity) or even Hypothesis 3 (non-universality), depending on the astronomer's prior expectations about the level of sampling variation to expect. In either case, the majority of samples will not provide particularly compelling evidence for Hypothesis 1, even

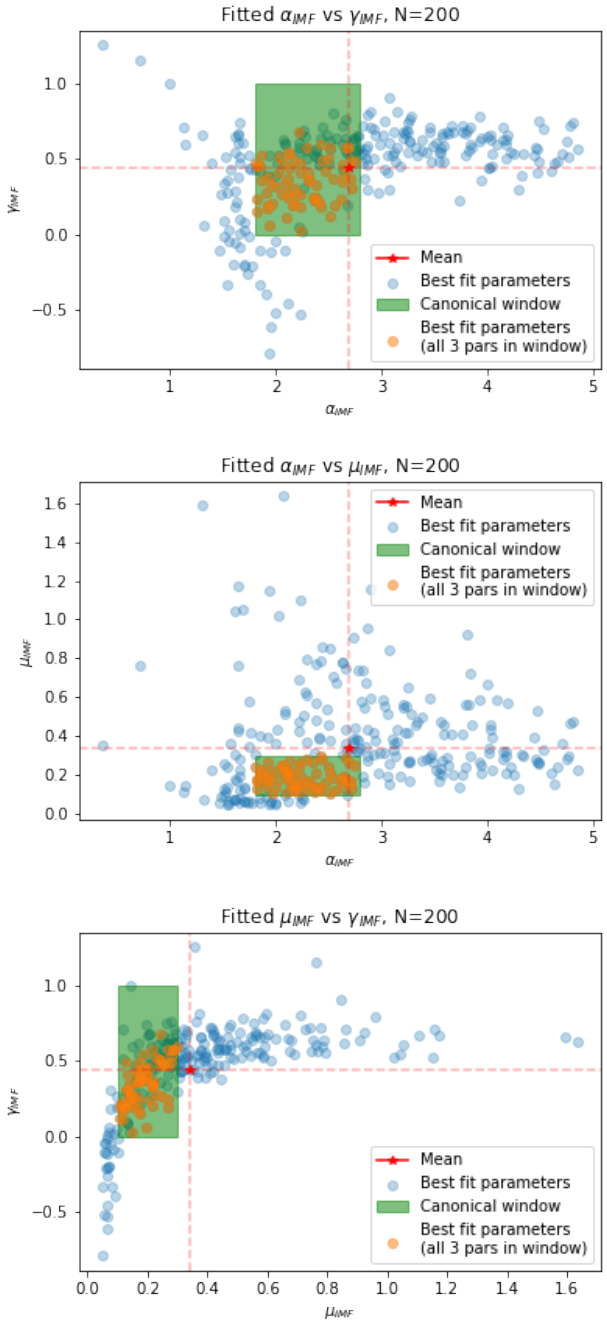

Figure 3.12: Variation of 300 samples parameters from SFIMF-1 population fitted to MIMF (blue dots). Top panel shows $\alpha_{\rm IMF}$ vs $\gamma_{\rm IMF}$, middle for $\alpha_{\rm IMF}$ vs $\mu_{\rm IMF}$ and bottom for $\gamma_{\rm IMF}$ vs $\mu_{\rm IMF}$. Orange dots: samples that are in the green canonical window for all three parameters, red star: average across all samples. Sample size: 200

though it is known to be the ground truth.

There are two main explanations of this. First, it is because of sample sizes and power law fits. It is important to note that IMFs are heavy-tailed distributions.

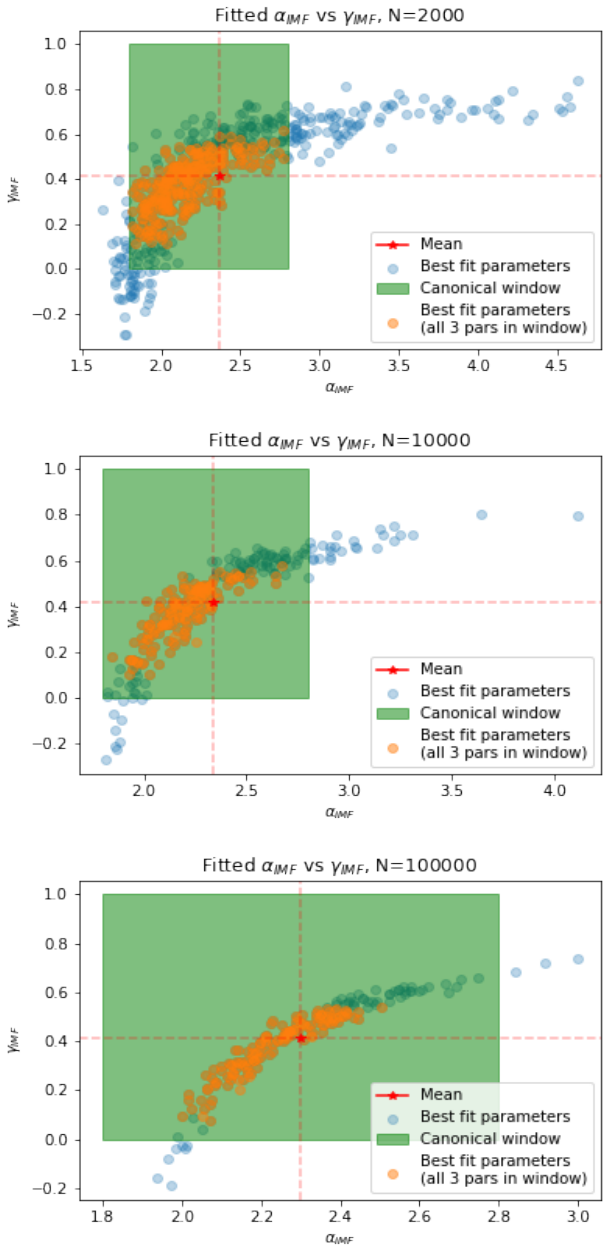

Figure 3.13: Variation of $\alpha_{\rm IMF}$ vs $\gamma_{\rm IMF}$ of 300 samples from SFIMF-1 population fitted to MIMF (blue dots). Sample size varies as 2000 for top panel, 10^4 for middle and 10^5 for bottom panel. The best fit parameters converge closer and closer to an asymptotic value and are more likely to fall within the canonical window. Orange dots: samples that are in the green canonical window for all three parameters, red star: average across all samples.

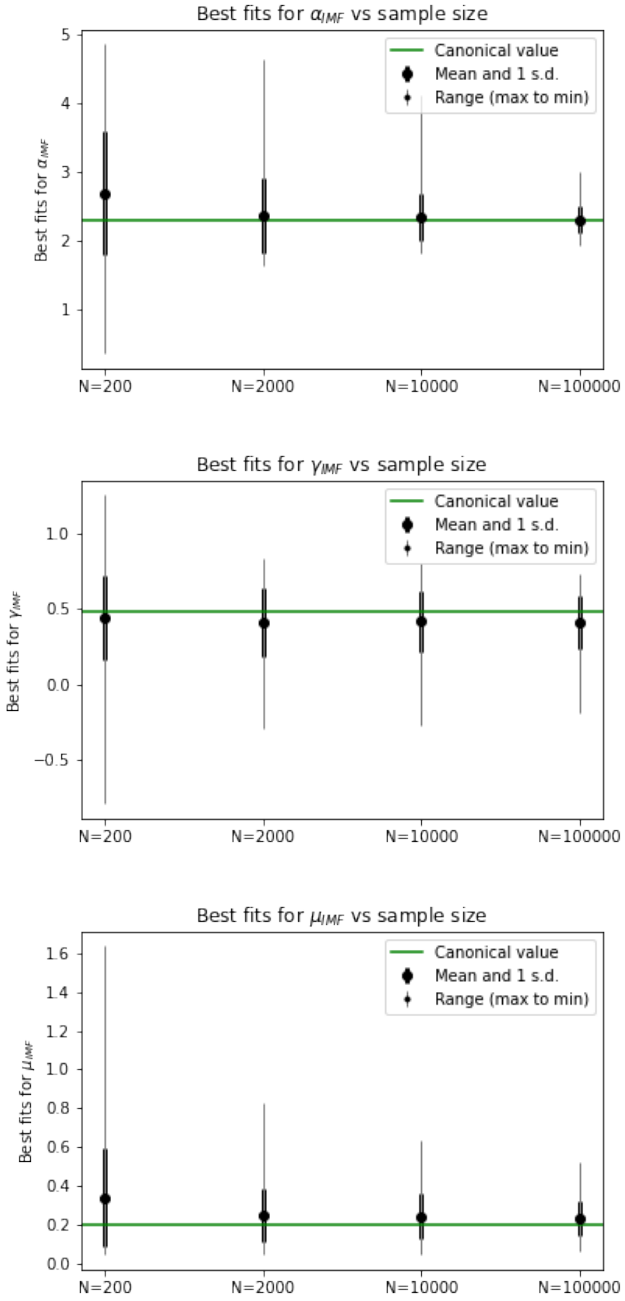

Figure 3.14: The summary statistics of 300 samples from SFIMF-1 population fitted to MIMF. Sample size varies as 200, 2000, 10^4 and 10^5. Top panel for $\alpha_{\rm IMF}$, middle $\gamma_{\rm IMF}$ and bottom $\mu_{\rm IMF}$), where the green line is the canonical parameter, the dark circle is the mean value and the error bars demonstrates the means, 1 standard deviation (thick grey), and maximum/minimum range (thin grey).

Table 3.2: Mean and standard deviation of 300 samples (of sample size 200) drawn from SFIMF-1 canonical population and fitted to MIMF parameters.

Parameter	Canonical Window	Hypothesis 1 (Mean)	Hypothesis 1 (standard deviation)
$\alpha_{\rm IMF}$	2.3 ± 0.5	2.7	0.9
$\gamma_{\rm IMF}$	0.48 ± 0.5	0.44	0.28
$\mu_{\rm IMF}$	0.2 ± 0.1	0.34	0.25
% of samples in canonical window		22%	

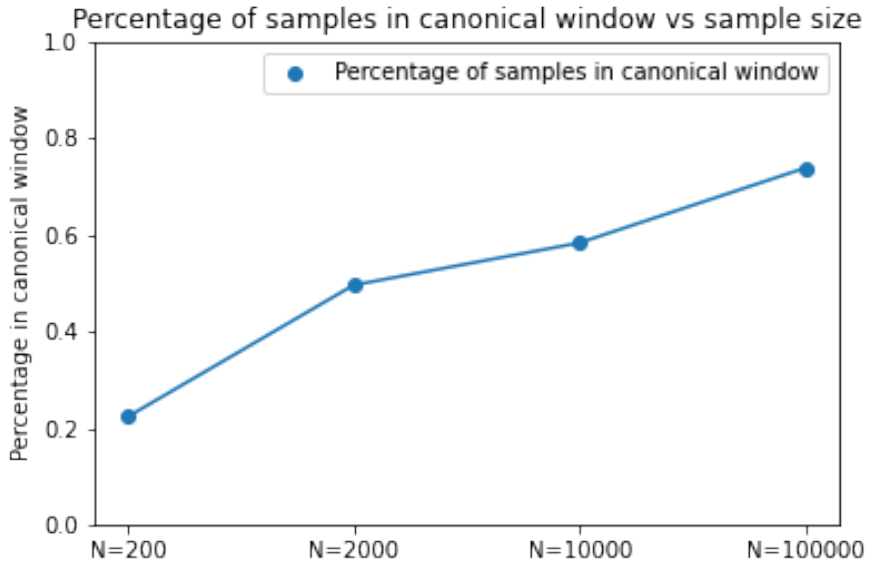

Figure 3.15: Percentage of 300 fitted (to MIMF) samples in the blue canonical window for sample sizes 200, 2000, 10^4 and 10^5. Population:canonical SFIMF-1.

This means that samples that are generated from such populations have extremely variable tails by design. For a small population, even a single star with heavy mass can drastically change the high mass slope, so high variation in the parameter estimates is quite unavoidable.

Secondly, as a result of "Parameter matching" heuristics. As highlighted previously, the standard methodology to draw conclusions about universality in IMFs is to use a "Parameter matching" heuristic, which is to say that parameters match the canonical parameters (and by extension, support the universality hypothesis) if they fall within the windows around the canonical parameters. This is opposed to, for example, a principled goodness-of-fit test to a null hypothesis, or even better, non-parametric methods as suggested by Bastian et al. (2010). In this scenario, it can be seen that taking this parameter matching heuristic seriously means that Hypothesis 1 looks less plausible than the alternatives, even when this is not correct.

In order to explore the sample size issue a bit further, the process was repeated by increasing the sample size to 2000, 10^4 and 10^5 to see how the conclusions might change. This time, for simplicity, only plots of $\alpha_{\rm IMF}$ vs $\gamma_{\rm IMF}$ are shown in Fig. 3.13. The top, middle and bottom panels show the plots for sample sizes of 2000, 10^4 and 10^5 respectively. It can be seen that the variation in the parameters shrink, but even at the largest sample size it is certainly not trivial.

The convergence of the summary statistics is shown in Fig. 3.3.1 (top panel for $\alpha_{\rm IMF}$, middle $\gamma_{\rm IMF}$ and bottom $\mu_{\rm IMF}$) for sample sizes of 200, 2000, 10^4 and 10^5. The green line is the canonical parameter, the dark circle is the mean value and the error bars demonstrates the means, 1 standard deviation (thick grey), and maximum/minimum range (thin grey).

It can be seen at sample sizes ($N = 200$, 2000), the variability in the fits is quite high. Note that the average parameters converge to the canonical parameters only at sample sizes that are unlikely to be feasible to observe in real stellar data (i.e. N $= 10^4$ or 10^5).

Fig. 3.15 shows as the sample size grows, the percentage inside the window increases, but even then the acceptance rate is very low. For $N = 200$, 2000, 10^4 and 10^5, sample fits are only inside the canonical windows are respectively 22%, 50%, 58% and 74%. Again, in reality observed cluster sizes range from around $N = 200$ to around $N = 2000$ (and the latter only in a few cases), so in a considerable majority of real cases, the best fit parameters would have fallen outside the canonical window and the support for Universality and/or Canonicity would have been weak.

3.3.2 Hypothesis 2

In the previous section it was shown that for typical sample sizes, under Hypothesis 1 (universality and canonicity), it is quite hard to infer the ground truth from the observed data, and the evidence can sometimes point to alternative Hypotheses. This section goes one step further and show that even if the underlying distribution changes quite significantly, it has barely any impact on the observable data and its parametric fits.

The ground truth in what follows will be Hypothesis 2 - the underlying distribution is universal but *not* canonical. In order to do so, the star formation process now uses $\theta_{\text{SFIMF}-2}$, which generates the non-canonical distribution seen previously in Figure 3.9. The main purpose of this subsection is to show how little the observed samples' parametric fits change under this quite considerable change in the underlying distribution. This means that all the challenges raised with noisy inferences in the previous section - that the available evidence could be used to justify either Hypotheses 1, 2 or 3 - apply equally to this case where the ground truth is quite different.

As before, the analysis begins by generating 300 samples of size 200. Out of 300 samples, 4 at random are shown in Fig. 3.16 as the empirical histogram (blue) and their best fits (orange). Top left, right and bottom left and right panels have fitted parameters values α_{IMF}, γ_{IMF}, μ_{IMF} respectively $(2.18, 0.45, 0.23)$, $(2.63, 0.76, 0.25)$, $(4.38, 0.73, 0.27)$ and $(1.4, 0.46, 0.2)$. It can be seen that, as before, there a good deal of variability and the samples are effectively indistinguishable to those observed for Hypothesis 1.

Again, like before, 300 samples are aggregated to get the bigger picture in Fig. 3.17. The top panel for α_{IMF} vs γ_{IMF}, middle α_{IMF} vs μ_{IMF} and bottom γ_{IMF} vs μ_{IMF} for 200 sample size. In these plots, the blue dots are the sample's fitted parameters, the orange dots are samples in the green "canonical" window for all three parameters. The highlighted red star is the average across all samples.

As before, wide variation in the best fit parameters can be seen. The summary statistics are presented in Table 3.3 alongside those from Hypothesis 1. As can be seen, the mean parameter fits are very close and heavily overlapping, despite the samples being drawn from two quite different underlying SF processes. Note in particular that the mean best fit from the non-canonical IMF (SFIMF-2) *is* just inside the canonical window, whereas the mean best fit from the canonical IMF (SFIMF-1) was just outside it. Furthermore, the percentage of the samples from SFIMF-2 that are all inside the canonical windows is marginally higher for the non-canonical

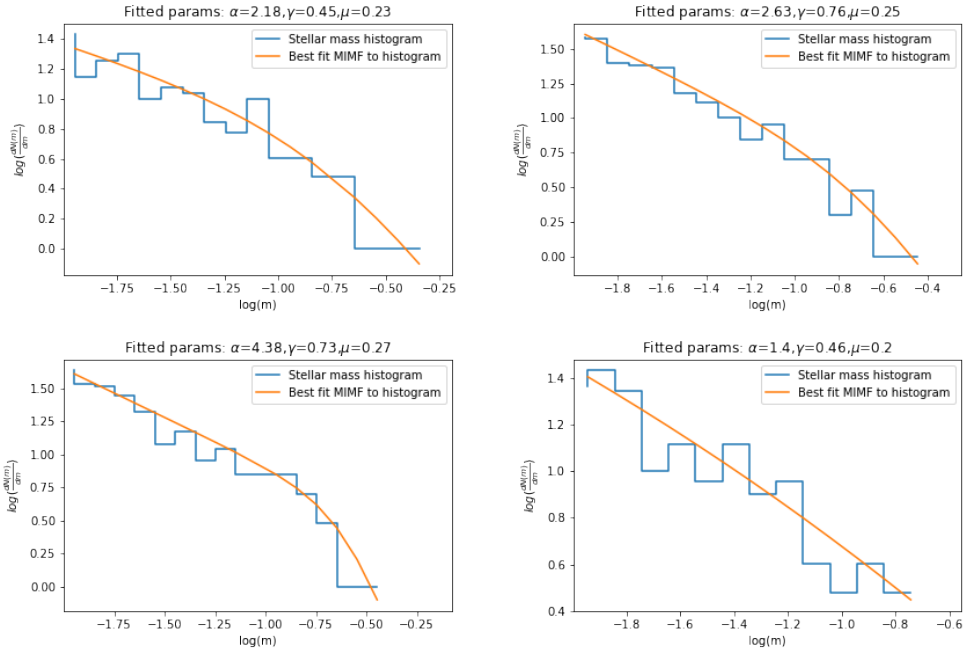

Figure 3.16: log-log histogram with 4 samples from SFIMF-2 population (blue) and their best fits (orange). The best fit parameters of samples from top left, top right, bottom left and bottom right: ($\alpha_{\rm IMF}$, $\gamma_{\rm IMF}$, $\mu_{\rm IMF}$) are respectively $(2.18, 0.45, 0.23)$, $(2.63, 0.76, 0.25)$, $(4.38, 0.73, 0.27)$ and $(1.4, 0.46, 0.2)$.

Table 3.3: Mean and standard deviation of 300 samples (of sample size 200) drawn from SFIMF-1 and SFIMF-2 populations and fitted to MIMF parameters. Here, SFIMF-1 refers to the canonical population and SFIMF-2, non-canonical.

Parameter	Canonical Window	Hypothesis 1 (canonical, universal)	Hypothesis 2 (non-canonical, universal)
$\alpha_{\rm IMF}$	2.3 ± 0.5	Mean: 2.7 (s.d.:0.9)	2.78 (0.93)
$\gamma_{\rm IMF}$	0.48 ± 0.5	0.44 (0.28)	0.64 (0.28)
$\mu_{\rm IMF}$	0.2 ± 0.1	0.34 (0.25)	0.24 (0.17)
% of samples in canonical window	-	22%	26%

Hypothesis (22% vs 26%). The little variation found in the sampling distribution actually made the samples under Hypothesis 2 slightly better evidence for Hypothesis 1, and vice versa!

The main issue, however, is the inability to meaningfully distinguish the sampling distributions for the parameter fits. The easiest way to observe the overlap between the samples drawn from these two populations is to overlay the best fit parameters directly. The two populations are overlaid in Fig. 3.18 with the canonical population's samples in blue and the non-canonical population's samples in red. It is indeed quite difficult to distinguish between the two populations when there is a typical sample size

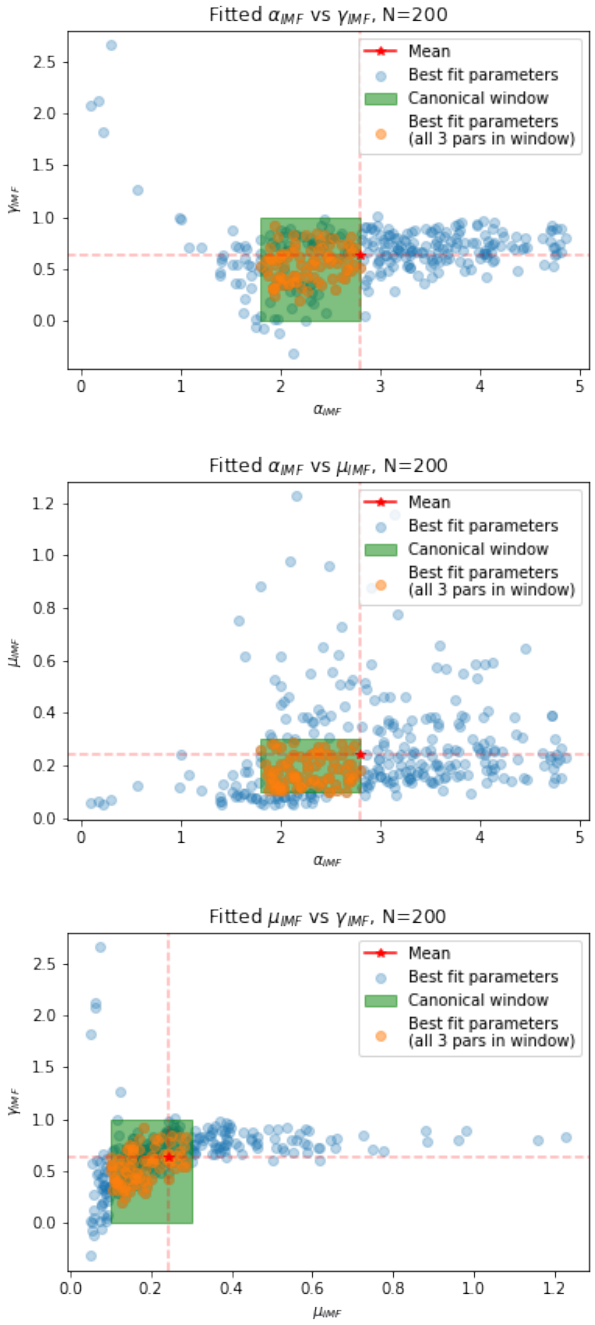

Figure 3.17: Variation of 300 samples' parameters from SFIMF-2 population fitted to MIMF (blue dots). Top panel shows $\alpha_{\rm IMF}$ vs $\gamma_{\rm IMF}$, middle $\alpha_{\rm IMF}$ vs $\mu_{\rm IMF}$ and bottom $\gamma_{\rm IMF}$ vs $\mu_{\rm IMF}$. Orange dots: samples that are in the green canonical window for all three parameters, red star: average across all samples. Sample size: 200

of around 200 stars. Since they are so hard to distinguish, all the previous inferential points that were made with regard to Hypothesis 1 can be extrapolated here: the sample data would support Hypothesis 1 (a canonical, universal population, due to the parameter averages close to the window and 26% of the parameter fits inside

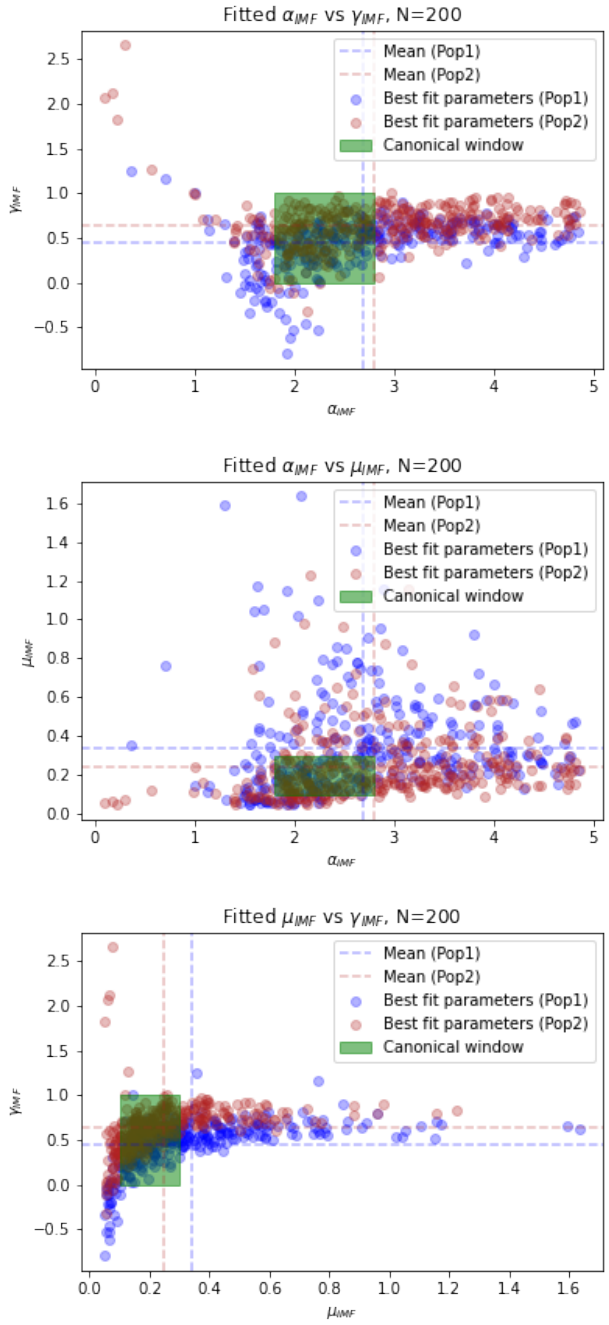

Figure 3.18: Overlay of 300 samples' best fit parameters from SFIMF-1 (canonical, blue dots) and SFIMF-2 (non-canonical, red dots) fitted to MIMF. Top panel shows $\alpha_{\rm IMF}$ vs $\gamma_{\rm IMF}$, middle $\alpha_{\rm IMF}$ vs $\mu_{\rm IMF}$ and bottom $\gamma_{\rm IMF}$ vs $\mu_{\rm IMF}$. As can be seen, it is very hard to observe a difference between the two distributions. Sample size: 200.

the window), Hypothesis 2 (a non-canonical population because of the 74% of the samples that were outside the canonical window) and Hypothesis 3 (a non-universal population, due to the parameter variability and the frequency of samples outside the window).

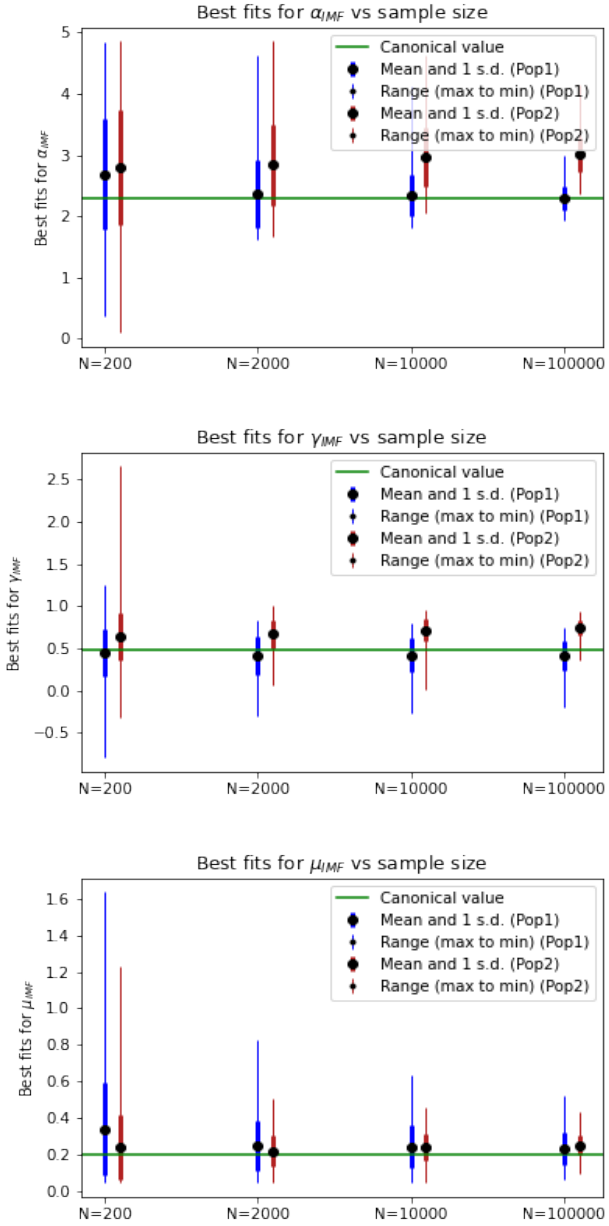

Figure 3.19: The summary statistics of 300 samples from SFIMF-1 ("canonical population" (Hypothesis 1) is in blue) and SFIMF-2 population(the "non-canonical" (Hypothesis 2) in red) fitted to MIMF. Sample size varies as 200, 2000, 10^4 and 10^5. Top panel for $\alpha_{\rm IMF}$, middle $\gamma_{\rm IMF}$ and bottom $\mu_{\rm IMF}$). Green line is the canonical parameter, the dark circle is the mean value and the error bars demonstrates the means, 1 standard deviation (thin), and maximum/minimum range (thick).

As the sample size increases, the difference between the statistics of the two populations becomes more clear. Fig. 3.19 shows the summary statistics for increase in sample size where top panel presents for $\alpha_{\rm IMF}$, middle $\gamma_{\rm IMF}$ and bottom $\mu_{\rm IMF}$). Once again the "canonical population" (Hypothesis 1) is in blue, the "non-canonical"

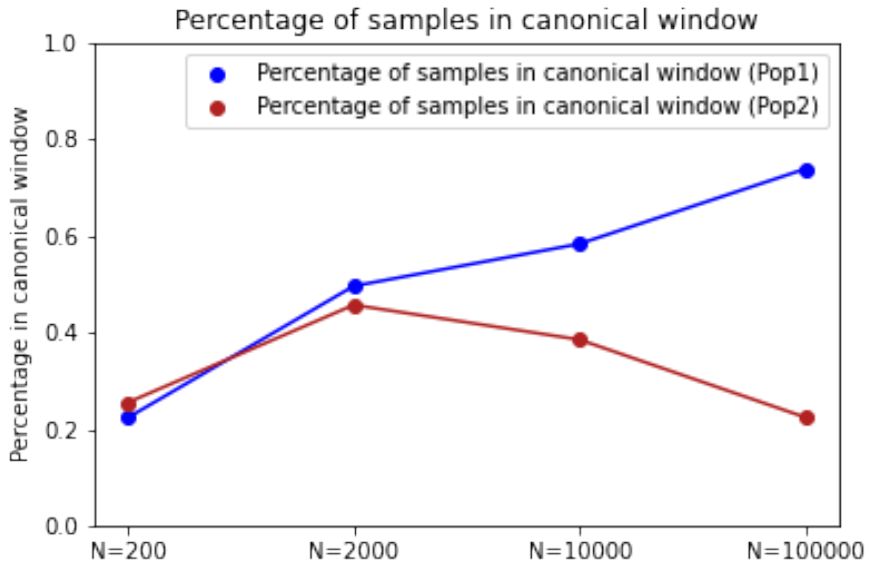

Figure 3.20: Percentage of samples from two populations (canonical SFIMF-1 (blue) and non-canonical SFIMF-2 (red)) that are contained in the canonical window for sample sizes 200, 2000, 10^4 and 10^5.

(Hypothesis 2) in red and the canonical parameter is referenced by the green line. For $N = 200$, the parameter fits heavily overlap. It can be seen that increasing the sample size makes it a little easier to distinguish the populations, but not by much; it is only by around $N = 10^4$ do the samples stop significantly rather than heavily overlapping in their parameter fits, and this is a sample size that is not available in practice.

Fig. 3.20 shows the percentage of parameter best fit in the canonical window for samples drawn from SFIMF-1 (blue) and SFIMF-2 (red). At $N = 200$, the non-canonical star formation process is actually slightly more likely to generate canonically fitting samples that the canonical star formation process. The canonical process has a slight favour by $N = 2000$, and thereafter the sampling variability has tightened enough around the asymptotic values that the non-canonical SFIMF becomes less likely to generate samples inside the canonical window. Again, this only becomes apparent with sample sizes that simply cannot be observed in real stellar data ($N = 10^4$).

As such, the main takeaway from Hypothesis 2 is that despite having a very different star formation process from Hypothesis 1, the samples can barely be distinguished and in some cases do a better job of supporting Hypothesis 1.

3.3.3 Hypothesis 3

Consider now the most extreme departure from the usual Hypothesis of canonical, universal IMFs. What if in fact there was no universal IMF, and different clusters have different underlying distributions?

In order to do this, samples are produced by first picking for each population one of the star formation processes: $\theta_{\text{SFIMF}-1}$, $\theta_{\text{SFIMF}-2}$ or $\theta_{\text{SFIMF}-3}$. The stellar sample is generated from the randomly picked star formation process. The process is repeated for numerous samples until 300 are produced. This effectively simulates Hypothesis 3: there is no universal IMF, and samples drawn from different regions have different underlying distributions.

As before, it can be seen that the generated samples are quite difficult to distinguish from the samples generated from Hypothesis 1. The overlaid parameter fits in Fig. 3.21 are once again quite hard to distinguish. Summary statistics in Table 3.4 also show similar distributions. Again, it can be seen that the mean parameters of Hypothesis 3 are just inside the canonical window and have a rate of canonical window acceptance even higher than for Hypothesis 1. Like the previous section, the ground truth of non-universality actually produces sampling distributions that slightly better support universality and canonicity than when those are taken as the ground truth!

Allowing the sample size to vary in Figure 3.22, it can be sees that even as the sample sizes get sufficiently large, the parameter distributions continue to heavily overlap. Finally, the percentage in the canonical window as sample sizes grow is shown in Figure 3.23. As can be seen, under Hypothesis 3 it is even more likely to see samples inside the canonical window than for Hypothesis 1, up until the infeasible sample sizes of $N = 10^4$.

All of this helps us reinforce the message raised in the previous section: with the features of the samples the way that they are, and with the very small sample sizes available in real world studies, methods of inference that rely on parametric comparisons seem to have weak power in distinguishing underlying hypotheses.

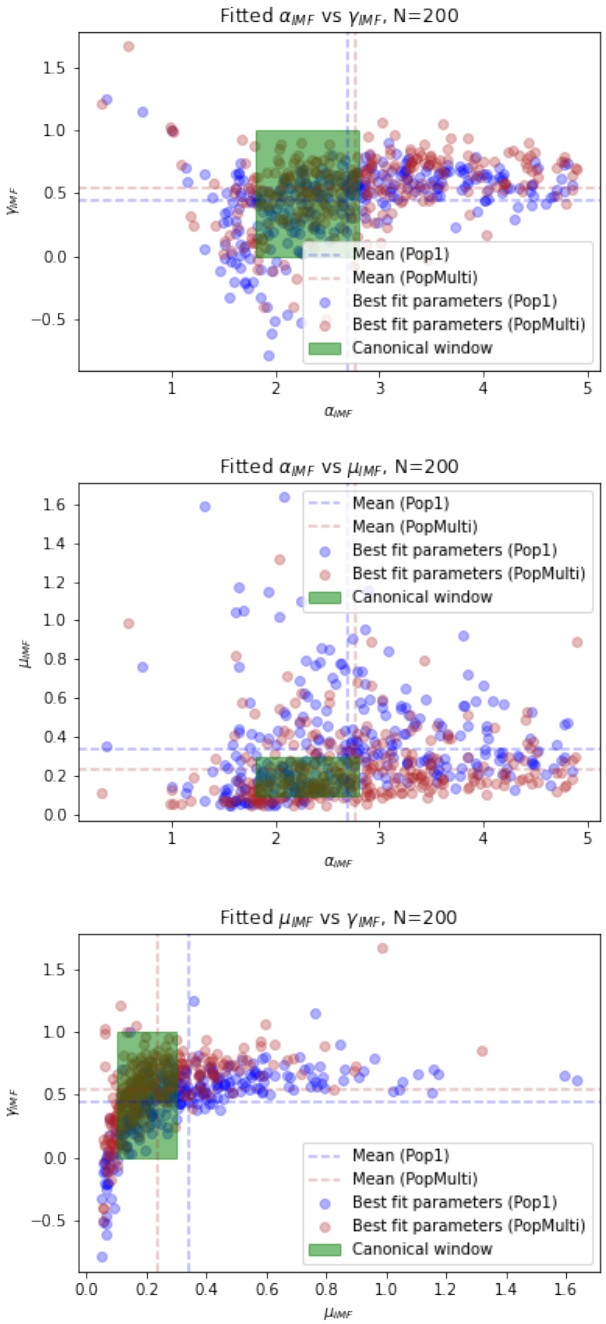

Figure 3.21: Overlay of 300 samples parameters from SFIMF-1(canonical,blue dots) and non-universal and non-canonical samples (red dots) uniform randomly taken from four different populations (as in Table 3.1) and then fitted to MIMF. Top panel shows $\alpha_{\rm IMF}$ vs $\gamma_{\rm IMF}$, middle $\alpha_{\rm IMF}$ vs $\mu_{\rm IMF}$ and bottom $\gamma_{\rm IMF}$ vs $\mu_{\rm IMF}$. It is very hard to distinguish the two distributions. Sample size: 200.

Table 3.4: Mean and standard deviation of best fit parameters for samples drawn from SFIMF-1 (canonical, universal) and non-universal populations.

Parameter	Canonical Window	Hypothesis 1 (canonical, universal)	Hypothesis 3 (non-universal)
$\alpha_{\rm IMF}$	2.3 ± 0.5	Mean: 2.7 (s.d.:0.9)	2.76 (0.88)
$\gamma_{\rm IMF}$	0.48 ± 0.5	0.44 (0.28)	0.54 (0.27)
$\mu_{\rm IMF}$	0.2 ± 0.1	0.34 (0.25)	0.24 (0.17)
% of samples in canonical window	-	22%	27%

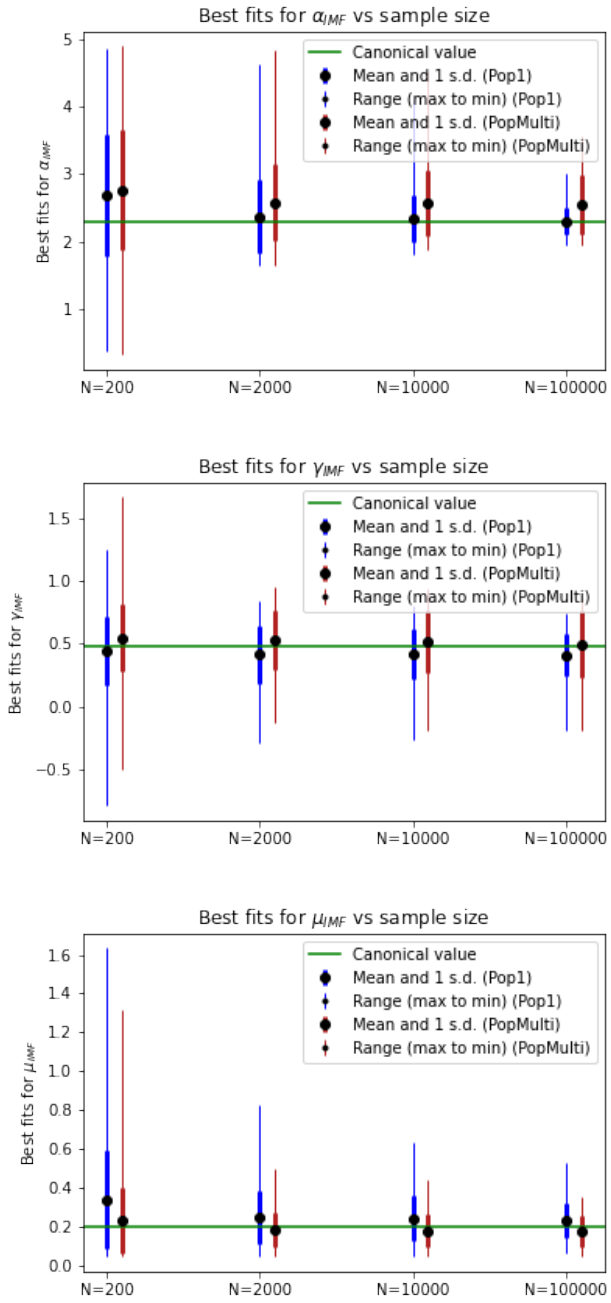

Figure 3.22: The summary statistics of 300 samples from SFIMF-1 ("canonical population", blue, Hypothesis 1) and non-universal samples (red dots, for Hypothesis 3) uniform randomly taken from four different populations (as in Table 3.1) and fitted to MIMF parameters. Sample size varies as 200, 2000, 10^4 and 10^5. Top panel for $\alpha_{\rm IMF}$, middle $\gamma_{\rm IMF}$ and bottom $\mu_{\rm IMF}$). The green line is the canonical parameter, the dark circle is the mean value and the error bars demonstrates the means, 1 standard deviation (thick grey), and maximum/minimum range (thin grey).

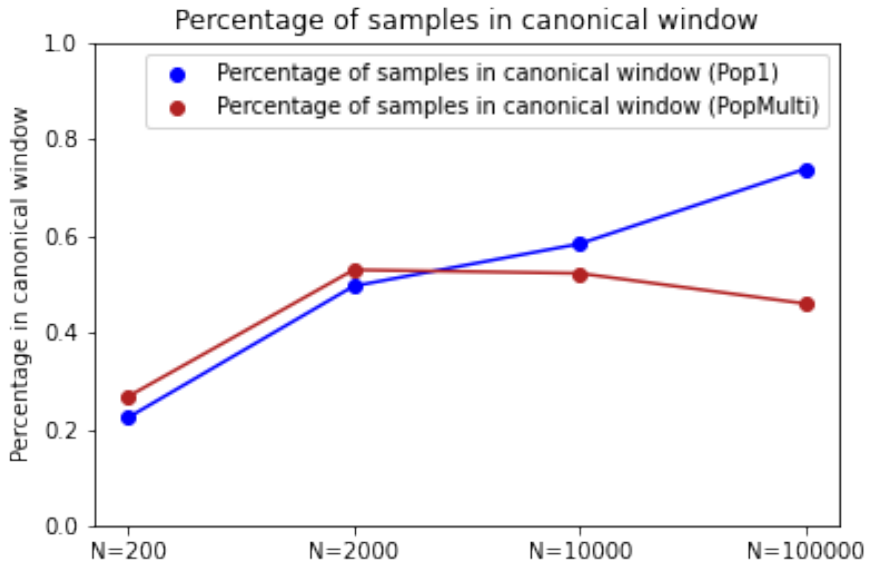

Figure 3.23: Percentage of 300 fitted (to MIMF) samples from canonical SFIMF-1 (blue) and non-canonical samples (red dots) in the blue canonical window for sample sizes 200, 2000, 10^4 and 10^5.

3.4 Discussion

The purpose of this chapter has been to investigate the methodology used to make inferences about IMFs from limited sample data. In particular, as stated in the introduction, many modern IMF inferences make use of parametric approaches, where they reduce the available sample data to a few summary parameters, and then use this to try and make inferences about the underlying distribution (such as reasoning about Universality or Canonical Forms). As a number of existing studies have alluded to, however, this strategy of parametric inference may come with some downsides and result in faulty inferences from available samples. This includes both general challenges around parametric methods (i.e. as illustrated in Figure 3.3, similarity in parameter space does not guarantee similarity in distribution space), and also more specific challenges for stellar mass data, such as heavy tails and sampling variation.

In order to investigate this in more detail, the following strategy was developed: a specific ground truth was fixed in place - either Universality with Canonicity, Universality with Non-Canonicity, or Non-Universality. A star formation process was then simulated under the assumption of one of these ground truths, generating the samples we should observe given that ground truth. Familiar parametric methods were then employed to try to then infer the ground truth from the available samples - fitting the samples to a parametric form, and comparing the fitted parameters to their canonical values.

The results were striking - under each Hypothesis, and using samples sizes typically observed in real life data, the samples were basically indistinguishable. Furthermore, each set of samples supplied evidence that could be argued to support any one of the ground truths. In each case, samples either fell into the canonical window, supporting Hypothesis 1 (canonical, universal), fell outside the canonical window, supporting Hypothesis 2 (non-canonical, universal), or exhibited high enough variation that Hypothesis 3 (non-universal) could have been plausible.

What was the particularly interesting was the ground truth of Hypothesis 1 (canonicity, universality), generated samples that seemed to provide weaker support for itself than the competing Hypotheses. That is, the samples generated by Hypothesis 2 and 3 both have mean parameter fits that were inside the canonical window when Hypothesis 1 did not. Furthermore, with typical sample sizes, both Hypothesis 2 and 3 generated more samples that fell inside the canonical window *more often than for Hypothesis 1.*

Some reasons why such inference challenges exist have already been discussed in Section 3.3.1. Firstly, the samples drawn are quite heavy tailed, so small samples

are both incapable of fully recreating the tails due to a lack of data, and variability due to the presence or absence of just one heavy star is quite unavoidable. Secondly, on a more methodological level, parameter matching heuristics to a canonical window are a poor substitute for more rigorous goodness of fit tests to see if a set of generated samples could indeed come from some defined parent population. As was demonstrated through these simulations, trying to draw too strong an inference on the underlying distributions simply based on the similarity to "canonical" parameters, can lead to inconsistent inferences.

What are the strategies we can take to try to better make inferences in the future? Consider firstly the question of how to distinguish Hypothesis 1 and 2. That is, assuming Universality is true, how can one do a better job of inferring the true shape of the underlying population? This is related to the first issue raised in the previous section - the shape of stellar mass data and the size of the available samples just do not 'play well' together and can often be misleading, and in order to tackle this we will need better statistical techniques to make population inferences from the data. Simply fitting existing histogram slopes using χ^2 minimization is open to all kinds of flaws (some of which were highlighted previously as per Bastian et al. (2010), such as the effect of bin width and fitting function).

In our simulations, the parameter convergence plots demonstrated that in i.e. SFIMF-1, the parameter estimates for $\alpha_{\rm IMF}$ and $\mu_{\rm IMF}$ were both systematically biased upwards, pushing the mean parameter estimates outside the canonical window, and only converging to their true canonical population value for very large sample sizes. It should be noted that the fact that sample parameter estimates can be systematically biased away from the true parameter value is not a novel concept - it is a well-studied phenomenon called the "bias of an estimator", the typical example being that the variance of a sample will in expectation be lower than the true variance of the population that generated the sample.

Part of the importance of trying to get these estimates accurate, and to mitigate these issues with bias, is that these population inferences are used for studies that use the IMF as a generating function. As was already discussed extensively in Section 3.1.3, many studies take the "canonical form" of the IMF as a ground truth to generate Monte Carlo simulations. However, if these parameter estimates are systematically biased away from their true values, then many such studies may be leading to incorrect conclusions. For example, even in this present study, Hypothesis 2 produced samples with parameter estimates that were closer to that of Hypothesis 1's distribution (canonical). It is entirely plausible that if there is a true underlying distribution, it is more like Fig. 3.9 ("non-canonical") than Fig. 3.8 ("canonical"), but

our limited samples have led us to believe otherwise. In this case, the studies that rely on Fig. 3.8 being the generating function would reach misleading conclusions.

All in all, therefore, it seems there is a strong case to be made for more statistical techniques being developed to make better inferences from the sample data that are available for IMF studies. This includes not only techniques that can cater to the bias induced by sample size and heavy tails, but also perhaps those that account for other specific astrophysical factors, such as the fact that the cluster masses are unlikely to be independently sampled due to common physical processes (a prime example of this is directly in our star formation process itself - the core splitting simulation means the masses of the stars generated are not independent).

The second set of problematic inferences are perhaps even more important - how can we better distinguish between the Hypothesis of Universality and Non-Universality? After all, this is one of the primary areas of controversy in such studies, and the simulations showed that the existing parametric inferences failed to distinguish them from the available data. In fact, the "canonical window" rule of thumb currently used proved to be particularly inappropriate, where the Non-Universality hypothesis more often falling into the canonical window than the Canonical hypothesis.

As has been argued throughout this chapter, parametric methods throw away a great deal of information that can be crucial to detect differences between samples, and this Chapter has shown how they generally distort the conclusions that follow. A sensible approach to address the particular question of Universality then might be to consider non-parametric approaches. Since they are directly set up to measure all the differences between samples without having to simplify to a parametric space, they might be better suited to this issue.

In order to test this, size 200 samples generated from our three Hypotheses were subjected to non-parametric tests. For each Hypothesis, $k = 5$ clusters were sampled at random. These samples were subject to a k-sample Anderson-Darling (AD) test[3] Scholz & Stephens (1987). This k-sample AD routine tests the hypothesis that k samples of size $n_1, n_2, \ldots n_k$ could have been generated from a single underlying distribution *that does not need to be specified*. It returns for every set of 5 sample populations a test statistic and associated p-value for the null hypothesis that the samples all came from the same population. We repeated this process 1000 times for each Hypothesis, generating a distribution of p-values.

[3]Multi-sample tests of other kinds can be considered such as multi-sample KS tests, etc. but Anderson-Darling tests are better at detecting differences in tails, which is important for the heavy-tailed data being dealt with here

If the null hypothesis is true (all the samples came from the same distribution), the p-values should be nearly uniformly distributed. If the null hypothesis is false (different samples came from different underlying distributions), then the p-values will be clustered at smaller values (for example, less than $p = 0.05$).

The results of the experiment are shown in Fig. 3.24. As can be seen, the p-values are distributed almost uniformly for Hypothesis 1 and 2, where samples were indeed drawn from the same underlying distribution. However, for Hypothesis 3, which was sampled from 3 different star formation processes, the p-values are very clearly clustered at a low value, with over 50% of the tests resulting in a p-value of below 0.05, successfully detecting that the samples were drawn from different underlying distributions. In other words, non-Universality was successfully detected without having to make any assumptions around any parametric form.

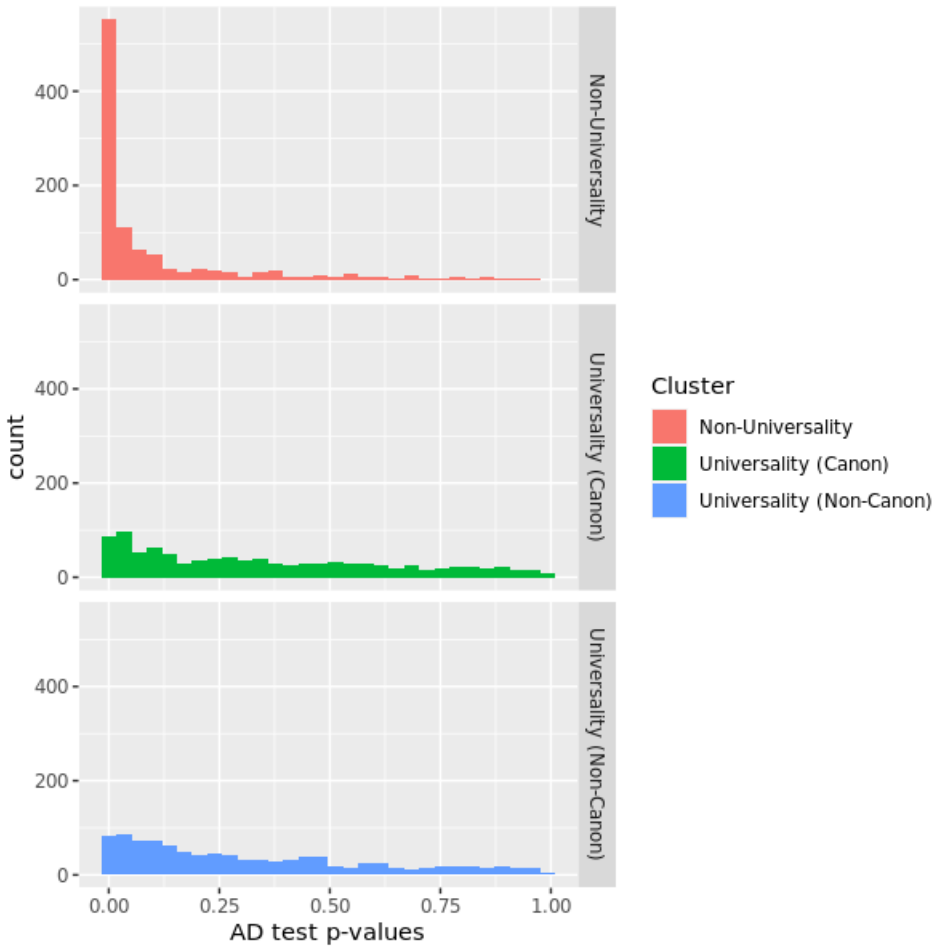

Figure 3.24: Distribution of p-values for k-sample Anderson Darling tests to test for the hypothesis that the stellar masses came from the same underlying distributions ("universality"), where $k = 5$, samples of size 200 were used, and the test was repeated 1000 times for each Hypothesis. For the two universality hypotheses, the p-values are almost uniformly distributed, indicating the null hypothesis (universality) is true. For the non-universality hypothesis, the p-values are clustered around 0, indicating the null hypothesis of universality was correctly rejected.

3.5 Conclusions

In this Chapter, the focus has been on the methodological challenges of inferring properties of an underlying star formation process from limited sample data. Along the way, the chapter was able to highlight the potential downsides of the parametric approaches and rules of thumb that are common in astrophysical studies. It did this by pointing to existing astrophysical studies that raise issues with the approach, and also reviewed some fundamental challenges with parametric statistics.

In order to verify this intuition, the analysis required the design of a stellar generation process that could generate samples according to different hypotheses of IMF properties, such as Universality and Canonicity. Statistical inferences were performed from these samples using the same parametric methods and rules of thumb that are common in the literature. The resulting statistical inferences failed to adequately determine the ground truth from the observable data, often better supporting incorrect alternative hypotheses.

A few solutions were reviewed. To better determine the true parameters of the IMF (assuming a universal form existed), the need for dedicated statistical techniques were discussed, in particular those that best accounted for heavy-tailed, small-sampled and dependently distributed stellar mass populations that astronomers typically have access to.

To better distinguish between Universality and Non-Universal hypotheses, the importance of non-parametric techniques were discussed. Such techniques do not throw away all the distributional information to focus on the similarity of a few noisy parameter estimates. Perhaps even more importantly, they do not require the assumption of a particular functional form, meaning that one begins the analysis with less subjectivity about how the underlying distributions should look.

In particular, the k-sample Anderson-Darling test was proposed, since it exhibits sensitivity towards heavy-tailed distributions. This test was able to detect the non-Universality quite easily, demonstrating the utility of this alternative approach.

Therefore, the key takeaways from the results of this chapter are - one should use parametric methods for IMFs with some caution. As the analysis demonstrates, the introduction of parametric forms introduces quite a few assumptions into the analysis, and can over time oversimplify the study of the extremely rich and subtle phenomenon that are IMFs. Where parameter inferences need to be made, consider specialised statistical methods that can deal with sampling bias and variability. When canonical IMFs are used as generating functions for other studies, consider the sensitivity of the conclusions to possible biases in the canonical parameter estimates. Finally, where

universality is being tested, consider non-parametric methods instead.

Finally, it should be noted that the conclusions reached in this regard are similar to that achieved by (Bastian et al. 2010) and quoted previously, summarised again here: "Specifically, we recommend that future IMF studies publish their derived space densities, such that IMF variations can be tested by using a direct statistical comparison of two measured IMFs, such as with a Kolmogorov-Smirnov test, rather than by comparing the parameters of the analytic fit adopted to characterize these increasingly rich datasets ... By providing a more statistically sound basis for IMF comparisons, we will be better poised to uncover IMF variations where they do exist and to quantify the limits on IMF variations imposed by measurements consistent with a universal IMF." However, this study was able to reinforce and extend this message: not only was it able to demonstrate quantitatively the dangers of a parameter-matching, it showed that specifically how non-parametric methods can correct the conclusions of an original parametric approach.

It is hoped the results provided in this chapter encourage researchers to review their fundamental assumptions on parametric forms, and future studies on universality consider a broader range of goodness of fit tests to draw conclusions.

Table 3.5: Repeated terminology used in this chapter

Term	meaning
CMF	Core Mass Function
q(U)	mass ratio fragmented in a uniform manner
N_o	No of fragmentation of Core
α	decline slope of the IMF from μ to $\mathrm{m_{up}}$
β	increase in slope of the IMF from $\mathrm{m_{low}}$ to μ
μ	characteristic mass of IMF
$\mathrm{m_{low}}$	lower mass limit of IMF
$\mathrm{m_{up}}$	upper mass limit of IMF
MIMF	The Maschberger IMF
SFIMF	simulated star formation IMF
α_{CMF}	decline slope of CMF from μ_{CMF} to m_{CMFup}
β_{CMF}	low mass exponent
γ_{CMF}	increase in slope of CMF from m_{CMFlow} to μ_{CMF}
μ_{CMF}	characteristic mass of CMF
m_{CMFlow}	lower mass limit of CMF
m_{CMFup}	upper mass limit of CMF
θ	parameter set for a distribution

Chapter 4

How to retrieve the true properties of binary stellar populations

4.1 Introduction

In astronomy, binary stars possess an important status as they can constrain star formation theories (Goodwin 2010). Among them, visual binaries are the most common type of observed binary stars. When we observe binary populations in a stellar region, selection effects often obscure their true properties. As discussed in Chapter 1, selection bias is an observational problem and causes a difference between the real and observed binary properties. This chapter addresses the issue of whether it is possible to extract true properties from an observed population under the influence of selection effects.

This chapter begins in the introduction by describing the challenge of observational selection effects on retrieving the true properties of binary population, as well as a high-level summary of how it is addressed in this work. Section 2 focuses on deriving the formulas that describe the physical process of interest, and uses these to implement a Monte Carlo simulation of the process.

In Section 3 a method is developed to retrieve the true parameters of a (simulated) binary stellar population without selection effects, using something called a Binary Search Tree Goodness of Split (BST-GOS) algorithm. It is demonstrated that this process successfully retrieves the true parameters with high accuracy.

Having established the effectiveness of this method, in Section 4 this method is applied to simulated binary stellar data where various levels of selection effects are applied. Depending on how the selection effects truncate the distribution of the observed data, the method can introduce error. This helps us clarify how, in

general, methods that rely on the shape of observed distributions can be affected by selection effects. In light of this, the effectiveness of the algorithm is considered when cutting-edge observational techniques are used, which mitigate the selection effects and therefore minimize the truncation of the distribution. It is shown that such techniques drastically improve performance, returning almost to the level achieved when no selection effects were present at all.

The conclusion recaps results, considers extensions and future work, and discuss best practices approaching the problem of retrieving true properties in the face of the challenges described.

4.1.1 Overview

True binary fractions and the associated orbital parameters of a stellar population are often obscured by observational selection effects. Observational limits on the 2D binary separation (S) and secondary to primary member star mass ratios (q) are the two major factors for selection effects. If the separation between the member stars is large, they are resolved as two stars, but binaries with small separation tend to look like one single star. Furthermore, for a system when the secondary to primary mass ratio remains nearly equal, we observe them as a single star with double luminosity. For smaller mass ratios, the secondary stars with low luminosity are unseen most of the time. Therefore for a separation (S) at which a binary system is resolvable depends also on their mass ratio (q).

In binary systems, the true orbit of the secondary star around the primary is an ellipse and they move around the centre-of-mass (COM). The motion is usually described by the secondary star relative to the primary star that is fixed in the focus. The average true 3D binary separation or semi-major axis is a bit more than one-half the long axis of the ellipse. From the Earth, we visualise the true orbit as a projected elliptical orbit on the plane of the sky. The projected binary separation can be very different from the true separation and add to the observational selection effects. As a result of these selection effects, the observed distribution of binary populations can be different from the true ones, and it becomes difficult to extract the true orbital parameters.

The estimation of orbital parameters from observations is an inverse problem of celestial mechanics and has been used for example, on asteroids. Four observations of the relative separation and position angle in principle could determine the orbital elements (Grundy et al. 2008). Practically only with long-term, precise observations can one determine the orbital parameters. The properties of the observed

binary population have been discussed in many works (Abt 2005, Grundy et al. 2008, Kouwenhoven et al. 2007, Raghavan et al. 2010, Grundy et al. 2011, Duchêne & Kraus 2013, Tokovinin & Kiyaeva 2015, Kovaleva et al. 2015).

This chapter presents a best fit technique to retrieve the true binary distribution parameters from observed population properties by a Binary Search Tree (BST) - Goodness of Split (GOS) algorithm. Details of the method are given later in Section 3. Instead of using long-term observations, the parameters can extracted statistically from a distribution of instantaneously observed binary separations (S) and mass ratios (q) of the binary systems of a region. The algorithm will take an observed binary stellar population (in the form of (q, S) data) and return a best estimate of their true properties.

According to Kovaleva et al. (2015) in the statistics of binary stars, astronomers collect data in different ways. For observational data the methods are (i) volume-limited (within a certain volume any type of stars such as A type, solar type, M type etc.) and (ii) from a cluster or association (same distance). For theoretical methods, these are simulated data based on observation and theoretical understanding. This chapter follows the latter approach.

An overview of the argument for this Chapter is presented in Figure 4.1. It begins in the simplified case where selection effects are ignored (Figure 4.1a). We start with an "observed" (q, S) distribution for all the binary pairs in the cluster (denoted in a filled orange box on the bottom). For the purposes of this study, this "observed" distribution is generated from a Monte Carlo simulation with known parameters, so there is a ground truth to compare our estimates to.

The method then iterate over a large set of binary population parameters (denoted by $\{\Phi_{BIN}, \Phi'_{BIN}, \Phi''_{BIN}\}$ in the Figure), each of which generates a new (q, S) distribution via the Monte Carlo method. For each one, we calculated the "goodness of split" of the generated distribution with our "observed" (q, S) distribution. This goodness of split is generated using the BST-GOS algorithm introduced shortly, and for now one can just think of it as a measure of similarity of two samples. The parameters that generate the best goodness of split scores are our optimal candidates for the true underlying parameters of our observed sample. In our illustration, it can be seen that Φ''_{BIN} produces the best fit. As demonstrated through a series of examples, this method works very well in practice and can successfully retrieve the true parameters for the "observed" samples.

Having established the BST-GOS methodology is sound, the analysis moves to the question of what impact selection effects have on retrieving the parameters. As demonstrated in Figure 4.1b, the selection effects have the impact of truncating the

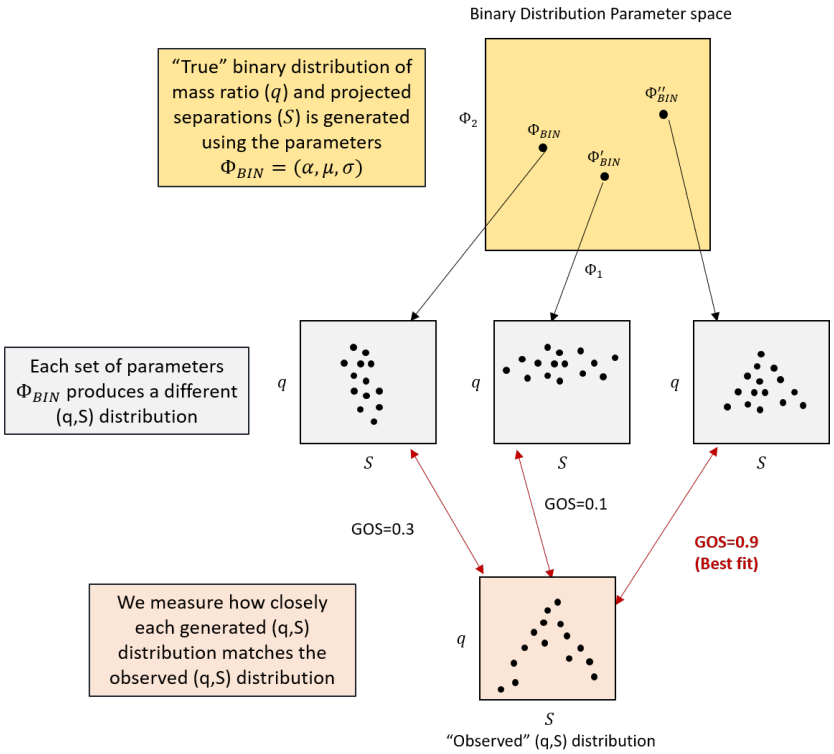

(a) No Selection Effects

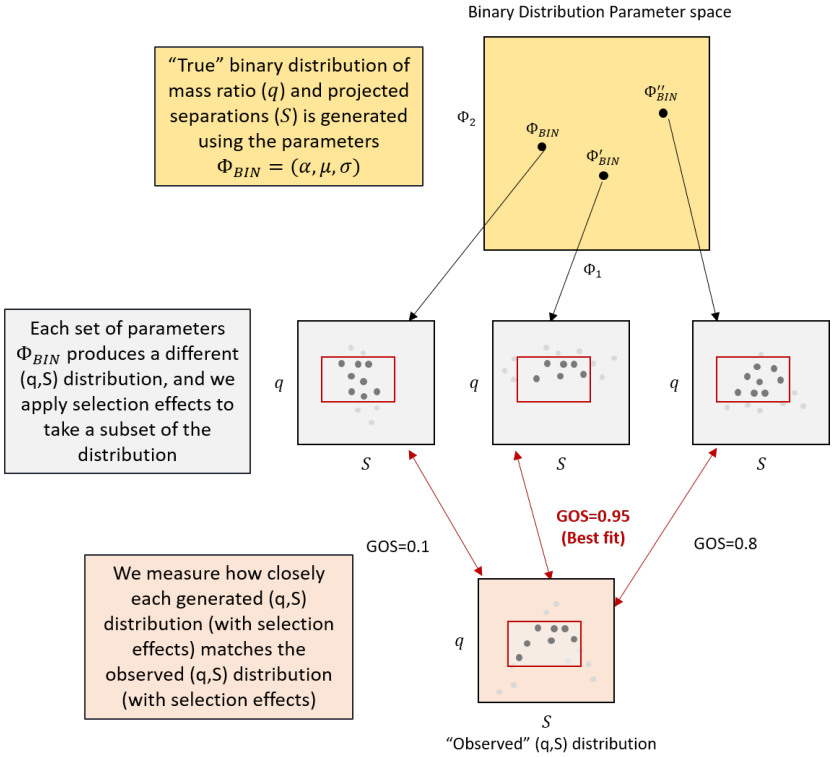

(b) Selection Effects

Figure 4.1: An overview of the methodology discussed in this Chapter, both without and with selection effects. Note that the truncation due to selection effects means that a previously poorly fit parameter set (from Φ'_{BIN}) is now the best fit.

range of visible (and/or resolvable) binary pairs. This truncation means that only a subset of the full (q, S) distribution is visible. Importantly, this means that the retrieval fails: The method requires that two distributions are compared for their similarity, but as the two distributions are trimmed, it can exclude a region that is likely crucial to distinguishing between the two distributions to identify the effect of different parameters. This is demonstrated in the toy illustration by showing that the middle parameter set (Φ'_{BIN}) appears to be (incorrectly) the best fit under the truncation, even though it is in fact the worst.

This means, even as the sample size gets large, one would not be able to retrieve the true parameters. Most importantly, it indicates that any kind of methodology that relies on comparing the similarity of distributions is likely to be fundamentally unsuccessful if the truncation effects too heavily change the shape of the distribution. In the final section, the best methods to handle such limitations are discussed.

The rest of the chapter fills in the details of the above argument. The details of the Monte Carlo procedure are first developed: how are binary distributions of mass ratios and projected separations produced from a simple underlying parameterisation? (These are the "black arrows" in the illustration in Figure 4.1). Then we discuss how to produce the goodness of fit measure between two-dimensional samples using the BST-GOS algorithm, which is well-suited to this problem. (These are the "red arrows" in the illustration in Figure 4.1). Putting these together, the results without selection effects are presented. Then selection effects are introduced (the red outlined boxes in Figure 4.1b) and it is shown how this affects the procedure. Finally, strategies to address these limitations are discussed.

4.2 The model of observed variables

This section derives the relevant formulas that capture the relationship between fundamental parameters and the distribution of the observable variables (this does not yet include selection effects, which will be introduced in a subsequent section). These formulas allow for the construction of a simulation procedure which will be used throughout this chapter.

4.2.1 Deriving our model

The observable variables of interest for us are the mass ratio q and the binary projected separation S. In order to understand how these observable variables are generated, one needs to understand how they arise as a function of a number of physical

processes. These physical processes are discussed now, and the next subsection discusses specifically the simulation procedure.

The mass ratio, q is straightforward:

$$q = \frac{m_2}{m_1} \tag{4.1}$$

where, m_1 and m_2 are respectively mass for primary and secondary stars.

The mass ratio can be estimated from the magnitude difference (brightness contrast) Δm between two stars:

$$\Delta m = 2.5 \log \frac{\mathrm{F}_2}{\mathrm{F}_1} \tag{4.2}$$

Here, F_1 and F_2 are the measured flux of the primary and secondary stars.

The binary projected separation S depends on the physical variables semi-major axis a, eccentricity e, and a set of random variables including the inclination angle (i) between the true and apparent projected orbit, the position angle (θ) between the binary stars in the true orbit, and the angle between true elliptical orbit major axis and the line of sight (ϕ). S is a function of:

$$S = f(a, e, \theta, \phi, i) \tag{4.3}$$

The three angles (i, θ, ϕ) are used to transform the true or real orbital system (consisting of a, e) into the observed separation. Figure 4.2 shows transformation of the true orbit into the apparent orbit using these three angles. The position angle, θ gets a 3D orientation via the inclination i and orientation ϕ.

To initiate the transformation, one needs to determine the position at a particular time in an orbit. This reference point comes from the initial point at time when the star was at the periastron (along the positive x axis). The eccentricity (e), semi-major axis (a) and true anomaly (θ) describe the position and motion of a body in its orbital plane. At first, start with the parameters a and e. All the three anomalies, or angles, in the orbital plane (mean, eccentric and true) are measured in the direction of motion starting from zero at periastron. The mean anomaly (M) and the eccentric anomaly (E) are measured from the centre of the auxiliary circle to the perpendicular projection of the secondary's position onto that circle. Both M and E are used to set θ. Here, θ is not uniformly distributed in time, but M is. Then, one has to use the Ephemeris formula to find the position coordinate.

Ephemeris Formula

For any time t, the orbital elements can be calculated by means of the Ephemeris

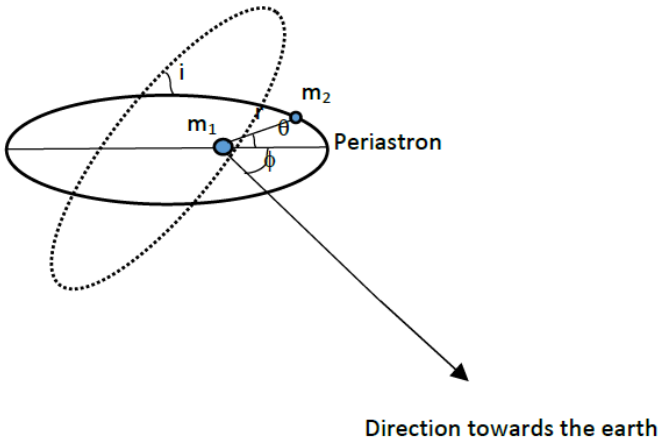

Figure 4.2: Schematic diagram of the true and apparent (projected) binary orbit inclined with each other at an angle i. m_1 and m_2 are respectively the primary and secondary stars separated by angular position r and θ.

formula. The calculation of the secondary star's position with time is usually carried out through the eccentric anomaly (E). Figure 4.3 shows the auxiliary circle with radius (a) to find the area of the ellipse, in terms of E.

Using Kepler's second law, E can be related to the mean anomaly, M, using Kepler's Equation

$$M = E - e\sin(E) \tag{4.4}$$

We can solve for E by iterating with the Newton Raphson method. This can then be used to derive θ and so r via.

$$\tan\frac{\theta}{2} = \sqrt{\frac{1+e}{1-e}}\tan\frac{E}{2} \tag{4.5}$$

$$r = a(1 - e\cos E) = \frac{a(1-e^2)}{(1+e\cos\theta)} \tag{4.6}$$

Assuming the origin of the coordinate systems as the focus of the orbit, the orbital plane can be expressed in polar coordinates in terms of r (the separation between the binary stars) and angle θ (true anomaly).

These coordinates (r, θ) in Figure 4.2 can be converted to cartesian coordinates (x, y, z). Here x and y are in the plane of the sky, and z is along the line of sight.

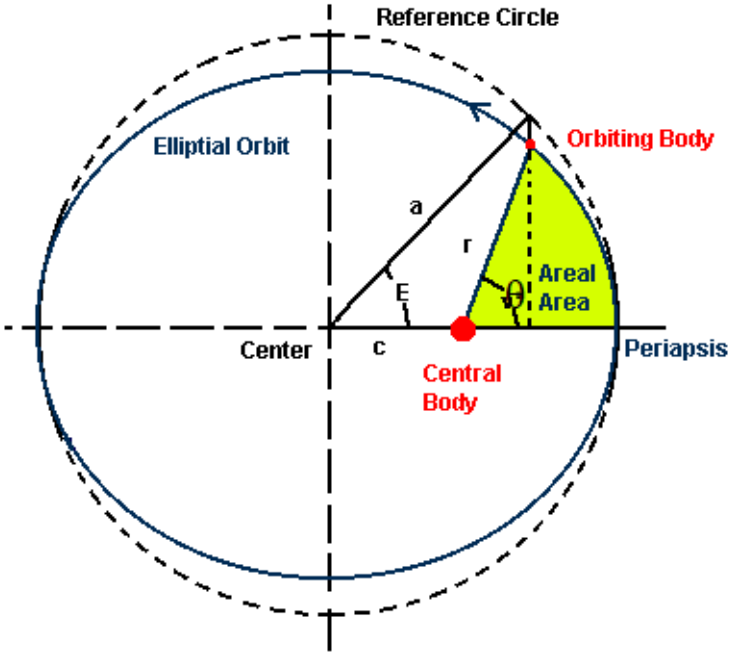

Figure 4.3: The centre of the ellipse is point of equivalent mass of the binary system, and the focus is point of the primary mass m_1. The eccentric anomaly of in the centre is the angle E. The anomalies or angles in the orbital plane are measured in the direction of motion starting from zero at periastron or periapsis.

$$x = r\cos\theta \tag{4.7}$$

$$y = r\sin\theta \tag{4.8}$$

The true anomaly θ, varies from 0^o to 360^o.

The values (x, y) are translated to a new position $(x^{'}, y^{'})$ by rotating through the viewing angle ϕ, giving:

$$x^{'} = x\cos\phi - y\sin\phi \tag{4.9}$$

$$y^{'} = x\sin\phi + y\cos\phi \tag{4.10}$$

Here ϕ, varies from 0^o to 360^o, resulting in:

$$x^{'} = r\cos\theta\cos\phi - r\sin\theta\sin\phi = r\cos(\theta+\phi) \tag{4.11}$$

$$y^{'} = r\cos\theta\sin\phi + r\sin\theta\cos\phi = r\sin(\theta+\phi) \tag{4.12}$$

The inclination angle i of a binary system orbits with our line of sight between (0^o to 180^o) and $(\cos i) \sim U[-1, 1]$. When i= 0^o we call it face-on and i= 90^o, edge-on.

Now rotating the orbit through angle i first around $x - y$ plane and then tilting it in $y - z$ plane, the new binary position is obtained.

$$x^{''} = x^{'} \tag{4.13}$$

$$y^{''} = y^{'}\cos i - z\sin i \tag{4.14}$$

$$z^{''} = y^{'}\sin i + z\cos i \tag{4.15}$$

As z=0 in the new position these equations become:

$$x^{''} = x\cos\phi - y\sin\phi \tag{4.16}$$

$$y^{''} = \cos i(x\sin\phi + y\cos\phi) = r\cos i(\sin(\theta+\phi)) \tag{4.17}$$

$$z^{''} = \sin i(x\sin\phi + y\cos\phi) = r\sin i(\sin(\theta+\phi)) \tag{4.18}$$

Therefore, the binary projected separation in the $x-z$ plane becomes:

$$S = s_{xz} = \sqrt{x''^2 + z''^2} = r\sqrt{(1 - (\sin(\theta + \phi)\cos i)^2)} \tag{4.19}$$

$$\Rightarrow S = \frac{a(1-e^2)}{(1 + e\cos\theta)}\sqrt{(1 - (\sin(\theta + \phi)\cos i)^2)} = f(a, e, \theta, \phi, i) \tag{4.20}$$

For completeness, the position angle in the $x-z$ plane is:

$$\alpha_{xz} = \tan^{-1}(\sin i \tan(\theta + \phi)) \tag{4.21}$$

4.2.2 Simulating a binary stellar population

Now that we have derived explicit formulas for S and q as a function of the physical variables, we can construct a method to simulate their distributions through Monte Carlo techniques.

4.2.2.1 Semi-major axes

Assuming the semi-major axis, a, distribution is log-normal, as suggested from observation (Raghavan et al. 2010, Ward-Duong et al. 2015). That is:

$$a \sim \text{lognormal}(\mu, \sigma) \tag{4.22}$$

Where, μ and σ are the mean and standard deviation. For large σ, the semi-major axis start to approach Öpik's law (log-flat).

4.2.2.2 Eccentricity

The eccentricity parameter f_e refers to the functional form of the distribution of the eccentricities. Jeans (1919) showed that dynamical interactions of stellar systems are responsible for binaries with thermal eccentricity distributions where they exchange energy and reach statistical equilibrium. If the orbital period is less than 10 days, tidal interactions circularise the orbit. Duquennoy & Mayor (1991) studied nearby solar-type primary stars and assumed a thermal eccentricity. Within periods of 10 and 1000 days the mean eccentricity is 0.31. At longer periods, they suggested that the eccentricity distribution was more likely thermal (the limitation of the study was small N). With a larger sample Raghavan et al. (2010) showed that the mean eccentricity (period between 10 and 1000 days) is 0.47 and the distribution is flat in the range [0-0.6]. Their study found no correlation between eccentricity and period

at $P > 10^3$ days. Abt (2005) showed that the binaries with periods (10-100 days) lack highly eccentric orbits. Binaries with periods greater than 1000 days have flat eccentricities (from 0 to nearly 1). Abt (2005) also showed that the circular orbits occur for periods of 10^5 days or more.

Different types of eccentricities:
4 models for the eccentricity distribution are considered, each one relying on a different functional form f_e:

1. f_e **= Flat**

$$e = f_e(u_e) = u_e \tag{4.23}$$

where, u_e is the short-hand for $u_e \sim U[0, 1]$.

That is for flat types, the distribution of e is a uniform distribution.

2. f_e **= Thermal**

$$e = f_e(u_e) = \sqrt{u_e} \tag{4.24}$$

3. $f_e(a)$ **= Thermal-circularised**

$$e = f_e(u_e) = \sqrt{u_e} \tag{4.25}$$

with an upper bound on the distribution $e_{\max} = 0.5(1 + \tanh(1.5 \log_{10}(a) + 1))$; when $e_{\max} < 0.01, e = 0$ (Parker et al. 2011).

4. f_e **= Mostly circular**

$$e = f_e(u_e) = u_e^2 \tag{4.26}$$

4.2.2.3 Angular variables

θ can be computed using the method outlined in Equation 4.5, where M is drawn uniformly:

$$M \sim U[0, 2\pi] \tag{4.27}$$

The remaining angles are drawn as follows:

$$\phi \sim U[0, 2\pi] \tag{4.28}$$

$$i = \arccos u_i : u_i \sim U[-1, 1] \tag{4.29}$$

The separation can then be computed as per Equation 4.20:

$$S = f(a, e, \theta, \phi, i) = \frac{a(1-e^2)}{(1 + e\cos\theta)}\sqrt{(1 - (\sin(\theta + \phi)\cos i)^2)} \tag{4.30}$$

4.2.2.4 Mass ratio

The mass ratio q is just drawn from a distribution as follows:

$$f(q) \propto q^{\alpha} \tag{4.31}$$

Therefore, $\alpha = 0$ is a flat mass distribution, $\alpha > 0$ is biased towards more equal-mass systems, and $\alpha < 0$ is biased to unequal-mass systems.

In order to sample this in practice, inverse CDF sampling is used. In order to sample from $f(q) \propto q^{\alpha}$ with $q \in [q_{\min}, 1]$, note that the CDF is just:

$$F(q) = \frac{q^{(1+\alpha)} - q_{\min}^{(1+\alpha)}}{1 - q_{\min}^{(1+\alpha)}}$$

Therefore, in order to sample from the distribution, $u_q \sim U[0, 1]$ is sampled transformed using the inverse CDF:

$$q = F^{-1}(u_q) = (u_q(1 - q_{\min}^{(1+\alpha)}) + q_{\min}^{(1+\alpha)})^{\frac{1}{1+\alpha}} \tag{4.32}$$

In this study, the lower bound mass ratio limit $q_{\min} = 0.1$ (Goodwin 2012) is used as a value to represent good contrast sensitivity to low mass secondary star.

4.2.2.5 Generating representative binary samples

We are interested in the effect of the parameters μ, σ and f_e on the distribution of S, and how the parameter α affects q. Together, this forms the (q, S) distribution. Figure 4.4 summarises the full data generation process as described above.

In this image, the parameters of the generation process are seen in black circles (α, μ, σ and the functional form f_e). Each of these lead directly to the distribution of the physical quantities q, a and e, and is captured in the blue outlined "Physical process".

In addition to this there is also a considerable amount of extra variation generated from the variables θ, i, ϕ, which is captured in the red outlined "Angular variables". The final distribution[1] of (q, S) is then a function of these physical processes and angular variables.

It is worth pointing out that the effect of angular variables is quite important and could possibly obscure the true physical process described. When the Monte Carlo process is simulated with large samples of N, one can effectively marginalize out this noise to get a better indication of the fundamental physical process, and this is the strategy followed when producing the reference populations described in the process above (using $N \sim 10^5 - 10^6$). However, this is not a luxury we have when it comes to the "observed population", and this is normally a much smaller sample ($N \sim 200 - 1000$). These implications will be seen in the analysis.

4.2.2.6 Why is the binary fraction is not included as a parameter?

The development of the Monte Carlo method described above is used to generate samples from a star cluster, where the properties of the binary population can be described by parameters $(\alpha, \mu, \sigma, f_e)$. These parameters described various physical properties of interest for binary pairs, such as the typical size of secondary to primary mass, the typical separation between them, etc.

Perhaps the most obvious "interesting" binary parameter missing is the binary fraction itself (f_{bin}) which was discussed in great detail in Chapters 1 and 2 of this thesis. In principle during the selection process one could include an overall f_{bin} parameter that determines what fraction of the stars in a given cluster of size N would be binary.

The reason it is excluded because this parameter will have no meaningful impact on the resulting sample distribution aside from just scaling the size of the sample. For example, simulating a stellar cluster of $10,000$ stellar systems with a 50% binary population to produce a (q, S) distribution for the binary systems would be exactly equivalent to just generating a sample of $5,000$ binary systems directly. It would not effect the shape of the resulting (q, S) distribution at all, and it is exactly that shape which allows us to perform any comparisons of fit between distributions.

Therefore, the parameter f_{bin} is not included specifically in the remainder of the analysis.

[1] Note, the selection effects have not yet been introduced.

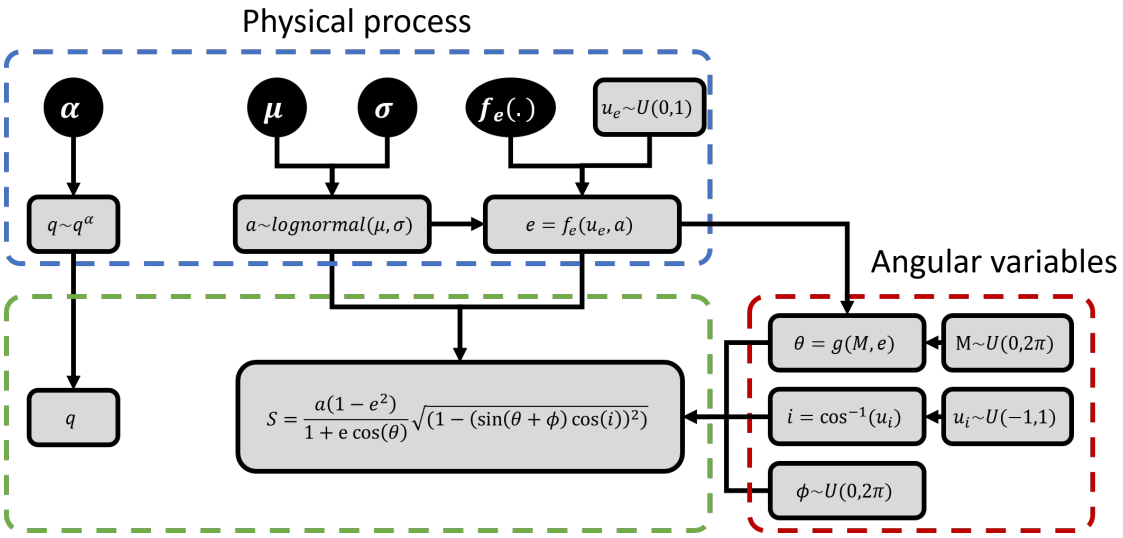

Figure 4.4: Outline of the Monte Carlo process, clearly separating the physical process (blue outline) from the angular variables (red outline) and the resulting (q, S) distribution (green outline). (Note, the variable θ does not have a closed form of M and e so it is just described as a function $g(M, e)$).

4.2.3 Can the parameter f_e be eliminated from the inverse problem?

In this subsection it is considered whether we can simplify the distribution of the variable S by eliminating the parameter (i.e. the functional form) f_e from our process. This is done by showing that changes in f_e have an effect on the distribution of S that is indistinguishable from small changes in μ and σ from the semi-major axis. As such, it is impossible to discriminate between distributions generated from different f_e in practice, so the analysis proceeds by assuming a fixed f_e.

As a starting point, however, it can be show that the effect of the eccentricity function on the S distribution is relatively small. Using the method described in section 1.3, a binary population of 10^6 "test" stellar systems is generated, with mean $\mu_0 = 0.5$ AU, standard deviation $\sigma_0 = 0.5$ AU and four different eccentricity distributions.

We have chosen smaller values of μ_0 and σ_0 to keep the maximum separation under 1000 AU. It helps us to visualise changes in the separation distribution due to changes in eccentricity distributions. These are similar to observed brown dwarf binary properties $\mu_0 = 0.66$ AU and $\sigma_0 = 0.4$ AU,(Burgasser et al. 2007, Thies & Kroupa 2007) where primary component mass are between 0.02 to 0.08 $M_{\odot}$.

In Figure 4.5 the CDFs of the separation are compared where the colours correspond to thermal (magenta), flat (blue), thermal circular (green) and mostly circular (red). For thermal, e is usually very eccentric and contributes to a larger binary

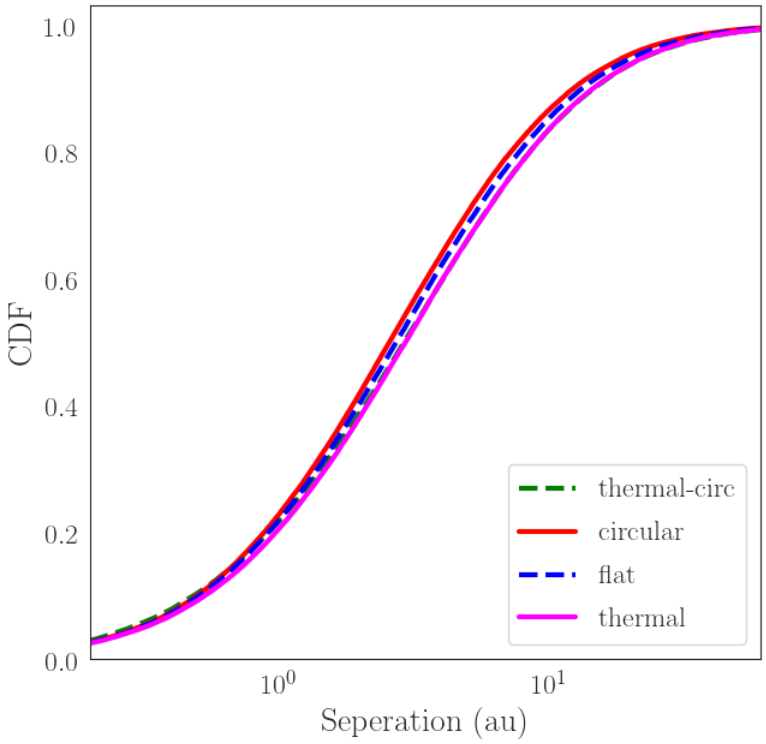

Figure 4.5: Cumulative distribution function (CDF) of binary seperation for 10^6 binary systems for four different types of eccentricities f_e. Colour blue represents (flat), magenta (thermal), red (mostly circular) and green (thermal circular). The parameters are mean $\mu_0 = 0.5$ and standard deviation $\sigma_0 = 0.5$.

separation S. For mostly circular, the eccentricity is usually very low and S is lower than the other eccentricity distributions. In-between are the separation distributions produced by flat and thermal circular eccentricities. The mean, standard deviation and median separation for thermal, flat, thermal circular and mostly circular eccentricities are respectively (6.3, 11.57 and 2.9 AU), (5.76, 10.49 and 2.7 AU), (6.29, 11.63, 2.8 AU) and (5.36, 9.56 and 2.55 AU).

Clearly, all the different eccentricity distributions resulted in a similar projected separation distributions. The minimum values correspond to mostly circular (mean 5.36 AU, median 2.55 AU) and maximum to thermal (mean 6.3 AU, median 2.93 AU).

Next we compared two separation distributions with different f_e and different (μ, σ). The first distribution is generated as before with thermal eccentricity and with $\mu_1 = 0.5$ AU, $\sigma_1 = 0.5$ AU. This is compared to a mostly circular eccentricity and with $\mu_2 = 0.54$ AU, $\sigma_2 = 0.52$ AU. Figure 4.6 shows the cumulative distribution

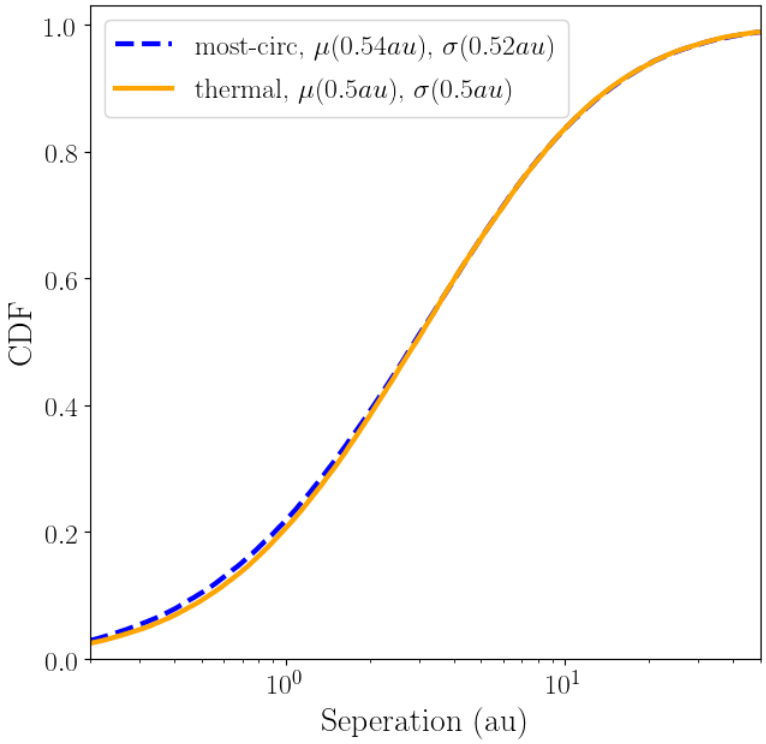

Figure 4.6: Cumulative distribution function (CDF) of binary separation for 10^6 binary systems for different values of mean and standard deviation of logarithmic semi-major axis (μ, σ) and eccentricity type f_e. The blue line depicts ($\mu_1 = 0.5, \sigma_1 = 0.5, f_e =$ "thermal"). The orange line depicts ($\mu_2 = 0.54, \sigma_2 = 0.52, f_e =$ "mostly circular"). The two distributions are barely distinguishable.

of the mostly circular in orange and thermal in blue. This results in mean, standard deviation and median separation of (6.3, 11.57, and 2.9 AU) for thermal and (6.3, 11.63, 2.9 AU) for mostly circular.

As such, it can be concluded that changes in f_e cannot be distinguished from small changes in μ and σ and so the rest of the analysis can keep f_e fixed (to, for example, $f_e =$ "flat") and proceed by varying μ and σ only. While this may result in very small uncertainty added to our estimates of μ and σ, it considerably simplifies our analysis and reduces the required permutations to simulate.

4.2.4 Our final model

Keeping f_e fixed at flat, the model can be simplified considerably. The updated generation process is outlined in Figure 4.7. It can be seen the process is a bit simpler, and the full parameterisation can be summarised with:

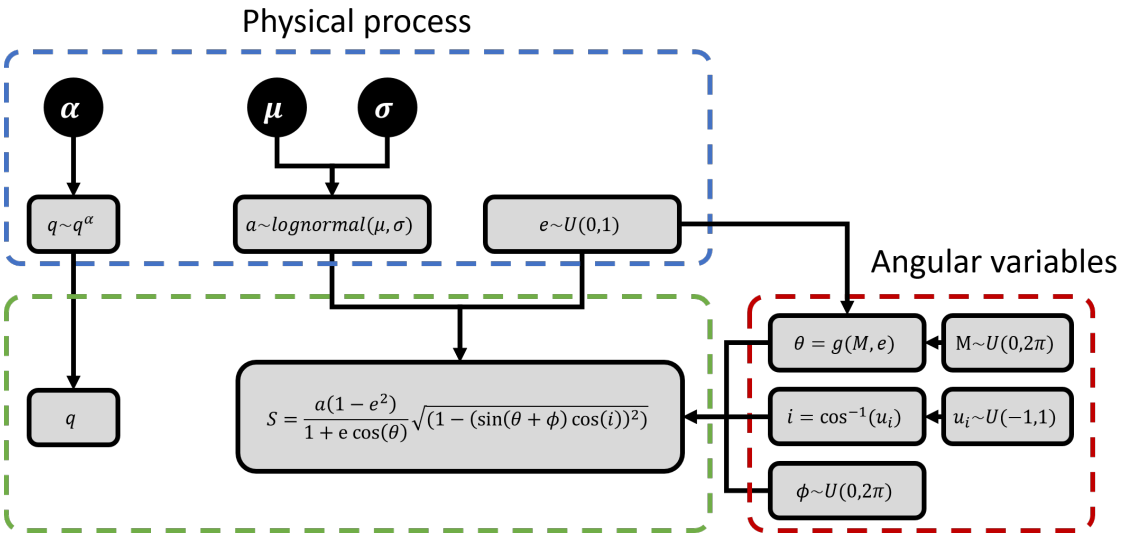

Figure 4.7: Updated outline of the Monte Carlo process, where f_e is fixed at "flat".

$$(q, S) \sim \mathbb{P}(q, S|\alpha, \mu, \sigma) \tag{4.33}$$

The purpose of the methods this chapter go on to describe is to retrieve these underlying parameters from observed samples of (q, S) by comparing the observed samples with Monte Carlo simulations of the samples. For convenience, the parameter vector is named $\Phi = (\alpha, \mu, \sigma)$.

In Figure 4.8, there are a few examples of (q, S) distributions generated from different values of Φ, so it can be demonstrated how the distributions change as the parameters change.

Cluster A was generated with $\Phi_A = (\alpha_A = -1.01, \mu_A = 1.5, \sigma_A = 1.5)$. Here it can be seen that since $q \sim q^{-1}$, the mass ratios are skewed towards the lower bound ($q_{min} = 0.1$). Cluster B was generated with $\Phi_B = (\alpha_B = 1, \mu_B = 2.5, \sigma_B = 2.5)$. Here it can be seen that since $q \sim q^1$, the mass ratios are skewed towards 1 (i.e. the primary and secondary stars are roughly the same mass). Cluster C was generated with $\Phi_C = (\alpha_C = 0, \mu_C = 0.5, \sigma_C = 0.5)$. Here, it can be seen that since $q \sim q^0 = 1$, the mass ratios are uniformly distributed between 0.1 and 1. For each of the cases, the total number of binary systems in the population is 10^5.

The final panel overlays the three clusters, so it can be seen clearly how the distributions of separation S change as the parameters μ and σ change. As expected, as μ increases the separations shift to the right, and as σ increases the spread increases also.

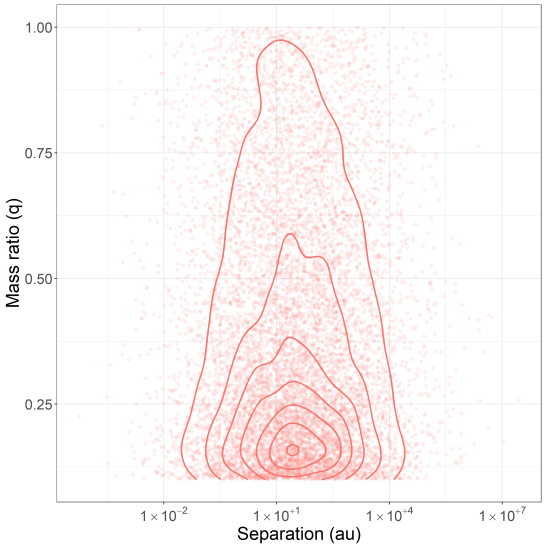

Cluster A: $\alpha = -1.01, \mu = 1.5, \sigma = 1.5$

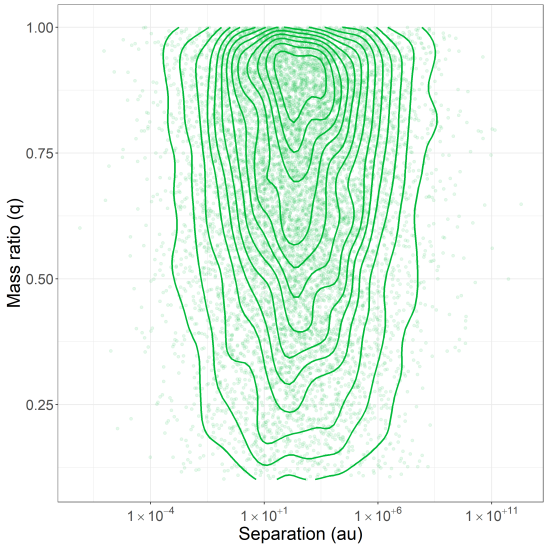

Cluster B: $\alpha = 1, \mu = 2.5, \sigma = 2.5$

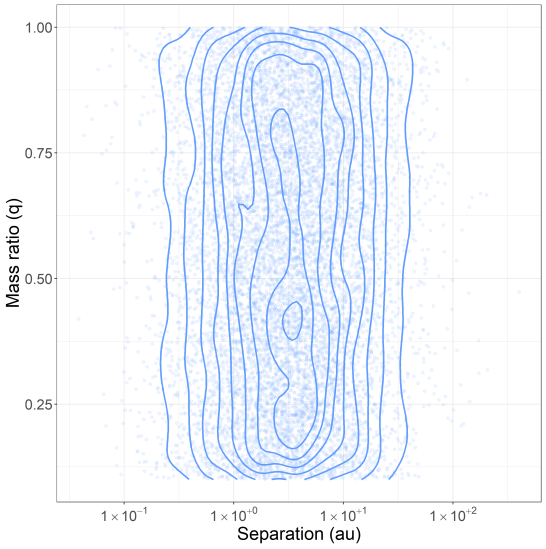

Cluster A: $\alpha = 0, \mu = 0.5, \sigma = 0.5$

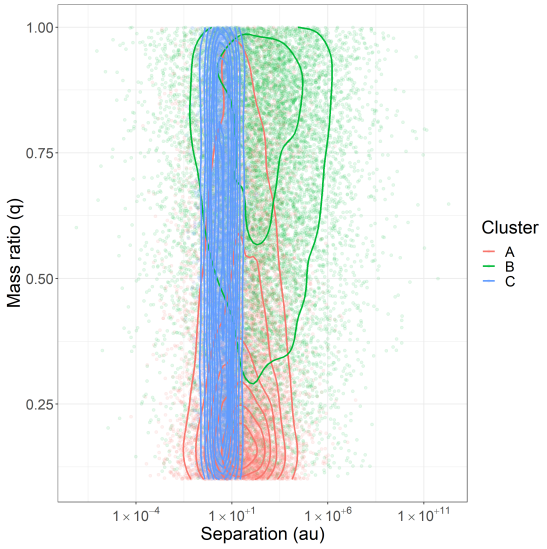

All clusters overlaid

Figure 4.8: Various (q, S) distributions generated from different parameter sets $\Phi = (\alpha, \mu, \sigma)$. The contours show the shape of the resulting distribution.

4.3 Retrieving binary parameters when there are no selection effects

In the previous section, the physical process of interest was introduced and a simulation method was derived to generate Monte Carlo samples of the distribution (q, S) from the parameters Φ. In this section an algorithm is introduced to compare such distributions with the "observed" or "test" data and to provide a goodness of fit in order to find best fit parameters. The "test" data is generated with some known set of parameters Φ_T, the (two-dimensional) sample is referred to as (q_T, S_T).

This method is tested in the scenario where there are no selection effects, and it will be shown that the method performs very well. In the next section, this method is extended to observation data with selection effects and the differences will be made clear.

4.3.1 The BST-GOS Algorithm

We begin by establishing the BST-GOS algorithm to take an observed binary stellar population (in the form of $(q_{\rm T}, S_{\rm T})$ data) and return a best estimate of the true parameters Φ_T. As discussed, the method generates many Monte Carlo $(q_{\rm MC}, S_{\rm MC})$ distributions over a grid search of parameter combinations of Φ. Each distribution is compared to the test set, and together they generate a score called its Goodness of Split (GOS), which is later used to find the best fit parameters. The GOS criteria is first explained, and then how it can be maximised using a Binary Search Tree method.

4.3.1.1 Measuring Goodness of Split

The objective of the algorithm is to measure the similarity between $(q_{\rm T}, S_{\rm T})$ and $(q_{\rm MC}, S_{\rm MC})$. While there are a large number of possible measures of similarity between two multivariate distributions, the study is interested in one that is both computationally effective and intuitive. This method is referred as Binary Search Tree - Goodness of Split. The method is inspired by how one can in theory use the cross-entropy of the two distributions to measure their similarity. In order to calculate this for our samples, the data is partitioned into bins, where some specific choices of the bins to allow for a very computationally convenient calculation (the details are provided below). The method was originally developed by Prof. Simon Goodwin and adapted for this work.

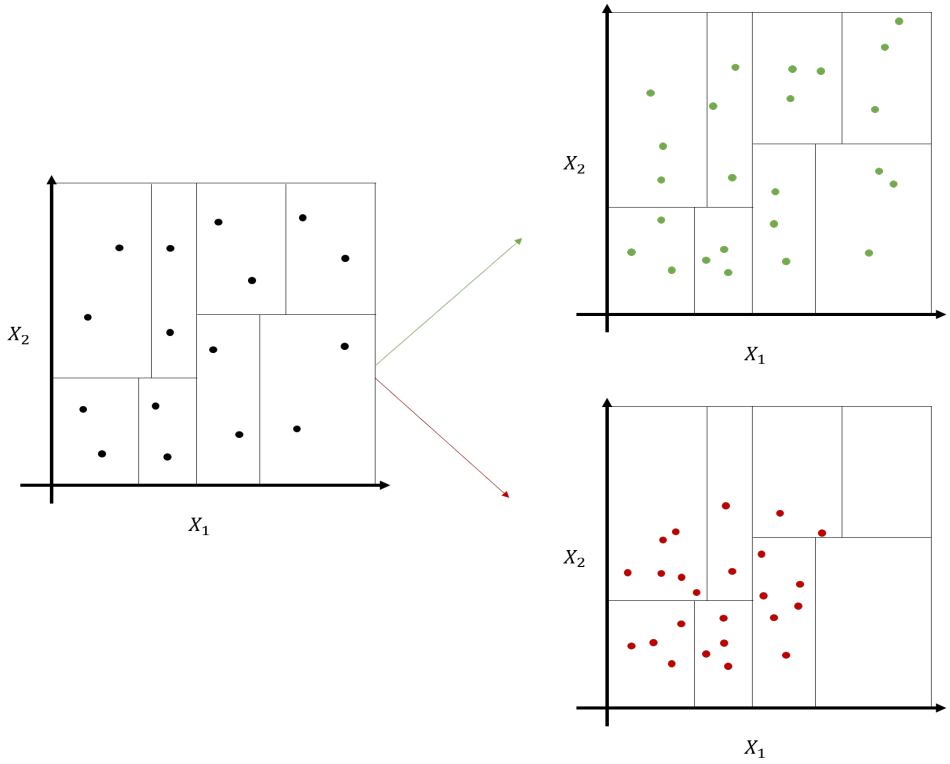

Figure 4.9: Illustrating the intuition of the BST-GOS algorithm. The test set (left, black) is compared to two reference populations (green, red). It can be seen how the even partition of the test set corresponds to an even partition of the green reference population, but not much at all of an even partition of the red reference population.

The basic idea of the algorithm is to create a partition of the space (q, S) such that if $(q_{\mathrm{T}}, S_{\mathrm{T}})$ and $(q_{\mathrm{MC}}, S_{\mathrm{MC}})$ are roughly evenly split between the cells, then the two distributions have the same fractions of spread throughout the space, and one can say that the distributions are similar. Conversely, if the two distributions are very different, then they will have different fractions of the sample in each partition.

The basic intuition is illustrated in Figure 4.9. A given "test" set (black dots, left) is taken and compared with two different reference populations (green, red). The test set is first used to construct a set of partitions that evenly split it into a number of cells (exactly 2 per cell, which is achieved by the "Binary Search Tree" algorithm, details below). Each reference distribution is taken to see how well they fit into this partition. It can be seen the green dots have exactly 3 samples in each cell, meaning it is evenly distributed over the same cells and therefore provides a perfect split between the bins (and hence the term "Goodness of Split"). This provides the highest possible Goodness of Split (GOS) score. The red dots are much more heavily concentrated on a few cells, meaning that it is very differently distributed to the test set, and will have a lower GOS.

The details of this intuition are as follows. In order to construct the even partition, a k-dimensional search tree algorithm is utilized. Generally speaking, the k-dimensional (k-d) tree is a space-partitioning data structure for arranging points in a k-dimensional space. The objective is to construct a set of partitions so that the points are evenly distributed between the partitions. A k-d tree can be constructed in $\mathrm{O}(n \log n)$ by recursively selecting the median point in a certain dimension as the position of the split.

In our case, $k = 2$ (corresponding to q and S), and this can be visualised as splitting the 2-dimensional space into rectangles (as in Figure 4.9). In this case the method is often referred to as "binary search trees" (BST). For binary search trees, one switches sequentially between the two variables X_1 and X_2, and for each rectangle along that dimension one partitions the rectangle into two sub-rectangles - values above the cut-off (the median value) or less than or equal to the cut-off. This continues until each cell has an almost equal number of points. If the algorithm has a recursive depth of l, then the final partition will have 2^l cells and $n/2^l \pm 1$ points in each cell.

In principle, one can run the BST algorithm over either the "test" set or Monte Carlo set. However, it is much more efficient to run it over the "test" set, as it is much smaller, and one can then re-use the partition for every subsequent Monte Carlo distribution (as in Figure 4.9).

Once the partition is obtained, we want to see how well the Monte Carlo reference population also adheres to this even partition. We quantify the GOS of some partition for the datasets $(q_{\mathrm{T}}, S_{\mathrm{T}})$ and $(q_{\mathrm{MC}}, S_{\mathrm{MC}})$ of total sample sizes $\mathrm{n_T}$ and $\mathrm{n_{MC}}$ as follows. Assume there are N cells and in each i-th cell the number of "test" observed points is $\mathrm{n_T(i)}$ and Monte Carlo observed points $\mathrm{n_{MC}(i)}$. Then, the GOS is the measure of the strength of the proposed split, and is defined as:

$$\mathrm{GOS} = \prod_{\mathrm{i}} \mathrm{n_{MC}(i)}^{\mathrm{n_T(i)}} \tag{4.34}$$

Then note that:

$$\text{GOS} = (\text{n}_{\text{MC}}(1))^{\text{n}_{\text{T}}(1)} \times (\text{n}_{\text{MC}}(2))^{\text{n}_{\text{T}}(2)} \times (\text{n}_{\text{MC}}(3))^{\text{n}_{\text{T}}(3)} \times \ldots (\text{n}_{\text{MC}}(\text{N}))^{\text{n}_{\text{T}}(\text{N})} \quad (4.35)$$

$$\Rightarrow \ln(\text{GOS}) = (\text{n}_{\text{T}}(1)\ln(\text{n}_{\text{MC}}(1))) + (\text{n}_{\text{T}}(2)\ln(\text{n}_{\text{MC}}(2))) + \ldots \quad (4.36)$$

$$= \sum_i \text{n}_{\text{T}}(\text{i}) \ln(\text{n}_{\text{MC}}(\text{i})) \quad (4.37)$$

$$\approx \frac{\text{n}_{\text{T}}}{2^l} \sum_i \ln(\text{n}_{\text{MC}}(\text{i})) \quad (4.38)$$

The last step made use of the fact that:

$$\text{n}_{\text{T}}(1) \approx \text{n}_{\text{T}}(2) \approx \text{n}_{\text{T}}(3) \ldots \approx \text{n}_{\text{T}}/2^{\text{l}} \quad (4.39)$$

That is, by design the number of test points in each cell is roughly equal. Thus, one ends up with a very simple calculation that can be easily implemented.

This quantity will be maximised whenever $\text{n}_{\text{MC}}(\text{i})$ is evenly split between each cell. That is:

$$\text{n}_{\text{MC}}(1) \approx \text{n}_{\text{MC}}(2) \approx \ldots \approx \text{n}_{\text{MC}}/2^{\text{l}} \quad (4.40)$$

4.3.1.2 Parameter estimation

The BST-GOS process is conducted for the parameter values of Φ_{MC} in a grid search, generating a GOS score for every parameter set. The final step is to aggregate this into an estimate for the true parameters Φ_{T}.

To generate a best point estimate the average of the parameter sets across the top 1% of GOS is calculated. Averaging over best performing sets (as opposed to simply taking the single best performing set) helps us smooth out the noise that arises in the estimate. The top 1% average value is not very different from the top 2%. For example, consider take a "test" sample size 700, $\mu_{\text{T}} = 1.7$, $\sigma_{\text{T}} = 1.7$ and $\alpha_{\text{T}} = 0.0$. If the BST-algorithm is run with a 10^6 Monte Carlo population with parameter grid (as done later in this Section) then the retrieved average values for μ, σ, α, GOS for top 1% are (1.7, 1.7, 0, 98.18) and for the top 2% are (1.7, 1.67, 0, 98.0).

Here, the best parameter estimate, $\hat{\Phi}$:

$$\hat{\Phi} = (\hat{\alpha}, \hat{\mu}, \hat{\sigma}) = \text{average}((\alpha_{\text{MC}_\text{i}}, \mu_{\text{MC}_\text{i}}, \sigma_{\text{MC}_\text{i}}) : \text{GOS}_\text{i} \in \text{Top } 1\%) \quad (4.41)$$

Where $(\hat{\alpha}, \hat{\mu}, \hat{\sigma})$ refer to our estimates of the parameters, $\hat{\Phi}$ is a shorthand notation for this vector, and $(\alpha_{\text{MC}_\text{i}}, \mu_{\text{MC}_\text{i}}, \sigma_{\text{MC}_\text{i}})$ refer to the i-th Monte Carlo parameter set.

In addition to a best estimate, it is important to analyse the performance of an algorithm by visualising how the Goodness of Split varies over pairs of parameters in (α, μ, σ). If one considers GOS as a function over the parameter space (similar to a likelihood function over the parameter space), then:

$$\text{GOS} = \text{f}(\Phi) = \text{f}(\alpha, \mu, \sigma) \tag{4.42}$$

It is difficult to visualise this GOS as a function of these parameters in three dimensions. In order to visualise the performance of three variable sets a third variable can be eliminated by averaging two variables over the 3rd one. To observe how GOS varies over μ and σ, average AGOS was obtained by averaging the GOS over α. For example if $\alpha \in (-1.01, 0, 1.01)$ then the AGOS is:

$$\text{AGOS}(\mu, \sigma) = \frac{1}{3}(\text{GOS}(\alpha = 1, \mu, \sigma) + \text{GOS}(\alpha = 0, \mu, \sigma) + \text{GOS}(\alpha = -1.01, \mu, \sigma)) \tag{4.43}$$

It can be emphasized here that this averaging is for visual purpose only. Parameter α was not averaged out in the algorithm.

When the GOS function varies smoothly with a clear single peak then the AGOS function will have a peak that coincides with the full GOS function (as calculated using $\hat{\Phi}$). We will see this is the case when there are no selection effects. However when the function is highly irregular (as can be seen later for selection effects) then it can be seen that the peaks of this AGOS can vary from the peaks of the full GOS. In that case, the AGOS can slightly misrepresent the true GOS it is attempting to visualise. Still, the AGOS provides us with at least a useful visualisation of the outputs.

4.3.2 Testing the algorithm

The algorithm is first tested in the absence of selection effects to show how effectively it can retrieve the parameters. The Monte Carlo fake populations are simulated across the parameter grid as follows:

- Mean of semi-major axis μ_{MC} where the minimum and maximum values are 0.5 and 2.5 respectively. Incremental values of 0.1 were used, leading to 20 possible values.

- Standard deviation of semi-major axis, σ_{MC} where the minimum and maximum values are 0.5 and 2.5 respectively. There are 20 possible values with an

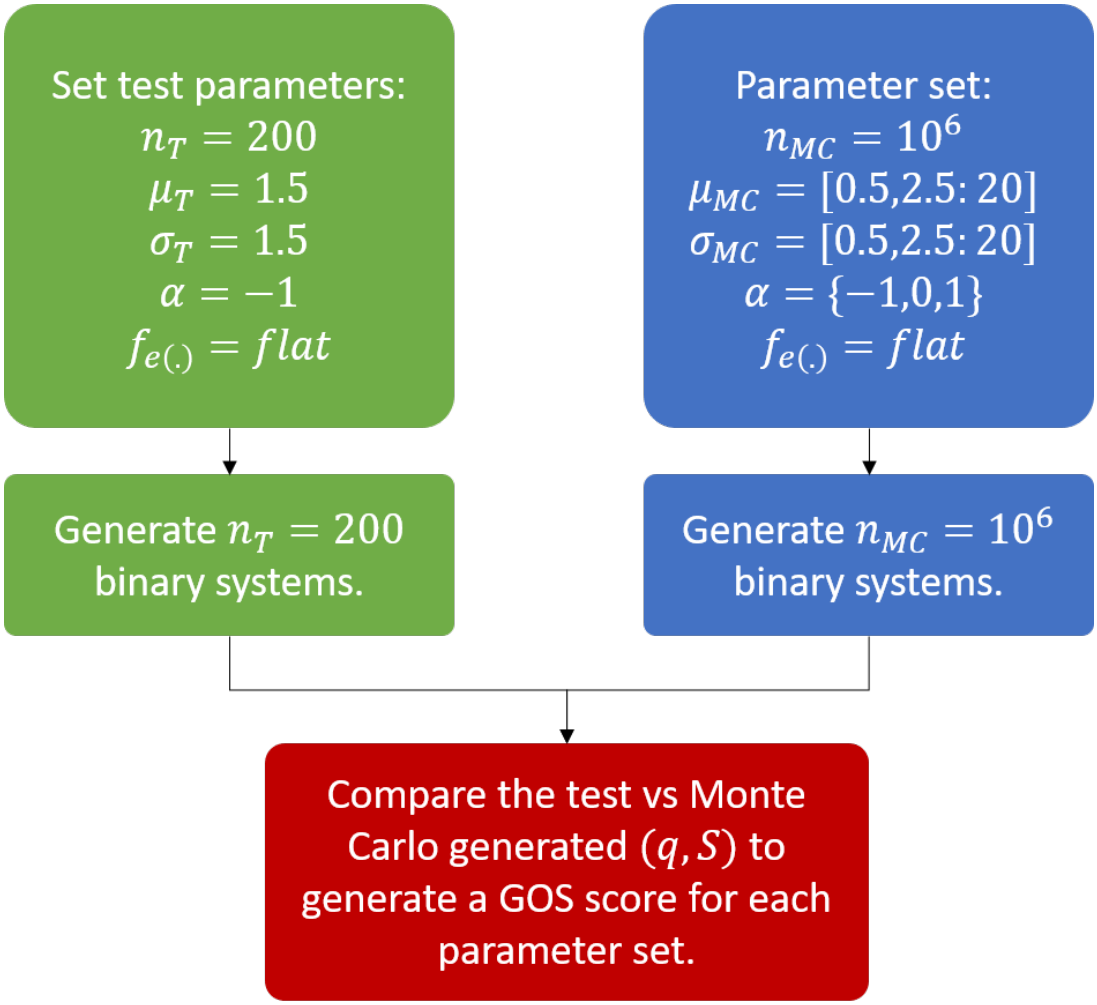

Figure 4.10: Flow chart detailing the simulation process (without observational selection effects)

increment of 0.1.

- The mass ratio parameter or the slope of mass ratio/secondary magnitude distribution is $\alpha_{\rm MC}$ with values of -1.01[2], 0 and 1.

These parameter sets will create 1200 MC datasets. Figure 4.10 presents the process in a case when there are no selection effects.

4.3.2.1 Performance of the algorithm

The application begins by generating nine "test" samples using the following parameters where the values of $\mu_{\rm T}$ and $\sigma_{\rm T}$ were taken from Parker & Meyer (2014), who took orbital period distributions of binary samples from De Rosa et al. (2013), Raghavan

[2]The value $\alpha = -1.01$ instead of $\alpha = -1$ is used to avoid divide by zero errors in the inverse CDF sampling process.

et al. (2010), Janson et al. (2012) and then converted them into distributions of the semi-major axes. The resulting parameters of these semi-major axis distributions are used for our samples:

- Set 1: n_T = 200, 700, 1000, μ_T = 1.7, σ_T = 1.7 α_T = 1.01 (De Rosa et al. 2013).
- Set 2: n_T = 180, 630, 900, μ_T = 2.5, σ_T = 0.7, α_T = -0.5 (Raghavan et al. 2010).
- Set 3: n_T = 120, 420, 600, μ_T = 1.2, σ_T = 0.8, α_T = 0 (Janson et al. 2012).

Following the implementation technique and generative process as outlined in Fig. 4.11, 1,200 Goodness of Split measures are computed, one for each Monte Carlo (MC) parameter set Φ_{MC_i} as output.

In the previous section, it was mentioned that visualisation the GOS in three dimensions as a function of three parameters is difficult.

We visualise these Goodness of Split results in the plots using the average GOS function AGOS(μ, σ) over α. Figure 4.11 shows the contour plots with parameters μ_{MC} and σ_{MC} for Set 1 (left panel), Set 2 (middle panel) and Set 3 (right panel). The total number of Monte Carlo stars is $n_{MC} = 10^6$. For Set 1, the "test" sample size n_T varies from top to bottom as 200, 700 and 1000. For Set 2 and Set 3 from top to bottom they respectively vary as (180, 630, 900) and (120, 420, 600). The Purple regions of these contour plots represent the highest (average) Goodness of Split scores. We also include the (μ_T, σ_T) as the true parameters (red circle) and the $\hat{\Phi}$ (black asterisk). Note here that the peak in the AGOS scores match the peak of the GOS scores as shown by $\hat{\Phi}$, indicating that the GOS function is performing well.

A full description of results as retrieved from the algorithm is presented in Table 4.1, which shows the values of $\hat{\Phi}$ $(\hat{\mu}, \hat{\sigma}, \hat{\alpha})$ and the average top 1% value of GOS. The top sub-table 4.1a shows the values for Set 1. The middle 4.1b and bottom sub-table 4.1c are respectively present retrieved values for Set 2 and Set 3. As can be seen from both Table 4.1 and Figure 4.11, the algorithm performs very well at recovering the true parameters.

For Set 1, with $n_T = 200$, the algorithm recovers $\hat{\mu}$ =1.64 and $\hat{\sigma}$ =1.8 close to the true parameters (1.7, 1.7). The retrieved parameters get even better as n_T grows to 700 (1.7, 1.7) and then 1000 (1.7, 1.7). The goodness of split rises when n_T rises, as with larger samples the GOS will be higher. In the two-dimensional AGOS plot, it can be seen that the AGOS reaches a peak in the purple region exactly where the 3D peak (the black asterisk, $\hat{\Phi}$ is a function of three parameters) occurs, indicating

Sub-Table 1.a: Set 1

	n_T	μ	σ	α	GOS
True	-	*1.7*	*1.7*	*1.01*	-
top	200	1.64	1.83	1.01	56
middle	700	1.7	1.7	1.01	98
bottom	1000	1.7	1.7	1.01	110

Sub-Table 1.b: Set 2

	n_T	μ	σ	α	GOS
True	-	*2.5*	*0.7*	*-0.5*	-
top	180	2.44	0.64	-0.3	52
middle	630	2.43	0.71	-0.3	93
bottom	900	2.44	0.71	-0.5	105

Sub-Table 1.c: Set 3

	n_T	μ	σ	α	GOS
True	-	*1.2*	*0.8*	*0*	-
top	120	1.11	0.9	0	38
middle	420	1.14	0.8	0	80
bottom	600	1.15	0.8	0	92

Table 4.1: $\hat{\Phi}$ ($\hat{\mu}, \hat{\sigma}, \hat{\alpha}$ based on top 1% of GOS score) the best parameter estimates and GOS without selection effects for Set 1 (Sub-Table 1.a), Set 2 (Sub-Table 1.b)and Set 3 (Sub-Table 1.c). For Set 1, the "test" sample value n_T for top, middle and bottom rows are 200, 700 and 1000. For Set 2 and Set 3 the n_Ts are respectively (180, 630, 900) and (120, 420 and 600). The row captioned "True" refers to the true parameter values for each set.

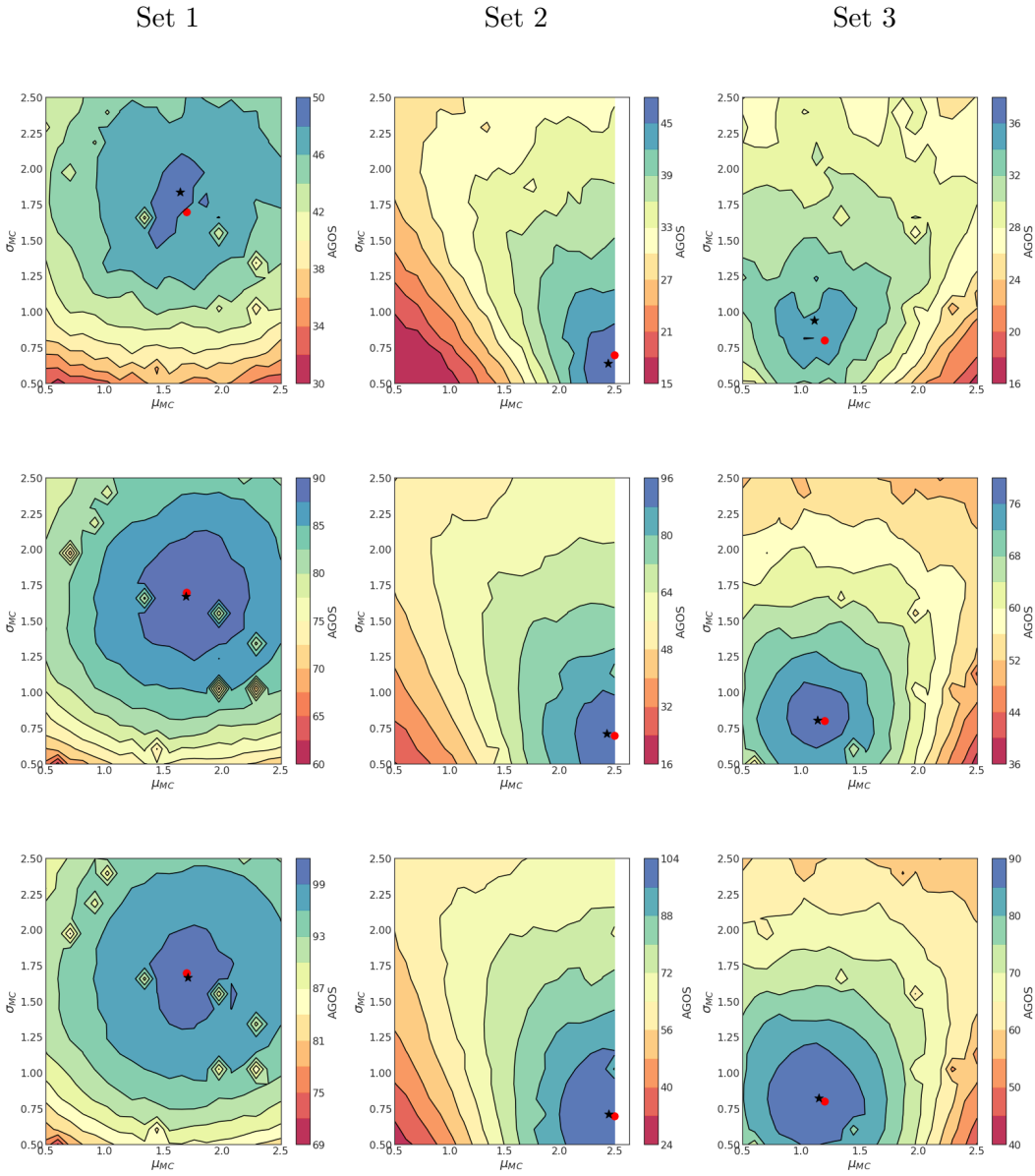

Figure 4.11: AGOS contour plots ($\sigma_{\rm MC}$ vs $\mu_{\rm MC}$) in terms of binary distribution properties without observational selection effects, where Monte Carlo fake systems ($n_{\rm MC} = 10^6$ stars) matched with known "test"sets by the BST-GOS algorithm. Colour red circle point refers to true parameter values and black asterisk the best fit parameter values ($\hat{\Phi}$) corresponding average top 1% of GOS values (Values are given in Table 4.1). The left panels present contours to Set 1, the middle to Set 2 and the right to Set 3. For Set 1, the "test" sample value $n_{\rm T}$ for top, middle and bottom rows are 200, 700 and 1000. For Set 2 and Set 3 the $n_{\rm T}$s are respectively (180, 630, 900) and (120, 420 and 600). The true "test" values $\mu_{\rm T}$, $\sigma_{\rm T}$, $\alpha_{\rm T}$ respectively for test Set 1, Set 2 and Set 3 are (1.7, 1.7, 1.01), (2.4, 0.7, -0.5) and (1.2, 0.8, 0). Note, the diamond shapes in the contours are plotting artifacts.

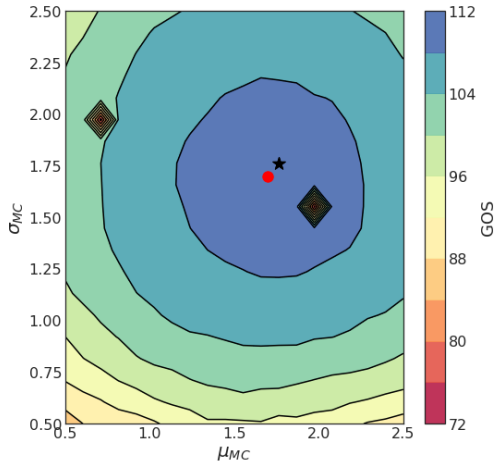

$\alpha_{MC} = 1.01$

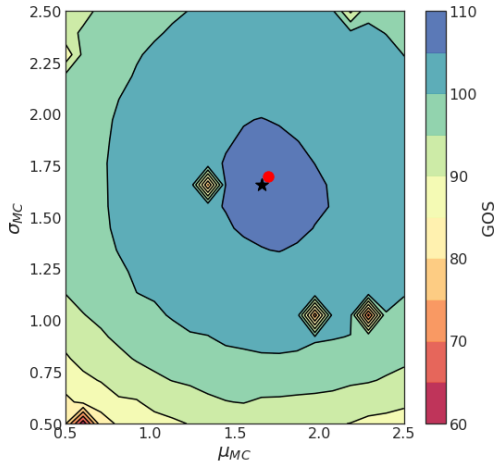

$\alpha_{MC} = 0$

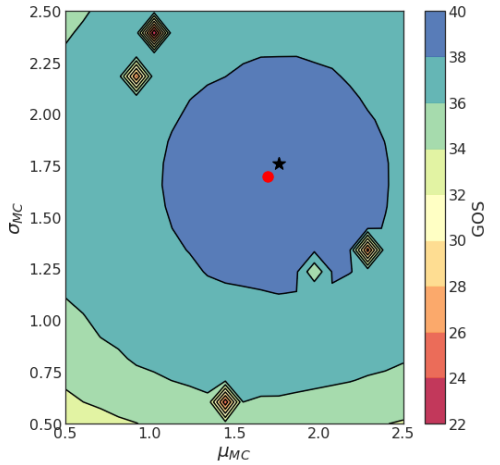

$\alpha_{MC} = -1.01$

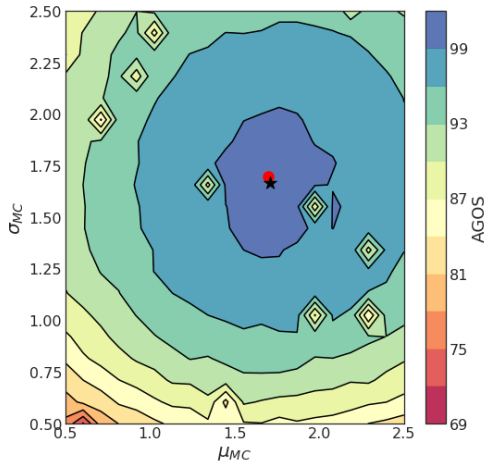

Average over all α_{MC}

Figure 4.12: GOS contour plots (σ_{MC} vs μ_{MC}) in terms of binary distribution properties for $\alpha = (1.01, 0, -1.01)$ and average AGOS of the first three plots (top (left, right) to bottom (left, right)) without selection effects. Colour red circle point refers to true parameter values of μ_T, σ_T. The black asterisk is the top GOS score for each α. The data is generated from Set 1 with $\mathrm{n_T} = 1000$, $\mu_{\mathrm{T}} = 1.7$, $\sigma_{\mathrm{T}} = 1.7$, $\alpha_{\mathrm{T}} = 1.01$. Note, the diamond shapes in the contours are plotting artifacts.

the well performing nature of the GOS function. The true parameters (red dot) also occur in this region.

For Set 2, similar behaviour can be observed, with performance good even for $n_{\mathrm{T}} = 180$ and improving as the sample size increases. Here, the true parameter values are (2.5, 0.7). The best parameter values $(\hat{\mu}, \hat{\sigma})$ for n_{T}=180, 630 and 900 are respectively (2.44, 0.64), (2.43, 0.71) and (2.45, 1.5). The contour plots and the table once again agree.

Finally, for Set 3 (true μ_{T} =1.2, σ_{T} =0.8), largely similar behaviour is observed. The best parameter values $(\hat{\mu}, \hat{\sigma})$ for n_{T}=120, 420 and 600 are respectively (1.11, 0.9), (1.14, 0.8) and (1.15, 0.82). Overall, the performance is still quite strong with the AGOS contours matching the GOS peak.

Table 4.1 shows the outcome from the algorithm is very robust, and all the retrieved values of $\hat{\alpha}$ matched the true "test" values (1.01 for Set 1, -0.3 to -0.5 for Set 2 and 0 for Set 3). In general as n_{T} increases, the top 1% value of GOS also increases.

For completeness, it is also shown how Set 1 varies in its full GOS over each value of α separately. This is illustrated in Figure 4.12. From top (left, right) to bottom (left) we plot the GOS function corresponding to $\alpha = 1.01$, $\alpha = 0$ and $\alpha = -1.01$ for Set 1, $n_{\mathrm{T}} = 1000$, without selection effects. The bottom right plot is the outcome of their average. The red dot represents the true values of $\mu_{\mathrm{T}}, \sigma_{\mathrm{T}}$. The black star now represents just the point in the space with the highest GOS (the peak). For $\alpha = 1.01$, $\alpha = 0$ and $\alpha = -1.01$ the retrieved $\hat{\mu}, \hat{\sigma}$, GOS values are respectively (1.76, 1.76, 110) (1.66, 1.66, 106) and (1.76, 1.76, 39). The GOS value is maximum where α =1.01 (also the true value) and minimum for α =-1.01. Still the peak position is very similar for all the cases around (1.7, 1.7) and they cover the purple region along with the true parameter values. As a result, their average peak remains nearly the same. We can see that as α changes the shape of the function does not drastically change in this instance. This means when the average is taken, the AGOS is a good reflection of the GOS function and the peak will stay fixed in the purple region of highest GOS.

In summary, this BST-GOS algorithm shows very good performance when there are no selection effects present, even for sample sizes as small as 120. the algorithm is able to return the true parameters with a high degree of accuracy. Performance generally decreases as sample sizes are smaller (meaning less binary systems are available to get (q, S) data). Next, the analysis is extended to consider the impacts of selection effects on this performance.

4.4 Retrieving binary parameters when there are selection effects

This section now consider the impact of selection effects. In reality, the possibility of observing a stellar binary depends on a number of criteria such as the detection limits in terms of binary separation and mass ratio. For visual binaries, this depends mainly on four observational selection effects: these are the minimum and maximum magnitude difference and the minimum and maximum angular separation related to the magnitude difference of the binary member stars. The angular separation ρ can be converted to the actual projected separation (S) of binary components, if the distance (d) is known, and the brightness contrast can be transformed as the mass ratio.

Depending on the mass ratio and projected separation members of a binary system can be viewed as a single or double stars. The companions can only be observed if the angular separation between the primary and secondary stars is larger than the angular resolution. When the angular separation is less than the angular resolution of the telescope, the system is observed as one star. At the same time too bright (or massive) a primary star will outshine the secondary star. This is called the brightness constraint.

In this study the joint effect of these two biases is examined to determine whether generated binary stars are visible or not. Stars that are closer together (lower S) will require a comparable luminosity so higher mass ratio (higher secondary mass) to ensure that the secondary star is not dimmed out. Conversely, stars that are further apart can be observed with a lower mass ratio before the second star is very faint and not visible. This relationship is expressed through the observational selection criteria in our model (flow chart of Figure 4.13), which states that a generated binary system is observed within a separation range if it fulfils the following criteria of angular separation of the telescope

$$\rho_{\rm min} < \rho < \rho_{\rm max} \tag{4.44}$$

Where, $\rho_{\rm min}$ or the minimum angular separation depends on the angular resolution of the telescope, $1.22\lambda/D$. Here λ is the wavelength of the light and D is the aperture diameter of the telescope. As λ falls and D becomes higher, the efficiency of detecting close binary systems gets better.

However, for very wide binaries it is difficult to measure $\rho_{\rm max}$. In Chapter 1 it was discussed that it is relatively easy to infer binary companions when they are at close

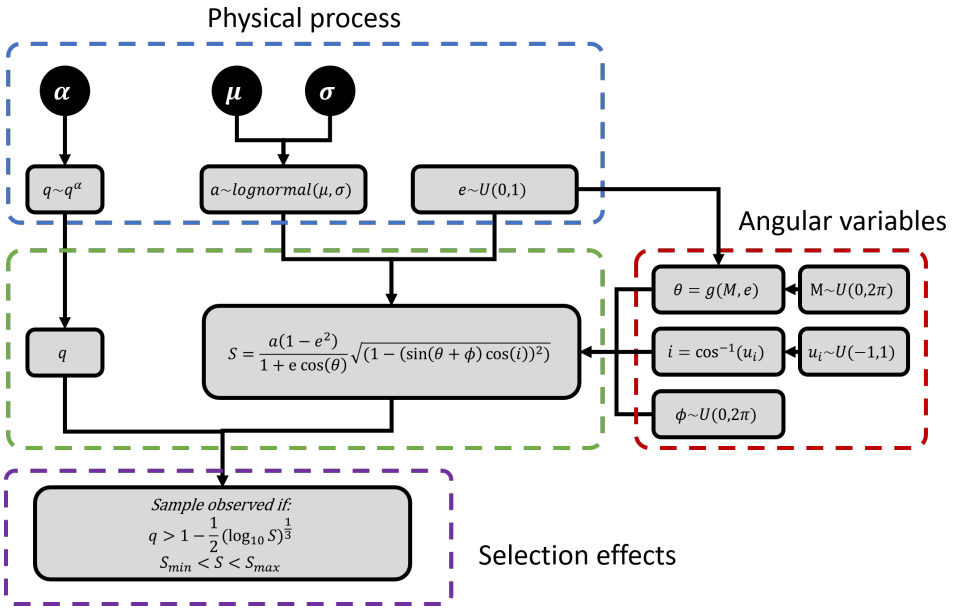

Figure 4.13: Applying observational selection effects to the q, S for each star system.

proximity. When they are further it is not always possible to know whether they are a binary system or two single system stars.

For this simulation, selection separation range $S_{\rm min}$, $S_{\rm max}$ from an observed cluster are assumed to be similar distances from the Earth.

$$S_{\rm min} < S < S_{\rm max} \tag{4.45}$$

Binary observation also requires that the system's separation can also be seen with a selected brightness or mass ratio $q_{\rm vis}$, and as such a "contrast sensitivity" condition is added:

$$q_{\rm vis} > 1 - \frac{1}{2}(\log_{10}(S))^{1/3} \tag{4.46}$$

This is a boundary to the selection limits in Fig. 1 of Caballero-Nieves et al. (2020) assuming a linear conversion from ΔK to q (which is probably not quite correct, but will serve our purpose here in illustrating the effects of realistic $q-S$ selection limits). This is an attempt, based on observational data, to add more realistic selection effects that take into account the q-S bias.

One outstanding question is what selection parameters can be used for ($S_{\rm min}$, $S_{\rm max}$). For this we turn to the literature. Examples of separation (arcsec) and separation ranges (au), and number of multiple systems are studied for nearby young stellar regions and a few prominent examples are King et al. (2012a,b) IC 348: 0.10-8.0 arcsec, 32-2530 AU, 14 (Duchene et al. 1999), Orion Nebula Cluster (ONC): 0.15-1.5

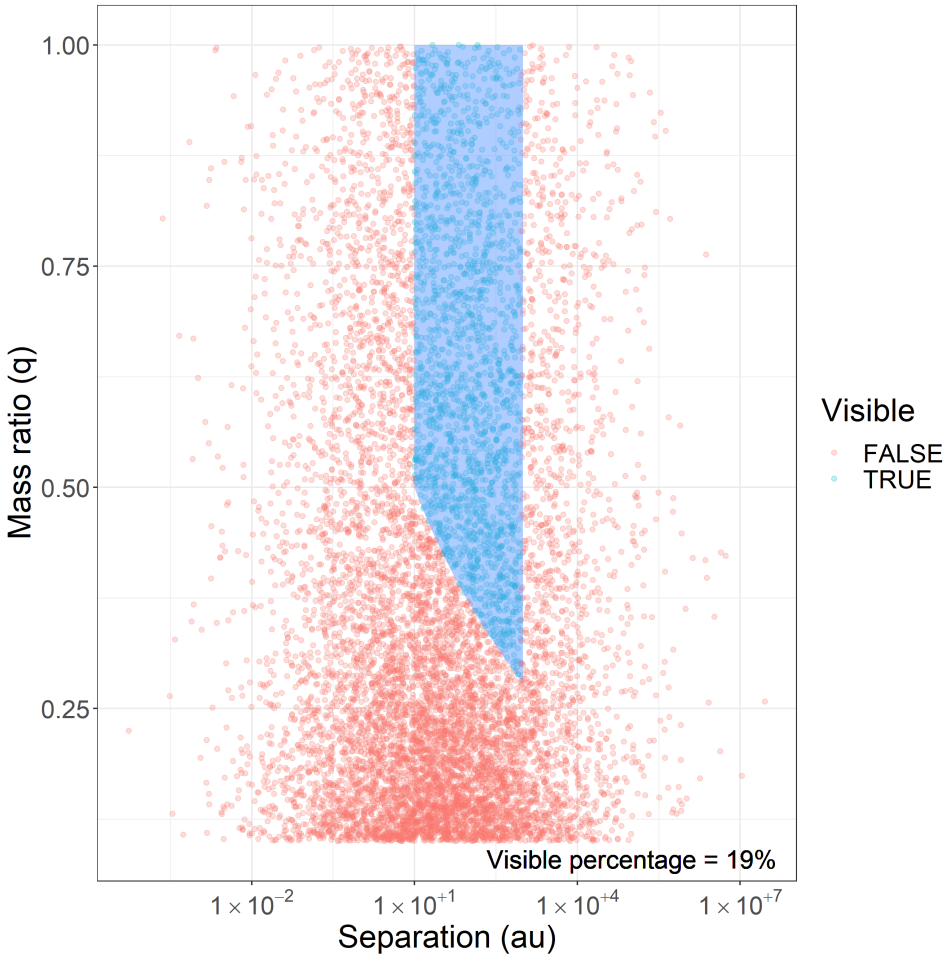

Figure 4.14: (q, S) pairs of a stellar region can only be observed in the blue region. All pairs outside this region are not registered as binary systems.

arcsec, 62-620 AU, 69 (Reipurth, Guimaraes, Connelley & Bally 2007), Chamaeleon I (Cha I):0.1-6 arcsec, 16-960 AU, 36 (Lafreniere et al. 2008) and Corona Australis (CrA): 0.13-6.0 arcsec, 17-774 AU, 19 (Köhler et al. 2008).

Within these separation ranges a binary system can be seen if their mass ratio satisfies Equation 4.46. As an example, consider a generated binary population with 10^5 systems, μ_{T} =1.5, σ_{T} =1.5, α_{T} =-1.01 and a flat eccentricity distribution. Choose minimum selection separation S_{min} and maximum separation S_{max} respectively as 10 and 1000 AU. Fig. 4.14 demonstrates the region where binary systems can be seen (blue) and outside this they are lost. Due to these observational selection effects, a potentially large number of binary systems will remain undetected, severely impacting the (q, S) distribution.

These selection effects exclude a region that is crucial to retrieve the parameter distributions. Observations will only tell us how many binary systems there are in

the blue region. In practice, the observer has no idea what lies outside this region, whether it is empty or full of binary systems. Without this information it is almost impossible to retrieve the whole population's properties only from the observed binary systems.

To illustrate this selection effect in more detail, again in Figure 4.15 consider a "test" set with sample size 1000, $\mu_{\rm T} = 1.7$, $\sigma_{\rm T} = 1.7$, $\alpha_{\rm T} = 0$. In the top panels of Figure 4.15, the distributions of separation and mass ratio before (left) and after (right) selection effects are demonstrated. Without selection effects, all the 1000 binary systems can be seen with a mass ratio starting from 0.1 to 1.0 and separation from 0.01 to 10^5 AU. Once we applied a separation range of $16 - 960$ AU (Lafreniere et al. 2008) and the corresponding mass ratio from Equations 4.46, there are only 210 binary systems left. Therefore instead of 1000 observed binary systems, selection effects reduce it to only 210, giving us much less data to work with. For sample sizes of 200 (of the same set), this same effect can result in effective sample sizes of only around $30 - 40$ stars.

Consider our example again in the top right panel of Fig. 4.15. At minimum separation of 16 AU it is only possible to see from mass ratio 0.6 to 1.0 and at the maximum separation of 960 AU one can only see from 0.45 to 1.0. Therefore, binary systems below these mass ratios have been undetected.

In the bottom left panel, a CDF of projected separations (S) after selection effects (black line) is compared to the full sample (red line). The black CDF is extremely different from the red one. The reason for this is clear - the selection effects on the observed samples truncate the distribution both above and below selection range. The close binaries with a separation less than 16 AU have become undetected as well as wider binaries with more than 960 AU.

The bottom right panel shows the cumulative distribution of mass ratios before (red line) and after selection (black line) effects. Before selection, the ratio (q) is visible from 0.1 to 1.0. After the selection it starts from 0.5 and ends at 1.0. This change to the shape for both (q, S) makes them unrecognisable from the original population. In short, the selection effects hide most of the binary systems in the sample and do not reflect their underlying distribution.

The next section will investigate how heavily selection effects impact the recovery of the parameters Φ.

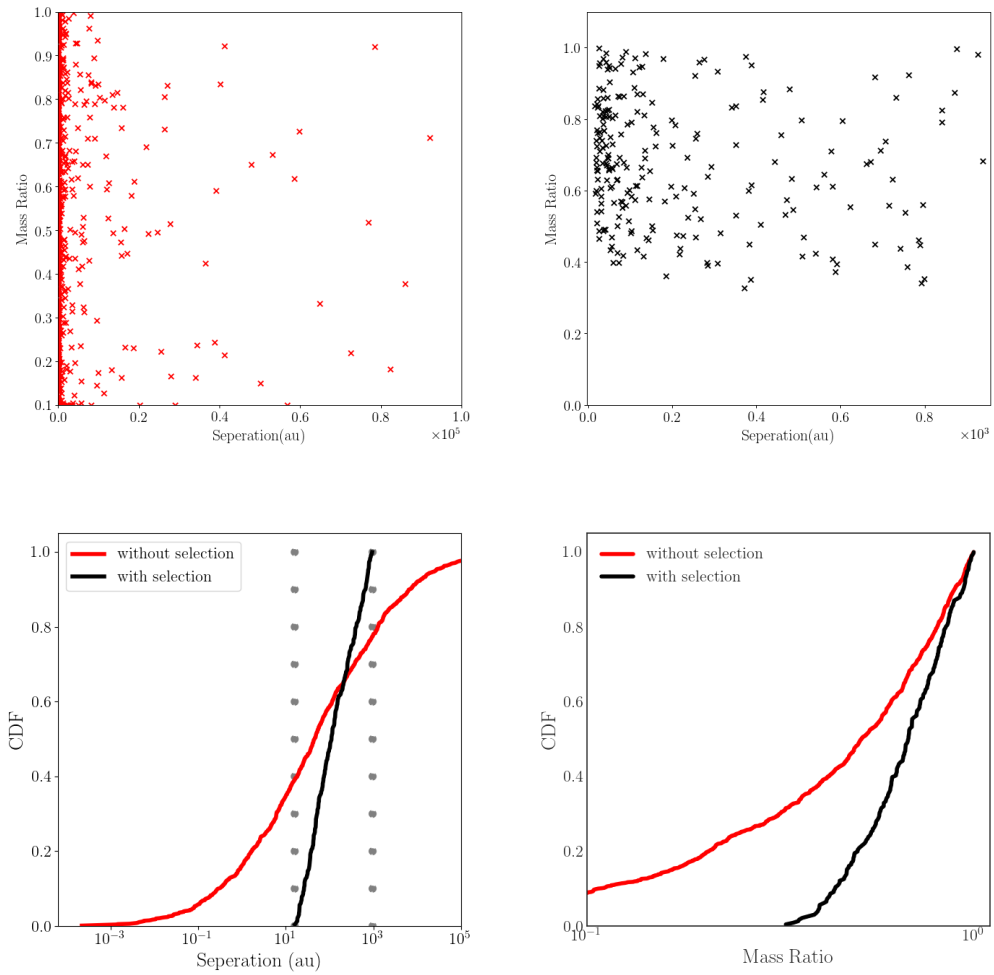

Figure 4.15: The mass ratio and separation distribution shown for test set before (top left) and after selection effects (top right). Bottom (left) shows CDF of the test population separation before (red) and after applying selection condition (black). Bottom (right) shows CDF of their mass ratio before (red) and after applying selection condition (black). Test Set: μ_T =1.7, σ_T =1.7, α_T =0, n_T before selection effects= 1000.

4.4.1 Implementing the algorithm with selection effects

The process in the presence of selection effects is largely similar to the process without, except in both the test dataset and the Monte Carlo datasets, an extra step is added to account for the selection effects. After the initial distribution is generated, the selection criteria are applied as per Equations 4.46 and 4.45. The selection effects can reduce the size of the observed 'test' population dramatically. The process of this flow diagram is presented in Figure 4.16. After passing selection effects, the remaining mass ratio and separation distributions from the "test" and Monte Carlo

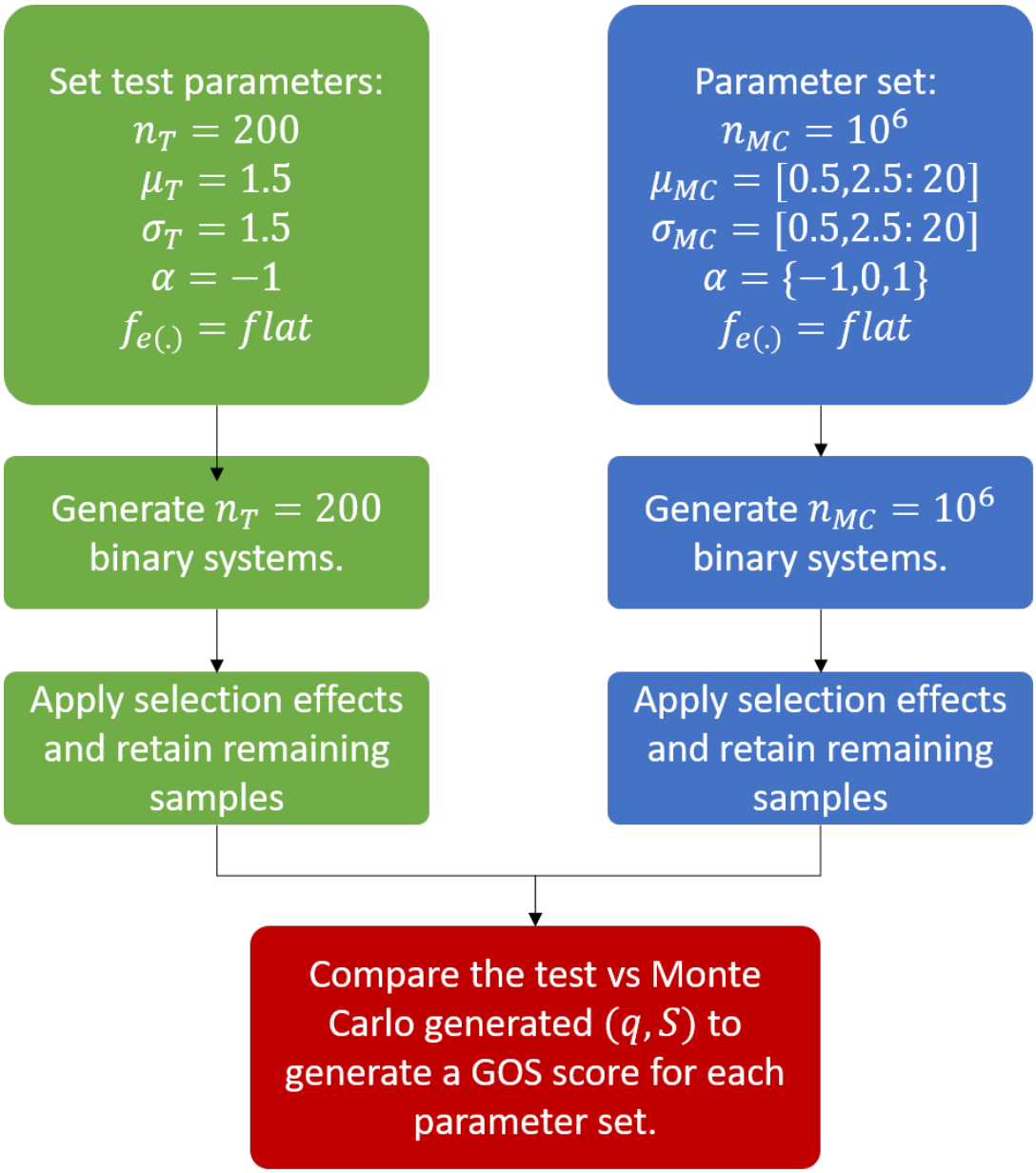

Figure 4.16: Flow chart detailing the simulation process (with observational selection effects)

datasets will be used in the BST algorithm to establish Goodness of Split for all parameter pairs.

In this work with observational selection effects, the separation range will be kept to the empirically reported ranges as mentioned in the beginning of section 3. All other aspects of the method are identical to the previous section, with the underlying binary parameters kept the same. The nine "test" set samples are used with following parameters:

- Set 4: $\mu_{\mathrm{T}} = 1.7$, $\sigma_{\mathrm{T}} = 1.7$, $\alpha_{\mathrm{T}} = 1.01$, $\mathrm{n_T} = 48$, 171, 244 observed after (200, 700, 1000) samples go through separation range of Chamaeleon I, 16-960 au (Lafreniere et al. 2008).

- Set 5: $\mu_{\mathrm{T}} = 2.5$, $\sigma_{\mathrm{T}} = 0.7$, $\alpha_{\mathrm{T}} = -0.5$, $\mathrm{n_T} = 36$, 113, 167 observed after (180, 630, 900) "test" samples pass separation range of Orion Nebula Cluster, 62-620 AU (Reipurth, Guimaraes, Connelley & Bally 2007).

- Set 6: $\mu_{\mathrm{T}} = 1.2$, $\sigma_{\mathrm{T}} = 0.8$, $\alpha_{\mathrm{T}} = 0$, $\mathrm{n_T} = 26$, 92, 123 observed after 120, 420, 600 go through separation range of IC 348, 32-2530 AU (Duchene et al. 1999).

Note, all these separation ranges along with contrast sensitivity (Equation 4.46) are taken from widely used general observations which does not include advanced techniques such as Adaptive Optics and interferometers. Section 4.4.2.2 will show how the BST-GOS method might perform if samples are taken with the mitigated selection effects one might expect from advanced observational technique surveys.

For each of the test sets $1,200$ Monte Carlo distributions will also be generated. The parameter estimate $\hat{\Phi}$ is calculated as per the previous method, and the visualisation will be done using the AGOS function over averaging out α.

4.4.2 Results in the presence of selection effects

As in the previous section, our results are reported in Table 4.2 and the contour plots, Fig. 4.17. The true parameters $(\mu_{\mathrm{T}}, \sigma_{\mathrm{T}})$ are shown by the red circle and the top 1% percentile average by black asterisk $(\hat{\Phi})$. The Purple regions of these contour plots represent the highest (average) Goodness of Split scores. Unlike Fig. 4.11, the first thing to note is that the results appear to be worse: the estimated parameters seem to drift quite far from the true values.

Let us review the results in brief. On a set by set basis, beginning with Set 4 (μ_{T}=1.7, σ_{T}=1.7, α_{T}=1.01), in Fig. 4.17 it can be seen that for $\mathrm{n_T} = 48$ the performance is poor. The individual parameter estimates $\hat{\Phi}$ $(\hat{\mu}, \hat{\sigma}, \hat{\alpha})$ from sub-table

Sub-Table 2.a: Set 4

	n_T	μ	σ	α	GOS
True	-	*1.7*	*1.7*	*1.01*	-
top	48	1.85	2.12	1.01	27
middle	171	1.31	2.14	1.01	63
bottom	244	1.5	2.23	1.01	74

Sub-Table 2.b: Set 5

	n_T	μ	σ	α	GOS
True	-	*2.5*	*0.7*	*-0.5*	-
top	36	1.27	1.2	-1.01	20
middle	113	2.4	0.86	-0.08	58
bottom	167	2.46	0.75	-0.08	70

Sub-Table 2.c: Set 6

	n_T	μ	σ	α	GOS
True	-	*1.2*	*0.8*	*0*	-
top	26	0.92	0.65	-0.6	12
middle	92	1.16	0.77	0	40
bottom	123	1.06	0.75	0	41

Table 4.2: $\hat{\Phi}$ $(\hat{\mu}, \hat{\sigma}, \hat{\alpha})$ based on top 1% of GOS score) and GOS of Set 4 (Sub-Table 2.a), Set 5 (Sub-Table 2.b) and Set 6 (Sub-Table 2.c) with selection effects. The row captioned "True" refers to the true parameter values of each set. n_T refers to the effective sample size (after selection effects are applied to the set).

4.2a are respectively (1.85, 2.12, 1.01). From Table 4.2 it can be seen that as n_T grows, the retrieved values of $\hat{\Phi}$ $(\hat{\mu}, \hat{\sigma}, \hat{\alpha})$ for 171 are (1.31, 2.14, 1.01) and then for 244 (1.5, 2.23, 1.01). Except the $\hat{\alpha}$, the other values are different from the true values.

Compare the retrieved values of with $n_T = 244$ with those of Set 1 without selection effects, where $n_T = 200$. For the same true parameters those values are 1.64, 1.83 and 1.01 (sub-table 4.1a). Therefore, selection effects prevent us from retrieving the true parameters effectively despite having the same underlying parameters.

We see a very similar story for Set 5 (μ_T=2.5, σ_T=0.7, α_T=-0.5). For $n_T = 36$ the retrieved parameters are far from true values (sub- table 4.2b). The best parameter

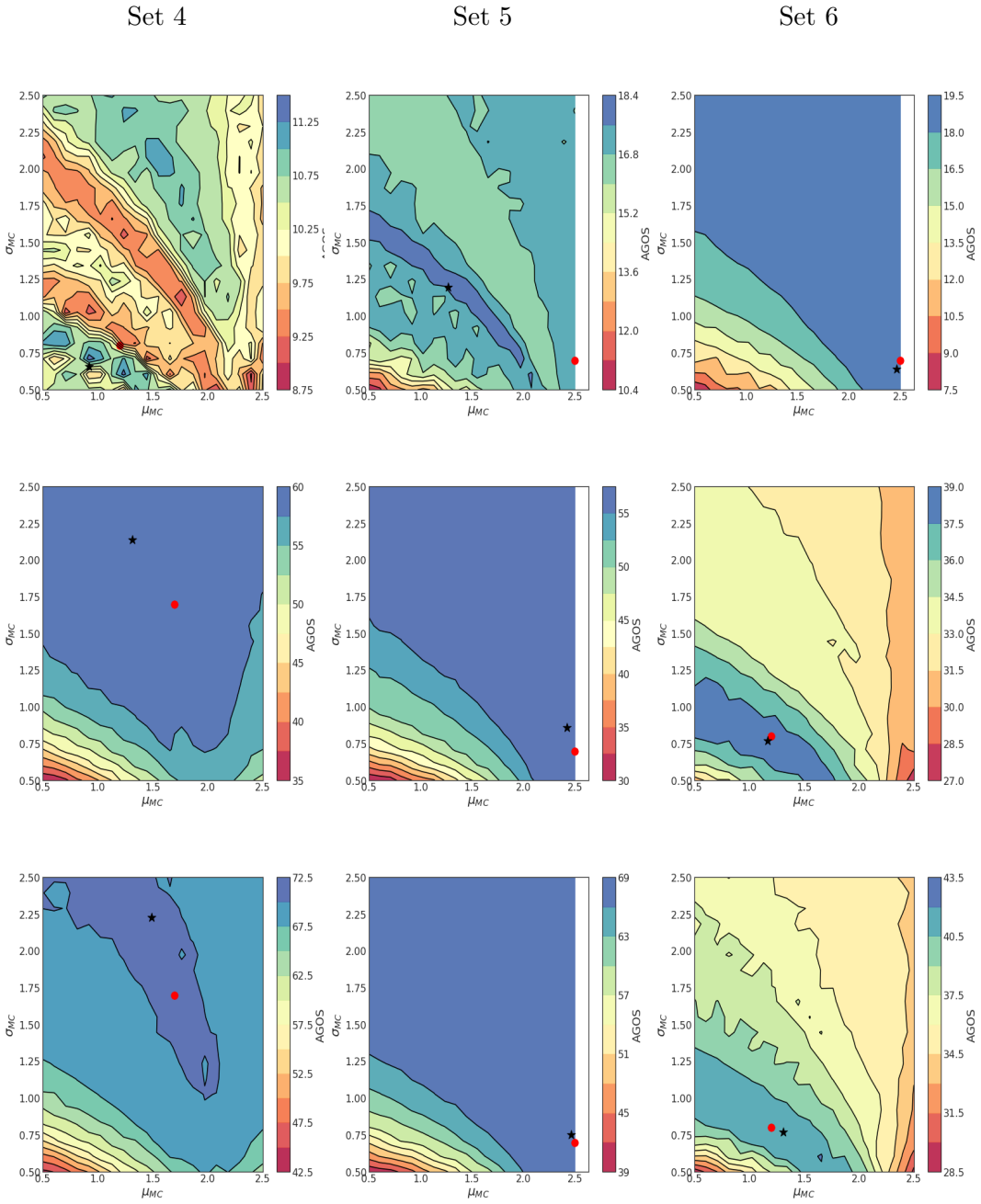

Figure 4.17: AGOS contour plots ($\sigma_{\rm MC}$ vs $\mu_{\rm MC}$) with observational selection process, where Monte Carlo fake systems ($n_{\rm MC} = 10^6$ stars) matched with known "test" sets by Binary Search Tree. Red points refers to the true parameter values and the black asterisk ($\hat{\Phi}$) corresponding top 1% of GOS value (values are given in Table 4.2). The left plots refers to Set 4, middle Set 5 and right Set 6. For Set 4, the "test" sample value $n_{\rm T}$ for top, middle and bottom rows are respectively 48, 171 and 244. For Set 5 and Set 6 the $n_{\rm T}$s are respectively (36, 113, 167) and (26, 92 and 123). The true "test" values $\mu_{\rm T}$, $\sigma_{\rm T}$, $\alpha_{\rm T}$ and binary separation range respectively for test Set 4, Set 5 and Set 6 are (1.7, 1.7, 1.01, 16-960 AU), (2.5, 0.7, -0.5, 62-620 AU) and (1.2, 0.8, 0, 32-2530 AU).

values $\hat{\Phi}$ for n_{T}=36, 113 and 167 are respectively (1.27, 1.2, -1.01), (2.4, 0.86, -0.08) and (2.46, 0.75, -0.08). The values of $(\hat{\mu}, \hat{\sigma})$ are better when n_{T} grows.

For Set 6 (μ_{T} =1.2, σ_{T} =0.8, α_{T}=0) however, quite an interesting picture can be seen. From sub-table 4.2c, we can see the estimated parameter values $\hat{\Phi}$ for $\mathrm{n_T}$=26, 92 and 123 are respectively (0.92, 0.65,-0.6), (1.16, 0.77, 0) and (1.06, 0.75, 0). The values are quite close to the true values especially for sample size 92 and 123 even the effective sample sizes are small. Most importantly, the success is not a one-off coincidence, as it is maintained for both of the larger samples. The success of this example is being investigated alongside the failure of the others in the next subsection.

4.4.2.1 Analysis of performance impacts due to selection effects

For Sets 4 and 5 it was shown the performance was quite poor. There are two most likely hypotheses to see such a reduction in performance. The first hypothesis is that sample size plays a small role. Even when the initial sample sizes are quite large, the *effective* sample size changes drastically with selection effects. Since so many stars are filtered out, only a small sample is left from the original set.

However this is clearly not enough to explain the full difference in performance. To see this notice that even for same true parameters (μ_{T}= 1.7, σ_{T}= 1.7, α_{T}= 0) when the effective sample size is filtered to 244, (sub-table 4.2a) the retrieving performance was still worse ($\hat{\mu}$ = 0.9, $\hat{\sigma}$= 2.0, $\hat{\alpha}$= 0) than those of Set 1 without selection effects where $\mathrm{n_T}$ = 200 ($\hat{\mu}$ = 1.6, $\hat{\sigma}$= 1.86, $\hat{\alpha}$= 0) (sub-table 4.1a). That is to say, for the given set of parameters in Set 4, the reduction in sample size did not really explain the lack of performance.

To see the biggest contributor to performance inefficiency, recall that the GOS method as described works by looking at the similarity in distribution between two samples, and how much they have similar concentration in different cells across the (q, S) space. However now that the distributions has been truncated, it could be the case that parts of the (q, S) space which clearly differentiate the distributions of two different potential parameter sets are now unavailable for comparison, meaning that poor fits can be given a high Goodness of Split.

In Fig. 4.15 it has been shown the distributions of separation and mass ratio before and after selection effects. Without detection limits, one can see all the binary systems no matter what are their mass ratio and separation distributions are. When the selection effects are applied, one is left with fewer binary systems. The observed samples do not represent their underlying distribution.

It seems that parameters like μ, σ and α influence the head and tails of the

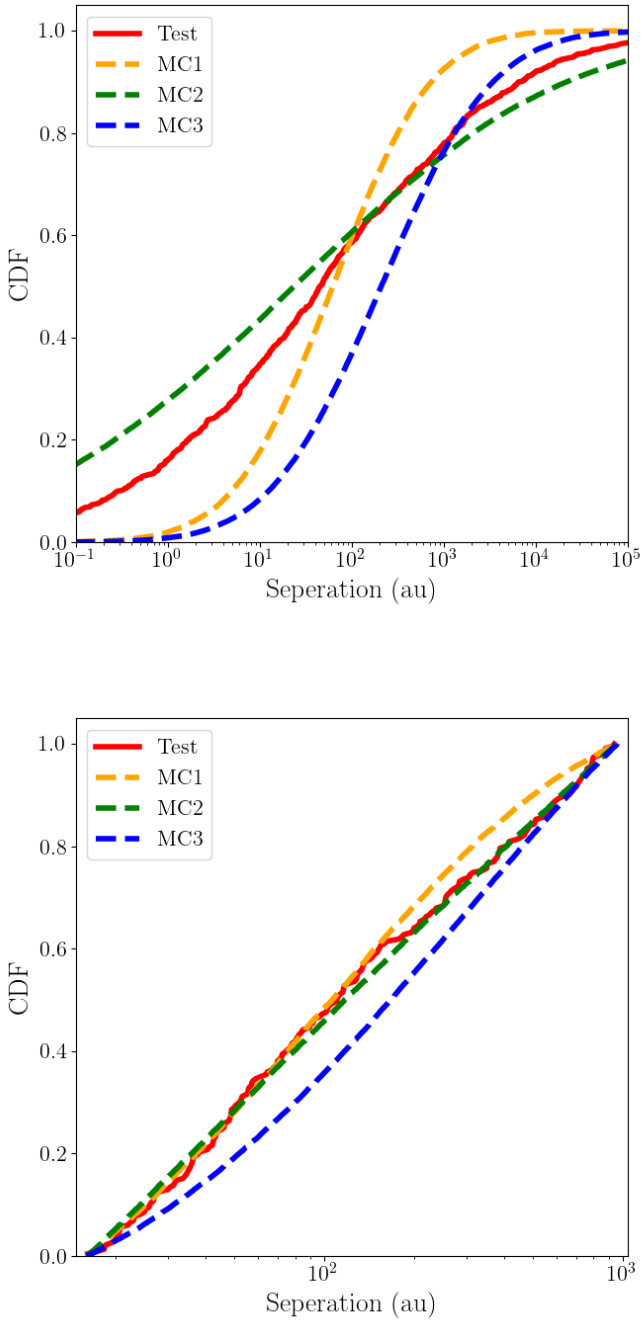

Figure 4.18: Three Monte Carlo populations are illustrated (MC1-orange, MC2-green, MC3-blue), where all three achieved the same GOS of 60.25 against a single test set. The top panel shows their full distribution over S. The bottom panel shows the S distribution after the selection effects. Test Set: $\mu_{\rm T} = 1.7$, $\sigma_{\rm T} = 1.7$, $\alpha_{\rm T} = 0$, $n_{\rm T}$= 1000. MC populations had a sample size of $n_{\rm MC}$= 10^5. Parameters $\mu_{\rm MC}$, $\sigma_{\rm MC}$ and $\alpha_{\rm MC}$ for MC1, MC2 and MC3 are respectively (1.86, 0.81, 0), (1.44, 2.28, 1) and (2.39, 0.92, 0).

distributions, and since they are truncated the differentiation between them is gone. Without them, as mentioned, vastly different samples may have the same Goodness of Split with our "test" data set.

As an example, in the top panel of Fig. 4.18 we plot the pre-selection separation distributions of 3 Monte Carlo populations (MC1 - orange, MC2 -green, MC3- blue) alongside the test data set (red). They are clearly all quite different from the test data set. The initial values of $\mu_{\rm MC}$, $\sigma_{\rm MC}$ and $\alpha_{\rm MC}$ for MC1, MC2 and MC3 are respectively (1.86, 0.81, 0), (1.44, 2.28, 1) and (2.39, 0.92, 0). None of their parameters match the true "test" population.

The bottom panel shows the same distributions after selection effects ($10 - 1000$ AU and eq. 4.46) are applied. It can be seen that they are all now much closer to the test data set and to each other. In fact, all three distributions achieved the same GOS score (60.25) against the "test" population, meaning that the algorithm will attempt to rank all these as good fits when it is known they are not.

As a result, even if the sample size gets large, under the truncation of sufficiently strong selection effects, it is impossible to retrieve the true parameters as the distribution is just too heavily distorted.

This intuition can be used to see why the results of Set 6 were so strong. Recall that for Set 6, we applied the selection effects of IC 348: 32-2530 AU. This results in the widest observable window of binary pairs (compared to the other sets). Furthermore, the distribution (q, S) itself has the narrowest variation for the S value, since $\sigma = 0.8$ was the lowest out of all the sets, squeezing the distribution into a range that fits within the observable window.

The net result of this is that the distribution of the binary separations is relatively well-maintained, and not too much of the distribution is truncated in a way that would distort its shape. Note this is not the same as saying that the sample was not heavily filtered: we still went from i.e. 600 binary pairs to only 123 in the largest sample. What this is saying is that within the remaining samples, the *shape* of the distribution was relatively well-maintained, and in regions where the shape allowed us the sufficiently distinguish it from other possible distributions. Furthermore, since $\alpha = 0$, the mass ratios were uniformly distributed, meaning every slice of the distribution was identically distributed.

Putting these together it can be seen that not only were the selection effects allowing for the widest window, but the underlying (q, S) distribution had a shape that was well distributed within the available window. This means that the distribution was not drastically altered in shape when it was truncated, and our BST-GOS algorithm was able to successfully match it to the correct Monte Carlo populations.

Comparing the results from Sets 4, 5 and 6, an interesting conclusion emerges. Firstly, selection effects can severely truncate the distribution of observable binary systems, and this undermines our ability to run any kind of analysis that relies on an accurate understanding of the full shape of the distribution.

However, there are two mitigating factors. One is self-evident: the less severe the selection effects, the less the distributional shape changes and the better our comparison algorithms work. The other is less immediately obvious: the shape of the underlying distribution also makes a big difference, as it can mean the shape of the distribution is preserved in whatever window is available. This can be true even if the sample sizes are heavily reduced.

In short, while our algorithm works best without selection effects as it can make use of the full shape of the (q, S) distribution, it will still work well for even quite heavily filtered samples so long as not too much of the shape is lost.

4.4.2.2 Effectiveness of the method under improved observation technologies

In the previous section, the BST-GOS method was implemented using selection effects that are widely found from general observational techniques. We can see the impact of selection effects are very strong on our resulting parameter estimates, but the effect is lessened for samples where the selection effects were not so severe.

This raises the important question of how much one can expect the method to work if we can reduce the selection effects in observed data. In this section, instead of using general observation techniques, we consider more advanced techniques available such as Adaptive Optics, interferometry etc. They are not used as frequently due to resource limitations, but provide an upper bound of how much these selection effects can be mitigated, and therefore how much better the BST-GOS method could perform in principle. We consider the effectiveness of the algorithm both in the scenario where the best cutting-edge techniques are used, as well as considering further improvements that could be available in the near future.

To minimise selection effects, one must consider technologies to detect close and wide binary systems as well as faint members with high contrast sensitivity. For close binary members we will need higher angular resolution techniques achieved via arrays of telescopes (optical or infrared) also known as astronomical interferometers (such as VLT, KECK etc). Interferometers, Common proper motion, wide field Adaptive Optics (AO) are different ways to resolve large separated binaries.

Interferometry itself is not efficient enough to increase contrast sensitivities of

faint binary members. AO imaging is a solution to this problem as they operate in near infra-red wave length ranges (K contrast ratio is much less than V band). Interferometry combining with AO imaging is an efficient technique to minimise the selection effects allowing separation range 1 to many thousands of AU (Adam 2017, Duchêne et al. 2013, Raghavan et al. 2010, Ward-Duong et al. 2015). In some cases they can even detect extreme mass ratio companions with $q < 0.1$ (De Rosa et al. 2014, Adam 2017).

For example without AO correction, the resolution of interferometer telescopes like VLT or Keck can be 1 arcsec while with AO it can be 10-20 mas (Hippler 2019). Therefore, they can add a significant number of close binary systems in the survey.

There are many types of AO facilities, such as single conjugate AO (SCAO) and multi-object adaptive optics (MOAO) systems. At present the MOAO corrected system allows a maximum separation of about 3.5 arcmin, which in the near future is planned to achieve separation from 5 to 10 arcmin (Hippler 2019).

In near future we are going to have next generation adaptive optics imaging and interferometry technique for both space and ground based telescopes. Besides the ground telescopes, the future large space telescopes are also planned to be equipped with AO to detect extremely high contrast faint binary objects (Sun et al. 2020).

Besides AO there are also method like aperture masking interferometry (AMI) which also helps to increase contrast sensitivities. For example, the James Webb Space telescope with its AMI feature will provide high resolution and contrast sensitivity up to $\sim 10^{-4}$ facilitating detecting many faint binary components (JWST-User-Documentation 2016).

In this section, two examples of improved minimum and maximum separations from the literature are used. For each of these, the BST-GOS method is applied to see whether the test parameters can be recovered with better observational techniques:

- Raghavan et al. (2010), presented a survey of 454 solar types of stars within 25 pc using interferometry and common proper motion method. Moe & Di Stefano (2017) converted the binary orbital period of the binary systems to separations which range from 1 to 30,000 AU. This separation limit is used for Case 1 below.

- Ward-Duong et al. (2015) conducted the M-dwarfs in Multiples (MINMS) survey using multiple AO and wide-field epochs within 15 pc and found large multiplicity samples covering separation range of ~ 0.1 arcsec to ~ 10 arcmin (i.e. 3 AU to 10,000 AU). This separation limit is used for Case 2 below.

To include contrast sensitivity, instead of Equation 4.46, we make use of boundaries to the selection limits as in Fig.4.19 from Ward-Duong et al. (2015). The Figure

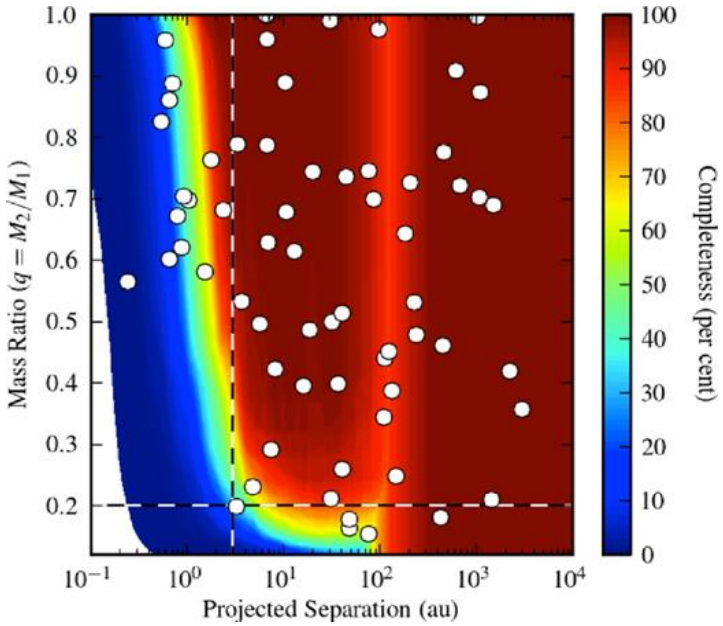

Figure 4.19: The completeness of the MINMS survey, in terms of the mass ratio. The horizontal dashed line at $q = 0.2$ is the mass ratio limit for uniform completeness, while the vertical dashed line indicates the minimum separation limit of 3 AU used to assess population statistics (Ward-Duong et al. 2015).

shows visibility for different completeness limits of the mass ratio and projected separation distributions. The survey was based on a total of 47 AO-detected and 20 wide-field-detected binary systems, and the completeness limit of the survey was high $> 95\%$.

When modelling the "current" advanced techniques, it is assumed the contrast sensitivity boundary occurs for the 90% completeness limit. That is, from Figure 4.19, we use only the region of the (q, S) distribution where completeness was above 90%. This contour can be measured from the Figure itself, and it can be fit to the following equation:

$$q_{\rm vis} > 1.54(S)^{-1.81} + 0.11 \tag{4.47}$$

To model near future advanced observational techniques, we assume the contrast sensitivity boundary occurs at the 40% completeness limit. That is, from Figure 4.19, we use only the region of the (q, S) distribution where completeness was above 40%. This contour again can be measured from the Figure itself, and it can be fit to the following equation:

$$q_{\rm vis} > 0.53(S)^{-1.37} \tag{4.48}$$

The two possible boundaries are used in each of the Cases, to model both the current and the near future scenarios.

Case 1 ("Set 7")

For Case 1, the parameter set corresponding to Sets 1 and 4 are taken for consistency ($\mu_{\rm T} = 1.7$, $\sigma_{\rm T} = 1.7$, $\alpha_{\rm T} = 1.01$). A medium sample of size 700 binaries is taken, but now passed through the selection range of $S_{min} = 1$ and $S_{max} = 30000$ AU, as per Raghavan et al. (2010). Initially, the "cutting edge" contrast sensitivity boundary of 90% is taken (as captured by Equation 4.47).

Fig. 4.20 top left panel shows retrieved parameters ($\mu_{\rm MC}$ vs $\sigma_{\rm MC}$) when better observation techniques are used. Out of 700 systems, 535 were left after passing the selection barrier.

The purple regions of these contour plots represent the highest (average) Goodness of Split scores. $(\mu_{\rm T}, \sigma_{\rm T})$ are also included as the true parameters (red circle) and the $\hat{\Phi}$ (black asterisk). The peak in the AGOS scores match the peak of the GOS scores as shown by $\hat{\Phi}$, indicating that the GOS function is performing well. The true test values are very close to retrieved values.

Table 4.3a shows that after using BST-GOS method the retrieved parameters ($\mu_{\rm MC}$, $\sigma_{\rm MC}$ and $\alpha_{\rm MC}$, gos) are (1.61, 1.78,1.01, 89.35).

For near future surveys with advanced technology telescopes such as JWST, the selection effects could be minimised more (Hippler 2019, Sun et al. 2020, JWST-User-Documentation 2016). For those scenerios, we keep all other parameters and selection limits as is, but model the constrast sensitivity for the 40% completeness limit, as per Equation 4.48. From a total of 700 systems, 565 left, showing a very mild improvement. The bottom left panel of Fig. 4.20 shows the resulting AGOS across the Monte Carlo parameter space.

The bottom row of Table 4.3a shows the retrieved parameters improve very slightly for the improved constrast sensitivity. For ($\mu_{\rm MC}$, $\sigma_{\rm MC}$ and $\alpha_{\rm MC}$, gos) the values are (1.64, 1.7, 1.01, 91).

The retrieved values for both contrast sensitivity examples are *slightly* less accurate than found in sub-table 4.1a where there are no selection effects and the test parameters are the same (specifically the second row, where a sample size of 700 was also taken). However, it is a marked improvement over the corresponding set in sub-table 4.2a where the selection effects due to general observational techniques were considered. High accuracy observational techniques massively improved the accuracy of the BST-GOS method in this case.

Case 2 ("Set 8"):

A second case is considered for generality. For Case 2, the parameter set corre-

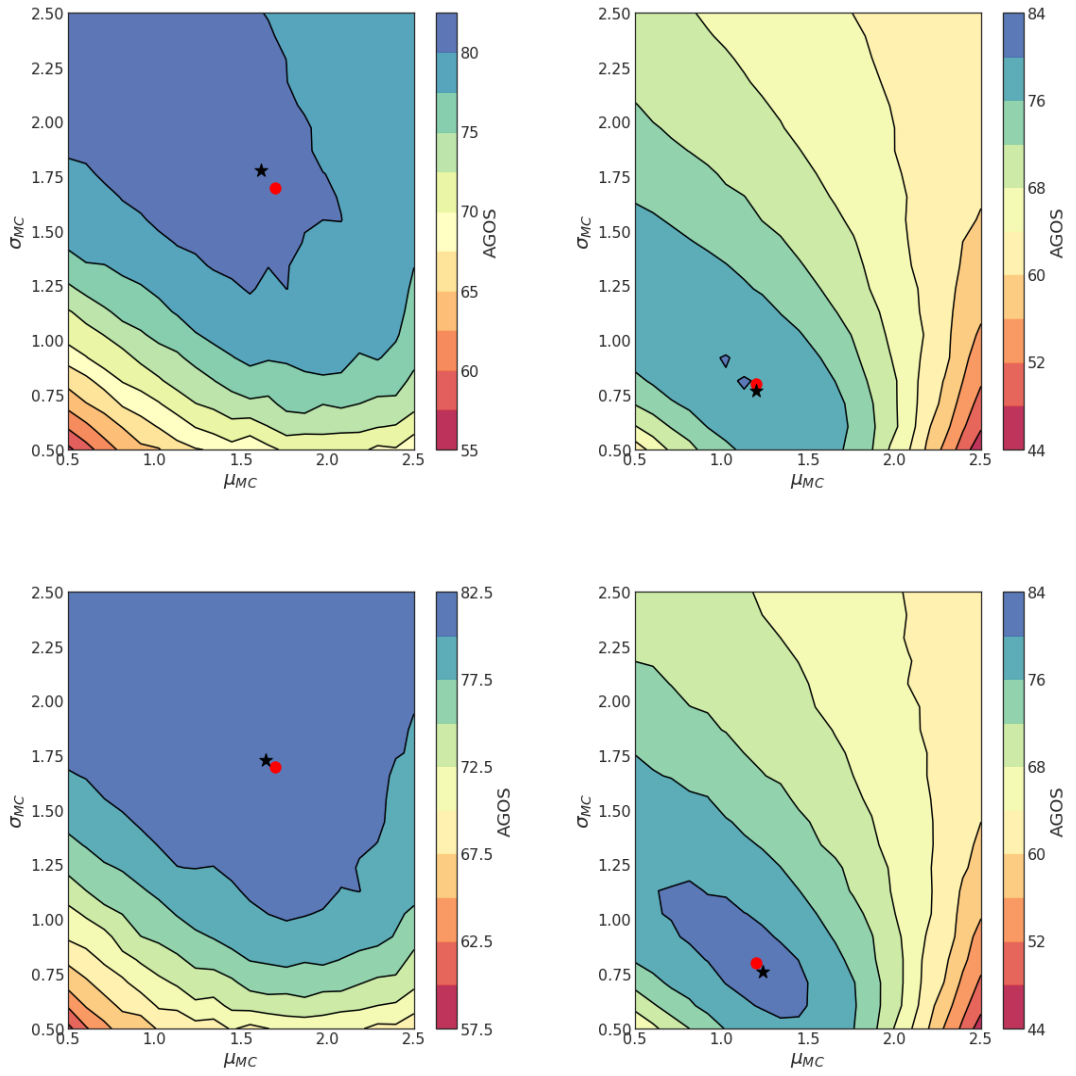

Figure 4.20: AGOS contour plots ($\sigma_{\rm MC}$ vs $\mu_{\rm MC}$) with observational selection process, where Monte Carlo fake systems ($n_{\rm MC} = 10^6$ stars) matched with known "test" sets by Binary Search Tree. Red points refers to the true parameter values and the black asterisk ($\hat{\Phi}$) corresponding top 1% of GOS value (values are given in Table 4.2). The left plots refers to Set 7 wit $n_{\rm T}$ =171 and right Set 8 with $n_{\rm T}$ =123. The "test" values $\mu_{\rm T}$, $\sigma_{\rm T}$, $\alpha_{\rm T}$ and binary separation range respectively for test Set 7 and Set 8 are (1.7, 1.7, 1.01, 1-30000 AU) and (1.2, 0.8, 0, 3-10000 AU). The top plots refer to contrast sensitivity using equation 4.47 for current interferometry and AO imaging technology. The bottom plots refer to contrast sensitivity using equation 4.48 for near future advanced telescopes such as JWST.

Sub-Table 3.a: Set 7

	n_T	μ	σ	α	GOS
True	-	*1.7*	*1.7*	*1.01*	-
top (eq.4.47)	535	1.61	1.78	1.01	89.35
bottom (eq.4.48)	565	1.64	1.7	1.01	91

Sub-Table 3.b: Set 8

	n_T	μ	σ	α	GOS
True	-	*1.2*	*0.8*	*0*	-
top (eq.4.47)	448	1.2	0.77	0	83.15
bottom (eq.4.48)	471	1.2	0.76	0	85

Table 4.3: $\hat{\Phi}$ $(\hat{\mu}, \hat{\sigma}, \hat{\alpha})$ based on top 1% of GOS score) and GOS of Set 7 and Set 8 with selection effects. The row captioned "True" refers to the true parameter values of each set. n_T refers to the effective sample size (after selection effects are applied to the set). The "test" values μ_T, σ_T, α_T and binary separation range respectively for test Set 7 and Set 8 are (1.7, 1.7, 1.01, 1-30000 AU) and (1.2, 0.8, 0, 3-10000 AU).

sponding to Sets 3 and 6 are taken for consistency ($\mu_T = 1.2$, $\sigma_T = 0.8$, $\alpha_T = 0$). A medium sample of size 600 binaries is taken, but now passed through the selection range of $S_{min} = 3$ and $S_{max} = 10000$ AU, as per Ward-Duong et al. (2015). As before, initially, the "cutting edge" contrast sensitivity boundary of 90% is taken (as captured by Equation 4.47).

The top right panel of Fig. 4.20 shows μ_{MC} vs σ_{MC} plots of retrieved parameters under these selection limits. The top row of Table 4.3b shows the retrieved parameters (μ_{MC}, σ_{MC} and α_{MC}, gos) are (1.2, 0.77, 0, 83.15). Out of 600 initial binary systems, 448 are retained after selection effects.

As before, initially, the "near future" contrast sensitivity boundary of 40% is also considered (as captured by Equation 4.48). The bottom right panel shows the plot under these limits. Table 4.3b shows retrieved parameters (μ_{MC}, σ_{MC} and α_{MC}, GOS) with 4.48 are respectively (1.2, 0.76, 0, 85). This selection barrier managed to keep 471 systems from 600, which is again a very mild improvement over the previous contrast sensitivity, but the parameter estimates are very mildly worse (though the difference is negligible).

As in the previous case, the retrieved values for both contrast sensitivity examples have almost exactly the same performance as under the corresponding parameter set

with no selection effects (4.1c, third row). However, again it is a much more noticeable improvement over the corresponding set in sub-table 4.2c (third row) where the selection effects due to general observational techniques were considered. High accuracy observational techniques also improved the accuracy of the BST-GOS method in this case.

In general, therefore, the use of high accuracy observation techniques with the BST-GOS helped demonstrate the following:

- Reducing, but not eliminating, selection effects through the use of high accuracy methods drastically improves the effectiveness of the BST-GOS method to retrieve the true parameters of the binary distribution.
- Improvements in the constrast sensitivity did not seem to deliver as much improvement in the accuracy over and above what was achievable by widening the selection limits.

4.5 Conclusions and Future Work

This chapter focused on studying the impact of observational selection effects on retrieving details of a stellar population's characteristics. A method was developed that used instantaneous stellar data in order to reconstruct the true initial parameters.

This began with first derived the equations that underpin the distribution of mass ratios and separations. This allowed one to simulate binary stellar clusters using a Monte Carlo method. The method began with four parameters (α, μ, σ, f_e), but the analysis was able to show that f_e does not affect the distribution distinctly enough to discriminate between values, so the remainder of the analysis kept it fixed as flat. A method was then introduced to retrieve the true parameters (the BST-GOS algorithm), which compares "test" sample distributions to Monte Carlo distributions, and uses their similarity (measured by Goodness of Split, GOS) to find well performing parameter estimates.

The efficacy of the method on data was shown when selection effects were absent. It was able to retrieve true parameters with high accuracy even with small sample sizes. Selection effects were then introduced to the process, and it was shown that the performance decays considerably if the selection effects truncate parts of the distribution that are required to reliably distinguish it from other distributions. Performance of the algorithm improve when selection effects are mitigated and/or the distribution covers regions that overlap with the selection windows. Most significantly, the performance improved drastically when selection windows available from

$S_{\min}$	$S_{\max}$	n_T	(Other selection parameters)	se_μ	se_σ	se_α
20	500	50	...	± 0.3	± 0.6	± 0.5
20	500	100	...	± 0.1	± 0.3	± 0.5
...	.....	...	...	...		
100	5000	2000	...	± 0.5	± 0.8	± 0.05

Table 4.4: Future work could attempt to estimate confidence intervals for parameter estimates for different levels of selection effects. *se* refers to standard error.

current cutting edge observational techniques are used, indicating the utility of the method improves as our observational techniques improve.

However, such high accuracy instruments are not always available, and one question remains on how one should proceed in practice based on these limitations for general observational methods. It is important to note that distributional similarity methods not just including Goodness of Split are in general a powerful method to help us solve inverse problems of these nature (as demonstrated in the absence of selection effects), so ideally we would like to be able to make use of them. However, the results demonstrated that such methods in general have considerable shortcomings in the face of strong selection effects.

In the face of limited resources however, the question arises: what is the cutoff? One possible future development of this work then would be to change the selection effects steadily against many (q, S) distributions and attempt to demonstrate how the expected performance of these distribution-comparison algorithms change. This at least would give us an estimate on the confidence intervals for the parameter estimates. One could then say how much they should trust parameter estimates computed using data from real life equipments with different levels of fidelity.

This idea with a hypothetical example in Table 4.4. In this table, we take possible "selection effect parameters" (such as $S_{\min}$, $S_{\max}$, and any other relevant selection effects one is interested in). For every single combination of these selection parameters, one could draw 1000s of random parameter sets (α, μ, σ). A test set can be created for each one and the algorithm is run to get an estimate of the true parameters, as well as a measure the error of the estimate. By averaging over 1000s of random parameter sets one would be able to get confidence intervals for all these estimates and create a look-up table.

In principle after getting observed binary data with known selection effects the astronomer could use the BST-GOS method as described and get parameter estimates. Then from the look-up table described above, they can get a confidence interval and add this to report their results.

Where resources *are* available, the analysis indicates that results can be improved by minimising selection effects, by observing wider range stars using strong telescopes with higher resolutions like VLT with adaptive optics. They are designed to observe wide range binaries and sensitive to high contrast of binary luminosity. Observing the deep sky for a long time can help retrieve more stars, and as demonstrated in the final set of examples, the BST-GOS algorithm performed much more strongly. Specifically, much of the accuracy gains seem to arise from expanding the selection limits, and improvements in the contrast sensitivity did not add a great deal of extra performance.

In conclusion, this chapter introduced a method to retrieve the properties of binary systems in observed stellar regions by measuring distributional similarity. It was shown that in principle the method works very well by retrieving true parameters without selection effects, but the distribution truncation with selection effects changes performance drastically. However, in the process of doing so we were able to demonstrate the role selection effects play in our efforts to retrieve parameters, and how by reducing the impact of truncation one can improve performance. Hopefully this provides a basis for future work that shows how the parameter estimates change as selection effects vary. The hope is that in future the Goodness of Split method can be utilised further to help us explore observational binary data.

Table 4.5: Terminology used in this chapter

Term	meaning
a	Semimajor axis
$f_{\rm bin}$	Binary Fraction
μ	Semimajor axis mean
σ	Semimajor axis standard deviation
e	Eccentricity
f_e	Eccentricity type
α	Mass ratio distribution parameter
GOS	Goodness of Split
n,	No of stellar systems
S	Binary Separation
q	Binary Mass ratio
$\hat{\Phi}$	Av. parameter values of top 1 percentile of GOS
subscript T	"test"
- MC	Monte Carlo (fake)
-vis	Can be seen after selection effect
- min	Minimum
- max	Maximum

Chapter 5

Conclusions

This thesis has been focused on exploring various statistical characteristics of star clusters - binary fractions, binary distribution properties and initial mass functions. In each of these cases, computational, statistical and analytic methods were combined to provide new perspectives on important questions in astrophysics. In this final chapter, the key results are briefly reviewed and ideas for future directions are proposed.

Much of the thesis (Chapters 2 and 4) has focused on binary systems. Most stars usually form in binary systems, and they are an integral part of our understanding of stellar processes, as studies of their orbits are the only means of directly determining stellar mass. The mass of a star is, in turn, important for understanding the formation, evolution and characteristics (radius, density etc.) of stars via different models. The origin of the binary separation/period distribution and the mass related multiplicity fraction is an important research area in star formation theory (Krumholz 2015). Therefore, studying binary stars are essential to estimate the initial mass function (the mass distribution of stars at birth) of a cluster. The IMF is thought to be one of the most important distributions in astrophysics. Almost all inferences of properties for unresolved stellar populations, models of galaxy formation and the ISM depend on an assumed form of the IMF (Krumholz 2015). In summary, therefore, the detection and resolution of binary stars are a critical step in building our understanding of the universe, so much time was dedicated in this work to studying how to better measure their frequency and distribution.

Within the realm of binary systems, two major questions were addressed. Firstly - how can we better measure the prevalence of binary systems across clusters that have varied morphologies? Secondly - what is the impact of observational selection effects in distorting our estimates of the properties of binary systems?

The first question forms the basis of Chapter 2. Star clusters can come with dif-

ferent patterns or "morphologies" - sub-structured, uniform etc. For example, young clusters are found to be clumpy and they gather mostly in the dense region of molecular gas. Current methods such as 2PCF can be used to statistically measure binary fractions in clusters. However, different morphologies can distort such methods, as it can mean stars that are close by virtue of being in a dense clump are mistaken for binary systems, and vice versa. Therefore, cluster morphology and density can add an error to the measured binary fraction.

A method was therefore developed to estimate the binary fractions of stellar objects in a cluster that is not dependent on cluster density and morphology. The key insight was to use ratios of distances instead of raw distances themselves, which helped mitigate density and morphology effects. From stellar positions in a cluster, we can calculate first and tenth-nearest neighbour ratio, d_1/d_{10} for all the stars and determine their cumulative distribution. If the cumulative distribution fits a single Gaussian CDF, then there is only one particular population, either 100% single or 100% binary. An extremely small d_1/d_{10} would indicate 100% binary, it would be 100% single otherwise. If the cumulative distribution fits a double Gaussian CDF, we can interpret that the cluster is composed of both single and binary stellar systems. From the Double Gaussian fit, we can get an estimated value of binary fractions in the star cluster. From a simulation study, it was shown that the estimates are accurate against simulated data with a given binary fraction (with a difference of only around 5%-15%).

The second question regarding binary systems asked how observational selection effects might impact the ability to infer properties of the systems. The selection effects occur when contrast sensitivity and angular separation of members do not allow us to resolve them as a binary system. Tight binaries can be resolved when their angular separation is within the limit of the angular resolution of the telescope. For very wide binaries it is difficult to measure the separation and in many cases can only be resolved with time-intensive common proper motion methods. So, generally in a star cluster, only binary pairs with certain separations and mass ratios can be resolved.

In Chapter 4 it was investigated whether there is a suitable method to reconstruct the original properties of parent cluster from the distorted observed cluster. A Monte Carlo method was first developed to simulate distributions of observed binary pairs, in particular the distributions of the mass ratios (q) and separations (S), all parameterised by a small set of distributional parameters α, σ, μ. Then, for a given empirical dataset of (q, S) for an "observed" cluster, the idea was to compare the closeness of this observed cluster distribution with all the possible Monte Carlo distributions that

could be generated over a large grid of potential parameter values. The closeness of the 2-d (q, S) distributions were measured with a BST-GOS approach, which efficiently computes a measure of similarity between two 2-dimensional datasets. The generated Monte Carlo distributions that had (q, S) distributions closest to our observed set were taken as the best matches, and the (average) of their parameters are used as an estimate for the true parameters of the observed cluster.

This method was then applied to three scenarios:

- For the first scenario, there were no selection effects to the test samples or the Monte Carlo simulated populations. In this situation, the method was able to retrieve the true underlying distribution with high accuracy.

- For the second scenario, strong selection effects typical of those found in the literature (Duchene et al. 1999, Reipurth, Guimaraes, Connelley & Bally 2007, Lafreniere et al. 2008) were applied to both the sample and Monte Carlo populations. The estimates of parameters were considerably less accurate than the first case, though some distributional and selection effect parameters led to worse accuracy than others. Investigating the difference in these results provided an important understanding of why the distribution-comparison method did not work - the truncation of the (q, S) distribution down to an observable window obscures features of the distribution that help distinguish it from others distributions (such as the tails).

- For the third scenario, an "intermediate" case was chosen. Instead of choosing selection effects found in general observational studies, it considered cutting-edge (and even near future) observation techniques such as AO and interferometry (Ward-Duong et al. 2015), where selection effects are not as severe. The minimum and maximum separations and contrast sensitivities were taken from the literature (Raghavan et al. 2010, Ward-Duong et al. 2015). What was found was that even though selection effects were far from eliminated (about a quarter of systems were obscured from the samples), the accuracy in the binary parameters was quite high, and very close to the levels achieved without any selection effects at all.

In conclusion, while the BST-GOS method shows limited accuracy when selection effects are too severe, cutting edge and near-future technologies can leverage it to produce quite accurate estimates of underlying binary system properties.

Beyond binary systems, Chapter 3 focused instead on the Initial Mass Function, the distribution of stellar masses at birth. Stellar mass distribution in a cluster is

important to understand the star formation process, which could be different for high or low mass stars. In astronomy, the IMF is considered to be universal (it is the same everywhere in space) though there are evidence of non-universality. The precise shape of the IMF is also important, and there is a debate around the idea of "canonical parameters" that given the shapes of the high and low mass distributions. For example, if the fitted parameters show the value of α is higher than the canonical window tolerance and γ is less, then the IMF is called top-heavy and when the opposite happens IMF is bottom-heavy. The accuracy of these canonical parameters are obviously important, because they are used to reason about various astrophysical phenomenon. For example in the case of galaxies, these top and bottom heavy IMFs can be linked to causal processes in galaxy chemical evaluation (Bekki 2013, De Masi et al. 2019). Furthermore, for simulation work, the canonical IMF is often taken as a starting point to generate distributions of stars (e.g. in (Lamb et al. 2010, Howard et al. 2014, Hopkins 2018, Bottrill et al. 2020, Hirai et al. 2020), to name a few). The conclusions of such studies are obviously pretty heavily affected if the canonical form is not correct.

Rather than tackle the question of Universality or Canonicity directly, the focus in Chapter 3 was to examine some of the methods used to analyse IMFs in the first place. In particular, the observation was that the study of IMFs place heavy emphasis on functional forms and parametric fits. This is great for convenience, but these are by nature simplifications of rich distributions, which can in principle result in misleading inferences when asking subtle questions such as those regarding Universality.

In order to explore this, the following method was proposed: simulate a Monte Carlo star formation process that produces IMFs that match, at least qualitatively, the samples we typically encounter in real studies. However, allow for some important differences to be modelled: one set of simulations where the population distribution was Universal and matched Canonical parameters (Canonical Hypothesis), one where the population distribution was universal and matched non-Canonical parameters (Non-Canonical Hypothesis), and finally one where the samples drawn at different times were from different distributions (Non-Universal Hypothesis). Parameter fitting and matching methods used in typical astrophysical studies were then applied to these generated samples, with the intention to see if they could distinguish which Hypothesis had generated the samples.

The results showed that these methods were quite unsuccessful in distinguishing the Hypotheses, especially at the sample sizes typically encountered in real life. In some cases, the samples generated stronger evidence for the Hypothesis that was explicitly not true, than for the Hypothesis that was true. The reasons for this were

discussed, and in particular it was identified that the small sample sizes, heavy tailed distributions, and parameter-matching heuristics were together likely the root cause of these results.

In contrast, when non-parametric methods were applied, the Universal and Non-Universal hypotheses were much more easily distinguished from the data. This allowed us to lead to our general conclusions for the chapter: parametric analysis of IMFs has its place, but it must be used with caution when trying to draw subtle inferences, and in many cases non-parametric alternatives enforce fewer assumptions and provide more robust results.

Between the studies of Binary Systems and Initial Mass Functions, this thesis has hopefully made important contributions in the debate about how to best use statistical methods to learn about the key building blocks of our universe.

5.1 Future Work

5.1.1 Chapter 2: Finding Binary Star Fractions Using the Nearest Neighbour Ratio Method

The method in Chapter 2 was demonstrated using simulation data only (in order to demonstrate how close the answers were to the true binary fraction). An obvious next step would be to use real observational data with this algorithm and see if the results provided are informative.

One limitation of this investigation in turn however will be the fact that the method as described does not account for the impact of selection effects. In order for us to fully realise the potential of this method one should try to explicitly adjust for selection effects in the estimate of the binary fraction.

Besides searching for binary stars, this method can be potentially applicable to other datasets where detection of closer-than-usual pairs is important.

5.1.2 Chapter 3: Universality of the IMF

The main contribution of Chapter 3 was to show how simplifying assumptions in the form of the IMF can lead to erroneous conclusions about its true distribution. In our conclusions, it was touched on how this means that non-parametric methods might be better suited to drawing conclusions about the universality of the underlying IMF.

An interesting direction would be to continue this line of inquiry and compare more detailed non-parametric methods. One could for example attempt to com-

pare the multi-sample Anderson-Darling with other multi-sample tests, such as the Kruskal-Wallis tests Kruskal et al. (1952), Jonckheere-Terpstra tests Lehmann & D'Abrera (1975), etc. to see whether different tests were better suited to detecting Non-Universality.

5.1.3 Chapter 4: Finding binary properties by Binary Search Tree technique

In the conclusions in Chapter 4 it was discussed how by explicitly considering how the level of error changes with the severity of the selection effects, one could create a lookup table to show how much uncertainty should be in our conclusions about stellar data with selection effects. One future avenue would be to build this reference explicitly as a resource for future studies. This would allow us also to comment on the relative gains of improvements in observational techniques. For example, it was shown that cutting edge observational techniques with wider resolvable separation windows could detect the underlying parameters with a level of accuracy approaching the situation without selection effects. Improvements in the contrast sensitivities help to find more binary systems. However, at this level, these added systems had little to no improvement in the accuracy of retrieved parameters. It would be interesting to extend this analysis to see which improvements in accuracy could give the best return in terms of improvements in these results.

There are also a number of ways to see how much one can generalize the conclusions that were drawn. In particular, note that the methods rely on the similarity of two samples. The analysis made use of the BST-GOS method as it was computationally efficient and intuitive, but other more recent measures of sample similarity have been gaining probability that could be tested. In particular methods such as Maximum Mean Discrepancy (Gretton et al. 2012) or Wasserstein Distance (Ramdas et al. 2017) have been proposed in Machine Learning. Given the detailed analysis of how the shape of the truncated samples change under selection effects, it seems quite unlikely that any kind of distribution-matching measure would be more successful. Still, it would be useful at the very least to test this assumption, and potentially show which distance measures perform the best under increasingly strong selection effects.

Bibliography

Aarseth, S. J., Henon, M. & Wielen, R. (1974), 'A comparison of numerical methods for the study of star cluster dynamics', *Astronomy and Astrophysics* **37**, 183–187.

Abt, H. A. (2005), 'Observed orbital eccentricities', *The Astrophysical Journal* **629**(1), 507.

Adam, C. (2017), The multiplicity of intermediate and high-mass B-type stars in the near infrared= Die Multiplizität mittelschwerer und massereicher B-Sterne im Nahen Infrarot, PhD thesis.

Allen, P. R. (2007), 'Star formation via the little guy: A bayesian study of ultracool dwarf imaging surveys for companions', *The Astrophysical Journal* **668**(1), 492.

Allison, R. J., Goodwin, S. P., Parker, R. J., De Grijs, R., Zwart, S. F. P. & Kouwenhoven, M. (2009), 'Dynamical mass segregation on a very short timescale', *The Astrophysical Journal Letters* **700**(2), L99.

Alves, J., Lombardi, M. & Lada, C. (2007), 'The mass function of dense molecular cores and the origin of the imf', *Astronomy & Astrophysics* **462**(1), L17–L21.

Andersen, M., Meyer, M., Greissl, J. & Aversa, A. (2008), 'Evidence for a turnover in the initial mass function of low-mass stars and substellar objects: analysis from an ensemble of young clusters', *The Astrophysical Journal Letters* **683**(2), L183.

André, P., Di Francesco, J., Ward-Thompson, D., Inutsuka, S.-i., Pudritz, R. E. & Pineda, J. (2014), 'From filamentary networks to dense cores in molecular clouds: toward a new paradigm for star formation', *Protostars and Planets VI* pp. 27–51.

Andre, P., Ward-Thompson, D. & Barsony, M. (1999), 'From pre-stellar cores to protostars: The initial conditions of star formation', *arXiv astro-ph/9903284* .

André, Ph, W.-T. D. . B. M. (1993), *ApJ* **406**, 122.

Bahcall, J. & Soneira, R. (1981), 'The distribution of stars to v= 16th magnitude near the north galactic pole-normalization, clustering properties, and counts in various bands', *The Astrophysical Journal* **246**, 122–135.

Baines, D., Oudmaijer, R. D., Porter, J. M. & Pozzo, M. (2006), 'On the binarity of herbig ae/be stars', *Monthly Notices of the Royal Astronomical Society* **367**(2), 737–753.

Basri, G. & Reiners, A. (2006), 'A survey for spectroscopic binaries among very low mass stars', *The Astronomical Journal* **132**(2), 663.

Bastian, N., Covey, K. R. & Meyer, M. R. (2010), 'A universal stellar initial mass function? a critical look at variations', *Annual Review of Astronomy and Astrophysics* **48**, 339–389.

Basu, S. & Auddy, S. (2017), 'From molecular clouds to the imf: spatial and temporal effects', *arXiv preprint arXiv:1710.06361* .

Bate, M. R. (2005), 'The dependence of the initial mass function on metallicity and the opacity limit for fragmentation', *Monthly Notices of the Royal Astronomical Society* **363**(2), 363–378.

Bate, M. R. (2009), 'The dependence of star formation on initial conditions and molecular cloud structure', *Monthly Notices of the Royal Astronomical Society* **397**(1), 232–248.

Bate, M. R., Bonnell, I. A. & Bromm, V. (2002), 'The formation mechanism of brown dwarfs', *Monthly Notices of the Royal Astronomical Society* **332**(3), L65–L68.

Bate, M. R., Bonnell, I. A. & Bromm, V. (2003), 'The formation of a star cluster: predicting the properties of stars and brown dwarfs', *Monthly Notices of the Royal Astronomical Society* **339**(3), 577–599.

Beckwith, S. V. (1999), Circumstellar disks, *in* 'The Origin of Stars and Planetary Systems', Springer, pp. 579–612.

Bekki, K. (2013), 'Origin of a bottom-heavy stellar initial mass function in elliptical galaxies', *The Astrophysical Journal* **779**(1), 9.

Benedettini, M., Pezzuto, S., Schisano, E., André, P., Könyves, V., Men'shchikov, A., Ladjelate, B., Di Francesco, J., Elia, D., Arzoumanian, D. et al. (2018), 'A catalogue of dense cores and young stellar objects in the lupus complex based on herschel gould belt survey observations', *Astronomy & Astrophysics* **619**, A52.

Bergfors, C., Brandner, W., Janson, M., Daemgen, S., Geissler, K., Henning, T., Hippler, S., Hormuth, F., Joergens, V. & Köhler, R. (2010), 'Lucky imaging survey for southern m dwarf binaries', *Astronomy & Astrophysics* **520**, A54.

Bergin, E. A. & Tafalla, M. (2007), 'Cold dark clouds: the initial conditions for star formation', *Annu. Rev. Astron. Astrophys.* **45**, 339–396.

Biller, B., Allers, K., Liu, M., Close, L. M. & Dupuy, T. (2011), 'A keck lgs ao search for brown dwarf and planetary mass companions to upper scorpius brown dwarfs', *The Astrophysical Journal* **730**(1), 39.

Bolatto, A. D., Wolfire, M. & Leroy, A. K. (2013), 'The co-to-h2 conversion factor', *Annual Review of Astronomy and Astrophysics* **51**, 207–268.

Bonnell, I. A. (1994), 'A new binary formation mechanism', *Monthly Notices of the Royal Astronomical Society* **269**(3), 837–848.

Bonnell, I. A., Larson, R. B. & Zinnecker, H. (2006), 'The origin of the initial mass function', *arXiv preprint astro-ph/0603447* .

Bottrill, A. L., Haigh, M. E., Hole, M. R., Theakston, S. C., Allen, R. B., Grimmett, L. P. & Parker, R. J. (2020), 'Exoplanet detection and its dependence on stochastic sampling of the stellar initial mass function', *The Astrophysical Journal* **895**(2), 141.

Brandeker, A. & Cataldi, G. (2019), 'Contrast sensitivities in the gaia data release 2', *Astronomy & Astrophysics* **621**, A86.

Brunt, C. M. & Mac Low, M.-M. (2004), 'Modification of projected velocity power spectra by density inhomogeneities in compressible supersonic turbulence', *The Astrophysical Journal* **604**(1), 196.

Burgasser, A., Reid, I., Siegler, N., Close, L., Allen, P., Lowrance, P. & Gizis, J. (2007), 'Protostars and planets v, ed'.

Burgers, J. (1974), 'The nonlinear diffusion equation (dordrecht: Reidel)'.

Burkert, A. & Bodenheimer, P. (2000), 'Turbulent molecular cloud cores: Rotational properties', *The Astrophysical Journal* **543**(2), 822.

Caballero-Nieves, S. M., Gies, D. R., Baines, E. K., Bouchez, A. H., Dekany, R. G., Goodwin, S. P., Rickman, E. L., Roberts Jr, L. C., Taggart, K., ten Brummelaar,

T. A. & Turner, N. H. (2020), 'A high angular resolution survey of massive stars in cygnus ob2: Jhk adaptive optics results from the gemini near-infrared imager', *Monthly Notices of the Royal Astronomical Society* **-**(-), –.

Cappellari, M., McDermid, R. M., Alatalo, K., Blitz, L., Bois, M., Bournaud, F., Bureau, M., Crocker, A. F., Davies, R. L., Davis, T. A. et al. (2012), 'Systematic variation of the stellar initial mass function in early-type galaxies', *Nature* **484**(7395), 485.

Cartwright, A. & Whitworth, A. P. (2004), 'The statistical analysis of star clusters', *Monthly Notices of the Royal Astronomical Society* **348**(2), 589–598.

Chabrier, G. (2003), 'Galactic stellar and substellar initial mass function', *Publications of the Astronomical Society of the Pacific* **115**(809), 763.

Chabrier, G., Corbelli, E., Palla, F. & Zinnecker, H. (2005), 'Astrophysics and space science library, vol. 327, the initial mass function 50 years later'.

Chen, H., Myers, P., Ladd, E. & Wood, D. (1995), 'Bolometric temperature and young stars in the taurus and ophiuchus complexes', *The Astrophysical Journal* **445**, 377–392.

Chen, X., Arce, H. G., Zhang, Q., Bourke, T. L., Launhardt, R., Jørgensen, J. K., Lee, C.-F., Foster, J. B., Dunham, M. M., Pineda, J. E. et al. (2013), 'Sma observations of class 0 protostars: a high angular resolution survey of protostellar binary systems', *The Astrophysical Journal* **768**(2), 110.

Chini, R., Barr, A., Buda, L., Dembsky, T., Drass, H., Nasseri, A., Hoffmeister, V. & Fuhrmann, K. (2013), 'The multiplicity of high-mass stars', *arXiv preprint arXiv:1306.1811* .

Chini, R., Hoffmeister, V., Nasseri, A., Stahl, O. & Zinnecker, H. (2012), 'A spectroscopic survey on the multiplicity of high-mass stars', *Monthly Notices of the Royal Astronomical Society* **424**(3), 1925–1929.

Clemens, D. P., Yun, J. L. & Heyer, M. H. (1991), 'Bok globules and small molecular clouds-deep iras photometry and (c-12) o spectroscopy', *The Astrophysical Journal Supplement Series* **75**, 877–904.

Codella, C., Cabrit, S., Gueth, F., Podio, L., Leurini, S., Bachiller, R., Gusdorf, A., Lefloch, B., Nisini, B., Tafalla, M. et al. (2014), 'The alma view of the protostel-

lar system hh212-the wind, the cavity, and the disk', *Astronomy & Astrophysics* **568**, L5.

Collaboration, G. et al. (2016), 'The gaia mission', *arXiv preprint arXiv:1609.04153* .

Connelley, M. S., Reipurth, B. & Tokunaga, A. T. (2009), 'An adaptive optics survey for close protostellar binaries', *The Astronomical Journal* **138**(5), 1193.

Covey, K. R., Ivezić, Ž., Schlegel, D., Finkbeiner, D., Padmanabhan, N., Lupton, R. H., Agüeros, M. A., Bochanski, J. J., Hawley, S. L., West, A. A. et al. (2007), 'Stellar seds from 0.3 to 2.5 μm: Tracing the stellar locus and searching for color outliers in the sdss and 2mass', *The Astronomical Journal* **134**(6), 2398.

Crowther, P. A., Schnurr, O., Hirschi, R., Yusof, N., Parker, R. J., Goodwin, S. P. & Kassim, H. A. (2010), 'The r136 star cluster hosts several stars whose individual masses greatly exceed the accepted 150 m_{odot} stellar mass limit', *Monthly Notices of the Royal Astronomical Society* **408**(2), 731–751.

De Masi, C., Vincenzo, F., Matteucci, F., Rosani, G., La Barbera, F., Pasquali, A. & Spitoni, E. (2019), 'Is the imf in ellipticals bottom-heavy? clues from their chemical abundances', *Monthly Notices of the Royal Astronomical Society* **483**(2), 2217–2235.

De Rosa, R. J., Bulger, J., Patience, J., Leland, B., Macintosh, B., Schneider, A., Song, I., Marois, C., Graham, J. R., Bessell, M. et al. (2011), 'The volume-limited a-star (vast) survey–i. companions and the unexpected x-ray detection of b6–a7 stars', *Monthly Notices of the Royal Astronomical Society* **415**(1), 854–866.

De Rosa, R., Patience, J., Wilson, P., Schneider, A., Wiktorowicz, S., Vigan, A., Marois, C., Song, I., Macintosh, B., Graham, J. et al. (2013), 'The vast survey–iii. the multiplicity of a-type stars within 75 pc', *Monthly Notices of the Royal Astronomical Society* **437**(2), 1216–1240.

De Rosa, R., Patience, J., Wilson, P., Schneider, A., Wiktorowicz, S., Vigan, A., Marois, C., Song, I., Macintosh, B., Graham, J. et al. (2014), 'The vast survey–iii. the multiplicity of a-type stars within 75 pc', *Monthly Notices of the Royal Astronomical Society* **437**(2), 1216–1240.

Delfosse, X., Forveille, T., Ségransan, D., Beuzit, J.-L., Udry, S., Perrier, C. & Mayor, M. (2000), 'Accurate masses of very low mass stars: Iv improved mass-luminosity relations', *arXiv preprint astro-ph/0010586* .

Delgado-Donate, E. J., Clarke, C., Bate, M. & Hodgkin, S. (2004), 'On the properties of young multiple stars', *Monthly Notices of the Royal Astronomical Society* **351**(2), 617–629.

Dib, S. (2014), 'Testing the universality of the imf with bayesian statistics: young clusters', *Monthly Notices of the Royal Astronomical Society* **444**(2), 1957–1981.

Draine, B. (2011), 'Physics of the interstellar and intergalactic medium princeton univ', *Press Princeton, NJ* .

Duchene, G., Bouvier, J., Bontemps, S., André, P. & Motte, F. (2004), 'Multiple protostellar systems-i. a deep near infrared survey of taurus and ophiuchus protostellar objects', *Astronomy & Astrophysics* **427**(2), 651–665.

Duchêne, G., Bouvier, J., Moraux, E., Bouy, H., Konopacky, Q. & Ghez, A. (2013), 'Substellar multiplicity in the hyades cluster', *Astronomy & Astrophysics* **555**, A137.

Duchene, G., Bouvier, J. & Simon, T. (1999), 'Low-mass binaries in the young cluster ic 348: implications for binary formation and evolution', *arXiv preprint astro-ph/9901034* .

Duchêne, G. & Kraus, A. (2013), 'Stellar multiplicity', *Annual Review of Astronomy and Astrophysics* **51**.

Dunham, M. K., Robitaille, T. P., Evans, I. N. J., Schlingman, W. M., Cyganowski, C. J. & Urquhart, J. (2011), 'A mid-infrared census of star formation activity in bolocam galactic plane survey sources', *The Astrophysical Journal* **731**(2), 90.

Dunham, M. M., Stutz, A. M., Allen, L. E., Evans, I. N. J., Fischer, W. J., Megeath, S. T., Myers, P. C., Offner, S. S., Poteet, C. A., Tobin, J. J. et al. (2014), 'The evolution of protostars: insights from ten years of infrared surveys with spitzer and herschel', *Protostars and Planets VI* pp. 195–218.

Duquennoy, A. & Mayor, M. (1991), 'Multiplicity among solar-type stars in the solar neighbourhood. ii-distribution of the orbital elements in an unbiased sample', *Astronomy and Astrophysics* **248**, 485–524.

Elmegreen, B. G. & Scalo, J. (2004), 'Interstellar turbulence i: observations and processes', *Annu. Rev. Astron. Astrophys.* **42**, 211–273.

Enoch, M. L., Evans, I. N. J., Sargent, A. I., Glenn, J., Rosolowsky, E. & Myers, P. (2008), 'The mass distribution and lifetime of prestellar cores in perseus, serpens, and ophiuchus', *The Astrophysical Journal* **684**(2), 1240.

Enoch, M. L., Glenn, J., Evans, I. N. J., Sargent, A. I., Young, K. E. & Huard, T. L. (2007), 'Comparing star formation on large scales in the c2d legacy clouds: Bolocam 1.1 mm dust continuum surveys of serpens, perseus, and ophiuchus', *The Astrophysical Journal* **666**(2), 982.

Evans, I. N. J. (1999), 'Physical conditions in regions of star formation', *Annual Review of Astronomy and Astrophysics* **37**(1), 311–362.

Evans, I. N. J., Dunham, M. M., Jørgensen, J. K., Enoch, M. L., Merín, B., Van Dishoeck, E. F., Alcalá, J. M., Myers, P. C., Stapelfeldt, K. R., Huard, T. L. et al. (2009), 'The spitzer c2d legacy results: star-formation rates and efficiencies; evolution and lifetimes', *The Astrophysical Journal Supplement Series* **181**(2), 321.

Federrath, C. & Klessen, R. S. (2012), 'The star formation rate of turbulent magnetized clouds: comparing theory, simulations, and observations', *The Astrophysical Journal* **761**(2), 156.

Frank, A., Ray, T., Cabrit, S., Hartigan, P., Arce, H., Bacciotti, F., Bally, J., Benisty, M., Eislöffel, J., Güdel, M. et al. (2014), 'Jets and outflows from star to cloud: observations confront theory', *Protostars and planets VI* **1**, 451–474.

Garnavich, P. M. (1988), 'Wide binary stars at the galactic poles', *The Astrophysical Journal* **335**, L47–L51.

Garnett, D., Walsh, J., Chu, Y.-H. & Lasker, B. (1999), 'Bok globules in the large magellanic cloud', *The Astronomical Journal* **117**(3), 1285.

Goodman, J. & Hut, P. (1993), 'Binary-single-star scattering. v-steady state binary distribution in a homogeneous static background of single stars', *The Astrophysical Journal* **403**, 271–277.

Goodwin, S. P. (2010), 'Binaries in star clusters and the origin of the field stellar population', *Philosophical Transactions of the Royal Society A: Mathematical, Physical and Engineering Sciences* **368**(1913), 851–866.

Goodwin, S. P. (2012), 'Binary mass ratios: system mass not primary mass', *Monthly Notices of the Royal Astronomical Society: Letters* **430**(1), L6–L9.

Goodwin, S. P. & Kroupa, P. (2005), 'Limits on the primordial stellar multiplicity', *Astronomy & Astrophysics* **439**(2), 565–569.

Goodwin, S. P., Kroupa, P. & Goodman, A. Burkert, A. (2007), 'Protostars and planets v'.

Goodwin, S. P., Nutter, D., Kroupa, P., Ward-Thompson, D. & Whitworth, A. P. (2008), 'The relationship between the prestellar core mass function and the stellar initial mass function', *Astronomy & Astrophysics* **477**(3), 823–827.

Goodwin, S. P., Whitworth, A. P. & Ward-Thompson, D. (2004*a*), 'The dynamical evolution of fractal star clusters: the survival of substructure', *Astronomy & Astrophysics* **413**(3), 929–937.

Goodwin, S. P., Whitworth, A. P. & Ward-Thompson, D. (2004*b*), 'Simulating star formation in molecular cloud cores-i. the influence of low levels of turbulence on fragmentation and multiplicity', *Astronomy & Astrophysics* **414**(2), 633–650.

Gretton, A., Borgwardt, K. M., Rasch, M. J., Schölkopf, B. & Smola, A. (2012), 'A kernel two-sample test', *The Journal of Machine Learning Research* **13**(1), 723–773.

Griffiths, D. W., Goodwin, S. P. & Caballero-Nieves, S. M. (2018), 'Massive, wide binaries as tracers of massive star formation', *Monthly Notices of the Royal Astronomical Society* **476**(2), 2493–2500.

Grundy, W., Noll, K., Nimmo, F., Roe, H., Buie, M., Porter, S., Benecchi, S., Stephens, D., Levison, H. & Stansberry, J. (2011), 'Five new and three improved mutual orbits of transneptunian binaries', *Icarus* **213**(2), 678–692.

Grundy, W., Noll, K., Virtanen, J., Muinonen, K., Kern, S., Stephens, D., Stansberry, J., Levison, H. & Spencer, J. (2008), '(42355) typhon–echidna: Scheduling observations for binary orbit determination', *Icarus* **197**(1), 260–268.

Gullikson, K. & Dodson-Robinson, S. (2012), 'Detection of low-mass-ratio stellar binary systems', *The Astronomical Journal* **145**(1), 3.

Haas, M. & Anders, P. (2010), 'Variations in integrated galactic initial mass functions due to sampling method and cluster mass function', *Astronomy & Astrophysics* **512**, A79.

Haisch, J. K. E., Greene, T. P., Barsony, M. & Stahler, S. W. (2004), 'A near-infrared multiplicity survey of class i/flat-spectrum systems in six nearby molecular clouds', *The Astronomical Journal* **127**(3), 1747.

Halbwachs, J.-L. (1988), 'Statistical studies on wide pairs', *Astrophysics and Space Science* **142**(1-2), 237–244.

Halbwachs, J., Mayor, M., Udry, S. & Arenou, F. (2003), 'Multiplicity among solar–type stars-iii. statistical properties of the f7–k binaries with periods up to 10 years', *Astronomy & Astrophysics* **397**(1), 159–175.

Hennebelle, P. & Chabrier, G. (2008), 'Analytical theory for the initial mass function: Co clumps and prestellar cores', *The Astrophysical Journal* **684**(1), 395.

Hennebelle, P. & Chabrier, G. (2009), 'Analytical theory for the initial mass function. ii. properties of the flow', *The Astrophysical Journal* **702**(2), 1428.

Hennebelle, P. & Chabrier, G. (2011), 'Analytical star formation rate from gravoturbulent fragmentation', *The Astrophysical Journal Letters* **743**(2), L29.

Hippler, S. (2019), 'Adaptive optics for extremely large telescopes', *Journal of Astronomical Instrumentation* **8**(02), 1950001.

Hirai, Y., Fujii, M. S. & Saitoh, T. R. (2020), 'Sirius project i: Star formation models for star-by-star simulations of star clusters and galaxy formation', *arXiv preprint arXiv:2005.12906* .

Holman, K., Walch, S., Goodwin, S. & Whitworth, A. (2013), 'Mapping the core mass function on to the stellar initial mass function: multiplicity matters', *Monthly Notices of the Royal Astronomical Society* **432**(4), 3534–3543.

Hopkins, A. (2018), 'The dawes review 8: measuring the stellar initial mass function', *Publications of the Astronomical Society of Australia* **35**.

Hopkins, P. F. (2012), 'The stellar initial mass function, core mass function and the last-crossing distribution', *Monthly Notices of the Royal Astronomical Society* **423**(3), 2037–2044.

Howard, C. S., Pudritz, R. E. & Harris, W. E. (2014), 'Cluster formation in molecular clouds–i. stellar populations, star formation rates and ionizing radiation', *Monthly Notices of the Royal Astronomical Society* **438**(2), 1305–1317.

Inutsuka, S.-i. (2012), 'Present-day star formation: From molecular cloud cores to protostars and protoplanetary disks', *Progress of Theoretical and Experimental Physics* **2012**(1).

Inutsuka, S.-i. & Miyama, S. M. (1997), 'A production mechanism for clusters of dense cores', *The Astrophysical Journal* **480**(2), 681.

Janson, M., Hormuth, F., Bergfors, C., Brandner, W., Hippler, S., Daemgen, S., Kudryavtseva, N., Schmalzl, E., Schnupp, C. & Henning, T. (2012), 'The astralux large m-dwarf multiplicity survey', *The Astrophysical Journal* **754**(1), 44.

Jeans, J. (1919), 'The origin of binary systems', *Monthly Notices of the Royal Astronomical Society* **79**, 408.

Jeans, J. H. (1902), 'I. the stability of a spherical nebula', *Philosophical Transactions of the Royal Society of London. Series A, Containing Papers of a Mathematical or Physical Character* **199**(312-320), 1–53.

Johnstone, D., Wilson, C. D., Moriarty-Schieven, G., Joncas, G., Smith, G., Gregersen, E. & Fich, M. (2000), 'Large-area mapping at 850 microns. ii. analysis of the clump distribution in the ρ ophiuchi molecular cloud', *The Astrophysical Journal* **545**(1), 327.

JWST-User-Documentation (2016), 'Niriss aperture masking interferometry'.

King, R., Goodwin, S. P., Parker, R. J. & Patience, J. (2012b), 'Testing the universality of star formation–ii, comparing separation distributions of nearby star-forming regions and the field', *Monthly Notices of the Royal Astronomical Society* **427**(3), 2636–2646.

King, R., Parker, R. J., Patience, J. & Goodwin, S. P. (2012a), 'Testing the universality of star formation–i. multiplicity in nearby star-forming regions', *Monthly Notices of the Royal Astronomical Society* **421**(3), 2025–2042.

Köhler, R., Neuhäuser, R., Krämer, S., Leinert, C., Ott, T. & Eckart, A. (2008), 'Multiplicity of young stars in and around r coronae australis', *Astronomy & Astrophysics* **488**(3), 997–1006.

Kolmogorov, A. (1941), 'Akademiia nauk sssr doklady, 30, 301', *This translation by Levin, V* .

Kouwenhoven, M., Brown, A., Goodwin, S., Zwart, S. P. & Kaper, L. (2009), 'Exploring the consequences of pairing algorithms for binary stars', *Astronomy & Astrophysics* **493**(3), 979–1016.

Kouwenhoven, M., Brown, A., Zwart, S. P. & Kaper, L. (2007), 'The primordial binary population. ii.-recovering the binary population for intermediate mass stars in scorpius ob2', *Astronomy & Astrophysics* **474**(1), 77–104.

Kouwenhoven, M., Goodwin, S., Parker, R. J., Davies, M. B., Malmberg, D. & Kroupa, P. (2010), 'The formation of very wide binaries during the star cluster dissolution phase', *Monthly Notices of the Royal Astronomical Society* **404**(4), 1835–1848.

Kovaleva, D., Malkov, O., Yungelson, L. & Chulkov, D. (2016), 'Visual binary stars: data to investigate formation of binaries', *Open Astronomy* **25**(4), 419–426.

Kovaleva, D., Malkov, O., Yungelson, L., Chulkov, D. & Yikdem, G. (2015), 'Statistical analysis of a comprehensive list of visual binaries', *Open Astronomy* **24**(4), 367–378.

Kraus, A. L. & Hillenbrand, L. A. (2009), 'Unusually wide binaries: Are they wide or unusual?', *The Astrophysical Journal* **703**(2), 1511.

Kraus, A. L., Ireland, M. J., Martinache, F. & Hillenbrand, L. A. (2011), 'Mapping the shores of the brown dwarf desert. ii. multiple star formation in taurus-auriga', *The Astrophysical Journal* **731**(1), 8.

Kraus, A. L., Ireland, M. J., Martinache, F. & Lloyd, J. P. (2008), 'Mapping the shores of the brown dwarf desert. i. upper scorpius', *The Astrophysical Journal* **679**(1), 762.

Kroupa, P. (2001*a*), 'The initial mass function and its variation', *arXiv preprint astro-ph/0102155* .

Kroupa, P. (2001*b*), 'On the variation of the initial mass function', *Monthly Notices of the Royal Astronomical Society* **322**(2), 231–246.

Kroupa, P. (2002), 'The initial mass function of stars: evidence for uniformity in variable systems', *Science* **295**(5552), 82–91.

Kroupa, P., Tout, C. A. & Gilmore, G. (1993), 'The distribution of low-mass stars in the galactic disc', *Monthly Notices of the Royal Astronomical Society* **262**(3), 545–587.

Kroupa, P., Weidner, C., Pflamm-Altenburg, J., Thies, I., Dabringhausen, J., Marks, M. & Maschberger, T. (2013), 'The stellar and sub-stellar initial mass function of simple and composite populations', *Planets, Stars and Stellar Systems: Volume 5: Galactic Structure and Stellar Populations* pp. 115–242.

Kruijssen, J. D. (2012), 'On the fraction of star formation occurring in bound stellar clusters', *Monthly Notices of the Royal Astronomical Society* **426**(4), 3008–3040.

Krumholz, M. R. (2015), 'Notes on star formation', *preprint arXiv:1511.03457* .

Kruskal, W. H. et al. (1952), 'A nonparametric test for the several sample problem', *The Annals of Mathematical Statistics* **23**(4), 525–540.

Lada, C. (1987), 'Star forming regions (iau symp. 115), ed. m. peimbert & j. jugaku'.

Lada, C. J. (2006), 'Stellar multiplicity and the initial mass function: most stars are single', *The Astrophysical Journal Letters* **640**(1), L63.

Lada, C. J. & Lada, E. A. (2003), 'Embedded clusters in molecular clouds', *Annual Review of Astronomy and Astrophysics* **41**(1), 57–115.

Lafreniere, D., Jayawardhana, R., Brandeker, A., Ahmic, M. & van Kerkwijk, M. H. (2008), 'A multiplicity census of young stars in chamaeleon i', *The Astrophysical Journal* **683**(2), 844.

Lamb, J., Oey, M., Werk, J. & Ingleby, L. (2010), 'The sparsest clusters with o stars', *The Astrophysical Journal* **725**(2), 1886.

Larson, R. B. (1981), 'Turbulence and star formation in molecular clouds', *Monthly Notices of the Royal Astronomical Society* **194**(4), 809–826.

Lehmann, E. L. & D'Abrera, H. J. (1975), *Nonparametrics: statistical methods based on ranks.*, Holden-day.

Lomax, O., Whitworth, A. P., Hubber, D., Stamatellos, D. & Walch, S. (2014), 'Simulating star formation in ophiuchus', *Monthly Notices of the Royal Astronomical Society* **439**(3), 3039–3050.

Lombardi, M. & Alves, J. (2001), 'Mapping the interstellar dust with near-infrared observations: An optimized multi-band technique', *Astronomy & Astrophysics* **377**(3), 1023–1034.

Longhitano, M. (2011), 'Wide binary stars in the galactic field-a statistical approach', *arXiv preprint arXiv:1102.0533* .

Longhitano, M. & Binggeli, B. (2010), 'The stellar correlation function from sdss-a statistical search for wide binary stars', *Astronomy & Astrophysics* **509**, A46.

Luhman, K. L. (2012), 'The formation and early evolution of low-mass stars and brown dwarfs', *Annual Review of Astronomy and Astrophysics* **50**, 65–106.

Machida, M. N., Inutsuka, S.-i. & Matsumoto, T. (2009), 'First direct simulation of brown dwarf formation in a compact cloud core', *The Astrophysical Journal Letters* **699**(2), L157.

Machida, M. N. & Matsumoto, T. (2012), 'Impact of protostellar outflow on star formation: effects of the initial cloud mass', *Monthly Notices of the Royal Astronomical Society* **421**(1), 588–607.

Machida, M. N., Tomisaka, K., Matsumoto, T. & Inutsuka, S.-i. (2008), 'Formation scenario for wide and close binary systems', *The Astrophysical Journal* **677**(1), 327.

Marsh, K., Kirk, J. M., André, P., Griffin, M. J., Könyves, V., Palmeirim, P., Men'Shchikov, A., Ward-Thompson, D., Benedettini, M., Bresnahan, D. et al. (2016), 'A census of dense cores in the taurus l1495 cloud from the herschel gould belt survey', *Monthly Notices of the Royal Astronomical Society* **459**(1), 342–356.

Maschberger, T. (2013), 'On the function describing the stellar initial mass function', *Monthly Notices of the Royal Astronomical Society* **429**(2), 1725–1733.

Mason, B. D., Hartkopf, W. I., Gies, D. R., Henry, T. J. & Helsel, J. W. (2009), 'The high angular resolution multiplicity of massive stars', *The Astronomical Journal* **137**(2), 3358.

Masunaga, H. & Inutsuka, S.-i. (2000), 'A radiation hydrodynamic model for protostellar collapse. ii. the second collapse and the birth of a protostar', *The Astrophysical Journal* **531**(1), 350.

Masunaga, H., Miyama, S. M. & Inutsuka, S.-i. (1998), 'A radiation hydrodynamic model for protostellar collapse. i. the first collapse', *the Astrophysical Journal* **495**(1), 346.

Matzner, C. D. & McKee, C. F. (2000), 'Efficiencies of low-mass star and star cluster formation', *The Astrophysical Journal* **545**(1), 364.

McKee, C. F. & Ostriker, E. C. (2007), 'Theory of star formation', *Annu. Rev. Astron. Astrophys.* **45**, 565–687.

Meixner, M., Panuzzo, P., Roman-Duval, J., Engelbracht, C., Babler, B., Seale, J., Hony, S., Montiel, E., Sauvage, M., Gordon, K. et al. (2013), 'The herschel inventory of the agents of galaxy evolution in the magellanic clouds, a herschel open time key program', *The Astronomical Journal* **146**(3), 62.

Michell, J. (1767), 'N/a', *Phil. Trans. R. Soc.* **57**(234).

Moe, M. & Di Stefano, R. (2017), 'Mind your ps and qs: the interrelation between period (p) and mass-ratio (q) distributions of binary stars', *The Astrophysical Journal Supplement Series* **230**(2), 15.

Molinari, S., Swinyard, B., Bally, J., Barlow, M., Bernard, J.-P., Martin, P., Moore, T., Noriega-Crespo, A., Plume, R., Testi, L. et al. (2010), 'Clouds, filaments, and protostars: the herschel hi-gal milky way', *Astronomy & Astrophysics* **518**, L100.

Motte, F., André, P. & Neri, R. (1998), 'The initial conditions of star formation in the rho ophiuchi main cloud: wide-field millimeter continuum mapping', *Astronomy and Astrophysics* **336**, 150–172.

Murillo, N. M., Bruderer, S., van Dishoeck, E. F., Walsh, C., Harsono, D., Lai, S.-P. & Fuchs, C. M. (2015), 'A low-mass protostar's disk-envelope interface: disk-shadowing evidence from alma dco+ observations of vla1623', *Astronomy & Astrophysics* **579**, A114.

Myers, P. & Ladd, E. (1993), 'Bolometric temperatures of young stellar objects', *the Astrophysical Journal* **413**, L47–L50.

Nayak, O., Meixner, M., Indebetouw, R., De Marchi, G., Koekemoer, A., Panagia, N. & Sabbi, E. (2016), 'A study of the relation between star formation and molecular clumps on subparsec scales in 30 doradus', *The Astrophysical Journal* **831**(1), 32.

Nutter, D. & Ward-Thompson, D. (2007), 'A scuba survey of orion–the low-mass end of the core mass function', *Monthly Notices of the Royal Astronomical Society* **374**(4), 1413–1420.

Oey, M. (2011), 'On the origin of the salpeter slope for the initial mass function', *The Astrophysical Journal Letters* **739**(2), L46.

Oey, M. S. & Clarke, C. (2005), 'Statistical confirmation of a stellar upper mass limit', *The Astrophysical Journal Letters* **620**(1), L43.

Offner, S. S., Clark, P. C., Hennebelle, P., Bastian, N., Bate, M. R., Hopkins, P. F., Moraux, E. & Whitworth, A. P. (2014), 'The origin and universality of the stellar initial mass function', *Protostars and Planets VI* **1**, 53–75.

Öpik, E. J. (1924), '–', *Tartu Obs* **25**(6), –.

Padoan, P., Federrath, C., Chabrier, G., Evans, N., Johnstone, D., Jørgensen, J. K., McKee, C. F. & Nordlund, Å. (2014), 'The star formation rate of molecular clouds', *Protostars and Planets VI* pp. 77–100.

Padoan, P., Jones, B. J. & Nordlund, Å. P. (1997), 'Supersonic turbulence in the interstellar medium: stellar extinction determinations as probes of the structure and dynamics of dark clouds', *The Astrophysical Journal* **474**(2), 730.

Padoan, P. & Nordlund, Å. (2002), 'The stellar initial mass function from turbulent fragmentation', *The Astrophysical Journal* **576**(2), 870.

Padoan, P. & Nordlund, Å. (2011), 'The star formation rate of supersonic magneto-hydrodynamic turbulence', *The Astrophysical Journal* **730**(1), 40.

Parker, R. J., Goodwin, S. P. & Allison, R. J. (2011), 'The evolution of binary populations in cool, clumpy star clusters', *Monthly Notices of the Royal Astronomical Society* **418**(4), 2565–2575.

Parker, R. J. & Meyer, M. R. (2014), 'Binaries in the field: fossils of the star formation process?', *Monthly Notices of the Royal Astronomical Society* **442**(4), 3722–3736.

Parravano, A., Hollenbach, D. & McKee, C. F. (2018), 'The high-mass slope of the imf', *Monthly Notices of the Royal Astronomical Society* **480**(2), 2449–2465.

Parravano, A., McKee, C. F. & Hollenbach, D. J. (2010), 'An initial mass function for individual stars in galactic disks. i. constraining the shape of the initial mass function', *The Astrophysical Journal* **726**(1), 27.

Pettini, M. (2009), 'Lecture 14: Structure and evolution of stars'.

Piétu, V., Guilloteau, S., Di Folco, E., Dutrey, A. & Boehler, Y. (2014), 'Faint disks around classical t tauri stars: small but dense enough to form planets', *Astronomy & Astrophysics* **564**, A95.

Plummer, H. C. (1911), 'On the problem of distribution in globular star clusters', *Monthly notices of the royal astronomical society* **71**, 460–470.

Polychroni, D., Schisano, E., Elia, D., Roy, A., Molinari, S., Martin, P., André, P., Turrini, D., Rygl, K., Di Francesco, J. et al. (2013), 'Two mass distributions in the l 1641 molecular clouds: the herschel connection of dense cores and filaments in orion a', *The Astrophysical Journal Letters* **777**(2), L33.

Pomohaci, R., Oudmaijer, R. D. & Goodwin, S. P. (2019), 'A pilot survey of the binarity of massive young stellar objects with k-band adaptive optics', *Monthly Notices of the Royal Astronomical Society* **484**(1), 226–238.

Price, D. J., Tricco, T. S. & Bate, M. R. (2012), 'Collimated jets from the first core', *Monthly Notices of the Royal Astronomical Society: Letters* **423**(1), L45–L49.

Pudritz, R., Ouyed, R., Fendt, C., Brandenburg, A., Reipurth, B., Jewitt, D. & Keil, K. (2007), 'Protostars and planets v', *University of Arizona Press, Tucson* p. 277.

Raghavan, D., McAlister, H. A., Henry, T. J., Latham, D. W., Marcy, G. W., Mason, B. D., Gies, D. R., White, R. J. & Theo, A. (2010), 'A survey of stellar families: multiplicity of solar-type stars', *The Astrophysical Journal Supplement Series* **190**(1), 1.

Ramdas, A., Trillos, N. G. & Cuturi, M. (2017), 'On wasserstein two-sample testing and related families of nonparametric tests', *Entropy* **19**(2), 47.

Ratzka, T., Köhler, R. & Leinert, C. (2005), 'A multiplicity survey of the ρ ophiuchi molecular clouds', *Astronomy & Astrophysics* **437**(2), 611–626.

Rawiraswattana, K. (2012), The Dynamics of Disks and Stars in Multiple Systems, PhD thesis, University of Sheffield.

Reipurth, B. & Clarke, C. (2001), 'The formation of brown dwarfs as ejected stellar embryos', *The Astronomical Journal* **122**(1), 432.

Reipurth, B., Guimaraes, M. M., Connelley, M. S. & Bally, J. (2007), 'Visual binaries in the orion nebula cluster', *The Astronomical Journal* **134**(6), 2272.

Reipurth, B., Jewitt, D. & Keil, K. (2007), *Protostars and Planets V*, University of Arizona Press.

Reipurth, B. & Zinnecker, H. (1993), 'Visual binaries among pre-main sequence stars', *Astronomy and Astrophysics* **278**, 81–108.

Rigby, A. J. (2016), Molecular clouds and star formation in the Inner Galaxy, PhD thesis, Liverpool John Moores University.

Rivilla, V., Jiménez-Serra, I., Martín-Pintado, J. & Sanz-Forcada, J. (2013), 'The role of low-mass star clusters in forming the massive stars in dr 21', *Monthly Notices of the Royal Astronomical Society* **437**(2), 1561–1575.

Roman-Duval, J., Jackson, J. M., Heyer, M., Rathborne, J. & Simon, R. (2010), 'Physical properties and galactic distribution of molecular clouds identified in the galactic ring survey', *The Astrophysical Journal* **723**(1), 492.

Rosolowsky, E., Pineda, J., Kauffmann, J. & Goodman, A. (2008), 'Structural analysis of molecular clouds: Dendrograms', *The Astrophysical Journal* **679**(2), 1338.

Sahlmann, J., Martín-Fleitas, J., Mora, A., Abreu, A., Crowley, C. & Joliet, E. (2016), Enabling science with gaia observations of naked-eye stars, *in* 'Space Telescopes and Instrumentation 2016: Optical, Infrared, and Millimeter Wave', Vol. 9904, International Society for Optics and Photonics, p. 99042E.

Salpeter, E. E. (1955), 'The luminosity function and stellar evolution.', *The Astrophysical Journal* **121**, 161.

Sana, H. & Evans, C. (2011), 'Active ob stars: Structure, evolution, mass loss, and critical limits (iau symp. 272), ed'.

Scalo, J. & Elmegreen, B. G. (2004), 'Interstellar turbulence ii: implications and effects', *Annu. Rev. Astron. Astrophys.* **42**, 275–316.

Schisano, E., Rygl, K. L. J., Molinari, S., Busquet, G., Elia, D., Pestalozzi, M., Polychroni, D., Billot, N., Carey, S., Paladini, R. et al. (2014), 'The identification of filaments on far-infrared and submillimiter images: Morphology, physical conditions and relation with star formation of filamentary structure', *The Astrophysical Journal* **791**(1), 27.

Scholz, F. W. & Stephens, M. A. (1987), 'K-sample anderson–darling tests', *Journal of the American Statistical Association* **82**(399), 918–924.

Segransan, D., Kervella, P., Forveille, T. & Queloz, D. (2003), 'First radius measurements of very low mass stars with the vlti', *Astronomy & Astrophysics* **397**(3), L5–L8.

Simon, J. D. (2018), 'Gaia proper motions and orbits of the ultra-faint milky way satellites', *The Astrophysical Journal* **863**(1), 89.

Simpson, R., Nutter, D. & Ward-Thompson, D. (2008), 'The initial conditions of star formation–viii. an observational study of the ophiuchus cloud l1688 and implications for the pre-stellar core mass function', *Monthly Notices of the Royal Astronomical Society* **391**(1), 205–214.

Struve, F. G. W. (1852), 'Stellarum fixarum imprimis duplicium et multiplicium positiones mediae pro epocha 1830.0, deductae ex observationibus meridianis annis 1822 ad 1843 in specula dorpatensi institutis', *Petropoli, ex Typographia academica, 1852.* .

Sun, H., Kasdin, N. J. & Vanderbei, R. (2020), 'Efficient wavefront sensing for space-based adaptive optics', *Journal of Astronomical Telescopes, Instruments, and Systems* **6**(1), 019001.

Tafalla, M., Myers, P., Caselli, P. & Walmsley, C. (2004), 'On the internal structure of starless cores-i. physical conditions and the distribution of co, cs, n2h, and nh3 in l1498 and l1517b', *Astronomy & Astrophysics* **416**(1), 191–212.

Testi, L. & Sargent, A. I. (1998), 'Star formation in clusters: A survey of compact millimeter-wave sources in the serpens core', *The Astrophysical Journal Letters* **508**(1), L91.

Thies, I. & Kroupa, P. (2007), 'A discontinuity in the low-mass initial mass function', *The Astrophysical Journal* **671**(1), 767.

Tobin, J. J., Hartmann, L., Chiang, H.-F., Wilner, D. J., Looney, L. W., Loinard, L., Calvet, N. & D'alessio, P. (2012), 'A 0.2-solar-mass protostar with a keplerian disk in the very young l1527 irs system', *Nature* **492**(7427), 83.

Tobin, J., Looney, L., Li, Z.-Y., Chandler, C., Dunham, M., Segura-Cox, D., Sadavoy, S., Melis, C., Harris, R. & Kratter, K. (2016), 'The vla nascent disk and multiplicity survey of perseus protostars (vandam). ii. multiplicity of protostars in the perseus molecular cloud', *The Astrophysical Journal* **818**(1), 73.

Tohline, J. E. (2002), 'The origin of binary stars', *Annual Review of Astronomy and Astrophysics* **40**(1), 349–385.

Tokovinin, A. & Kiyaeva, O. (2015), 'Eccentricity distribution of wide binaries', *Monthly Notices of the Royal Astronomical Society* **456**(2), 2070–2079.

Toomre, A. (1964), 'On the gravitational stability of a disk of stars', *The Astrophysical Journal* **139**, 1217–1238.

Treu, T., Auger, M. W., Koopmans, L. V., Gavazzi, R., Marshall, P. J. & Bolton, A. S. (2010), 'The initial mass function of early-type galaxies', *The Astrophysical Journal* **709**(2), 1195.

Van Dokkum, P. G. & Conroy, C. (2011), 'Confirmation of enhanced dwarf-sensitive absorption features in the spectra of massive elliptical galaxies: further evidence for a non-universal initial mass function', *The Astrophysical Journal Letters* **735**(1), L13.

Walch, S., Naab, T., Whitworth, A., Burkert, A. & Gritschneder, M. (2010), 'Protostellar discs formed from turbulent cores', *Monthly Notices of the Royal Astronomical Society* **402**(4), 2253–2263.

Ward-Duong, K., Patience, J., De Rosa, R., Bulger, J., Rajan, A., Goodwin, S., Parker, R. J., McCarthy, D. & Kulesa, C. (2015), 'The m-dwarfs in multiples (minms) survey–i. stellar multiplicity among low-mass stars within 15 pc', *Monthly Notices of the Royal Astronomical Society* **449**(3), 2618–2637.

Weidner, C. & Kroupa, P. (2006), 'The maximum stellar mass, star-cluster formation and composite stellar populations', *Monthly Notices of the Royal Astronomical Society* **365**(4), 1333–1347.

Wheelwright, H., Oudmaijer, R. & Goodwin, S. (2010), 'The mass ratio and formation mechanisms of herbig ae/be star binary systems', *Monthly Notices of the Royal Astronomical Society* **401**(2), 1199–1218.

Whittet, D. (2015), 'Interstellar dust', *Encyclopedia of Astrobiology* pp. 1232–1236.

Whitworth, A. & Lomax, O. (2016), 'A theoretical perspective on the formation and fragmentation of protostellar discs', *Publications of the Astronomical Society of Australia* **33**.

Yoo, J., Chaname, J. & Gould, A. (2004), 'The end of the macho era: limits on halo dark matter from stellar halo wide binaries', *The Astrophysical Journal* **601**(1), 311.

Zheng, Z., Flynn, C., Gould, A., Bahcall, J. N. & Salim, S. (2001), 'M dwarfs from hubble space telescope star counts. iv.', *The Astrophysical Journal* **555**(1), 393.

Ziegler, C., Law, N. M., Baranec, C., Morton, T., Riddle, R., De Lee, N., Huber, D., Mahadevan, S. & Pepper, J. (2018), 'Measuring the recoverability of close binaries in gaia dr2 with the robo-ao kepler survey', *The Astronomical Journal* **156**(6), 259.